Design of new nanostructured materials for application in biosensorics; theoretical study of optical properties of noble metal bio-nano hybrids

Perić Bakulić, Martina

Doctoral thesis / Disertacija

2022

Degree Grantor / Ustanova koja je dodijelila akademski / stručni stupanj: **University of Split, Faculty of Science / Sveučilište u Splitu, Prirodoslovno-matematički fakultet**

Permanent link / Trajna poveznica: https://urn.nsk.hr/urn:nbn:hr:166:134502

University of Split
Faculty of Science
Postgraduate university study in biophysics

Doctoral thesis

DESIGN OF NEW NANOSTRUCTURED MATERIALS FOR APPLICATION IN BIOSENSORICS; THEORETICAL STUDY OF OPTICAL PROPERTIES OF NOBLE METAL BIO-NANO HYBRIDS

Martina Perić Bakulić

Split, July 2022

Sveučilište u Splitu
Prirodoslovno-matematički fakultet
Poslijediplomski sveučilišni studij biofizike

Doktorski rad

DIZAJN NOVIH NANOSTRUKTURNIH MATERIJALA ZA PRIMJENU U BIOSENZORICI; TEORIJSKO ISTRAŽIVANJE OPTIČKIH SVOJSTAVA BIO-NANO HIBRIDA PLEMENITIH METALA

Martina Perić Bakulić

Split, srpanj 2022.

Sveučilište u Splitu, Prirodoslovno-matematički fakultet

Odjel za fiziku, Poslijediplomski sveučilišni doktorski studij Biofizika

"DIZAJN NOVIH NANOSTRUKTURNIH MATERIJALA ZA PRIMJENU U BIOSENZORICI; TEORIJSKO ISTRAŽIVANJE OPTIČKIH SVOJSTAVA BIO-NANO HIBRIDA"

Doktorski rad autorice Martine Perić Bakulić kao dio obaveza potrebnih da se dobije doktorat znanosti, izrađen je pod vodstvom mentorice prof. dr. dr. h. c. Vlaste Bonačić-Koutecký i komentora prof. dr. sc. Mile Dželalije.

Dobiveni akademski naziv i stupanj: doktorica prirodnih znanosti iz polja fizika.

Povjerenstvo za ocjenu i obranu doktorskog rada u sastavu:

1. _____

   prof. dr. sc. Ante Bilušić

   (Prirodoslovno-matematički fakultet u Splitu, predsjednik)

2. _____

   doc. dr. sc. Viljemka Bučević-Popović

   (Prirodoslovno-matematički fakultet u Splitu, članica)

3. _____

   prof. dr. sc. Katarina Vukojević

   (Medicinski fakultet u Splitu, članica)

Potvrđuje da je disertacija obranjena dana _____

Voditelj studija: prof. dr. sc. Mile Dželalija

_____

Dekan: prof. dr. sc. Nikola Koceić-Bilan

_____

BASIC DOCUMENTATION CARD

University of Split, Faculty of Science Ph.D. thesis

DESIGN OF NEW NANOSTRUCTURED MATERIALS FOR APPLICATION IN BIOSENSORICS; THEORETICAL STUDY OF OPTICAL PROPERTIES OF NOBLE METAL BIO-NANO HYBRIDS

Martina Perić Bakulić

Thesis performed at

- Center of Excellence for Science and Technology - Integration of Mediterranean Region (STIM) at Interdisciplinary center for Advanced science and technology (ICAST), Faculty of Science, University of Split
- Institut Lumière Matière, UMR CNRS 5306 and Université Claude Bernard Lyon 1, Université de Lyon, France
- The Mediterranean Institute for Life Sciences (MedILS), Split, Croatia

Abstract:

The focus of this doctoral thesis is to address the linear and nonlinear optical properties of noble metal nanoclusters (NCs) belonging to the nonscalable regime (~ 2 nm). They can be embedded in the biological environment as bio-nano hybrids or protected with biomolecules as liganded NCs. Compared to standard bioimaging techniques (organic dyes and quantum dots) better sensitivity can be reached with the combination of two-photon spectroscopy and noble metal bio-nano systems. The research presented in this doctoral thesis is based on an investigation by computational chemistry methods. The combination of the QM/MM method with Density Functional Theory (DFT) and its time-dependent version (TD-DFT) allows the determination of structural and optical properties for bio-nano hybrids (silver trimer intercalated in DNA and silver doped gold-cysteine supramolecular assemblies) and liganded NCs ($Au_{10}SG_{10}$, $Au_{12}Zwitterions_4$, and $Au_{15}SG_{13}$ NCs). Research in this doctoral thesis demonstrated that their unique optical properties (huge fluorescence for investigated bio-nano hybrids and bio-labeling capacity of liganded NCs) have the potential for applications in bioimaging and medical diagnostics. New routes of theoretical exploration are expected to lead the research towards biosensorics of superior sensitivity. Theoretical results will be compared with experimental results obtained by expert collaborators.

(122 pages, 32 figures, 2 cover pages, 6 tables, 72 references, 2 appendices, original in English)

Thesis deposited in:
- National and University Library in Zagreb
- University Library in Split
- Library of the Faculty of Science, University of Split

Keywords: DFT, TD-DFT, linear and nonlinear optical properties, noble metal NCs, bio-nano hybrids, QM/MM,

Supervisor: Prof. Vlasta Bonačić-Koutecký, dr. dr. h. c.
Co-supervisor: Prof. Mile Dželalija, Ph. D.

Reviewers:
1. Prof. Ante Bilušić, Ph. D.
2. Assoc. Prof. Viljemka Bučević-Popović, Ph. D.
3. Prof. Katarina Vukojević, Ph. D.

Thesis accepted: 13.07.2022.

TEMELJNA DOKUMENTACIJSKA KARTICA

Sveučilište u Splitu, Prirodoslovno-matematički fakultet Doktorski rad

DIZAJN NOVIH NANOSTRUKTURNIH MATERIJALA ZA PRIMJENU U BIOSENZORICI; TEORIJSKO ISTRAŽIVANJE OPTIČKIH SVOJSTAVA BIO-NANO HIBRIDA PLEMENITIH METALA

Martina Perić Bakulić

Rad je izrađen na:

- Centru izvrsnosti za znanost i tehnologiju-Integracija Mediteranske regije (STIM) pri Interdisciplinarnom centru za naprednu znanost i tehnologiju (ICAST), Prirodoslovno-matematički fakultet, Sveučilište u Splitu
- Institut Lumière Matière, UMR CNRS 5306 i Sveučilištu Claude Bernard Lyon 1, Sveučilište u Lyonu, Francuska
- Mediteranskom institutu za istraživanje života (MedILS), Split, Hrvatska

Sažetak:

Težište ovog doktorskog rada počiva na linearnim i nelinearnim optičkim svojstvima nanoklastera plemenitih metala koji pripadaju neskalirajućim sustavima (~ 2 nm). Mogu biti ugrađeni u biološki okoliš kao bio-nano hibridi ili zaštićeni biomolekulama kao ligandirani nanoklasteri. U usporedbi sa standardnim tehnikama bio-oslikavanja u medicinskoj dijagnostici (organske boje i kvantne točke) bolja osjetljivost može se postići kombinacijom dvofotonske spektroskopije i bio-nano sustava plemenitih metala. Istraživanje predstavljeno u ovom doktorskom radu temelji se na metodama računalne kvantne kemije. Kombinacija QM/MM metode s teorijom funkcionala gustoće (DFT) i njezinom vremenski ovisnom inačicom (TD-DFT) omogućuje određivanje strukturnih i optičkih svojstava za bio-nano hibride (trimer srebra interkaliran u DNK i supramolekularni sklopovi zlata i cisteina dopirani s jednim atomom srebra) te ligandirane nanoklastere ($Au_{10}SG_{10}$, $Au_{12}Zwitterions_4$, i $Au_{15}SG_{13}$). Istraživanje u ovom doktorskom radu pokazalo je da njihova jedinstvena optička svojstva (intezivna fluorescencija kod bio-nano hibrida te značajan kapacitet u bio-označavanju kod ligandiranih nanoklastera) imaju potencijal za primjenu u bio-oslikavanju i medicinskoj dijagnostici. Očekuje se da će novi pravci teorijskog istraživanja voditi istraživanja prema biosenzorici visoke osjetljivosti. Teorijski rezultati će se usporediti s eksperimentalnim rezultatima dobivenim od strane eksperimentalnih stručnjaka.

(122 stranice, 32 slike, 2 naslovnice, 6 tablica, 72 citata, 2 priloga, jezik izvornika: engleski jezik)

Rad je pohranjen u:

- Nacionalnoj sveučilišnoj knjižnici u Zagrebu
- Sveučilišnoj knjižnici u Splitu
- Knjižnici Prirodoslovno-matematičkog fakulteta na Sveučilištu u Splitu

Ključne riječi: DFT, TD-DFT, linearna i nelinearna optička svojstva, nanoklasteri plemenitih metala, bio-nano hibridi, QM/MM

Mentorica: prof. dr. dr. h. c. Vlasta Bonačić-Koutecký

Komentor: prof. dr. sc. Mile Dželalija

Ocjenjivači:

1. prof. dr. sc. Ante Bilušić
2. doc. dr. sc. Viljemka Bučević-Popović
3. prof. dr. sc. Katarina Vukojević

Rad prihvaćen: 13.07.2022.

ACKNOWLEDGEMENT

My research path has been marked by many people that enriched my scientific experience. To begin with, I would like to express my sincere and deepest gratitude to my mentor prof. dr. dr. h. c. Vlasta Bonačić-Koutecký, whose undoubted dedication marked this research from the very beginning to the end. She taught me a lot about the importance of perseverance and patience in science and I will carry that with me forever. It is important to always be open to new perspectives as you never know what will inspire you for new exciting research. I express my gratitude to prof. Mile Dželalija, for all the support and fruitful discussions at our postgraduate university study in biophysics.

I would also like to express my gratitude to dr. Rodolphe Antoine for bringing to our group constant inspiration and support for our research that pushed us in new and exciting directions. I also thank all the members of SpectroBio Lab at Institute Lumière Matière at the University of Lyon for a very pleasant scientific collaboration and welcoming atmosphere. I am extending my gratitude to prof. Miroslav Radman and his Mediterranean Institute for Life Sciences for beautiful working environment as well as for new theoretical-experimental collaboration that just recently emerged thanks to prof. Vlasta Bonačić-Koutecký and experimental scientists from the MedILS.

I wish to thank my friends and colleagues from our group in Split, Željka Sanader-Maršić, Antonija Mravak, and Margarita Bužančić for all the support in the most challenging occasions, and for all the funny anecdotes that I will always remember. Also, I would like to thank all my colleagues from the Center of Excellence (STIM) for being always the team players, as well as to all the good people from Doctoral Study of Biophysics at the Faculty of Science in Split.

In the end, I owe my family, my parents and my husband lifetime gratitude for their constant support. Special thanks to my brothers who guided me into the tech and programming environments. They encouraged my science path. And to my precious son Zrin; thank you for making me a better mother and scientist while at the same time giving new meaning to it all.

List of publications

The following publications constitute the main part of the thesis:

1. Vlasta Bonačić-Koutecký, Martina Perić, Željka Sanader, "Why Do Silver Trimers Intercalated in DNA Exhibit Unique Nonlinear Properties That Are Promising for Applications?", *J. Phys. Chem. Lett.*, **2018**, 9, 10, 2584–2589, 10.1021/acs.jpclett.8b00819

2. Hussein Fakhouri, Martina Perić, Franck Bertorelle, Philippe Dugourd, Xavier Dagany, Isabelle Russier-Antoine, Pierre-François Brevet, Vlasta Bonačić-Koutecký, Rodolphe Antoine, "Sub-100 nanometer silver doped gold–cysteine supramolecular assemblies with enhanced nonlinear optical properties", *Phys. Chem. Chem. Phys.*, **2019**, 21, 23, 1463-9076, 10.1039/C9CP00829B

3. Martina Perić, Željka Sanader Maršić, Isabelle Russier-Antoine, Hussein Fakhouri, Franck Bertorelle, Pierre-François Brevet, Xavier le Guével, Rodolphe Antoine and Vlasta Bonačić-Koutecký, "Ligand shell size effects on one- and two-photon excitation fluorescence of zwitterion functionalized gold nanoclusters", *Phys. Chem. Chem. Phys.*, **2019**, 21, 23916-23921, 10.1039/C9CP05262C

4. Srestha Basu, Martina Perić Bakulić, Hussein Fakhouri, Isabelle Russier-Antoine, Christophe Moulin, Pierre-François Brevet, Vlasta Bonačić-Koutecký*, and Rodolphe Antoine, "Rationale Strategy to Tune the Optical Properties of Gold Catenane Nanoclusters by Doping with Silver Atoms", *J. Phys. Chem. C*, **2020**, 124, 35, 19368–19374, 10.1021/acs.jpcc.0c05402

5. Guillaume F. Combes, Hussein Fakhouri, Christophe Moulin, Marion Girod, Franck Bertorelle, Srestha Basu, Romain Ladouce, Martina Perić Bakulić, Željka Sanader Maršić, Isabelle Russier-Antoine, Pierre-François Brevet, Philippe Dugourd, Anita Krisko, Katarina Trajković, Miroslav Radman, Vlasta Bonačić-Koutecký and Rodolphe Antoine, "Functionalized Au_{15} nanoclusters as luminescent probes for protein carbonylation detection", *Commun Chem*, **2021**, 4, 69, 10.1038/s42004-021-00497-z

The following publications are included in the appendix:

1. Clothilde Comby-Zerbino, Martina Perić, Franck Bertorelle, Fabien Chirot, Philippe Dugourd, Vlasta Bonačić-Koutecký and Rodolphe Antoine, "Catenane Structures of Homoleptic Thioglycolic Acid-Protected Gold Nanoclusters Evidenced by Ion Mobility-Mass Spectrometry and DFT Calculations", *Nanomaterials*, **2019**, 9, 3, 457

2. Guillaume F. Combes, Ana-Marija Vučković, Martina Perić Bakulić, Rodolphe Antoine, Vlasta Bonačić-Koutecky and Katarina Trajković, "Nanotechnology in Tumor Biomarker Detection: The Potential of Liganded Nanoclusters as Nonlinear Optical Contrast Agents for Molecular Diagnostics of Cancer", *Cancers*, **2021**, 13, 16, 4206

Contents

Chapter 1

Is There Plenty of Room at the Bottom?

1.1 Introduction

Nanoscience and nanotechnology have become increasingly important scientific areas in recent decades [1, 2]. They comprehend the general concept of this doctoral thesis: theoretical design of nanoscale materials and their application in biosensorics. Perhaps the most significant sentence in this context is "There is Plenty of Room at the Bottom" by the physicist Richard Feynman. He emphasized the importance of science on a very small scale and its future progress [3]. The scale between 1 and 100 nm is an interesting range where a plethora of physical properties can be observed. The unique structural and optical properties of newly emerging nanostructured materials offer a springboard for the development of biosensors.

Optical molecular imaging uses the ability of light to penetrate biological tissue and fluids for the purpose of imaging samples in the medical diagnostics. Presently, medical diagnostics relies on standard biosensor techniques ("in vitro" and "in vivo" bioimaging and biolabeling) based on commercially available organic dyes and quantum dots. Dyes and dots are integral part of the fluorescence spectroscopy, the most common method used for bioanalytical purposes, which is a very sensitive and fast method. Traditional cancer screening methods are not sufficiently accurate for early diagnosis which is crucial for early initiation of targeted therapy during the pre-invasive stage. Delayed diagnosis of tumor biomarkers is one of the main causes of death in cancer patients. Standard fluorescent markers do not possess sufficient sensitivity and specificity. An efficient way to bypass

these drawbacks is to search for new molecules that can serve as improved fluorescent markers. Improved sensitivity can be further achieved within multiphoton fluorescence microscopy for the purpose of advancing early medical diagnostics using noble metal bio-nano systems, bio-nano hybrids and liganded nanoclusters.

Atomically precise metal quantum clusters - nanoclusters (NCs) have attracted great interest in biosensorics applications due to their attractive properties such as ultra-small size, low toxicity, photostability, intense photoluminescence, and excellent biocompatibility. They belong to the class of nanoparticles (NPs) composed of a small number of atoms exhibiting molecular-like properties with discrete electronic states and size-dependent fluorescence. Precisely due to discrete electronic energy levels NCs exhibit luminescence. NCs are built from a small number of atoms which puts them in the size regime up to 2 nm, while NPs contain a large number of atoms falling into the size regime above 2 nm where molecular orbitals become metal energy band. Increasing the number of noble metal atoms, NCs become NPs (Compare sizes and electronic structures at Figure 1.1). Increasing the size, the quantum confinement weakens and the absorption peaks become less prominent due to the scalable regime. Metal NPs display localized surface plasmons resonances (LSPR), bosonic quasiparticle excitations of the conduction electrons excited utilizing an electromagnetic field. On the contrary, optical properties of nanoclusters are higly dependent on the each atom in the structure, thus are more prominent and very different from the bulk materials. That uniqueness is what makes the metal nanoclusters very adaptable for multifaceted applications. NCs are the bridge between a single atom and bulk materials.

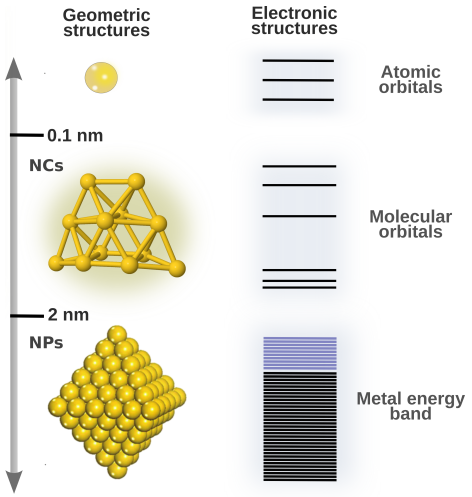

Figure 1.1: Geometry (left) and electronic structure (right) of single atom, nanoclusters (NCs) and nanoparticles (NPs)

Distinct class of metal NCs built from metallic atoms resistant to oxidation under normal atmosphere carries the name "noble". These are platinum, ruthenium, rhodium,

osmium, iridium, palladium, silver and gold. Among the noble metal NCs those of gold and silver are the most researched due to their versatile applications. Their optical and chemical properties are very sensitive to a small change in structure as a consequence of the strong quantum confinement placing them in a nonscalable regime where each atom counts. Gold and silver nanoclusters have different optical properties due to different electronic states. The experimental and theoretical investigation on gold nanocrystal molecules was initiated in 1997[4]. Size dependency of the frequency-dependent dielectric function was explained through a transition to electronic structure. On the example of small silver clusters was demonstraded that d-electrons as well as s-d gap play a crucial role for absorption spectra. Again, it was demonstrated that optical properties of such clusters are size dependent[5, 6].

Noble metal NCs are inadequate to perform alone as biosensors since they dissolve in the biological environment failing to maintain their structural and optical properties. Their application in biosensorics is based on functionalization by various biological molecules that not only protect them from the environment keeping them intact but also offer target-recognition specificity, reduced toxicity and enhancement of their emissive properties[7]. Promising candidates for biosensors of superior detection are silver and gold bio-nano hybrids (noble metal nanoclusters embedded in biomolecular environment) and liganded NCs (noble metal nanoclusters protected with biomolecules) due to their outstanding optical properties that can be adjusted through their size, composition and structure (examples shown on Figure 1.4). Integration of the structure of the noble metal NC with biomolecules is crucial for the high intensity of their absorption and photostable emission, which is a necessary condition for biosensors of superior detection [8, 9]. Two-photon fluorescence microscopy is becoming increasingly popular in biomedical diagnostics thanks to its higher resolution and deep penetration into tissues. Two-photon absorption (TPA) properties of noble metal liganded NCs are several orders of magnitude better than commercially available organic dyes and have the potential for application in theranostics (combined diagnostics and therapy)[10]. This doctoral thesis is a volume of novel theoretical research on gold and silver bio-nano systems; their principles, design, and applications in the context of recent progress in sensing applications; bioimaging, and

medical diagnostics.

1.2 Characterization tools for nanostructured materials

There are no two nanoparticles that are the same. Controlling their size to atomic precision leads us to the ultrasmall size regime; nanoclusters with unique physical and chemical properties. Noble metal NCs have discrete electronic energy levels while plasmonic NPs have a continuous band. Nanoclusters, simply defined as quantum-sized nanoparticles, show multiple optical absorption peaks in the optical spectrum as compared to single surface plasmon resonance (SPR) for nanoparticles. These phenomena give NCs unique fluorescent and structural properties[11, 12, 13]. The first X-ray structure of gold nanoparticle was published in 2007[14]. It showed gold atoms not only in the core but also in the ligand layer, as part of gold-thiol interactions. The experimental determination of X-ray structure was guided by the theoretical DFT model of $Au_{38}(SR)_{24}$ that demonstrated a novel form of gold core protection by gold-thiolate tetraunits[15]. This advocated the significance of joint experimental and theoretical investigation for progress on structural and optical properties of nanosized materials. Since then there have been many explorations of noble metal liganded nanoclusters with various applications in biomedicine, biosensing and bioimaging, optics, energy conversion, and catalysis[16, 17, 18, 19, 20, 21].

The optical properties of noble metal bio-nano hybrids and liganded NCs are size- and composition-dependent. Thus, to be able to understand the origin of their properties and to design novel "superior" NC, it is very important to develop a precise set of characterization tools; efficient synthesis with “high purity” of such nanostructured materials, mass spectrometry for determining molecular weight, X-ray crystallography for the size and atomic composition, NMR and optical spectroscopy. Electrospray ionization mass spectrometry (ESI-MS) is indispensible for nanocluster characterization and is indeed critical for determination of cluster formula. Compared to matrix-assisted laser desorption/ionization mass spectrometry (MALDI-MS), ESI-MS is a much softer ionization technique and usually does not result in fragmentation of NPs. The appearance of peaks with spectral broadening is due to molecule-like transitions. This suggests that

optical spectroscopy holds great value in determining properties of NCs[11, 21].

Nonlinear optics emerged in the last decades as the new exciting tool for investigating materials due to its high specificity. Linear and nonlinear optics study the optical phenomena that occur during the interaction of laser lights with the matter. Contrary to the one-photon absorption (OPA) (linear optics) which depends linearly on the intensity of light, two-photon absorption (TPA) (nonlinear) increases with the square of the light intensity. For linear optical properties absorption coefficient is independent of the optical intensity while for nonlinear optical properties, the absorption coefficient is a function of intensity (linear or higher-order). It was first analyzed theoretically through simultaneous absorption of the two photons by the same molecule by Nobel laureate Maria Goeppert Mayer in 1931[22] after which the two-photon cross-section unit is named (GM). The first experimental demonstration came 30 years later in 1961[23].

Two-photon excitation enables 3D flourescence imaging which is important application of the near-infrared (NIR) microscopy. NIR multiphoton microscopy, specifically two-photon, is a state-of-the-art tool for fluorescence imaging. NIR light (700-2500 nm) penetrates biological tissue offering advantage over the visible spectral range. The first two-photon excited fluorescence imaging of living samples using a 100 NIR laser was published more than three decades ago[24].

Part of the NIR region between 1000 and 1350 nm wavelength is known as the "second biological window". It provides a higher penetration depth of biological tissues. Simulations and modeling studies of optical imaging of tissue or blood suggested improvement of signal-to-noise ratios by using quantum dot fluorophores that emit light at 1320 nm. New fluorescent probes are in demand to achieve spectral imaging in the second biological window. Stepping forward into medical applications requires probes to be biocompatible and to exceed conventional and well-established fluorophores. New fluorescent probes should be able to demonstrate high cross-sections for multiphoton absorption as well as high emission. In general, they should fit in the definition of push-pull chromophores that consist of donor and acceptor part providing a large charge transfer along the molecule upon multiphoton excitation[25, 26].

Liganded noble metal NCs and bio-nano hybrids present a promising route for design-

ing the new chromophores for nonlinear optics. Their cross-sections are several orders of magnitude larger than commercially available dyes[27, 28]. The choice of ligand molecules that protect cluster core plays an important role in enhancing the emissive properties of noble metal nanoclusters[29, 30]. Liganded noble metal NCs can be presented with a simplified scheme of a multishell system consisting of three shells; metal core, metal-ligand interface which includes "staple motifs" rich in noble metal-sulfur bonds, and surface ligand molecules (See schematic representation in Figure 1.2). These shells are engaged in charge transfer from the ligand to the metal core. This class of noble metal nanomaterials is called "ligand-core" NLO-phores[31].

The theoretical approach is one of the crucial characterization tools since it leads the research toward understanding the connection between the structure and optical properties of the novel noble metal nanomaterials. Time-dependent density functional theory (TD-DFT) brings research closer to the origin of optical properties on liganded noble metal NCs and bio-nano hybrids[32, 33, 34, 34, 35, 36, 37, 38, 39, 40, 41]. More details on the theoretical approach and portrait of its unique contribution to this doctoral thesis will be presented in the next section (Section 1.3) as well as in Chapters 2 and 3.

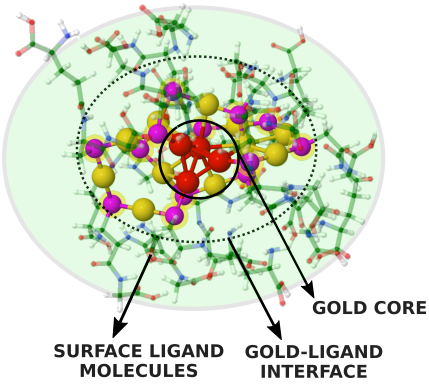

Figure 1.2: Schematic representation of gold nanocluster $Au_{15}SG_{13}$ as a multishell system: gold core, gold-ligand interface and surface ligand molecules

1.3 Methodology

1.3.1 Introduction

Computational chemistry is combination of mathematical methods with fundamental laws of physics to determine properties of nano and biophysical systems. It is widely used in explorations of interactions among biomolecules. The tools of computational chemistry are quantum chemistry (ab initio and semiempirical methods), molecular modelling (force fields) and molecular dynamics[42].

To determine electronic structure of atom and molecules, quantum mechanics is focused

on Born-Oppenheimer approximation as a starting point in solving time-independent Schrödinger equation[43]. In Born-Oppenheimer approximation coupling between the nuclei and electronic motion is neglected. Instead of solving the Schrödinger equation for all the particles simultaneously, we regard the nuclei as fixed in position and solve the Schrödinger equation for the electrons in the static electric potential arising from the nuclei (with nuclear position as parameters). Resulting potential energy surface (PES) forms the basis for solving nuclear motion[44]. The set of solutions so obtained allows us to identify the equilibrium conformation of the molecule with the lowest point on potential energy surface. The Born-Oppenheimer approximation is very reliable for ground electronic states, but it is less reliable for excited states[43].

Schrödinger equation (time independent):

$$\mathbf{H}\Psi = E\Psi \tag{1.1}$$

where $\mathbf{H}$ is called Hamiltonian, Ψ denotes wavefuntion and $\mathbf{E}$ is the energy of the system.

There are two main wave function approaches to the solution of the Schrödinger equation *ab initio* and *semiempirical*:

- ***Ab initio***: Model is chosen for the electronic wave function and equation (1.1) is solved using as input values of the fundamental constants and the atomic numbers of nuclei. Accuracy depends on model that is chosen for wave function. For large numbers of atoms in molecule, *ab initio* calculations are computationally expensive.

- ***Semiempirical method*** has been developed to treat a wider variety of chemical species, and it uses simplified form for Hamiltonian plus adjustable parameters from experimental data.

Once you calculate electronic energy and electronic wave function it is possible to determine wide range of physical properties.

The simplest of the wavefunction-based methods is Hartree–Fock (HF) method where electron correlation is neglected and the motion of electrons is described in an average fashion, mean-field approach. The purpose of post-Hartree–Fock calculations is to treat

correlated motion better than does the Hartree–Fock method[42]. Post HF methods include Møller–Plesset perturbation theory (MP2) and Coupled Cluster (CC) hierarchy. They are improvements of the HF method. Møller–Plesset perturbation theory adds electron correlation effects by introduction of Rayleigh–Schrödinger perturbation theory, usually to second order. Coupled Cluster theory constructs multi-electron wavefunctions on the basis of HF method. The alternative to wavefunction-based methods is Density Functional Theory (DFT) based on the principle that the ground state energy can be determined from the electron density.

1.3.2 Density Functional Theory (DFT)

Ab initio and the *semiempirical* approaches calculate a molecular wavefunction and molecular orbital energies, and thus represent wavefunction methods. A wavefunction is not a measurable feature of a molecule or atom. Density functional theory is not focused on the wavefunction, but on the *electron probability density function* $\rho(x, y, z)$ or $\rho(\mathbf{r})$(electron density function, electron density or the charge density). Electron density function is a function of position (just three variables (x, y, z)) while the wavefunction of an *n-electron* molecule is a function of $4n$ variables, three spatial coordinates and one spin coordinate, for each electron. No matter how big is the molecule, the electron density remains a function of three variables. In that way $\rho(\mathbf{r})$ is mathematically more tractable.
Density functional theory is based on the *Hohenberg–Kohn* theorems:

1. The ground-state properties of an atom or molecule are determined by its electron density function.

2. Trial electron density must give an energy greater than or equal to the true energy.

In the *Kohn–Sham* approach the energy of a system is formulated as a deviation from the energy of an idealized system with non-interacting electrons. By minimizing the energy with respect to the Kohn–Sham orbitals the Kohn–Sham equations can be derived.

Basic Principles of DFT It can be shown that $\rho(x, y, z)$ is related to the "component" one-electron spatial wavefunctions Ψ_i (the molecular orbitals) of a single-determinant

wavefunction Ψ by

$$\rho = \sum_{i=1}^{n} n_i |\Psi_i|^2 \tag{1.2}$$

With given $\rho(\mathbf{r})$ we can calculate any ground state property, for example the energy, E_0:

$$\rho_0(x, y, z) \rightarrow E_0 \tag{1.3}$$

The relationship (1.3) means that E_0 is a functional of ρ_0. Functional is a rule that transforms a function into a number. The first Hohenberg- Kohn theorem says that any ground state property of a molecule is a functional of the ground state electron density function.

$$E_0 = F[\rho_0] = E[\rho_0] \tag{1.4}$$

The theorem is an *existence theorem*: it says that a functional F exists, but does not tell us how to find it. Finding good functionals is the main problem in DFT. Term *FUNCTIONAL* is akin to function[42].

The second Hohenberg–Kohn theorem is the DFT analogue of the wavefunction variation theorem. In DFT molecular calculations the electronic energy from a trial electron density is the energy of the electrons moving under the potential of the atomic nuclei. This nuclear potential is called the "external potential",and it is designated $v(\mathbf{r})$, and the electronic energy is denoted by $E_v = E_v[\rho_0]$. The second Hohenberg–Kohn theorem can be stated as:

$$E_v[\rho_t] \geq E_0[\rho_0] \tag{1.5}$$

where ρ_t is trial electronic density and $E_0[\rho_0]$ is the true ground state energy that corresponds to true electronic density ρ_0. The exact functional is unknown, so actual DFT calculations use approximate functionals (they can give an energy below the true energy)[42].

Kohn-Sham's approach Kohn-Sham's approach permitted the exact computation of kinetic energy for a noninteracting reference system, the Kohn-sham determinant. It facilitated DFT into a practical computational chemistry tool.

- Express molecular energy as a sum of terms, only one of which, a relatively small

term, involves the unknown functional.

- Use an initial guess of the electron density in the KS equations (analogous to the HF equations) to calculate an initial guess of the KS orbitals and energy levels. This initial guess is then used to iteratively refine KS orbitals and energy levels. The process is repeated until the density and exchange–correlation energy have converged to within some tolerance.

- The final KS orbitals are used to calculate an electron density and the energy[42].

Kohn and Sham showed that the exact ground state electronic energy of n-electron system (where paired electrons are described by the same spatial one-electron orbitals) can be written as sum of electron kinetic energies, the nucleus-electron attraction potential energies, Coulomb interaction between total charge distribution at r_1 and r_2, and *exchange correlation energy* of the system:

$$E[\rho] = -\frac{\hbar^2}{2m_e}\sum_{i=1}^{n}\int \Psi_i^*(r_i)\nabla_1^2\Psi_i(r_1)dr_1 - j_0\sum_{I=1}^{N}\frac{Z_I}{r_{I1}}\rho(r_1)dr_1 + \frac{1}{2}j_0\int\frac{\rho(r_1)\rho(r_2)}{r_{12}}dr_1dr_2 + E_{XC}[\rho] \tag{1.6}$$

where one-electron wavefunction Ψ_i are the Kohn-Sham orbitals (solutions to KS equations).

The KS orbitals are found by solving the Kohn–Sham equations, which are derived by applying the variational principle to the electronic energy $E[\rho]$ with the charge density. KS equations for the one-electron orbitals $\Psi_i(r_1)$ have the form:

$$\left\{-\frac{\hbar^2}{2m_e}\nabla_1^2 - j_0\sum_{I=1}^{N}\frac{Z_I}{r_{I1}} + j_0\int\frac{\rho(r_2)}{r_{12}}dr_2 + V_{XC}(r_1)\right\}\Psi_i(r_1) = \varepsilon_i\Psi_i(r_1) \tag{1.7}$$

where ε_i are the KS orbital energies and exchange correlation potential V_{XC} is the functional derivative of the exchange correlation energy $V_{xc}[\rho] = \frac{\delta E_{XC}[\rho]}{\delta\rho}$. If E_{XC} is known, then V_{XC} can be obtained.

Electron correlation is the phenomenon of the motion of pairs of electrons in atoms or molecules being connected ("correlated"). Hartree–Fock method ignores electron correlation and does not take in to account quantum mechanical effects on electron distributions which is not suitable for excited states calculations [42]. Since DFT method models exact

electron density, it also takes into account the approximately electron correlation effect. The computation time required for a DFT calculation formally scales as the third power of the number of basis functions; as a result, DFT methods are computationally more efficient than HF-based formalisms, which scale as the fourth power of the number of basis functions[43].

Exchange-correlation functionals The main source of error in DFT comes from the approximate nature of E_{XC}. This functional is often separated into an exchange functional (representing exchange energy) and a correlation functional (representing dynamic correlation energy). In the local density approximation (LDA), the exchange–correlation functional is:

$$E_{XC} = \int \rho(r)\varepsilon_{xc}[\rho(r)]dr \tag{1.8}$$

where $\varepsilon_{xc}[\rho(r)]$ is exchange correlation energy per electron in a homogeneous electron gas of constant density. To account for the in-homogeneity of the electron density, a non-local correction involving the gradient of ρ is often added to the exchange correlation energy given in (1.8).

1.3.3 Time-dependent Density Functional Theory (TD-DFT)

In 1984. Runge and Gross proved a theorem stating that the time dependent density uniquely determines the time dependent external potential and vice versa. Time-dependent density functional theory (TD-DFT) is useful for the investigation of the response of molecular systems to electric and magnetic fields. TD-DFT can be used to determine polarizabilities and hyperpolarizabilities as well as excitation energies and electronic absorption spectra. The time-dependent Kohn–Sham equations:

$$\left\{-\frac{\hbar^2}{2m_e}\nabla_1^2 - j_0\sum_{I=1}^{N}\frac{Z_I}{r_{I1}} + j_0\int\frac{\rho(r_2,t)}{r_{12}}dr_2 + V_{ext}(t) + V_{XC}(r_1,t)\right\}\Psi_i(r_1,t) = i\hbar\frac{\partial}{\partial t}\Psi_i(r_1,t) \tag{1.9}$$

$$\rho = \sum_{i=1}^{n}|\Psi_i(r,t)|^2 \tag{1.10}$$

where V_{ext} external potential, the exchange correlation potential and KS orbitals and the density are all time-dependent. The goal of TD-DFT is to find how the density changes

in response to the varying external potential. It can be shown, based on perturbation theory arguments, that excitation energies and polarizabilities depend on only the first-order change in density[43].

1.3.4 Linear and Nonlinear Response Theory

Quantum chemical methods offer a possibility to investigate a variety of complex molecular properties. Time-independent properties of a molecular system can be obtained from the derivatives of the energy with respect to the perturbing field, which is not the case for time-dependent properties; frequency-dependent linear polarizability, excitation energies, oscillator strengths parameters for excited-state properties, etc. For time-dependent properties perturbation theory is used since these molecular properties are dynamic (changing in time) that can be treated with response theory[45, 46]. In the limit of the static perturbation, time-dependent perturbation theory comes down to time-independent perturbation theory. The time development of the exact state is determined by employing the Ehrenfest theorem that determines the equations of motion for the response functions and should be satisfied in each order in the field strength. These equations show how molecular properties containing the electric dipole operator can be expressed in equivalent forms involving the momentum operator. Interaction of molecule with time-dependent electromagnetic field leads to polarization of the molecular system oscillating with a specified frequency.

The response of the observable may be expanded in powers of the field strength: the linear response of the system is determined by the linear response function, the nonlinear (quadratic response) of the system by the quadratic response function. Response functions (linear, quadratic, and cubic) are derived from the exact reference state. They become frequency-dependent polarizability, hyperpolarizability, and second hyperpolarizability, determining the polarization of the molecular system through first, second, and third order in the field strength.

The iterative procedure of response theory addresses the lowest excitations, which is usually adequate for relatively small systems. In the case of more complex molecular systems where there is a large number of excited states present, this approach may not be

sufficient. Since theoretical results are being compared to the experimental ones, damped response theory can fix the problem of access to all excitation energies of interest. It is based on the approach where the excited states are multiplied by a damping factor $[exp(-2\gamma t)]$, where γ represents the inverse effective lifetime of the excited-state lifetime broadening parameter. This allows the introduction of complex excitation energies removing the singularities of the response functions at resonance frequencies [47, 48, 49].

Since the research presented in this thesis has a strong focus on one and two-photon absorption (TPA) properties as well as on general applications of spectroscopy in bioimaging and medical diagnostics, residues of these response functions are used to determine one and two-photon absorption matrix elements.

1.3.5 Quantum Mechanics/Molecular Mechanics

For large systems, pure ab initio calculations are very computationally expensive methods. In many practical applications, we are only interested in the properties of a few molecules of a system or part of a large molecule. Many calculations are therefore only limited to these molecules or part of a large molecule. QM/MM is the general name given for methods that combine quantum mechanics and molecular mechanics that were originally devised for calculation on complex problem of proteins and enzymes. It is now used in a wide variety of problems. QM/MM methods are also very important in the study of the spectroscopy of liquid systems. QM is needed to study the quantization of the energy levels and MM can be used to generate the liquid structure at nonzero temperatures. QM/MM methods have seen an extraordinary development allowing quantum chemistry to investigate larger systems. The necessity for a QM treatment (needed in spectroscopy and reactions, for instance) together with the difficulties of treating the entire system by QM imposes some compromising. This compromising comes by adding classical mechanics in a partition of the system. It is also considered in excited state dynamics, where the fate of the excitation energy depends on the environment around the chromophore. QM/MM method was a beneficial approach in this research for determining structural and optical properties of liganded noble metal nanoclusters and bio-nano hybrid systems by taking into account full ligands and the biological environment.

The development of QM/MM methods is a very active research area. In a combined QM/MM method, the system to be studied is partitioned into two parts; a QM part and an MM (Figure 1.3). The QM part has small number of atoms. It may be a molecule or several molecules, a fragment (or part) of a large molecule or a molecular complex. The QM part corresponds to object of a study. Atoms in this part are expressed as electrons and nuclei and are described quantum mechanically. The MM part is the "environment" to the QM part. Usually, it has much larger number of atoms than the QM part. This part is most often "nonreactive" and is treated by using a classical MM force field. "Nonreactive" also means that there is no charge transfer or other "chemical" exchange between the QM and MM parts[50].

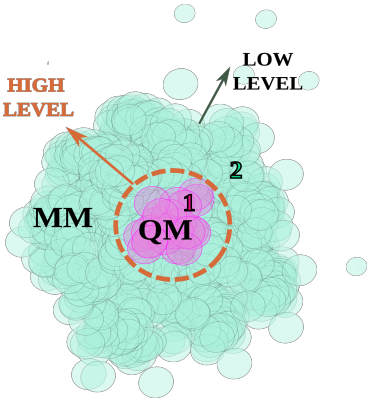

Figure 1.3: Schematic representation of two-layer QM/MM method: High level includes quantum mechanics (QM) region, and low level includes molecular mechanincs (MM) region

Energy for QM/MM system:

$$E_{QM/MM} = E_{QM} + E_{MM} + E_{QM-MM} \tag{1.11}$$

The QM/MM coupling Hamiltonian E_{QM-MM}, generally includes bonded interactions for covalent bond(s) bisecting the QM/MM boundary and nonbonded interactions (van der Waals and electrostatic interactions)[51].

The coupling is important when properties related to the energy, such as free energies, are studied. In QM/MM calculations, there are two types of interactions between the QM and MM parts. One type is the van der Waals interaction that represents the dispersion interactions and the other is the short-range repulsive interactions between the QM and MM atoms. It is often expressed as the Lennard-Jones potential:

$$E_{vdW}(QM/MM) = \sum_{i \in QM} \sum_{j \in MM} 4\varepsilon_{ij} [\frac{\sigma_{ij}}{R_{ij}}^{12} - \frac{\sigma_{ij}}{R_{ij}}^{6}] \tag{1.12}$$

where R_{ij} is the distance between a QM atom i and an MM atom j. σ_{ij} and ε_{ij} are the standard Lennard-Jones parameters. The Lennard-Jones parameters are taken directly

from a force field.

TREATMENT OF THE QM/MM BOUNDARY The intermediate region between the two parts should be treated so that the effects from partitioning the QM and the MM parts across the covalent bonds on the QM atoms are minimized. Among the widely used ways are those using a hybrid orbital or a link atom to satisfy the valence. One single hybrid atomic orbital is placed on each MM atom, originally connected to a QM atom. These hybrid atomic orbitals are then involved in the calculation of the QM part to satisfy the valences. The most commonly used link atom is hydrogen, but in some other implementations, other types of atoms, such as halogen atoms are also used. The link atoms have the following characteristics:

- A link atom is placed in the direction of the QM/MM bond and replaces the corresponding MM atom in the QM calculation. Link atoms are explicitly represented by electrons and nuclei. They are exactly treated quantum mechanically.
- Link atoms are "invisible" to the MM atoms. In other words, there is no interaction between the link atoms and MM atoms. The interactions within the MM part are treated as if there were no link atoms. In ideal cases, link atoms and other MM atoms should simulate the effects of the fragments that are removed from the QM treatment[50].

COMPUTATIONAL ASPECT The QM calculations are performed according to the following Hamiltonian:

$$\hat{H}_{eff} = \hat{H}_{QM} + \hat{H}_{ES}(QM/MM) \tag{1.13}$$

$\hat{H}_{eff}$ involves the interactions of the electrons in the QM part with the point charges in the MM part so additional integral calculations are needed. $\hat{H}_{ES}$ is the Hamiltonian representing the interactions of nuclei and electrons (QM) with the point charges of MM parts. Integrals correspond to those of QM calculations of a molecular system in the presence of point charges:

$$I_{\mu\nu} = \int \chi_\mu (-\frac{Q_m}{r_{im}}) \chi_\nu d\vec{r}_i \tag{1.14}$$

where Q_m is the point charge on the MM atom m. $\vec{r}_i$ is the position of electron i in the QM region. χ_μ and χ_ν are basis functions, that are combined in linear combinations to create molecular orbitals. The above type of integrals is added to the one-electron Hamiltonian matrixes during the SCF calculations of the QM part[50].

ONIOM method One of the most used and well known QM/MM approaches is ONIOM approach integrated in Gaussian computational chemistry software[54]. ONIOM stands for Our own N-layered Integrated molecular Orbital and molecular Mechanics. This computational technique models large molecules by defining two or three layers within the structure that are treated at different levels of approximation.

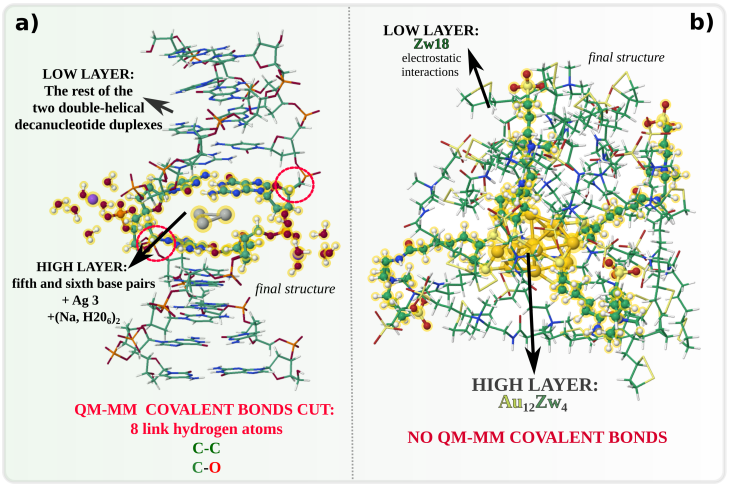

Figure 1.4: Examples of two-layer ONIOM method: a)Ag_3 cation intercalated in DNA structure $d(GCGCGCGCGC)_2$ with link atoms [52] and b) liganded gold nanocluster Au_{12}-$Zwitterions_4$ surrounded by shell of 18 zwitterionic molecules of bidentate thiol with no link atoms. [53]

Even though ONIOM can be used as a two-layer QM/MM method, it can easily be extended to multiple layers. It was developed by the Morokuma group. That group developed several computational strategies aiming at the spectroscopic studies of macro-systems as a discrete/continuum approach that can be nicely integrated with the hybrid scheme offered by own N-layered integrated molecular orbital and molecular mechanics (ONIOM) to perform QM/MM molecular dynamics (MD) simulations of complex systems in solution and effective schemes to include vibrational effects within the time-independent framework. ONIOM calculations can use a Molecular Mechanics method for the system as a whole and an ab initio one for the site of interest; such calculations are referred to as MO:MM calculations (indicating a molecular orbital method is combined with Molecular Mechanics) or as QM:MM (quantum mechanics with MM). Two ab initio methods can also be combined ([50],[51]).

ONIOM LAYERS In an ONIOM calculation, the molecular system (the entire molecule is referred to as the Real System) is defined as 2 or 3 region, typically referred to as "layers":

The *High Layer* (Small Model System (SM)) is the smallest one, and it is treated with the most accurate method. Bond formation and breaking takes place in this region.

The *Low Layer* consists of the entire molecule in a 2-layer ONIOM model. The calculation on this region corresponds to the environmental effects of the molecular environment on the site of interest. It is typically treated with an inexpensive model chemistry: molecular mechanics, a semi-empirical method, or an ab initio method such a Hartree-Fock.

The *Middle Layer* (Intermediate Model System (IM)) is defined in a 3-layer ONIOM model and it is treated with a more sophisticated method. It models the electronic effects of the molecular environment on the high layer.

Important tips for QM/MM calculations Bond breaking or formation should not take place within the MM region. Atoms linked by double or triple bonds should be placed within the same ONIOM region. Region boundaries should not fall within aromatic rings. In the case of a reaction, all Molecular Mechanics parameters must be the same within the Real and Model systems for both the reactants and the products. Atoms at the Model/Real system boundary are modeled using link atoms. For example, a carbon atom which is bonded to another carbon within the SM system is typically replaced by a hydrogen in the computations.

There are many nanostructures of interest that are too large for pure QM computational approach, so two-layer ONIOM is the method of choice. Described methodology was employed in theoretical investigation of such large complex structures in this doctoral thesis. Two examples are presented in Figure 1.4. More details of this research are described in Chapter 2 and 3.

1.4 Research Spotlight

Stabilization and protection of noble metal nanoclusters from the environment can be achieved by: i) embedding them within biomolecules (bio-nano hybrids) and by ii) coating them with biomolecules - ligands (liganded NCs). Functionalization is indispensable for

the application of NCs in the biological environment. Biomolecules that protect NCs can be of different origins; amino acids, peptides, proteins, small organic molecules, polymers, DNA. The most commonly used ligands are thiol molecules (sulfur analog alcohols of general formula R-SH), which participate in strong Au-S or Ag-S binding with a sulfur atom, and also contribute to the emission properties of liganded nanoclusters due to their role as a charge donor to the metal core. Systematization of criteria for theoretical and experimental design of bio-nano hybrids and liganded noble metal NCs in the direction of improving their optical (linear and nonlinear) properties began with a joint synergy of theory and experiment[21, 31].

This research followed two pathways simultaneously:

I *Modeling and investigating novel noble metal bio-nano hybrids*
(Chapter 2)

Bio-nano hybrid system as silver trimer intercalated into DNA was modeled with different nucleotide content in order to investigate optical properties of such system. The influence of the "doping" of silver atoms on the structural as well as optical properties of noble metal bio-nano hybrids and catenane structures of gold nanoclusters was investigated both theoretically and experimentally. The improvement of non-linear optical properties of investigated systems was achieved. Investigation of adjusting the absorption/emission of supramolecular assemblies arranged in "nanowire-like" structures by doping with with silver atoms brought more conclusive knowledge on the origin of these effects.

II *Modeling different functionalizations of liganded noble metal nanoclusters*
(Chapter 3)

The influence of full ligands on the structural and optical properties of liganded nanoclusters of precious metals was investigated using available methods of the computational chemistry, within the computationally available equipment; density functional theory (DFT), its time-dependent version (TD-DFT), polarizable embedding QM method and Quantum Chemistry/Molecular Mechanics method (QM/MM). The potential of different functionalizations of liganded gold nanoclusters was also explored in order to improve detection of biomolecular changes in the context of

early medical diagnostics.

The results presented in this part of the thesis indicate strongly that for future progress of biosensorics it is extremely important to examine new directions of theoretical design of noble metal bio-nano hybrids and liganded NCs in order to improve the efficiency of biosensors, especially those involving multiphoton fluorescence, but also targeted detection through new functionalizations of liganded noble metal nanoclusters. The motivation was to push the design of nanostructured materials closer to applying scientific knowledge in medical diagnostics.

1.4.1 Noble Metal Bio-Nano Hybrid Systems

The convergence of biotechnology and nanotechnology gave rise to a new generation of nanostructured materials for advanced biosensorics; bio-nano hybrid systems[55, 56, 57, 58]. They represent the synergy of two classes of structures: i) noble metal small cluster with its unique electronic and optical properties and its environment ii) biomolecule that not only protects the cluster but also contributes to its optical properties. Few atom silver nanoclusters encapsulated in the biocompatible environment (dendrimer- and peptide-encapsulated few atom Ag cluster) produced scaffold-specific single-molecule (SM) Stokes and antiStokes Raman scattering[59]. Small silver clusters forming hybrids with peptides have shown extended and enhanced optical absorption in comparison to pure peptides[8]. Key concept for the enhanced optical properties of noble metal bio-nano hybrid system is interaction between intracluster excitations and π-π^* excitation within aromatic rings of biomolecules. The Chapter 2 is summary of my contribution in investigation of the recent bio-nano hybrids in the context of bioimaging and biosensorics.

The first example of bio-nano hybrid system in this doctoral thesis is silver trimer intercalated in DNA (See Chapter 2, Section 2.1). Metallic quantum clusters functionalized with single stranded oligonucleotides together with their optical properties have been researched in last two decades theoretically and experimentally [60, 61, 62, 63, 64, 65]. Different surroundings consisting of guanine-cytosine and adenine-thymine nucleotides have been investigated theoreticaly by two-layer Quantum Mechanics/Molecular Mechanics (QM/MM) approach. Theoretical investigation OPA and TPA of silver trimer interca-

lated in DNA based on TDDFT approach showed enhanced optical properties of silver trimer intercalated in guanine and cytosine reach DNA as well as large TPA cross section favorable in advanced biosensorics. The Ag_3-DNA model [66] is very attractive since the the small silver trimer interacts with DNA through Van der Waals bonding. Very large TPA cross sections around 530 nm can be achieved thanks to the interaction of Ag_3^+ and (GCGC) nucleotides. In the NIR regime, TPA cross sections of 10 GM are present, which are valuable intensities important for application. In the case of (ATAT), modest values of TPA cross sections have been calculated in visible and near-infrared regime. Theoretical research presented demonstrated the potential of bio-nano hybrid system composed of silver nanocluster and DNA as biological environment as novel NLO-phore with potential of application in medical diagnostics.

Gold chemistry has also produced impressive bio-nano hybrids promising as optical materials. Gold-thiolate bio-nano hybrid systems can self-assemble into supramolecular assemblies with unique structural and optical properties. Owning to their Au-S coordination and aurophilic interactions between Au(I) they offer rich morphological variations[67, 68, 69]. An interesting example of such a system is the sub-100 nanometer gold-cysteine supramolecular system. In order to enhance its linear and nonlinear optical properties, the silver-doping strategy was explored (See Chapter 2, Section 2.2). DFT and TD-DFT methods were employed to study the structural and optical properties of the models built theoretically to represent the aforementioned assemblies of gold-cysteine as well as its silver-doped versions. Theoretical qualitative model systems are useful from a conceptual point of view. The main focus was to provide insight into the origin of two-photon absorption enhancement upon silver-doping strategy. Results show that due to different gold and silver relativistic effects, Au-S affinity as well as the heterogeneity of structures enhancement of TPA properties was observed for doped systems.

1.4.2 Liganded Noble Metal Nanoclusters

In the last two decades, ligand-protected silver and gold nanoclusters have emerged as a very attractive material at the nanoscale with interesting optical properties. They have shown tremendous potential in applications from nanoelectronics and catalysis to

biological sensing and biomedicine. Ligands play a very important role not only for stability but also in the structural and optical properties of noble metal NCs. The ligand shell is responsible for the solubility of the clusters in the biological environment. The most popular ligands are thiols, especially in the case of gold nanoclusters. In the case of thiol ligands, the sulfur atom holds an important position in the ligand-metal interface. Sulfur and gold atoms are joined in the key feature of the gold-thiolate interface named staple motif; the -SR-[Au-SR-]x oligomers for x=1, 2, etc [39, 70]. Chapter 3 is focused on a thiolated gold nanocluster with two types of ligands: one with two sulfur atoms joint in staple motifs (bidentate thiol zwitterionic ligand) and one with only one sulfur atom participating in the staple motifs (glutathione). Since "each atom counts" in retrieving their properties they are represented by the well-defined formula $Au_n[SR]_m$, where n and m represent the number of metal atoms and thiolate ligands (–SR), respectively. The theoretical investigation was focused on the introduction of full ligands and not only SCH_3 models in the majority of the calculations thanks to the combination of DFT and TD-DFT methods with QM/MM approach.

Principal part of this research are linear (one-photon absorption) and nonlinear optical properties (two-photon absorption). For tuning the properties of thiolated-gold nanoclusters three strategies were explored:

i) Introduction of bidendate thiol zwitterionic shell protecting the $Au_{12}Zw_4$ nanocluster, where Zw represents zwitterionic organic molecule $C_{15}H_{30}N_2O_4S_3$, resulted with enhanced nonlinear response, specifically two-photon excitation fluorescence. The synergy of DFT and TD-DFT within QM/MM succeeded in structural elucidation of the clusters with explicit zwitterionic ligands as well as in determining their key optical signatures (one-photon absorption and two-photon absorption). Results pushed research towards investigation of different surface shell protection strategies; introduction of bulky counter-ions or protein templated AuNCs. The details of this strategy are described in Chapter 3, Section 3.1.

ii) A strategy to tune the optical properties of gold catenane nanoclusters by doping with silver atoms was conducted on $Au_{10}SG_{10}$ (SG: glutathione). $Au_{10}(SG)_{10}$ gold nanocluster is a catenane structure with interlocked ring motifs and without a typical gold core. Chapter 3, Section 3.2 describes details of this strategy. Appendix A is an experimental-

theoretical research on catenane gold nanoclusters protected with thioglycolic acid ligands. The motivation for the "silver doping" of liganded nanoclusters strategy came from previous research where doping of gold-cysteine bio-nano hybrids systems with one silver atom has led to enhanced nonlinear optical properties[71]. Theoretical DFT study as well as experimental and computed X-ray diffraction patterns demonstrated that catenane structures remain preserved upon doping. Experimental optical studies revealed that $Au_{10-x}Ag_xSG_{10}$ with x= 1-4 shows a blue shift in absorption and a redshift in the two-photon emission spectrum in contrast to $Au_{10}SG_{10}$. Time-dependent DFT together with a quadratic response approach was employed to calculate optical properties including one-photon absorption, two-photon absorption, β hyperpolarizabilities, and circular dichroism spectra upon silver doping. OPA spectra are not influenced by silver doping, while TPA cross-section is increased by doping with three silver atoms. In summary doping of thiolated gold nanoclusters with silver atoms is a powerful strategy to tune multiphoton excitation properties and in the meantime preserving the structure of nanoclusters.

iii) Strategy to tailor thiolated gold NCs for the precise detection of a specific biomarker is bringing the research step closer to application in medical diagnostics. In this research biomarker of interest is protein carbonylation which accumulates during aging and oxidative stress [72]. Chapter 3, Section 3.3 is focused on the production of atomically precise cluster $Au_{15}SG_{13}$ and its functionalization with thiolated aminooxy moiety in order to bind to carbonylated sites on the protein of interest. This research demonstrated that functionalized AuNCs are capable to detect protein carbonyls in one-dimensional gel electrophoretic (1DE) analysis by one-photon fluorescence and two-photon excited fluorescence imaging. Theoretical investigation contributed through the combination of DFT and QM/MM approach in-detailed analysis of $Au_{15}SG_{12}$-aminooxy-lysozyme structural complex bringing forward the hydrogen bonding network as well as penetration of water to the interface of AuNC-protein interaction. As a result, this research was recognized as a valuable one since it is the first application of an AuNC that detects post-translational modification as a nonlinear optical probe. Calculating the optical properties of such complex systems with a large number of atoms remains a challenge for theoretical investigation

in the future.

All three strategies are described in Chapter 3 by joint theoretical and experimental investigation, which makes this research a very valuable step for future applications.

Chapter 2

Optical Properties of Noble Metal Bio-Nano Hybrids

2.1 Silver Trimer Intercalated in DNA

Reproduced from:

Vlasta Bonačić-Koutecký, Martina Perić, Željka Sanader, "Why Do Silver Trimers Intercalated in DNA Exhibit Unique Nonlinear Properties That Are Promising for Applications?", *J. Phys. Chem. Lett.*, **2018**, 9, 10, 2584–2589

2.2 Silver Doped Gold-Cysteine Supramolecular Assemblies

Reproduced from:

Hussein Fakhouri, Martina Perić, Franck Bertorelle, Philippe Dugourd, Xavier Da, Isabelle Russier-Antoine, Pierre-François Brevet, Vlasta Bonačić-Koutecký, Rodolphe Antoine, "Sub-100 nanometer silver doped gold–cysteine supramolecular assemblies with enhanced nonlinear optical properties", *Phys. Chem. Chem. Phys.*, **2019**, 21, 23, 1463-9076

THE JOURNAL OF PHYSICAL CHEMISTRY Letters

Letter

Cite This: J. Phys. Chem. Lett. 2018, 9, 2584−2589

pubs.acs.org/JPCL

Why Do Silver Trimers Intercalated in DNA Exhibit Unique Nonlinear Properties That Are Promising for Applications?

Vlasta Bonačić-Koutecký,*[,†,‡] Martina Perić,[†] and Željka Sanader[§]

[†]Center of Excellence for Science and Technology-Integration of Mediterranean Region (STIM) at Interdisciplinary Center for Advanced Sciences and Technology (ICAST), University of Split, Poljička cesta 35, 21000 Split, Croatia

[‡]Chemistry Department, Humboldt University of Berlin, Brook-Taylor-Strasse 2, 12489 Berlin, Germany

[§]Faculty of Science, University of Split, Ruđera Boškovića 33, 21000 Split, Croatia

Supporting Information

ABSTRACT: Our investigation of one-photon absorption (OPA) and nonlinear optical (NLO) properties such as two-photon absorption (TPA) of silver trimer intercalated in DNA based on TDDFT approach allowed us to propose a mechanism responsible for large TPA cross sections of such NLO-phores. We present a concept that illustrates the key role of quantum cluster as well as of nucleotide bases from the immediate neighborhood. For this purpose, different surroundings consisting of guanine−cytosine and adenine−thymine such as (GCGC) and (ATAT) have been investigated that are exhibiting substantially different values of TPA cross sections. This has been confirmed by extending the immediate surroundings as well as using the two-layer quantum mechanics/molecular mechanics (QM/MM) approach. We focus on the cationic closed-shell system and illustrate that the neutral open-shell system shifts OPA spectra into the NIR regime, which is suitable for applications. Thus, in this contribution, we propose novel NLO-phores inducing large TPA cross sections, opening the route for multiphoton imaging.

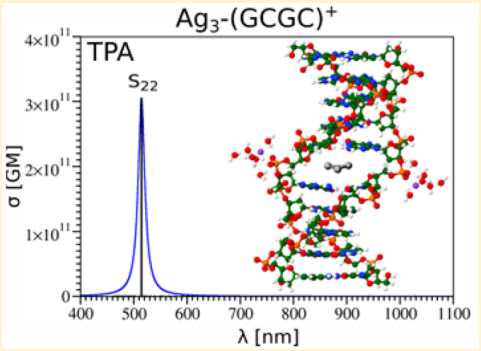

Noble-metal nanomaterials have received large interest in biomedical applications.[1,2] The promising use of ultrasmall gold and silver quantum clusters with ligand-protected shells has been proposed as new class of radiosensitizers for cancer radiotherapy that do not damage normal tissues.[3] In addition, noble-metal quantum clusters display NIR emission[4,5] and allow imaging within the tissue transparency window. This property together with their multiphoton excitation might permit deep-tissue penetration while minimizing background fluorescence and scattering problems. Therefore, the idea of replacing dyes by ligand-protected quantum clusters has been successful because ligands induce NLO properties[6,7] of noble-metal clusters,[8−11] by analogy to acceptor−donor substitution of organic dyes.[12] The aim of this contribution, based on theoretical findings, is to show why the smallest quantum clusters, silver trimer intercalated in DNA, might induce large TPA.

Single-stranded oligonucleotides and amine dendrimers have functionalized metallic quantum clusters, and the resulting properties have been reported in pioneering contributions by Dickson et al.[13−15] Their investigation of these fascinating systems has been expanded to explore their remarkable nonlinear optical properties, such as strong two-photon absorption. Water-soluble polydisperse DNA-Ag clusters exhibit large two-photon absorption cross sections reaching 50 000 GM, with high quantum yields in the red and near-IR regime.[16] Later, Goodson et al.[17] showed that an enhancement in emission using the hybridization of single-stranded DNA by a complementary strand with a guanine-rich tail was possible. Also, two-photon excited fluorescence (TPEF) with emission at 630 nm (upon excitation at 800 nm) was observed for the first time for DNA-templated metal clusters.[17]

Recently, the activities investigating the interactions of small silver clusters with DNA have been significantly increased.[16,18−21] In particular, intercalation of silver trimer into DNA[22] attracted our attention because it provides a stable system in which the van der Waals interaction of quantum clusters with DNA is conceptually different from those of ligated silver clusters in which the influence of ligands through sulfur−silver bonds on TPA is essential.

In this contribution, we wish to address the key role of metallic quantum clusters and stabilizing environment, particularly in the context of TPA properties. This has been accomplished by studying, for the first time, OPA and TPA properties of silver trimer intercalated in DNA, which offers a special type of protection without forming direct binding with metallic atoms. In other words, the characteristic features of silver trimer in the OPA spectrum might remain partially preserved (cf. Figure S1), although the interaction with selected subunits belonging to DNA might be involved in excitations of

Received: March 16, 2018
Accepted: May 1, 2018
Published: May 1, 2018

DOI: 10.1021/acs.jpclett.8b00819
J. Phys. Chem. Lett. 2018, 9, 2584−2589

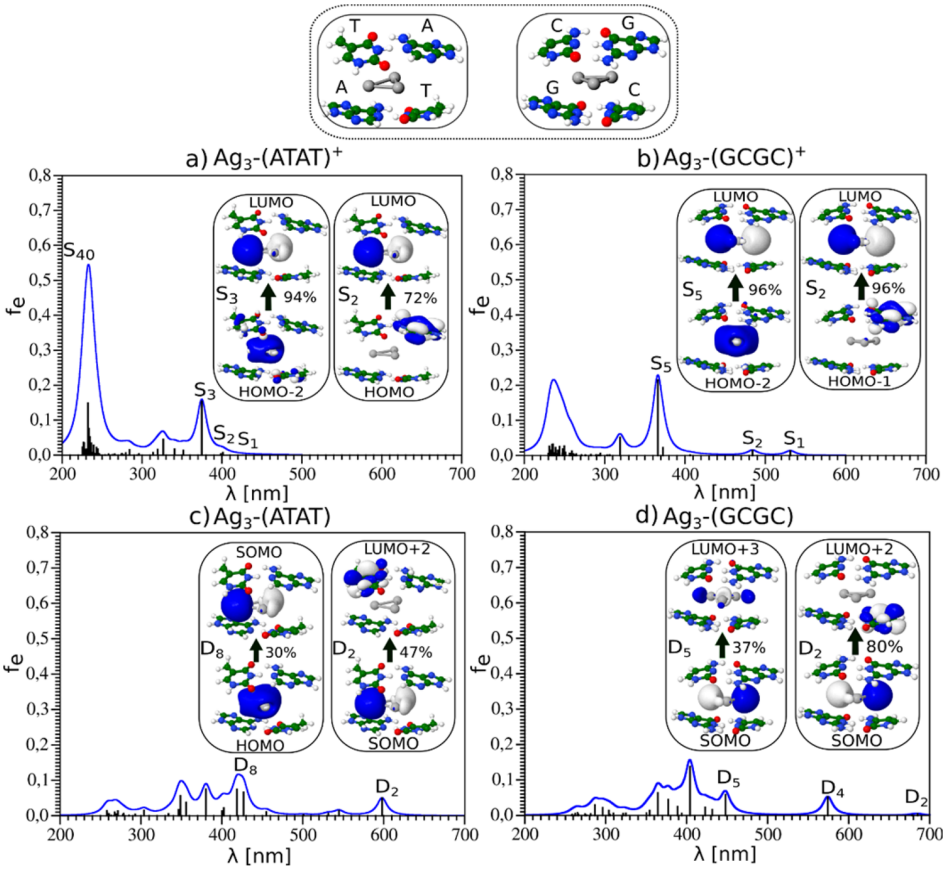

Figure 1. TDDFT OPA spectra for $Ag_3^{+,0}$ intercalated in (ATAT) (left) and (GCGC) (right) nucleotide bases of cationic closed-shell systems (S_n labels singlet states) (a,b) and neutral open-shell systems (D_n labels doublet states; SOMO denotes single occupied MO) (c,d) systems. Leading excitations within silver cluster and between base and silver are shown in the insets.

states with low intensities. Notice that the influence of the immediate neighborhood is smaller in OPA than in TPA because in the former case it is always present a state in which excitations only within the trimer occur. Here we address a conceptual issue based on understanding the mechanisms responsible for TPA properties of such NLO-phores and suggest an application aspect, which could be useful in the imaging and detection area.[23,24]

Our theoretical study is based on Ag_3 intercalated in double-helical decanucleotide duplexes $d(ATATATATAT)_2$ and $d(GCGCGCGCGC)_2$ using the QM/MM approach, which has shown that triangular Ag_3 is placed between the fifth and sixth base pairs.[22] We use the structural properties determined in ref 22 for neutral Ag_3-DNA. Adenine−thymine (AT) and guanine−cytosine (GC) label Watson−Crick pairs.[25,26]

Our previous findings, concerning the optical properties of hybrid systems Ag_3^+ and biomolecules (peptides), showed that silver clusters strongly influence the absorption of biomolecules.[27] Therefore, the question can be raised about the influence of nucleotide bases on the optical properties of silver trimer intercalated within DNA as well as on the double-helical structure. Because it is known that the charge can substantially influence the optical properties, we compare first the OPA spectra for the model system, which take into account two classes of nucleotide bases such as Ag_3-$(ATAT)^{+,0}$ and Ag_3-$(GCGC)^{+,0}$, as shown in Figure 1. Cationic systems had to be considered because the calculations of TPA are accessible only for closed-shell systems. Figure 1 confirms the role of silver clusters in OPA spectra (cf. Figure S1) and the contribution of the nucleotide bases in the lowest-lying states (cf. Figure 1a,b). In addition, Figure 1c,d clearly shows that for neutral systems the excited states are shifted considerably to longer wavelengths, which is important in the context of applications. This is in agreement with the previous findings for spectra of a pure Ag_3^+ and Ag_3[28] (cf. also Figure S1). The analysis of leading excitations for the states shown in Figure 1 illustrates the involvement of silver trimer as well as an individual base, in agreement with the donor−acceptor concept for both cationic and neutral systems. In the case of Ag_3-$(ATAT)^+$ (Figure 1a), Ag_3 is partly positively charged, and excitation from adenine to Ag_3 involves a donor (nitrogen atom) to acceptor transition. An analogous situation occurs for Ag_3-$(GCGC)^+$, where guanine (nitrogen atom) acts as a donor and partly positively charged Ag_3 acts as an acceptor (Figure 1b). In the case of neutral system Ag_3-(ATAT) and Ag_3-(GCGC), because Ag_3 is partly negatively charged, silver trimer acts as a donor and thymine is an acceptor in the former case, while cytosine is an acceptor in the latter case, as shown in Figure 1c,d. This means that by analogy to ligands[9,10] the participation of the nucleotide bases in excitation responsible for two-photon properties is also fulfilled for neutral systems.

The calculated TPA spectra for Ag_3-$(ATAT)^+$ and Ag_3-$(GCGC)^+$, shown in Figure 2, illustrate the influence of ATAT and GCGC environment on nonlinear properties. In the GCGC, the resonance between S_1 and S_{16} states has been reached at 530 nm, causing a very large TPA cross section that

DOI: 10.1021/acs.jpclett.8b00819
J. Phys. Chem. Lett. 2018, 9, 2584−2589

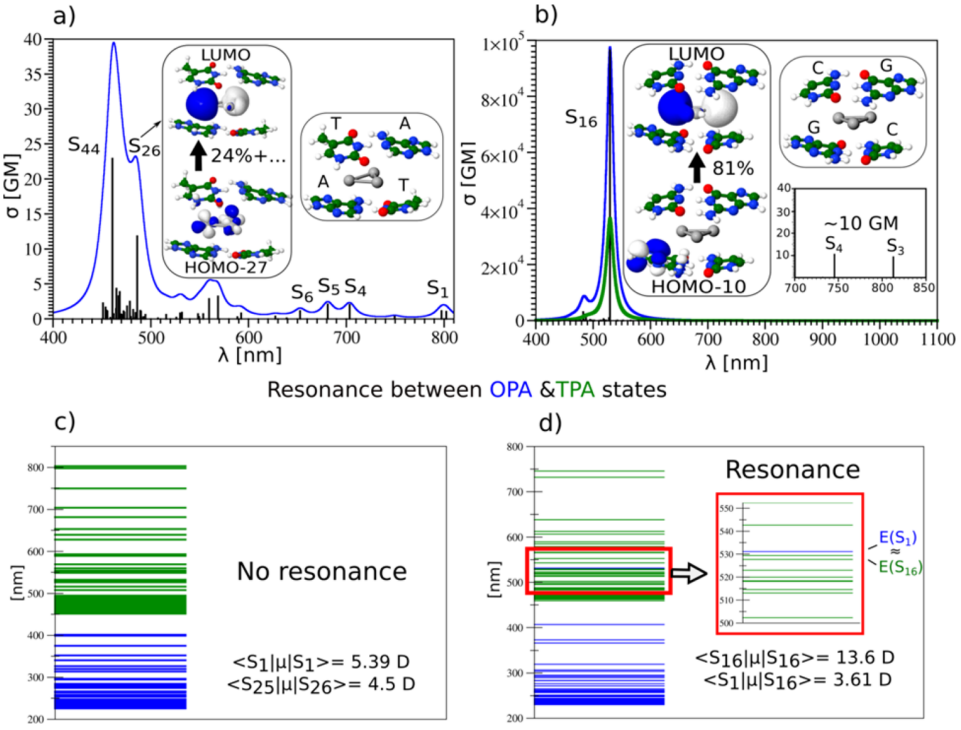

Figure 2. TDDFT TPA spectra for Ag_3^+ intercalated in (ATAT) (a) and (GCGC) (b) nucleotide bases. Inserts contain structural configurations and leading excitations for singlet excited states with dominant TPA features (upper panel). Insert (bottom) in panel b shows low values of TPA cross sections in the NIR regime. Illustration of no resonance for (ATAT) (c) and resonance for (GCGC) (d) between OPA (blue levels) and TPA (green levels) states. Damping factor $\Gamma = 0.01$ (green) allows us to lower artificially large TPA cross sections due to resonance between OPA and TPA states (d). The obtained values are of qualitative nature.

became realistic after introducing the damping procedure.[29] The importance of interplay between the individual bases and silver quantum cluster for TPA is explicitly shown. Notice that the change from cationic (singlet states, S_n) to neutral system (doublet states, D_n) causes the shift of the spectral wavelengths of OPA toward the NIR. Therefore, the resonance of OPA with TPA states is expected to also occur in NIR, which is in favor of applications. The estimated shift ranges from 80 to 140 nm.

Thus this simplest model, allowing us to propose the concept, stimulated us to consider more realistic models, as shown below.

Therefore, to partly include the real surrounding, we have taken into account the fifth and sixth base pairs as well as the influence of $(Na\text{-}6H_2O)_2$, altogether forming the quantum mechanical (QM) part corresponding to $d(AT)_2$ and $d(GC)_2$ (cf. Figure 3). Finally, the two-layer quantum mechanics/molecular mechanics (QM/MM) approach for two complexes, $d(ATATATATAT)_2$ and $d(GCGCGCGCGC)_2$, is shown in Figure 4. The comparison of the TDDFT results for OPA and TPA spectra allows us to identify the influence of the DNA parts on the Ag_3^+ cluster, particularly on nonlinear optical properties.

Notice that intense transitions of OPA spectra of all models of Ag_3 intercalated in DNA have common characteristics due to the involvement of excitation within silver trimer. In contrast, different immediate neighborhoods influence TPA spectra differently.

The enlargement of the surroundings within the QM part does not change leading features of OPA and TPA spectra of Ag_3-$d(AT)_2^+$ and Ag_3-$d(GC)_2^+$, as shown in Figure 3. In fact, for the QM model with $d(GC)_2$ distribution of nucleotide bases, the resonance between singlet S_1 and S_{22} states as well as relatively large dipole moments, as shown in Figure S2, is responsible for large TPA cross sections. Under biological conditions, the presence of cation−water networks near the phosphate backbone is known to provide stability to cellular DNA.[25,26] Therefore, we included one Na atom and six water molecules on each phosphate group. Moreover, the inclusion of a double-helix within the MM approach does not have an additional influence on the OPA and TPA spectra, as shown in Figure 4.

Altogether, particularly large TPA cross sections around 530 nm can be achieved if the interaction between Ag_3^+ and (GCGC) nucleotide bases is present, although, in the near-infrared regime, TPA cross sections of ∼10 GM are present. In the case of (ATAT), modest values of TPA cross sections have been calculated in the near-infrared regime. The mixed surroundings, a combination of GC and AT, as shown in Figure S3, give rise to linear optical properties related to (GCGC) (cf. Figure 1b). The above findings allow us to conclude that the proper choice of nucleotide bases surrounding Ag_3^+ cluster can induce large nonlinearity around 530 nm. Moreover, it is to expect that for neutral systems these features will be shifted toward near-infrared regime, which can be verified experimentally and used for labeling and imaging.

In summary, our findings reflect the presence of exact size-selected trimer intercalated in DNA with different base environments and provide a conceptual approach allowing us to propose unique NLO properties of silver trimers intercalated in DNA. In fact, we have found two types of surroundings, (GCGC) and (ATAT), which are inducing different classes of TPA for the cationic system. The large TPA cross-section

DOI: 10.1021/acs.jpclett.8b00819
J. Phys. Chem. Lett. 2018, 9, 2584−2589

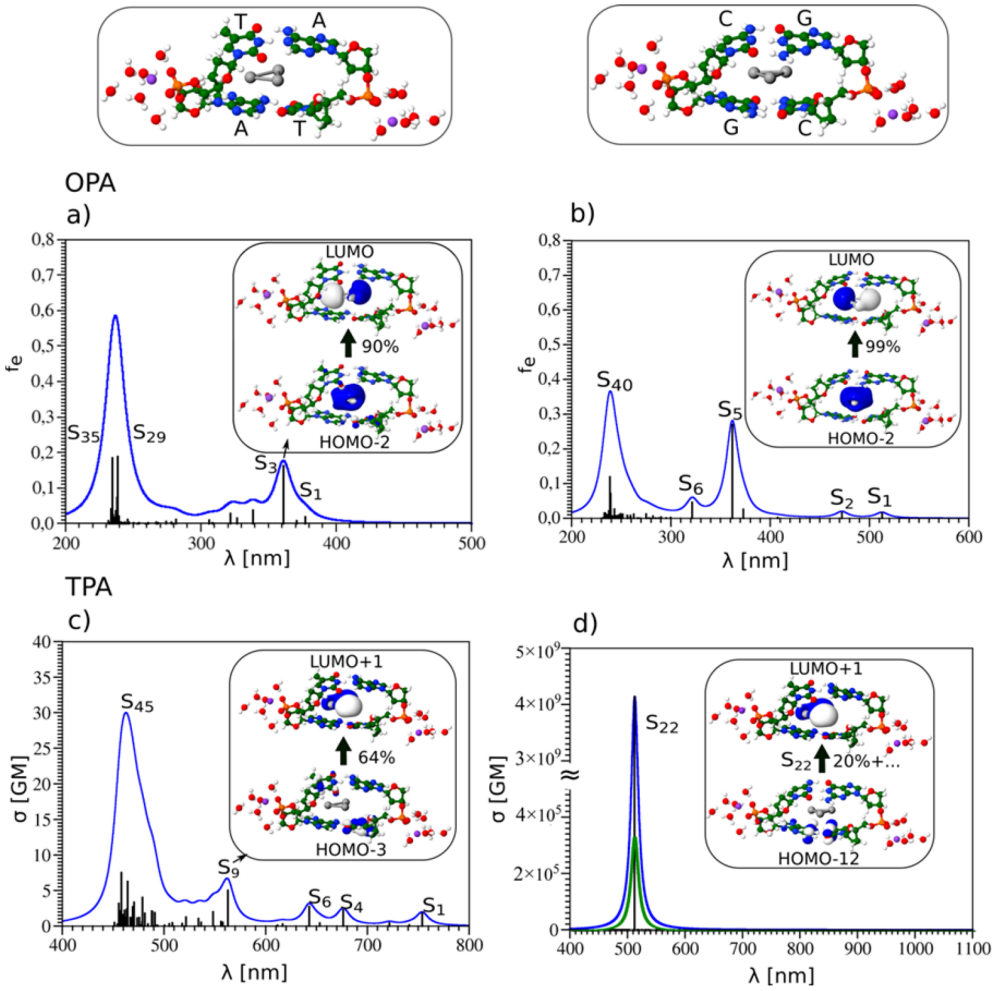

Figure 3. . TDDFT OPA and TPA spectra for Ag_3^+ intercalated within the fifth and sixth base pairs and $(Na+6H_2O)_2$ containing (ATAT) (left) and (GCGC) (right). The structures are shown in the upper part. The inserts contain leading excitations for dominant OPA and TPA states. The damped TPA cross sections are of qualitative nature.

values obtained for the (GCGC) surroundings suggest that similar TPA values in the NIR regime can be expected for neutral systems, which is promising for multiphoton imaging. The key finding for the optimal design for enhanced two-photon absorption in silver trimer intercalated in DNA is both the role of silver quantum cluster and the adequate distribution of surroundings inducing transition-dipole moments necessary for large TPA cross sections.

Altogether, an understanding of the leading factors responsible for TPA properties of silver trimer intercalated in DNA presented in this communication allows us to propose novel ligand-core NLO-phores with potential for different applications. For this purpose, the NLO-phores have to be designed with similar properties, as proposed here.

THEORETICAL SECTION

For the silver atoms the 19-e^- relativistic effective core potential (19-e^- RECP) from the Stuttgart group[30] taking into account scalar relativistic effects has been employed. For all atoms, split valence polarization (SVP) atomic basis sets have been used.[31] The coulomb-attenuated version of Becke's three-parameter nonlocal exchange functional together with the Lee–Yang–Parr gradient-corrected correlation functional (CAM-B3LYP)[32] have been employed to calculate optical properties.

The optimized structures for Ag_3 intercalated in two double-helical decanucleotide duplexes $d(ATATATATAT)_2$ and $d(GCGCGCGCGC)_2$ obtained with two-layer quantum mechanics/molecular mechanics calculations[22] have been used. The fifth and sixth base pairs and Ag_3 cluster intercalated between them are described by quantum mechanical (QM) approaches, while the remaining base pairs are described by molecular mechanical (MM) approaches. PEQM (monopoles taken from Amber force field) method implemented in Dalton package programs[33,34] has been used for the QM/MM approach. The obtained OPA results are in agreement with those obtained from ONIOM approach, using MM-Amber force field,[35] compare Figure S4 in the Supporting Information.

One- and two-photon OPA and TPA absorption properties were determined using time-dependent version of TDDFT[33,34] and quadratic response approach. For the calculation of TPA the cross section (σ),[12] the two-photon absorption probability (δ) is needed, which can be obtained from two-photon absorption transition matrices from the ground to the excited state using either single-residue or double-residue quadratic response procedure.[29,36] In the latter case, the sum-over-states (SOS) approach can be used that also contains the damping factor Γ serving to prevent the TPA cross sections from blowing up near the one-photon resonances. This allowed us to

DOI: 10.1021/acs.jpclett.8b00819
J. Phys. Chem. Lett. 2018, 9, 2584–2589

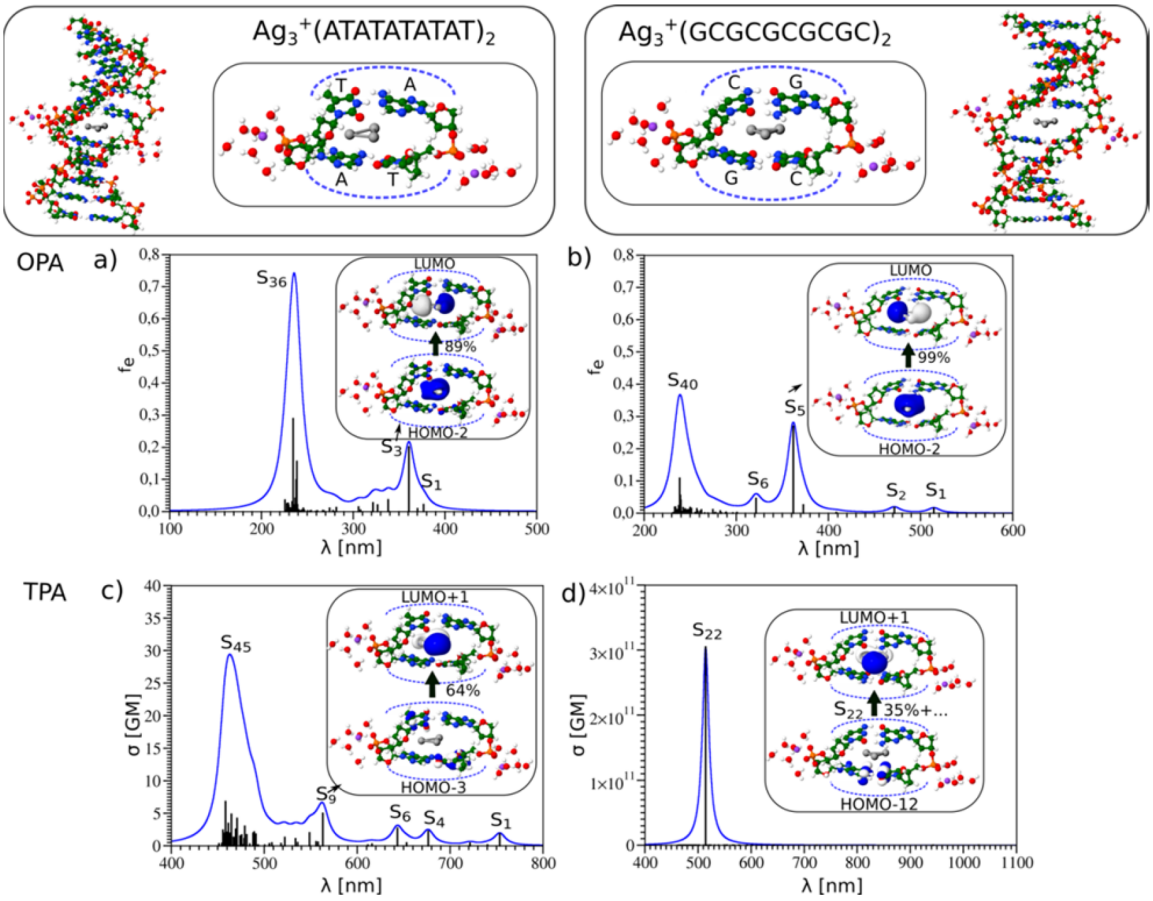

Figure 4. QM/MM OPA and TPA spectra for $Ag_3^+(ATATATATAT)_2$ (left) and $Ag_3^+(CGCGCGCGCG)_2$ (right). The structures are shown in the upper part. The dashed lines label the border between QM and MM parts. The inserts contain leading excitations for dominant OPA and TPA states. The overestimated TPA cross section for S_{22} state should be lowered for several orders of magnitude after introducing the damping factor.

adequately correct the TPA cross sections when necessary as well as to include the manifold of states (20−30 excited states). For calculations, the DALTON[33,34] program and its modified version were used. In our previous contributions on ligated silver clusters, all details have been described.[9,10]

■ ASSOCIATED CONTENT

Supporting Information

The Supporting Information is available free of charge on the ACS Publications website at DOI: 10.1021/acs.jpclett.8b00819.

TDDFT spectra of bare trimers; illustration of resonance between OPA and TPA states of system presented in Figure 3; and OPA spectrum for Ag_3-$(GTAC)^+$ system (PDF)

■ AUTHOR INFORMATION

Corresponding Author

*E-mail: vbk@chemie.hu-berlin.de.

ORCID

Vlasta Bonačić-Koutecký: 0000-0001-6142-5932

Martina Perić: 0000-0002-9134-5500

Notes

The authors declare no competing financial interest.

■ ACKNOWLEDGMENTS

We thank Arthuro Lopez Quientela for attracting our attention to intercalated Ag_3-DNA systems and Giampaolo Barone for supplying us with structural properties of Ag_3-DNA systems. The funding from Center of Excellence (STIM) at the University of Split is appreciated. This research was supported by STIM - REI, a project funded by European Union from European Structural and Investment Funds 2014−2020, Contract Number KK.01.1.1.01.0003. V.B.-K., M.P., and Ž.S. acknowledge the Center for Advanced Computing and Modelling (CNRM) for providing computing resources of the supercomputer Bura at the University of Rijeka in Rijeka, Croatia.

■ REFERENCES

(1) Muthu, M. S.; Agrawal, P.; Singh, S. Theranostic nanomedicine of gold nanoclusters: an emerging platform for cancer diagnosis and therapy. *Nanomedicine* **2016**, *11* (4), 327−330.

(2) Chen, G.; et al. Nanochemistry and Nanomedicine for Nanoparticle-based Diagnostics and Therapy. *Chem. Rev.* **2016**, *116* (5), 2826−2885.

(3) Zhang, X. D.; et al. Ultrasmall Au10−12(SG)10−12 Nanomolecules for High Tumor Specificity and Cancer Radiotherapy. *Adv. Mater.* **2014**, *26* (26), 4565−4568.

(4) Le Guével, X. L.; et al. Highly fluorescent silver nanoclusters stabilized by glutathione: a promising fluorescent label for bioimaging. *Nano Res.* **2012**, *5* (6), 379−387.

(5) Stensberg, M. C.; et al. Toxicological studies on silver nanoparticles: challenges and opportunities in assessment, monitoring and imaging. *Nanomedicine* **2011**, *6* (5), 879−898.
(6) Guevel, X. L.; et al. Ligand effect on the size, valence state and red/near infrared photoluminescence of bidentate thiol gold nanoclusters. *Nanoscale* **2014**, *6* (14), 8091−8099.
(7) Aldeek, F.; et al. Growth of Highly Fluorescent Polyethylene Glycol- and Zwitterion-Functionalized Gold Nanoclusters. *ACS Nano* **2013**, *7* (3), 2509−2521.
(8) Russier-Antoine, I.; et al. Tuning Ag29 nanocluster light emission from red to blue with one and two-photon excitation. *Nanoscale* **2016**, *8* (5), 2892−2898.
(9) Sanader, Z.; et al. Two-photon absorption of ligand-protected Ag15 nanoclusters. Towards a new class of nonlinear optics nanomaterials. *Phys. Chem. Chem. Phys.* **2016**, *18* (18), 12404−12408.
(10) Russier-Antoine, I.; et al. Ligand-core NLO-phores: a combined experimental and theoretical approach to the two-photon absorption and two-photon excited emission properties of small-ligated silver nanoclusters. *Nanoscale* **2017**, *9* (3), 1221−1228.
(11) Yau, S. H.; Varnavski, O.; Goodson, T. An Ultrafast Look at Au Nanoclusters. *Acc. Chem. Res.* **2013**, *46* (7), 1506−1516.
(12) Frediani, L.; Rinkevicius, Z.; Ågren, H. Two-photon absorption in solution by means of time-dependent density-functional theory and the polarizable continuum model. *J. Chem. Phys.* **2005**, *122* (24), 244104.
(13) Petty, J. T.; et al. DNA-templated Ag nanocluster formation. *J. Am. Chem. Soc.* **2004**, *126* (16), 5207−5212.
(14) Vosch, T.; et al. Strongly emissive individual DNA-encapsulated Ag nanoclusters as single-molecule fluorophores. *Proc. Natl. Acad. Sci. U. S. A.* **2007**, *104* (31), 12616−12621.
(15) Zheng, J.; Nicovich, P. R.; Dickson, R. M. Highly fluorescent noble-metal quantum dots. *Annu. Rev. Phys. Chem.* **2007**, *58*, 409−431.
(16) Patel, S. A.; et al. Water-Soluble Ag Nanoclusters Exhibit Strong Two-Photon-Induced Fluorescence. *J. Am. Chem. Soc.* **2008**, *130* (35), 11602−11603.
(17) Yau, S. H.; et al. Bright two-photon emission and ultra-fast relaxation dynamics in a DNA-templated nanocluster investigated by ultra-fast spectroscopy. *Nanoscale* **2012**, *4* (14), 4247−4254.
(18) Petty, J. T.; et al. DNA-Templated Molecular Silver Fluorophores. *J. Phys. Chem. Lett.* **2013**, *4* (7), 1148−1155.
(19) Gwinn, E.; et al. DNA-Protected Silver Clusters for Nanophotonics. *Nanomaterials* **2015**, *5* (1), 180−207.
(20) Maksimov, D. A.; Pomogaev, V. A.; Kononov, A. I. Excitation spectra of Ag3−DNA bases complexes: A benchmark study. *Chem. Phys. Lett.* **2017**, *673*, 11−18.
(21) Ye, Y. D.; et al. DNA-stabilized silver nanoclusters and carbon nanoparticles oxide: A sensitive platform for label-free fluorescence turn-on detection of HIV-DNA sequences. *Biosens. Bioelectron.* **2016**, *85*, 837−843.
(22) Buceta, D.; et al. Ag2 and Ag3 Clusters: Synthesis, Characterization, and Interaction with DNA. *Angew. Chem., Int. Ed.* **2015**, *54* (26), 7612−7616.
(23) Obliosca, J.; et al. DNA/RNA Detection Using DNA-Templated Few-Atom Silver Nanoclusters. *Biosensors* **2013**, *3* (2), 185−200.
(24) Shah, P.; et al. Design Aspects of Bright Red Emissive Silver Nanoclusters/DNA Probes for MicroRNA Detection. *ACS Nano* **2012**, *6* (10), 8803−8814.
(25) Bloomfield, V. A.; Crothers, D. M.; Tinoco, I. *Nucleic Acids: Structure, Properties, and Functions*; University Science Books: 2000.
(26) Saenger, W. *Principles of Nucleic Acid Structure*; Springer: New York, 1984.
(27) Bonacic-Koutecky, V.; et al. Silver cluster-biomolecule hybrids: from basics towards sensors. *Phys. Chem. Chem. Phys.* **2012**, *14* (26), 9282−9290.
(28) Bonačić-Koutecký, V.; et al. An accurate relativistic effective core potential for excited states of Ag atom: An application for studying the absorption spectra of Agn and Agn+ clusters. *J. Chem. Phys.* **1999**, *110* (8), 3876−3886.
(29) List, N. H.; et al. Relation between Nonlinear Optical Properties of Push−Pull Molecules and Metric of Charge Transfer Excitations. *J. Chem. Theory Comput.* **2015**, *11* (9), 4182−4188.
(30) Andrae, D.; et al. Energy-adjustedab initio pseudopotentials for the second and third row transition elements. *Theoret. Chim. Acta* **1990**, *77* (2), 123−141.
(31) Weigend, F.; Ahlrichs, R. Balanced basis sets of split valence, triple zeta valence and quadruple zeta valence quality for H to Rn: Design and assessment of accuracy. *Phys. Chem. Chem. Phys.* **2005**, *7* (18), 3297−3305.
(32) Yanai, T.; Tew, D. P.; Handy, N. C. A new hybrid exchange−correlation functional using the Coulomb-attenuating method (CAM-B3LYP). *Chem. Phys. Lett.* **2004**, *393* (1−3), 51−57.
(33) Aidas, K.; et al. The Dalton quantum chemistry program system. *Wiley Interdiscip. Rev. Comput. Mol. Sci.* **2014**, *4* (3), 269−284.
(34) *Dalton, a molecular electronic structure program*, Release Dalton2016.0, 2015. http://daltonprogram.org.
(35) Wang, J.; Cieplak, P.; Kollman, P. A. How well does a restrained electrostatic potential (RESP) model perform in calculating conformational energies of organic and biological molecules? *J. Comput. Chem.* **2000**, *21* (12), 1049−1074.
(36) Norman, P. A perspective on nonresonant and resonant electronic response theory for time-dependent molecular properties. *Phys. Chem. Chem. Phys.* **2011**, *13* (46), 20519−20535.

DOI: 10.1021/acs.jpclett.8b00819
J. Phys. Chem. Lett. 2018, 9, 2584−2589

Volume 21 | Number 23 | 21 June 2019 | Pages 12047–12708

PCCP

Physical Chemistry Chemical Physics

rsc.li/pccp

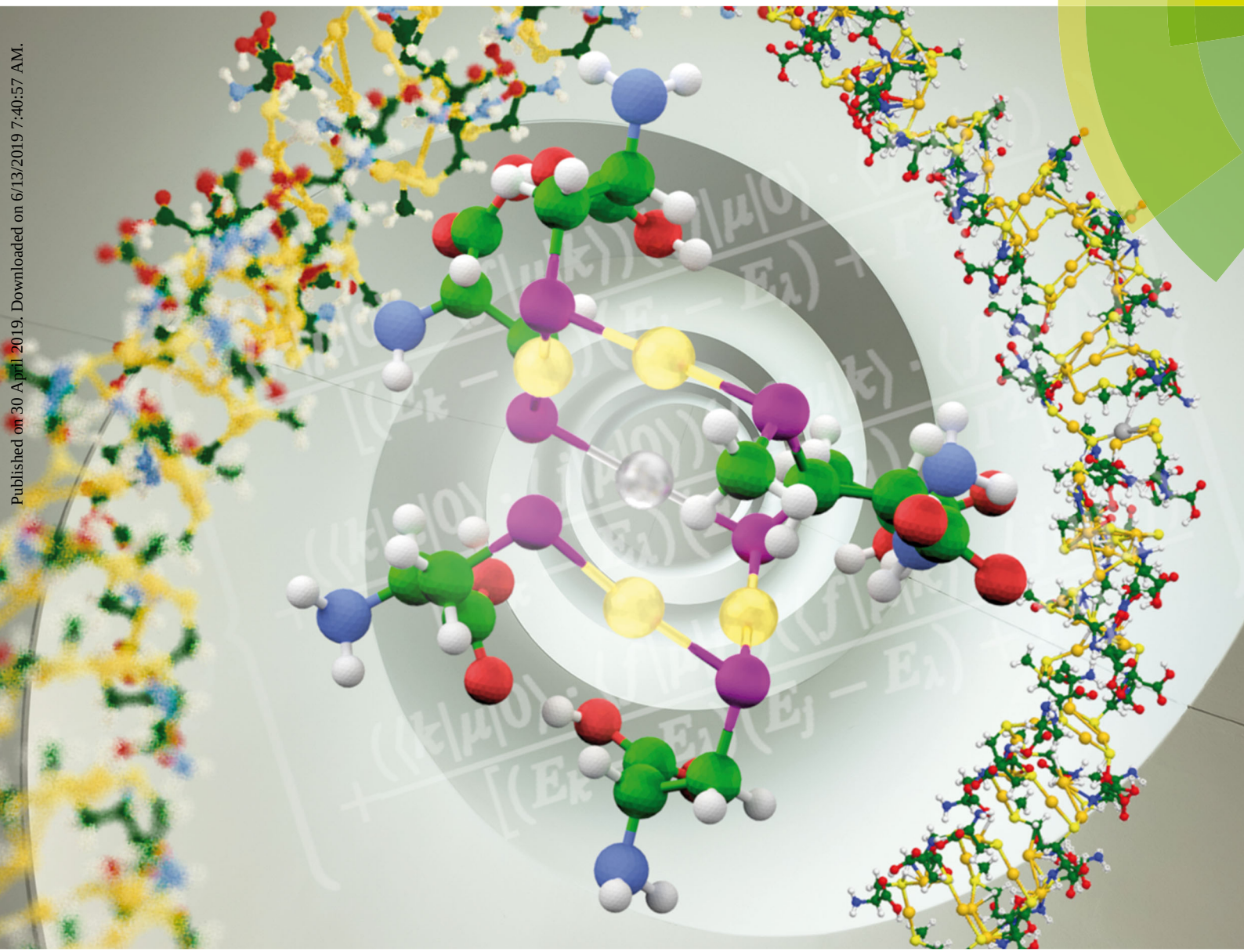

ISSN 1463-9076

ROYAL SOCIETY OF CHEMISTRY | Celebrating IYPT 2019

PAPER

Rodolphe Antoine *et al.*

Sub-100 nanometer silver doped gold–cysteine supramolecular assemblies with enhanced nonlinear optical properties

PCCP

PAPER

Cite this: *Phys. Chem. Chem. Phys.*, 2019, **21**, 12091

Sub-100 nanometer silver doped gold–cysteine supramolecular assemblies with enhanced nonlinear optical properties†

Hussein Fakhouri,[a] Martina Perić,[b] Franck Bertorelle,[a] Philippe Dugourd,[a] Xavier Dagany,[a] Isabelle Russier-Antoine,[a] Pierre-François Brevet,[a] Vlasta Bonačić-Koutecký[bc] and Rodolphe Antoine *[a]

Received 11th February 2019,
Accepted 30th April 2019

DOI: 10.1039/c9cp00829b

rsc.li/pccp

The ability of gold(I) thiolates to self-assemble into supramolecular architectures opens the route for a new class of nanomaterials with a unique structure–optical property relationship. However, for a confirmed structure–optical property relationship, a control of the supramolecular architectures is required. In this work, we report a simple synthesis of sub-100 nanometer gold–cysteine and silver doped gold–cysteine supramolecular assemblies. We explore in particular silver-doping as a strategy to enhance the optical properties of these supramolecular assemblies. By an accurate characterization of as-synthesized supramolecular nanoparticles, we have been able to measure for the first time, their absolute two-photon absorption cross-section, two-photon excited fluorescence cross-section and first hyperpolarizabilities at different near-IR wavelengths. Huge values are obtained for silver doped gold–cysteine supramolecular assemblies, as compared to their corresponding undoped counterpart. In addition, we employ DFT and TD-DFT methods to study the geometric and electronic structures of model gold–cysteine and silver doped gold–cysteine compounds in order to address the structure–linear/nonlinear optical property relationship. The aim is to gain insights into the origin of the nonlinear optical enhancement of silver-doped gold supramolecular assemblies.

Introduction

Supramolecular nanoarchitectures self-assembled from gold thiolate –Au–SR– polymers[1] have attracted much attention due to their high morphological variation.[2,3] Indeed, the uniqueness of such nanomaterials resides in their multiple-type and multiple-strength weak interactions, such as Au–S coordination, aurophilic interactions between Au(I), and inter-ligand interactions including H-bonding, electrostatic interactions and hydrophobic interactions. Because of the interplay of these interactions, nanomaterials can self-assemble into hierarchical structures. In particular, by using cysteine as the thiolate compound, the synergetic interplay of the electrostatic interaction between cysteine side chains and the Au(I)···Au(I) aurophilic attraction in the Au(I)–Cys polymeric backbone may result in some helicity.[4–6] On the other hand, under controlled external parameters (temperature, pH, *etc.*), Au(I)–cysteine polymers can further assemble into a bulky precipitate with lamellar structures.[7] This capability to self-assemble into hierarchical structures also leads to an unusual structure–optical property relationship.[4,7] Usually, a strong absorption band in the near UV range for Au(I)–thiolate supramolecular assemblies is attributed to a ligand-to-metal charge transfer (LMCT) mixed with ligand-to-metal–metal charge transfer (LMMCT) excitation.[4] The high order in Au(I)–thiolate supramolecular structures is a key factor for the aurophilic effect, which in turn provides luminescent properties.[8,9] Furthermore, due to the inherent chirality of cysteine molecules, cysteine Au(I)-supramolecular assemblies display circular dichroism (CD) and constitute efficient targets for bio-sensing in particular for enantiomeric drug analysis.[6]

The investigation of the nonlinear optical (NLO) properties of silver and gold thiolated supramolecules is still in its infancy, and only few reports on NLO measurements have been reported.[5,10,11] We have recently shown that, although non-fluorescent through one-photon excitation, gold–cysteine

[a] *Univ Lyon, Université Claude Bernard Lyon 1, CNRS, Institut Lumière Matière, Lyon, UMR5306, France. E-mail: rodolphe.antoine@univ-lyon1.fr*
[b] *Center of Excellence for Science and Technology-Integration of Mediterranean Region (STIM) at Interdisciplinary Center for Advanced Sciences and Technology (ICAST), University of Split, Poljička cesta 35, 21000 Split, Croatia*
[c] *Chemistry Department, Humboldt University of Berlin, Brook-Taylor-Strasse 2, 12489 Berlin, Germany. E-mail: vbk@chemie.hu-berlin.de*

† Electronic supplementary information (ESI) available: Size distributions for NPs in aqueous solutions obtained by dynamic light scattering. Quantitative XPS data and spectra. UV-vis absorption spectra of α-Au–Cys as a function of pH. TPEF spectra of Ag-doped Au–Cys NP aqueous solution. HRS line intensity for NPs in aqueous solution. TDDFT OPA and TPA spectra of model structures. See DOI: 10.1039/c9cp00829b

supramolecular assemblies present two-photon excited fluorescence. They also exhibit second harmonic generation. Between large plasmonic gold metal nanoparticles (NPs),[12] gold NP hybrids[13,14] and gold quantum nanocluster NLO-phores,[15,16] chiral supramolecular gold–cysteine assemblies constitute therefore a new class of nanomaterials with favorable NLO properties driven by their supramolecular nanoarchitecture. Nevertheless, the exact supramolecular architecture of these systems remains a key feature to design efficient NLO systems. Indeed, centrosymmetry plays a major role in bestowing quadratic NLO properties for instance. It has been shown for example that the first hyperpolarizability of ligated-Au_{25} clusters is strongly enhanced by silver alloying.[17] Furthermore, both one-[18] and two-photon[19] excited fluorescence of ligated gold nanoclusters can be dramatically enhanced by alloying the core with silver atoms.

For a confirmed structure–optical property relationship, a control of the supramolecular architectures is required. However, synthetic control over the exact supramolecular architecture is usually difficult. Indeed, the spontaneous interactions of a gold salt with cysteine result in the formation of non-controllable self-assembly structures that can reach the micrometer size range.[20] In this work, we describe conditions for the controlled synthesis of sub-100 nanometer gold–cysteine and silver doped gold–cysteine supramolecular assemblies. We propose a two-step process involving (i) the reduction of Au(III) ions to Au(I) ions by cysteine (Cys) and the formation of polymeric structures of the form –[Cys–Au(I)]$_n$– at high pH in the presence of trimethylamine (TEA), and (ii) acidic conditions allowing the formation of helical supramolecular assemblies with a size range lower than 100 nm. We also explore a silver-doping strategy to enhance the linear and nonlinear optical properties of gold–cysteine supramolecular assemblies. By an accurate characterization of the as-synthesized NPs (in particular thanks to their molar mass measurements), we have been able to measure for the first time, their absolute two-photon absorption and two-photon excited fluorescence cross-sections and their first hyperpolarizabilities. Huge values are obtained for silver doped gold–cysteine supramolecular assemblies, as compared to their corresponding undoped counterparts. In addition, we employ DFT and TD-DFT methods to study the geometric and electronic structures of model gold–cysteine and silver doped gold–cysteine compounds in order to address the structure-linear/nonlinear optical property relationship in order to gain insights into the origin of the nonlinear optical enhancement of silver-doped gold supramolecular assemblies.

Results and discussion

Gold–cysteine and silver doped gold–cysteine supramolecular architectures and their characterization

The self-assembly of chiral –[Cys–Au(I)]$_n$– into supramolecular assemblies has already been reported in the literature[4,6,7] and usually involves a one-step simple reaction of $HAuCl_4$ with D-Cys, L-Cys, or D/L-Cys at pH values ranging between 3 and 7, a pH at which the Cys side chain groups are in their zwitterionic form. Cys is a mild reducing agent for the reduction of Au(III) ions to Au(I) ions. It subsequently complexes with Au(I) to form polymeric helical structures of the form –[Cys–Au(I)]$_n$– with a diameter larger than 500 nm.[4,6,7] In this work, gold–cysteine and silver doped gold–cysteine supramolecular assemblies are produced with a different mechanism leading to smaller particles with a diameter range lower than 100 nm (see below). We propose a two-step process for the self-assembly and characterization of gold–cysteine and silver doped gold–cysteine supramolecular assemblies leading to helical nanostructures. Step i: the Au(III) ions are first reduced by Cys to Au(I) ions and subsequently form polymeric –[Cys–Au(I)]$_n$– structures at high pH, where amine side chains are in their neutral form. Due to the presence of triethylamine (TEA) leading to ion-pairing with the Cys carboxylic groups and thus some steric hindrance, the formation of helical structures is avoided. Note that we measured the optical spectra during this first step. The absorption spectra (displayed in Fig. S1 in ESI†) do not show any band at $\sim$350 nm which is indicative of the absence of helical motifs formed during the first step with TEA addition. Step ii: with the addition of acetic acid, the pH drops to $\sim$4, and TEA molecules are removed from the –[Cys–Au(I)]$_n$– polymeric structures, allowing the formation of helical structures. The presence of TEA in the first step is possibly the key factor for producing NPs with a size range lower than 100 nm.

Gold–cysteine (with two different morphologies, coined α-Au–Cys NPs, and β-Au–Cys NPs, see Experimental section) and silver doped gold–cysteine supramolecular assemblies were characterized by different techniques. We have obtained molar mass information for the samples of supramolecular assemblies diluted in a water–methanol mixture (50 : 50 v/v). As mentioned in the Experimental section, charge detection mass spectrometry (CDMS)[21–23] was used to measure the mass of individual ions thanks to the independent measurement of the m/z ratio and the charge z for thousands of individual ions. Mass histograms for the 3 samples are shown in Fig. 1. α-Au–Cys, β-Au–Cys, and Ag-doped Au–Cys NPs show an average mass of 1.1 GDa, 1.5 GDa and 1.8 GDa, respectively. Of note, the accurate and direct measurement of the molar mass for supramolecular assemblies allows a quantitative determination of the NP solution concentrations, an essential requisite for the absolute measurement of the TPA cross section and the first hyperpolarisability.

Fig. S2 (ESI†) shows the size distributions of α-Au–Cys, β-Au–Cys, and Ag-doped Au–Cys NPs in aqueous solutions obtained by dynamic light scattering (DLS). Only one component was observed in all cases, with a mean hydrodynamic diameter (HD) of 71 nm, 62 nm, and 102 nm for α-Au–Cys, β-Au–Cys, and Ag-doped Au–Cys NPs, respectively. The average mass extracted from the CDMS spectra can be converted to an average NP diameter using the spherical shape approximation and an average density of Au–Cys nanoparticles of $\sim$3 (by averaging the density, considering 19.3 for gold and $\sim$1.3 for cysteine). Thus, α-Au–Cys, β-Au–Cys, and Ag-doped Au–Cys NPs show an average estimated diameter of 106 nm, 119 nm, and 125 nm, respectively (in fair agreement with DLS measurements).

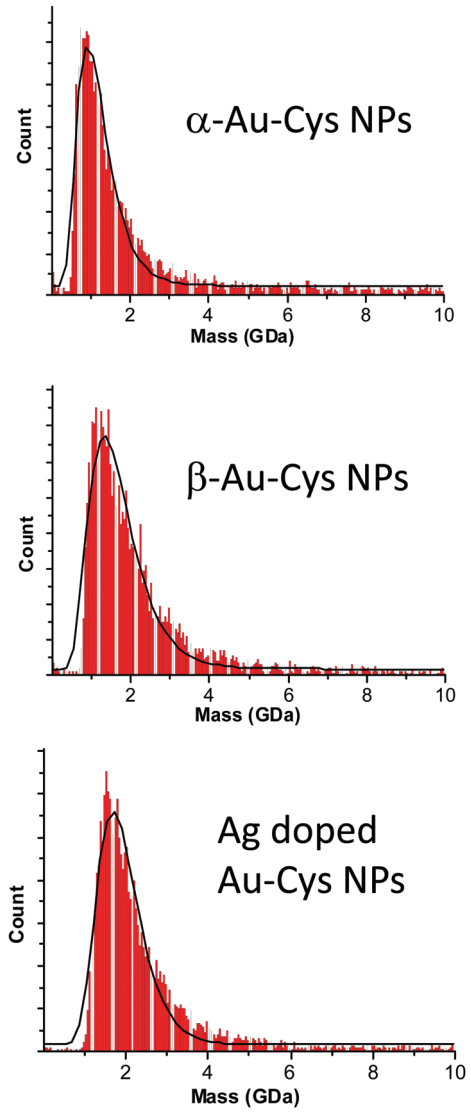

Fig. 1 Mass histograms for the 3 samples α-Au–Cys, β-Au–Cys, and Ag-doped Au–Cys NPs, obtained by charge-detection mass spectrometry (CDMS) measurements. Experimental distributions are fitted with lognormal distributions. The corresponding full widths at half maximum are 0.8, 1.1 and 1 GDa for α-Au–Cys, β-Au–Cys, and Ag-doped Au–Cys NPs respectively.

Quantitative XPS measurements confirmed that the Au : Cys ratio is close to a 1 : 1 stoichiometry in α-Au–Cys, β-Au–Cys, and Ag-doped Au–Cys NPs (see Table S1 and Fig. S3, ESI†). We also used XPS to investigate the valence state of the gold atoms in the NPs. XPS spectra of 20 nm colloidal Au(0) NPs standard and polymeric GS–Au(I) thiolates (where GS stands for glutathione) were obtained. They exhibit the Au $4f_{7/2}$ binding energies (BE) of 83.8 and 85.0 eV, respectively.[24] As shown in Fig. S4 (ESI†), Au $4f_{7/2}$ binding energy (BE) for the three NP samples is close to that of Au(I) (BE 85.0 eV) in polymeric GS–Au(I) NPs, confirming the existence of Au(I) in α-Au–Cys, β-Au–Cys, and Ag-doped Au–Cys NPs. Also in Fig. S4 (ESI†), Ag 3d binding energy (BE) curves confirm the presence of Ag only for Ag-doped Au–Cys NP samples. High-resolution Ag 3d binding energy (BE) for Ag-doped Au–Cys NPs samples is close to that of Ag(I) (BE 374 eV and 368.5 eV) in $AgNO_3$,[20] suggesting the existence of Ag(I) in Ag-doped Au–Cys NPs (see Fig. S4, ESI†).

Linear optical properties

A UV-vis absorption peak (see Fig. 2a) is located at approximately 350–370 nm, a characteristic wavelength for transitions involving supramolecular gold–cysteine assemblies.[4] While the α-Au–Cys NPs are found to be non-fluorescent in water, both β-Au–Cys and Ag-doped Au–Cys NPs have orange-red emission (maximum at 635 nm for β-Au–Cys and 670 nm for Ag-doped Au–Cys), large Stokes shift (> 250 nm), and a long fluorescence lifetime component (200 ns and 400 ns for β-Au–Cys Ag-doped Au–Cys NPs respectively). It was shown that β-Au–Cys NPs adopted lamellar-like assemblies and strongly interplay with each other[7] leading to a kind of "stiffening" of the –(Au–Cys)– chains by additional hydrogen bonding enabling fluorescence emission (as compared to non-fluorescent α-Au–Cys NPs).[25] The quantum yield (QY) of the strongest fluorescent species in water, *i.e.* Ag-doped Au–Cys NPs is ~0.6%, as determined by comparison with DCM (4(dicyanomethylene)-2-methyl-6-(*p*-dimethylaminostyryl)-4*H*-pyran), see Experimental section for details. However, the obtained QY value is probably underestimated because of the intensive light scattering of NPs in water. The stability of as-formed α-Au–Cys NPs was explored as a function of pH. The same absorption spectra are observed for pH values ranging from ~5 to 11, confirming the stability of NPs over a large pH range. At low pH (< 5), α-Au–Cys NPs might aggregate, leading to a distinct absorption spectrum (see Fig. S5, ESI†).

The circular dichroism (CD) signals for α-Au–Cys and Ag-doped Au–Cys NPs supramolecular assemblies present a positive band at ~360 nm, signature of the formation of a helical chiral structure.[4–6] L-Cysteine, a chiral natural amino-acid is used in this work. The structure suggesting chirality over some length scale might be due to the specific electrostatic interaction among the –SR side chains in the Au(I)–Cys polymeric backbone, which likely results in some helicity. Interestingly, for β-Au–Cys, the CD signal is blue-shifted and increases by more than a fourfold factor as compared to the one recorded for α-Au–Cys (see Fig. 2c). This band shift accompanied with a strong enhancement might be the signature of a structural change between α-Au–Cys and β-Au–Cys as evidenced by Söptei *et al.*[7] Indeed, upon heating, α-Au–Cys NPs transform into β-Au–Cys NPs adopting a multilayer superlattice structure.[7] Chiral effects might be enhanced with the aggregation of Au–Cys units into sheets and multilayers. Of note the chiral signal of Ag-doped Au–Cys NPs is very similar to the one observed for α-Au–Cys (see Fig. 2c). Most likely, the addition of the silver salt does not alter the helical chiral structure.

Clearly, the addition of silver salt to α-Au–Cys NP solution (1 : 20 Au/Ag molar ratio) leads to a dramatic enhancement, from non-measurable fluorescence signals for α-Au–Cys NPs to intense red emission (with QY ~ 0.6%) for Ag-doped Au–Cys NPs. A smaller Au : Ag molar ratio (< 1 : 20) leads to less fluorescent species (but with similar fluorescence spectra).

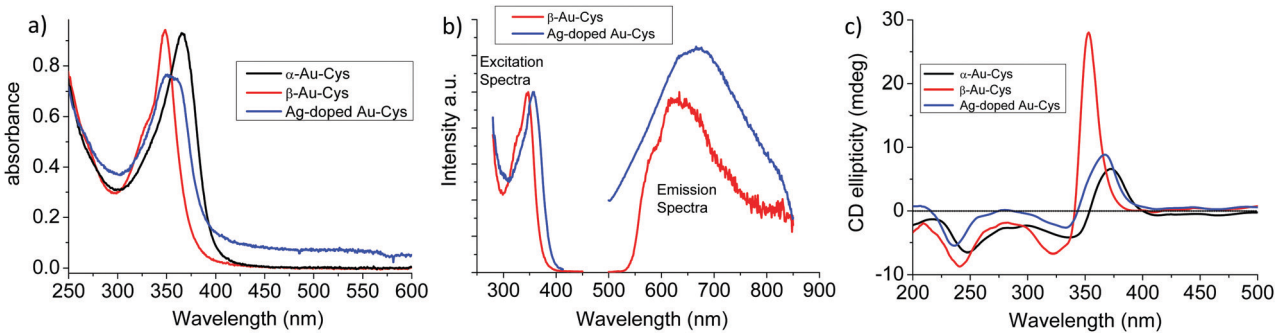

Fig. 2 (a) UV-vis absorption spectra of α-Au–Cys, β-Au–Cys and Ag-doped Au–Cys NPs prepared in water. (b) Excitation and emission spectra of β-Au–Cys and Ag-doped Au–Cys NPs. The fluorescence of α-Au–Cys is not measurable. The fluorescence intensities excited at 355 nm are plotted in arbitrary units. (c) CD spectra of α-Au–Cys, β-Au–Cys and Ag-doped Au–Cys NPs prepared in water.

On the other hand, increasing the Au : Ag molar ratio (>1 : 20) leads certainly to the aggregation of Ag into small Ag clusters since a new band at ~400 nm emerges which may be attributed to the signature of a plasmon band. Of note, NPs produced with an Au : Ag molar ratio of >1 : 20 are less stable with time and tend to precipitate. From a structural point of view, the addition of the silver salt has led to the incorporation of Ag^+ ions in the –(Au–Cys)– chains. Two possible incorporation sites have to be considered: (i) external: an intramolecular chelation effect fostered by the formation of a five-membered chelation ring between the COO^- and NH_2 groups with Ag^+, (ii) internal: Ag^+/Au^+ substitution in the –(Au–Cys)– chain motifs. Of note, the external incorporation would lead to the interruption of intercysteine H-bonds and thus the destruction of the helical chiral structure.[26] The fact that the α-Au–Cys and Ag-doped Au–Cys NP CD signals are similar precludes this external incorporation scenario, and most likely –(Au–Cys)– chain motifs are randomly substituted by Ag^+/Au^+ within the polymer chain.

Nonlinear optical properties

The TPEF spectra with excitation ranging between 720 and 850 nm, were recorded for the supramolecular assemblies, as shown in Fig. S6 (ESI†). For TPEF, a broad band in the visible range between 350 and 600 nm centered at about 450 nm was observed. A similar spectrum was obtained for $Au_{10}(SG)_{10}$ catenane (SG stands for glutathione) nanoclusters.[27] $Au_{10}(SG)_{10}$ is a cyclic polymeric –(Au–SG)– chain-like structure. Calculations showed that the leading excitations within the S_1 state involve Au···Au units together with neighboring sulfur atom subunits.[27] Table 1 shows the TPEF cross-sections in GM units for Au–Cys and Ag doped Au–Cys supramolecular assemblies in the 720–850 nm wavelength range. TPEF cross-sections exceed 1000 GM and reach 5430 GM for Ag-doped Au–Cys NPs at 720 nm, following the trend TPEF(α-Au–Cys) < TPEF(β-Au–Cys) < TPEF(Ag-doped Au–Cys). Also for each NP, the TPEF cross-section increases as the laser wavelength excitation decreases. This behavior is due to a resonance effect.[28] Indeed, below 800 nm, the two-photon excitation step can reach the electronic state responsible for the absorption band at ~360 nm. Both TPA and TPEF cross-sections are dramatically larger than those reported for Au NCs (<1 GM).[27,29] These sub-100 nm supramolecular assemblies are therefore potentially interesting for multiphoton applications.

The first hyperpolarizability of as-prepared supramolecular assemblies was obtained using the hyper-Rayleigh scattering (HRS) technique.[29] The HRS intensity was recorded for several concentrations of the NPs dispersed in aqueous solutions (Fig. S7, ESI,† and Fig. 3) and short-range spectra were recorded around the HRS wavelength. The subtraction of the fluorescence background was performed as described in our previous works.[29] Table 1 also displays the first hyperpolarizability values in units of 10^{-27} esu for Au–Cys supramolecular assemblies and Ag doped Au–Cys supramolecular assemblies in the 720–850 nm wavelength range. Hyperpolarizabilities exceed 100×10^{-27} esu and reach 476×10^{-27} esu for Ag-doped Au–Cys NPs at 720 nm excitation. They follow the trend β(α-Au–Cys) < β(β-Au–Cys) < β(Ag-doped Au–Cys), similar to the TPEF cross-section. Likewise, for each NP, the β values increase as the excitation laser wavelength decreases. This behavior is due to the resonance effect, similar to the TPEF case.[28] Finally, we would like to emphasize that the hyperpolarizability values reported here for Au–Cys NPs and Ag-doped Au–Cys NPs are in the same order of magnitude as the values reported for spherical plasmonic Au NPs with sizes in the range of 50–100 nm (Au 50 nm: 124×10^{-27} esu; Au 80 nm: 342×10^{-27} esu;

Table 1 Absolute magnitude of the first hyperpolarizability, two-photon absorption (TPA) and two-photon excited fluorescence cross-sections (TPEF) for α-Au–Cys, β-Au–Cys and Ag-doped Au–Cys NPs at several laser excitation wavelengths

	First hyperpolarizability ($\times 10^{-27}$ esu)				TPA cross section (GM)	TPEF cross section (GM)			
	720 nm	750 nm	800 nm	850 nm	720 nm	720 nm	750 nm	800 nm	850 nm
α-Au–Cys NPs	91	102	65		6.3×10^7		1660	867	
β-Au–Cys NPs	194	142	105		6.3×10^7		2880	1780	
Ag-doped Au–Cys NPs	476	356	225	208	12.9×10^7	5430	3630	2400	1300

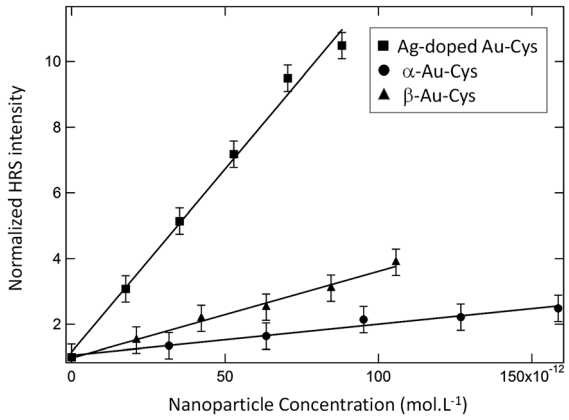

Fig. 3 Linear plots of the normalized HRS intensity for aqueous solutions of α-Au–Cys, β-Au–Cys and Ag-doped Au–Cys NPs as a function of concentration for an 800 nm fundamental laser excitation. The continuous lines correspond to linear adjustments of the experimental data.

and Au 100 nm: 668 × 10^{-27} esu at 800 nm laser excitation, determined using the known first hyperpolarizability for pure water).[12,30] However, the hyperpolarizability for plasmonic NPs has a different origin compared to that of supramolecular assemblies. Indeed, it has been demonstrated that the hyperpolarizability finds its origin from the breaking of centrosymmetry at the surface for plasmonic NPs. Here, for supramolecular assemblies, the origin of hyperpolarizability may stem from the non-centrosymmetric molecular structure of the NP volume due to the molecular structure and, also due to chirality. The charge transfer nature of the –(Au–Cys)– motif and silver doping may then be key factors enhancing the first hyperpolarizabilities, as reported in this work.

Insights from theoretical approach: structure–optical property relationship

Two model systems for the experimentally prepared supramolecular assemblies have been considered, namely M_3–Cys_4–CH_3 with M = Au_3 and Ag–Au_2 and M_5–Cys_6–CH_3 with M = Au_5 and Ag–Au_4 in order to determine the role of silver atoms and the transition from the smallest subunit to larger subunits for which the helical structure is supposed to form. Notice that the CH_3 terminal group introduced in these model systems serves as an end-protection and provides an even number of electrons. In addition, the ion-pairing of cysteines (zwitterionic form) in both model systems have been introduced by taking into account water as a solvent.

We focus on the influence of doping Au–Cys systems with silver atoms on the linear and nonlinear optical properties from a conceptual point of view. For all model systems, doping with silver atoms does not influence considerably the linear absorption properties, OPA (one-photon absorption), due to the fact that excitations take place between molecular orbitals which are energetically very similar in pure Au–Cys and Ag doped Au–Cys. The OPA spectra of two isomeric structures of Ag doped and pure Au M_5–Cys_6–CH_3 (where M stands for the metal,

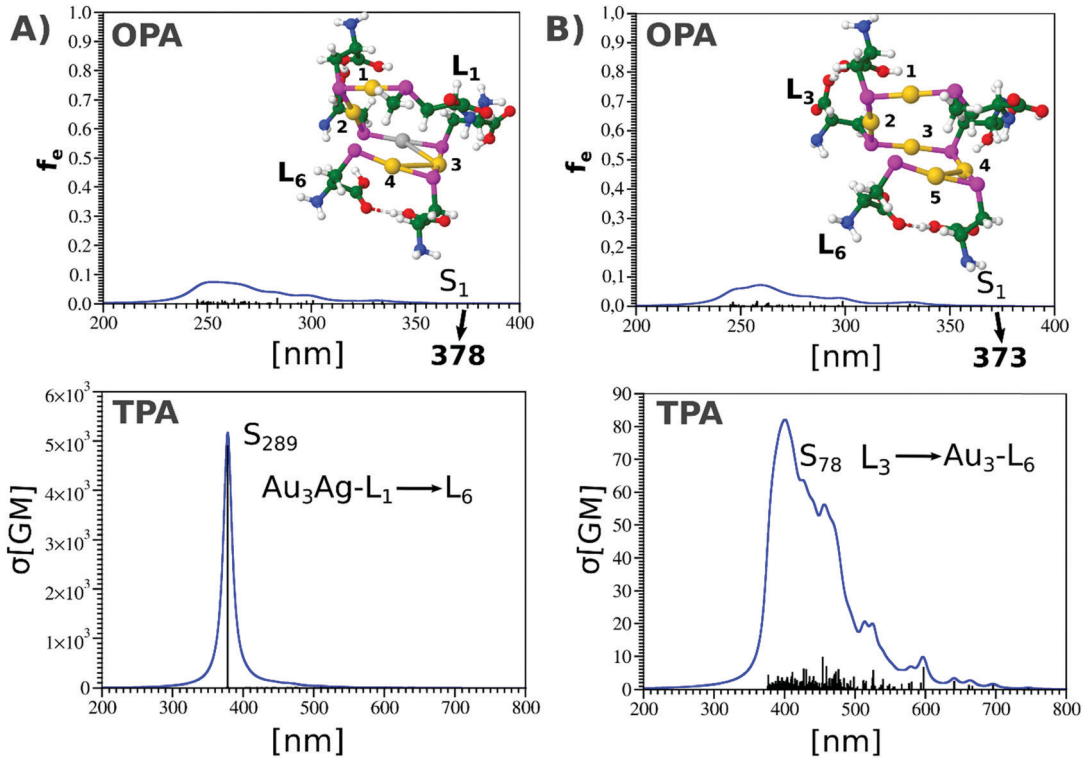

Fig. 4 TDDFT (upper part) OPA and (lower part) TPA spectra for optimized structures of the model systems: (A) Au_4–Ag–Cys_6–CH_3 and (B) Au_5–Cys_6–CH_3. Structure parts involved in the leading excitations of the S_{289} and S_{78} states are labeled according to the structures shown in the upper part. Broadening of the spectral lines is simulated with a Lorentzian profile with a half-width of 15 nm (blue lines). (Ag-grey, Au-yellow, S-magenta, C-green, O-red, N-blue, and H-white.)

either Au or Ag) together with molecular orbitals responsible for one-photon transitions are shown in Fig. S8 (ESI†) illustrating that silver atoms do not have influence on the OPA properties of the system.

In contrast, silver atoms play a key role in deciding the nonlinear properties. The latter are several orders of magnitude larger in doped systems as compared to the pure undoped Au–Cys systems (*cf.* Fig. 4 and Fig. S10, ESI†). OPA and TPA (two photon absorption) optical properties of helical model compounds are shown in Fig. 4 and confirm the experimental findings, in particular the huge enhancement of nonlinear absorption is due to the silver atom doping effect which induces large transition dipole moments. Notice that it is an open question whether doping with other noble metal atoms (*e.g.* Cu) with a similar energy ordering of orbitals, might cause similar effects or not. This might be important for design of new doped supramolecular assemblies inducing enhanced nonlinear properties.

Metal atoms as well as ligands are involved in transitions with large cross-sections. The resonance between one-photon and two-photon excited states at 377 nm, in Au_4–Ag–Cys_6–CH_3 (see Fig. S9, ESI†) is responsible for the blowing up of the TPA cross-section. The latter can be brought back to the realistic value by introducing an adequate damping factor.[31] It is interesting to notice that enlargement of the system may influence the TPA cross-section enhancement due to Ag atom doping as shown by experimental findings. In contrast, for pure Au–Cys systems, no resonance between one-photon and two-photon excited states has been found. As a result, the two-photon cross-sections are very low.

The key role of Ag atom doping for two photon absorption has also been found for the smallest M_3–Cys_4–CH_3 system which does not have a helical structure, as shown in Fig. S10 (ESI†). The pure Au–Cys compound has a negligible TPA cross-section in comparison with the two isomers in which a Ag atom is present. In contrast, for linear optical absorption properties, the Ag atom does not have any substantial influence, as shown in Fig. S11 (ESI†). Moreover, the role of the silver atom for the enhancement of nonlinear properties remains unchanged in the smallest model system in comparison with the helical model system.

In summary theoretical findings support experimental results and allow for the generalization of single Ag atom doping in the context of the enhancement of the nonlinear optical properties of doped Au–Cys supramolecular assemblies. Moreover, the ion-pairing of cysteine in Au_2–Ag–Cys_4–CH_3 and in the helical model system Au_4–Ag–Cys_6–CH_3 has been illustrated by taking into account water as the solvent (*cf.* Computational section and Fig. S12, ESI†). For Au_2–Ag–Cys_4–CH_3 with ion-pairing of cysteines, according to TDDFT calculations, the resonance between OPA and TPA states also confirms the presence of a large TPA cross-section.

Our model systems serve three purposes: (i) to show the appearance of the helical structure; (ii) to illustrate similarities between the gas phase and solvent and (iii) to compare the quantitative influence of different functionals (*cf.* Computational).

Conclusions

In this work, we have proposed a simple and robust two-step process route at elevated pH using trimethylamine for the self-assembly and formation of Au–Cys supramolecular assemblies. Unlike many other reported works, involving a simple one-step process at pH 3–7 and leading to sub μm nanoparticles, our synthesis leads to sub-100 nm supramolecular nanostructures. These nanostructures are found to be stable in a wide pH range (from ∼5 to 11). Two strategies were proposed to enhance their nonlinear optical properties: (i) thermal heating that induces coiling, aggregation, and ultimately formation of lamellar structures and (ii) alloying of the NPs with silver atoms. Silver-doping leads to the dramatic enhancement of the optical properties of Au–Cys supramolecular assemblies in the nonlinear optical regime. This has been confirmed by theoretical investigations of one and two-photon optical properties for model systems. Huge enhancement of the two-photon absorption cross section arises with the doping of Au–Cys supramolecular assemblies with a single silver atom. These findings open new routes for the preparation of novel materials with enhanced nonlinear optical properties. The combination of strong circular dichroism activities along with enhanced emission properties in particular after two-photon absorption should enlarge the toolbox of supramolecular nanoarchitectures for bio-applications.

Experimental and calculations

Materials

All chemicals were commercially available and used as received. Tetrachloroauric(III) acid trihydrate ($HAuCl_4{\cdot}3H_2O$) and silver trifluoroacetate were purchased from Acros Organics, L-cysteine, triethylamine (TEA), glacial acetic acid, methanol (MeOH), and diethyl ether (Et_2O) were purchased from Sigma-Aldrich. Ultrapure water with a specific resistivity of 18.2 MΩ was used throughout the synthesis.

Synthesis of α- and β-Au–Cys NPs

Briefly, 0.38 mmol cysteine was dissolved in 20 ml of water and 0.5 ml of triethylamine. 0.5 ml of gold salt (0.127 mmol, 50 mg) was quickly added and the solution was stirred 30 s by inversion (the color becomes slightly yellow). Quickly, 1 ml of glacial acetic acid was added to induce precipitation of α-Au–Cys NPs which was centrifuged (5 min/6000 rpm). The supernatant was removed and α-Au–Cys NPs were redispersed in water (2 ml with 100 μl of TEA, vortex time 5 min). 20 ml of methanol was then added to precipitate α-Au–Cys NPs with centrifugation (10 min/6000 rpm). α-Au–Cys NPs were also redispersed in 2 ml of water with 10 μl of TEA and precipitated with MeOH (10 ml)/Et_2O (10 ml). After centrifugation (10 min/6000 rpm), the product was dried in air. For all experiments, the resulting powder was dissolved in water containing 0.1% v/v of TEA (pH ∼ 11). For producing β-Au–Cys NPs, the solution containing α-Au–Cys NPs was heated at 70 °C for 16 h. It is thought that, upon heating, polymeric chains from α-Au–Cys NPs coiled,

aggregated, and ultimately formed more compact lamellar sheets.[7,32]

Synthesis of silver-doped Au–Cys NPs

The NPs are synthesized in 2 steps, first, the α-Au–Cys NPs solution was used, silver trifluoroacetate (1 : 20 Au/Ag molar ratio) was added to the solution and the solution was stirred for 24 h. Then in a second step, the solution was heated to 70 °C for 60 h. After that the solution was purified following the same steps as described for α-Au–Cys NPs.

Characterization

Charge-detection mass spectrometer (CDMS) is a home-made instrument used to measure mass distribution; it extends the limit of other MS devices by measuring molar weights in the range of mega- to giga-Daltons thus allowing the study of larger system such as viruses,[33] bio-particles[22] and even NP assemblies.[21,23] Experiments were performed on a custom-built charge detection mass spectrometer with an electrospray ionization (ESI) source. This instrument is described in detail elsewhere.[34] The samples were injected at flow rates of 0.2–0.6 ml h^{-1}, and entered the electrospray chamber through a 0.1 mm internal diameter stainless steel capillary tube located inside the needle tip. Nitrogen drying gas was injected between the end cap and the transfer glass capillary and passed through a heater typically set at 200 °C. The vacuum interface was composed of a glass transfer capillary that passes the ions into the first stage of the vacuum system, an end cap, a skimmer between the first and second vacuum stages, an hexapole ion guide and an exit lens. The charge detection device was used in a single pass mode.[35] The signal induced on the tube was picked up by a JFET transistor and was amplified by a low-noise, charge-sensitive preamplifier and then shaped and differentiated by a home-built amplifier. The signal was recorded on a waveform digitizer card that recorded the entire waveform for each ion passing through the detector tube at a sampling rate of 10 MHz. The data were transferred to a desktop computer where they were analyzed to compute the charge and mass of each ion. Internal calibration in charge was performed using a test capacitor that allowed a known amount of charge to be pulsed into the pick-up tube. In addition, an external calibration was performed using NIST traceable size standards.[21] Mass histograms are built from the collection of a statistically relevant number of single mass measurements for each sample (>2000 typically).

Hydrodynamic particle diameters were measured by dynamic light scattering (DLS) using a Malvern Zetasizer Nano ZS. A 633 nm wavelength laser beam was sent to a diluted sample maintained at 25 °C and the scattered signal intensity was analyzed at an angle of 173°. The cumulant analysis method was used.

X-ray photoelectron spectroscopy (XPS) measurements were carried out using a PHI Quantera SXM instrument (Physical Electronics, Chanhassen, USA) equipped with a 180° hemispherical electron energy analyzer and a monochromatized Al Kα (1486.6 eV) source operated at 15 kV and 4 mA. The analysis spot had a diameter of 200 μm and the detection angle relative to the substrate surface was 45°.

UV-visible, fluorescence and circular dichroism (CD) measurements

UV-vis spectra in solution were recorded using an AvaSpec-2048 fiber optic spectrometer and an AvaLight-DH-S deuterium-halogen light source. Fluorescence excitation and emission spectra were obtained using a Fluoromax-4 Horiba fluorimeter. With the same device (Fluoromax-4 Horiba), a complementary module allows the acquisition of fluorescence decay curve. A nano-LED excitation at 370 nm is used for the pulsed excitation with a duration of the order of ten picoseconds. Time correlated single photon counting with a resolution of 7 ps per channel allows the measurement of lifetimes from 200 ps to 0.1 ms.

The quantum yield value is obtained using an external reference with a known quantum yield value. We used DCM (4(dicyanomethylene)-2-methyl-6-(*p*-dimethylaminostyryl)-4*H*-pyran), the quantum yield of this molecule is 43% and to calculate the QY we used the following equation:

$$\varnothing_x = \varnothing_{\mathrm{Ref}} \times \frac{A_{\mathrm{Ref}}}{A_x} \times \frac{F_x}{F_{\mathrm{Ref}}} \times \left(\frac{n_x}{n_{\mathrm{Ref}}}\right)^2 \quad (1)$$

where $\varnothing$ is the QY, A is the value of absorption, F is the area of fluorescence spectra and n is the refraction indices of the solvent used (x and Ref stand to NP's used and reference respectively).

CD spectra were recorded using a home-made setup based on photo elastic modulator and lock-in amplifier detection devices previously described in ref. 36.

Nonlinear optical measurements

The set-up for hyper-Rayleigh scattering (HRS) and two-photon emission (TPE) has been described in detail in previous works.[28,29,37] Briefly, the light source for the HRS and TPEF measurements was a mode-locked femtosecond Ti:sapphire laser delivering at the fundamental wavelength pulse with a duration of about 140 fs at a repetition rate of 80 MHz. After passing through a low-pass filter to remove any unwanted harmonic light generated prior to the cell, the fundamental beam of about 300 mW was focused by a low numerical aperture microscope objective into a 0.5 cm spectrophotometric cell containing the aqueous solutions. The HRS and two-photon emission fluorescence (TPEF) light were collected at an angle of 90° from the incident direction by a 2.5 cm focal length lens. The HRS light was separated from the excitation light by a high-pass filter and a monochromator set at the second harmonic wavelength. The HRS light was then detected with a photomultiplier tube working in the single photon counting regime.

For the TPEF signal, the wavelength of the spectrometer (Jobin-Yvon, iHR320 spectrometer) was scanned between 350 nm and 750 nm but the same detection unit was used. For the two-photon excited fluorescence cross section, σ_{TPEF}, the ratio of the integrated fluorescence intensities (I) for the

reference and studied samples can be expressed as:

$$\sigma_{\mathrm{TPEF}} = \frac{\eta^{\mathrm{ref}}\sigma_2^{\mathrm{ref}}c^{\mathrm{ref}}}{c}\frac{I}{I^{\mathrm{ref}}} \quad (2)$$

Here, the index ref denotes values related to the reference measurements. c is the concentration of the molecules, and η and σ_2 are the fluorescence efficiency and two-photon absorption cross section, respectively. For reference materials, we have chosen fluorescein dye. From the literature, we assume at the excitation wavelength of 780 nm: σ_2 (fluorescein) = 33.3 GM using a quantum yield of 0.9 and a two photon absorption cross-section of 37 GM.[38]

The two-photon absorption cross section was probed using the P-scan (or Power-scan) technique during which the incident power is directly varied and the induced changes in the sample transmission are measured, as described in ref. 28.

Computational

The structural and one- and two-photon absorption (OPA and TPA) properties of model systems of gold–cysteine and silver doped supramolecular assemblies were determined using DFT, TDDFT[39,40] and a quadratic response approach[41,42] as implemented in the DALTON[43,44] program package. For gold atoms and silver 19 e^- relativistic effective core potential (19 e^- RECP) taking into account scalar relativistic effects has been employed.[45] For all atoms split valence polarization (SVP) atomic basis set have been used.[46] Structural and optical properties (OPA, TPA) were determined using the hybrid B3LYP functional.[47–49] In addition OPA and TPA spectra have been calculated using CAM-B3LYP[50] functional showing the expected blue shift of the energy of excited states with respect to the B3LYP functional (*cf.* Fig. S13, ESI†). Electron density difference between S_1 and S_0 presented in Fig. S14 (ESI†) illustrates that the role of doped Ag atom is more visible in Au_2–Ag–Cys_4–CH_3 than in Au_4–Ag–Cys_6–CH_3 due to a more compact Au–Ag–Au subunit. In both cases Au–S interaction due to presence of cysteine is pronounced (*cf.* Fig. S14, ESI†). In order to illustrate ion-pairing of cysteines in both model systems doped with a Ag atom, water solvent effect has been included using the SMD approach (*cf.* Fig. S12, ESI†).[51] Notice that in solvent the blue shift of absorption obtained using the CAM-B3LYP functional is also present. Quantitative comparison of model systems with experimental findings is difficult due to the 100 nm scale system used in the experiment but qualitatively model systems are useful for conceptual point of view.

Conflicts of interest

There are no conflicts to declare.

Acknowledgements

The authors would like to thank Céline Brunon from Science et Surface (www.science-et-surface.fr) for XPS spectra, Amina Bensallah-Ledoux (iLM) for CD spectra and Fabien Rossetti (iLM) for DLS measurements. The authors thank CNRS French-Croatian international lab (NCBA) for travel funding. This research was partially supported by the project STIM – REI, Contract Number: KK.01.1.1.01.0003, funded by the European Union through the European Regional Development Fund – the Operational Programme Competitiveness and Cohesion 2014–2020 (KK.01.1.1.01). V. B. K. and M. P. acknowledge the Center for Advanced Computing and Modelling (CNRM) for providing computing resources of the supercomputer Bura at the University of Rijeka and SRCE at University of Zagreb Croatia and Prof. Miroslav Radman at MedILS and Split-Dalmatia County for support.

References

1 R. J. Puddephatt, *Chem. Soc. Rev.*, 2008, **37**, 2012–2027.
2 H. Nie, M. Li, Y. Hao, X. Wang and S. X.-A. Zhang, *Chem. Sci.*, 2013, **4**, 1852–1857.
3 H. Nie, M. Li, Y. Hao, X. Wang, S. Gao, P. Wang, B. Ju and S. X.-A. Zhang, *RSC Adv.*, 2014, **4**, 50521–50528.
4 H.-Y. Chang, Y.-T. Tseng, Z. Yuan, H.-L. Chou, C.-H. Chen, B.-J. Hwang, M.-C. Tsai, H.-T. Chang and C.-C. Huang, *Phys. Chem. Chem. Phys.*, 2017, **19**, 12085–12093.
5 I. Russier-Antoine, F. Bertorelle, A. Kulesza, A. Soleilhac, A. Bensalah-Ledoux, S. Guy, P. Dugourd, P.-F. Brevet and R. Antoine, *Prog. Nat. Sci.: Mater. Int.*, 2016, **26**, 455–460.
6 Y.-T. Tseng, H.-Y. Chang, S. G. Harroun, C.-W. Wu, S.-C. Wei, Z. Yuan, H.-L. Chou, C.-H. Chen, C.-C. Huang and H.-T. Chang, *Anal. Chem.*, 2018, **90**, 7283–7291.
7 B. Söptei, J. Mihály, I. C. Szigyártó, A. Wacha, C. Németh, I. Bertóti, Z. May, P. Baranyai, I. E. Sajó and A. Bóta, *Colloids Surf., A*, 2015, **470**, 8–14.
8 S.-H. Cha, J.-U. Kim, K.-H. Kim and J.-C. Lee, *Chem. Mater.*, 2007, **19**, 6297–6303.
9 J. M. Forward, D. Bohmann, J. P. Fackler and R. J. Staples, *Inorg. Chem.*, 1995, **34**, 6330–6336.
10 H. Xu, Y. L. Song, X. R. Meng, H. W. Hou, M. S. Tang and Y. T. Fan, *Chem. Phys.*, 2009, **359**, 101–110.
11 X. Hong, S. Yinglin, M. Xiangru, H. Hongwei and F. Yaoting, *J. Appl. Polym. Sci.*, 2012, **125**, 682–689.
12 I. Russier-Antoine, E. Benichou, G. Bachelier, C. Jonin and P. F. Brevet, *J. Phys. Chem. C*, 2007, **111**, 9044–9048.
13 C. Quintana, M. Morshedi, H. Wang, J. Du, M. P. Cifuentes and M. G. Humphrey, *Nano Lett.*, 2019, **19**(2), 756–760.
14 J. Moreau, F. Lux, M. Four, J. Olesiak-Banska, K. Matczyszyn, P. Perriat, C. Frochot, P. Arnoux, O. Tillement, M. Samoc, G. Ponterini, S. Roux and G. Lemercier, *Phys. Chem. Chem. Phys.*, 2014, **16**, 14826–14833.
15 R. Antoine and V. Bonacic-Koutecky, *Liganded silver and gold quantum clusters. Towards a new class of nonlinear optical nanomaterials*, Springer, Cham, 2018.
16 R. Philip, P. Chantharasupawong, H. Qian, R. Jin and J. Thomas, *Nano Lett.*, 2012, **12**, 4661–4667.
17 N. Van Steerteghem, S. Van Cleuvenbergen, S. Deckers, C. Kumara, A. Dass, H. Häkkinen, K. Clays, T. Verbiest and S. Knoppe, *Nanoscale*, 2016, **8**, 12123–12127.

18 S. Wang, X. Meng, A. Das, T. Li, Y. Song, T. Cao, X. Zhu, M. Zhu and R. Jin, *Angew. Chem., Int. Ed.*, 2014, **53**, 2376–2380.
19 K. Brach, M. Waszkielewicz, J. Olesiak-Banska, M. Samoc and K. Matczyszyn, *Langmuir*, 2017, **33**, 8993–8999.
20 J.-S. Shen, D.-H. Li, M.-B. Zhang, J. Zhou, H. Zhang and Y.-B. Jiang, *Langmuir*, 2011, **27**, 481–486.
21 T. Doussineau, A. Désert, O. Lambert, J.-C. Taveau, M. Lansalot, P. Dugourd, E. Bourgeat-Lami, S. Ravaine, E. Duguet and R. Antoine, *J. Phys. Chem. C*, 2015, **119**, 10844–10849.
22 T. Doussineau, C. Mathevon, L. Altamura, C. Vendrely, P. Dugourd, V. Forge and R. Antoine, *Angew. Chem., Int. Ed.*, 2016, **55**, 2340–2344.
23 M. Loumaigne, C. Midelet, T. Doussineau, P. Dugourd, R. Antoine, M. Stamboul, A. Debarre and M. H. V. Werts, *Nanoscale*, 2016, **8**, 6555–6570.
24 C. Zhou, C. Sun, M. Yu, Y. Qin, J. Wang, M. Kim and J. Zheng, *J. Phys. Chem. C*, 2010, **114**, 7727–7732.
25 F. Bertorelle, C. Moulin, A. Soleilhac, C. Comby-Zerbino, P. Dugourd, I. Russier-Antoine, P.-F. Brevet and R. Antoine, *ChemPhysChem*, 2018, **19**, 165–168.
26 R. Randazzo, A. Di Mauro, A. D'Urso, G. C. Messina, G. Compagnini, V. Villari, N. Micali, R. Purrello and M. E. Fragalà, *J. Phys. Chem. B*, 2015, **119**, 4898–4904.
27 F. Bertorelle, I. Russier-Antoine, N. Calin, C. Comby-Zerbino, A. Bensalah-Ledoux, S. Guy, P. Dugourd, P.-F. Brevet, Ž. Sanader, M. Krstić, V. Bonačić-Koutecký and R. Antoine, *J. Phys. Chem. Lett.*, 2017, **8**, 1979–1985.
28 I. Russier-Antoine, F. Bertorelle, N. Calin, Z. Sanader, M. Krstic, C. Comby-Zerbino, P. Dugourd, P.-F. Brevet, V. Bonacic-Koutecky and R. Antoine, *Nanoscale*, 2017, **9**, 1221–1228.
29 I. Russier-Antoine, F. Bertorelle, M. Vojkovic, D. Rayane, E. Salmon, C. Jonin, P. Dugourd, R. Antoine and P.-F. Brevet, *Nanoscale*, 2014, **6**, 13572–13578.
30 J. Duboisset, G. Matar, I. Russier-Antoine, E. Benichou, G. Bachelier, C. Jonin, D. Ficheux, F. Besson and P. F. Brevet, *J. Phys. Chem. B*, 2010, **114**, 13861–13865.
31 P. N. Day, K. A. Nguyen and R. Pachter, *J. Chem. Theory Comput.*, 2010, **6**, 2809–2821.
32 C. Dai, Y. Hao, Y. Yu, M. Li and S. X.-A. Zhang, *J. Phys. Chem. A*, 2018, **122**, 5089–5097.
33 C. A. Lutomski, N. A. Lyktey, Z. Zhao, E. E. Pierson, A. Zlotnick and M. F. Jarrold, *J. Am. Chem. Soc.*, 2017, **139**, 16932–16938.
34 J. Pansieri, M. A. Halim, C. Vendrely, M. Dumoulin, F. Legrand, M. M. Sallanon, S. Chierici, S. Denti, X. Dagany, P. Dugourd, C. Marquette, R. Antoine and V. Forge, *Chem. Sci.*, 2018, **9**, 2791–2796.
35 M. A. Halim, F. Bertorelle, T. Doussineau and R. Antoine, *Rapid Commun. Mass Spectrom.*, 2018, 1–5, DOI: 10.1002/rcm.8204.
36 S. Guy, A. Stoita-Crisan, A. Bensalah-Ledoux, T. Vautey and L. Guy, *Opt. Mater.*, 2011, **34**, 347–350.
37 I. Russier-Antoine, F. Bertorelle, R. Hamouda, D. Rayane, P. Dugourd, Z. Sanader, V. Bonacic-Koutecky, P.-F. Brevet and R. Antoine, *Nanoscale*, 2016, **8**, 2892–2898.
38 M. A. Albota, C. Xu and W. W. Webb, *Appl. Opt.*, 1998, **37**, 7352–7356.
39 V. Bonačić-Koutecký, A. Kulesza, L. Gell, R. Mitrić, R. Antoine, F. Bertorelle, R. Hamouda, D. Rayane, M. Broyer, T. Tabarin and P. Dugourd, *Phys. Chem. Chem. Phys.*, 2012, **14**, 9282–9290.
40 F. Bertorelle, R. Hamouda, D. Rayane, M. Broyer, R. Antoine, P. Dugourd, L. Gell, A. Kulesza, R. Mitric and V. Bonacic-Koutecky, *Nanoscale*, 2013, **5**, 5637–5643.
41 P. Norman, *Phys. Chem. Chem. Phys.*, 2011, **13**, 20519–20535.
42 N. H. List, R. Zaleśny, N. A. Murugan, J. Kongsted, W. Bartkowiak and H. Ågren, *J. Chem. Theory Comput.*, 2015, **11**, 4182–4188.
43 *Dalton, a molecular electronic structure program, Release v2016.2*, 2017, see http://daltonprogram.org.
44 K. Aidas, C. Angeli, K. L. Bak, V. Bakken, R. Bast, L. Boman, O. Christiansen, R. Cimiraglia, S. Coriani, P. Dahle, E. K. Dalskov, U. Ekström, T. Enevoldsen, J. J. Eriksen, P. Ettenhuber, B. Fernández, L. Ferrighi, H. Fliegl, L. Frediani, K. Hald, A. Halkier, C. Hättig, H. Heiberg, T. Helgaker, A. C. Hennum, H. Hettema, E. Hjertenæs, S. Høst, I.-M. Høyvik, M. F. Iozzi, B. Jansik, H. J. Aa. Jensen, D. Jonsson, P. Jørgensen, J. Kauczor, S. Kirpekar, T. Kjærgaard, W. Klopper, S. Knecht, R. Kobayashi, H. Koch, J. Kongsted, A. Krapp, K. Kristensen, A. Ligabue, O. B. Lutnæs, J. I. Melo, K. V. Mikkelsen, R. H. Myhre, C. Neiss, C. B. Nielsen, P. Norman, J. Olsen, J. M. H. Olsen, A. Osted, M. J. Packer, F. Pawlowski, T. B. Pedersen, P. F. Provasi, S. Reine, Z. Rinkevicius, T. A. Ruden, K. Ruud, V. Rybkin, P. Salek, C. C. M. Samson, A. Sánchez de Merás, T. Saue, S. P. A. Sauer, B. Schimmelpfennig, K. Sneskov, A. H. Steindal, K. O. Sylvester-Hvid, P. R. Taylor, A. M. Teale, E. I. Tellgren, D. P. Tew, A. J. Thorvaldsen, L. Thøgersen, O. Vahtras, M. A. Watson, D. J. D. Wilson, M. Ziolkowski and H. Ågren, The Dalton quantum chemistry program system, *Wiley Interdiscip. Rev.: Comput. Mol. Sci.*, 2014, **4**, 269–284, DOI: 10.1002/wcms.1172.
45 D. Andrae, U. Häußermann, M. Dolg, H. Stoll and H. Preuß, *Theor. Chim. Acta*, 1990, **77**, 123–141.
46 F. Weigend and R. Ahlrichs, *Phys. Chem. Chem. Phys.*, 2005, **7**, 3297–3305.
47 A. D. Becke, *Phys. Rev. A: At., Mol., Opt. Phys.*, 1988, **38**, 3098–3100.
48 A. D. Becke, *J. Chem. Phys.*, 1993, **98**, 1372–1377.
49 C. Lee, W. Yang and R. G. Parr, *Phys. Rev. B: Condens. Matter Mater. Phys.*, 1988, **37**, 785–789.
50 T. Yanai, D. P. Tew and N. C. Handy, *Chem. Phys. Lett.*, 2004, **393**, 51–57.
51 A. V. Marenich, C. J. Cramer and D. G. Truhlar, *J. Phys. Chem. B*, 2009, **113**, 6378–6396.

Chapter 3

Optical Properties of Liganded Noble Metal Nanoclusters

3.1 Zwitterion Functionalized Gold Nanoclusters

Reproduced from:

Martina Perić, Željka Sanader Maršić, Isabelle Russier-Antoine, Hussein Fakhouri, Franck Bertorelle, Pierre-François Brevet, Xavier le Guével, Rodolphe Antoine and Vlasta Bonačić-Koutecký, "Ligand shell size effects on one- and two-photon excitation fluorescence of zwitterion functionalized gold nanoclusters", *Phys. Chem. Chem. Phys.*, **2019**, 21, 23916-23921

3.2 Gold Catenane Nanoclusters Doped by Silver Atoms

Reproduced from:

Srestha Basu, Martina Perić Bakulić, Hussein Fakhouri, Isabelle Russier-Antoine, Christophe Moulin, Pierre-François Brevet, Vlasta Bonačić-Koutecký*, and Rodolphe Antoine, "Rationale Strategy to Tune the Optical Properties of Gold Catenane Nanoclusters by Doping with Silver Atoms", *J. Phys. Chem. C*, **2020**, 124, 35, 19368–19374

3.3 Towards Application: Au15 Nanoclusters as Luminescent Probes for Protein Carbonylation Detection

Reproduced from:

Guillaume F. Combes, Hussein Fakhouri, Christophe Moulin, Marion Girod, Franck Bertorelle, Srestha Basu, Romain Ladouce, Martina Perić Bakulić, Željka Sanader Maršić, Isabelle

Russier-Antoine, Pierre-François Brevet, Philippe Dugourd, Anita Krisko, Katarina Trajković, Miroslav Radman, Vlasta Bonačić-Koutecký and Rodolphe Antoine, "Functionalized Au_{15} nanoclusters as luminescent probes for protein carbonylation detection", *Commun Chem*, **2021**, 4, 69

PCCP

PAPER

View Article Online
View Journal

Cite this: DOI: 10.1039/c9cp05262c

Ligand shell size effects on one- and two-photon excitation fluorescence of zwitterion functionalized gold nanoclusters†

Martina Perić,[a] Željka Sanader Maršić,[a] Isabelle Russier-Antoine,[b] Hussein Fakhouri,[b] Franck Bertorelle,[b] Pierre-François Brevet,[b] Xavier le Guével,[c] Rodolphe Antoine*[b] and Vlasta Bonačić-Koutecký*[ad]

Received 26th September 2019,
Accepted 22nd October 2019

DOI: 10.1039/c9cp05262c

rsc.li/pccp

Gold nanoclusters (Au NCs) are an emerging class of luminescent nanomaterials but still suffer from moderate photoluminescence quantum yields. Recent efforts have focused on tailoring their emission properties. Introducing zwitterionic ligands to cap the metallic kernel is an efficient approach to enhance their one-photon excitation fluorescence intensity. In this work, we extend this concept to the nonlinear optical regime, *i.e.*, two-photon excitation fluorescence. For a proper comparison between theory and experiment, both ligand and solvent effects should be considered. The effects of ligand shell size and of aqueous solvent on the optical properties of zwitterion functionalized gold nanoclusters have been studied by performing quantum mechanics/molecular mechanics (QM/MM) simulations.

A. Introduction

In the past decade, gold nanoclusters (Au NCs)[1] have emerged as fascinating luminescent nanomaterials.[2,3] However, the photoluminescence quantum yield (QY) of most nanoclusters is still relatively low (generally of a few percent). Recent efforts focus on tailoring the emission properties,[4] including photoluminescence (PL) intensity and emission wavelength, the two basic characteristics of fluorescence. Some strategies such as surface ligand engineering,[5–7] aggregation-induced fluorescence,[8–10] silver doping,[11–16] and ligand-shell rigidifying[17,18] have been achieved. In particular, the surface shell rigidification permits to decrease the energy loss due to intramolecular rotations and vibrations, thus increasing the PL intensity of nanoclusters. Introducing bidentate thiol zwitterionic ligands to cap the metallic kernel is another efficient approach to rigidify the surface structure of metal nanocluster.[19] Several groups have prepared bright fluorescent nanoclusters using this strategy.[20–23] The PL intensity and emission wavelength of these nanoclusters can be easily tailored *via* controlling the functional groups of the zwitterionic ligands.[24] Indeed, due, to the zwitterionic form of the tails of ligands, strong intermolecular electrostatic interactions occur allowing for the formation of different ligand shells on the surface of the gold clusters.[24,25]

Although it was found that the surface of Au NCs plays a major role in fluorescence generation, several fundamental issues are still not well understood. In particular, the extent to which the ligand shell and the metal core are coupled and how this coupling modulates the emission properties remain to be clarified. Therefore, theoretical explorations of the structural and electronic properties of various nanoclusters in the ground and excited states have been reported to address the origin of the photoluminescence enhancement.[26,27] The Aikens group investigated the geometric and electronic structural changes of gold nanoclusters upon photoexcitation using time-dependent density functional theory (TD-DFT) method.[28–30] Moreover it was also shown that the inclusion of full ligands in calculations was needed to accurately describe the experimental optical spectra.[27,28,31]

The combination of DFT with molecular mechanics within QM/MM approach appears to be appropriate and was recently used for structural elucidation of the clusters with explicit ligands.[32] Akola and coworkers[33,34] used QM/MM simulations to study the influence of aqueous solvent and explicit ligands (*e.g.*, glutathione ligands) on the structural and electronic properties of thiolate-protected $Au_{25}(SR)_{18}^-$ clusters. In this article, we show that

[a] *Center of Excellence for Science and Technology-Integration of Mediterranean Region (STIM) at Interdisciplinary Center for Advanced Sciences and Technology (ICAST), University of Split, Poljička cesta 35, 21000 Split, Croatia*
[b] *Institut Lumière Matière, UMR5306, Université Claude Bernard Lyon1-CNRS, Univ. Lyon 69622, Villeurbanne Cedex, France. E-mail: rodolphe.antoine@univ-lyon1.fr*
[c] *Institute for Advanced Biosciences, University of Grenoble Alpes/INSERM1209/CNRS-UMR5309, Grenoble, France*
[d] *Chemistry Department, Humboldt University of Berlin, Brook-Taylor-Strasse 2, 12489 Berlin, Germany. E-mail: vbk@chemie.hu-berlin.de*

† Electronic supplementary information (ESI) available: Composition of AuZW nanoclusters by XPS and ESIMS analysis. Experimental optical spectra of AuZw NCs. Calculated OPA and TPA spectra obtained by TD-DFT for model clusters and by QM/MM approach for entire AuZw NCs. See DOI: 10.1039/c9cp05262c

the introduction of bidentate thiol zwitterionic ligands to cap the metallic kernel is another efficient approach to enhance nonlinear response in particular two-photon excitation fluorescence. In order to address better the ingredients responsible for their enhanced photo emission, we employ a QM/MM approach with explicit ligands. This approach permits us to address the linear and nonlinear optical regime of zwitterion functionalized gold nanoclusters (AuZw NCs) evaluating effects of ligand shell size. Optical properties including one- and two-photon absorption spectra obtained at the QM/MM level of theory are in qualitative agreement with optical measurements. Ligand shell rigidification should prevent excited state geometry relaxation through intramolecular motions, as well as through the associated non-radiative energy decay pathways. For this purpose we investigated the influence of ligand shell size and the charge on linear and nonlinear properties of zwitterion functionalized gold nanoclusters. Also, we studied the penetration of water molecules into AuZw NCs depending on the ligand shell sizes and their possible role as quencher for emission properties of AuZw NCs.

B. Results and discussion

Au NCs with thioctic-zwitterion ligand (Zw, $C_{15}H_{30}N_2O_4S_3$, MW = 399 g mol^{-1}, see Fig. 1) were synthesized following the protocol described elsewhere.[22] As-synthesized Au NCs were characterized by X-ray photoelectron spectroscopy (XPS)[19] and by electrospray mass spectrometry (ESI-MS).[22] By controlling the initial molar ratio of Au per Zw molecules: Au : Zw, three zwitterion stabilized Au NCs with different ligand shell sizes were synthesized (named in the following as Au : Zw 1 : 1, Au : Zw 1 : 2 and Au : Zw 1 : 5). XPS measurements[19] show that for AuZw 1 : 1; 1 : 2 and 1 : 5 the ratio Au^0/Au^+ is ≈ 2. XPS measurements can also give a ratio between Au and sulfur atoms (~ 0.2).

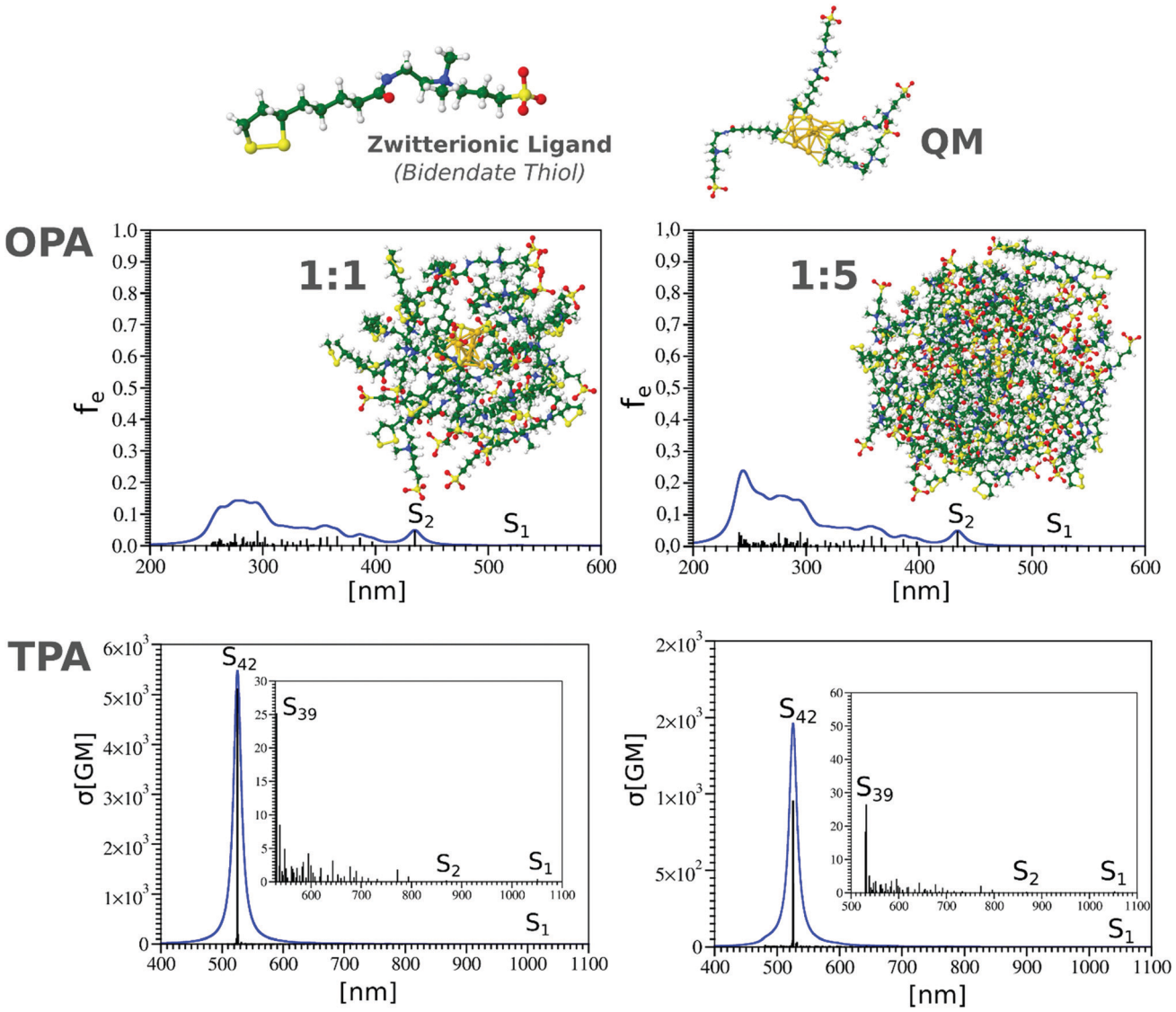

Fig. 1 Comparison of OPA and TPA spectra obtained by QM/MM approach for $Au_{12}Zw_4$ (QM-TDDFT) with 1 : 1 and 1 : 5 ratio of Au/zwitterions (MM).

By coupling these results with mass spectrometry data, one can build AuZw clusters with a model ''core'' structure surrounded by a ligand shell of different size (*e.g.*, different number of Zw molecules) (see ESI† for more details). Thus, possible molecular formula for AuZw 1 : 1 (≈11 kDa), AuZw 1 : 2 (≈17 kDa) and AuZw 1 : 5 (≈29 kDa) could be $Au_{12}Zw_{22}$, $Au_{12}Zw_{37}$ and $Au_{12}Zw_{66}$ respectively. In other words, the three AuZw nanoclusters can be built with a $Au_{12}Zw_4$ subunit surrounded by 18, 33 and 62 Zw molecules in the outer shell.

Experimental optical spectra, *i.e.*, one-photon absorption (OPA), one- and two-photon excited fluorescence, are given in ESI† (Fig. S1 and S2). One and two-photon quantum yields (1PQY and 2PQY), first hyperpolarizability values as well as two-photon absorption and excited fluorescence cross sections (TPA and TPEF) are collected in Table 1. The one-photon absorption spectra of the as-synthesized AuZw NCs are very similar and show a monotonic increase of intensity below ∼500 nm. Fluorescence signals are strongly enhanced when Zw > Au as it was previously reported.[22] Furthermore, TPEF spectra for AuZw 1 : 5 display two bands in the blue and red region of visible range (see Fig. S2, ESI†). Note that for AuZw 1 : 1 and AuZw 1 : 2 NCs, TPEF spectra display only one band in the blue with a weak intensity (data not shown). One and two-photon quantum yields of 1.4% and 5×10^{-3}% respectively are reported for AuZw 1 : 5 NCs. Experimentally, for AuZw 1 : 5, we found that the TPEF cross section at 800 nm excitation is 0.5 GM and the two-photon absorption (TPA) cross section 10 000 GM. The first hyperpolarizability determined for an excitation wavelength of 800 nm for the AuZw NCs is found in the same range of the hyperpolarizability values reported for other protected gold nanoclusters.[35–37]

The important point here is that linear absorption properties are not drastically changed by changing the ligand shell size and for the AuZw NCs surrounded by the largest ligand shell (*i.e.*, AuZw 1 : 5), but dramatic enhancements in the one- and two-photon excited fluorescence signals are observed.

The effects of ligand shell size on both the linear and nonlinear optical properties of zwitterion functionalized gold nanoclusters (AuZw NCs) have been investigated by performing QM/MM simulations. For the QM/MM study, the 12 gold atoms and the 4 zwitterionic ligands form the QM region. Ligands are either explicit zwitterions or modeled by S–CH_2–CH_2–CH_2–S. The outer shell, surrounded by 18 or 62 explicit Zw molecules for AuZw ratios 1 : 1 and 1 : 5, are taken into account in the MM part (see Computational section for more details). TDDFT QM/MM results obtained for OPA and TPA spectra for both systems are shown in Fig. 1.

OPA spectra are located between 550 and 350 nm and are in qualitative agreement with experimental findings. They are of low intensities confirming that there is no explicit metallic core with delocalized electrons. In fact, structural properties of $Au_{12}Zw_4$ are characterized by 7 Au atoms forming two tetrahedral subunits connected by central Au atom. Note that 6 Au atoms are also part of the staple motifs (*cf.* Fig. 1). Calculated OPA spectrum for $Au_{12}Zw_4$ (given in Fig. S3 and S4 in ESI†) is similar to those calculated for NCs with the full ligand shell (compare Fig. 1 and Fig. S3, ESI†). Due to the fact that the S_1 state in OPA is located at ∼525 nm, the lowest two-photon transition occurs approximately at ∼1050 nm with a negligible value of cross section. The leading transitions for TPA involve ligand-core excitations. The calculations of additional TPA states give rise to S_{42} located at about 525 nm with a high value of TPA cross section (*cf.* Fig. 1). Both OPA and TPA spectra are not dependent from the ligand shell size (compare spectra for AuZw 1 : 1 and 1 : 5) as observed experimentally for linear absorption spectra. Calculated spectra are also very similar to those obtained for $Au_{12}L_4$ with L modeled by S–CH_2–CH_2–CH_2–S (see Fig. S3, ESI†) confirming that linear absorption properties of S_1 and S_2 excited states are mainly due to excitations between central and neighboring Au atoms and therefore they do not depend on the lengths of ligands.

Our findings indicate that linear absorption properties of studied systems do not depend significantly from: (i) ligand size (S–CH_2–CH_2–CH_2–S *vs.* explicit Zw ligand) and (ii) ligand shell size (from 1 : 1 to 1 : 5). The question can be raised whether the charge has effect on optical properties. Therefore we introduced the positive charge (+1) placed near to central Au atom for system with modeled and explicit zwitterion ligands as show in Fig. S5 and S6 (ESI†). The charge induces significant red shift of dominant features at experimentally accessible wavelengths. This is expected due to the lack of one electron.[38]

An origin on the effect of ligand shell size on emission properties may be rigidification effect brought by the ligand shell on the gold kernel. However, already for AuZw 1 : 1, the number of ligands, the steric hindrance brought by the long-chain ligands as well as strong electrostatic interactions between permanent charges of terminal zwitterions may be enough to produce a strong rigidification of the gold kernel. The addition of external ligand shells with AuZw 1 : 2 and AuZw 1 : 5 might have a moderate influence on the overall rigidity. Another origin may be due to a possible quenching effect due to water penetration propensity through the ligand shell. To better address this possible quenching effect due to water penetration propensity through the ligand shell, we investigated the density of water molecules within ligated gold clusters with AuZw ratio 1 : 1 and

Table 1 Absolute magnitude of the first hyperpolarizability, two-photon absorption (TPA) and two-photon excited fluorescence cross-sections (TPEF) for AuZw clusters at 800 nm laser excitation wavelength. Of note, the measurements TPA and TPEF cross sections for AuZw 1 : 1 and AuZw 1 : 2 were not possible due to their poor photostability under laser irradiation (requiring higher concentrations for measurements as compared to HRS experiments)

AuZW cluster	Formula	1PQY (%)	Hyperpolarizability (esu)	TPA cross section (GM)	TPEF cross section (GM)	2PQY (%)
AuZw 1 : 1	$Au_{12}ZW_{22}$	<0.01	$89(2) \times 10^{-30}$	N/A	N/A	
AuZw 1 : 2	$Au_{12}ZW_{37}$	0.1	$146(1) \times 10^{-30}$	N/A	N/A	
AuZW 1 : 5	$Au_{12}ZW_{66}$	1.4	$82(1) \times 10^{-30}$	10 000	0.5	5×10^{-3}

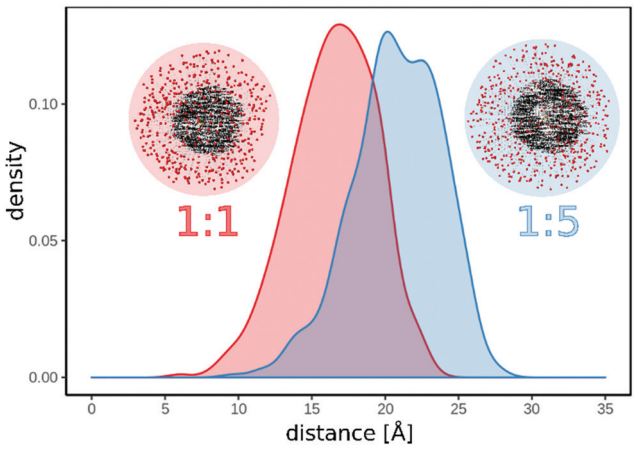

Fig. 2 Density of water molecules as a function of radial distance from central Au atom within ligated gold clusters for ratio 1:1 (red) and 1:5 (blue).

1:5. Fig. 2 illustrates that penetration of water is significantly higher for 1:1 than for 1:5 AuZw ratio. This suggests that quenching effects produced by the interaction of water with the gold kernel will be less with 1:5 ratio than with 1:1 ratio for NCs and might be responsible for measured larger emissive properties for AuZw 1:5 than in the case of AuZw 1:1. Interestingly, some analogy can be found with the ligand effects on the catalytic activities of polymer-protected gold nanoclusters. Okumura and co-workers.[39–41] investigated the effects of polymer type and size, and it turned out that the polymer of low active polymer-protected gold nanoclusters inhibit the penetration of H_2O and of reactants.

C. Experimental and computational details

Experimental details

Chemicals. All chemical products were purchased from Sigma Aldrich (France).

Synthesis of AuZw nanoclusters. Lipoic acid-based sulfobetaine ligand (Zw, 399 g mol^{-1}) was synthesized following the procedure described elsewhere.[42] Au NCs were prepared with different molar ratios of Au per Zw (Au:Zw) = 1:1; 1:2, and 1:5 under basic conditions in the presence of sodium borohydride as a reducing agent. Briefly, in a standard experiment for the molar ratio Au:Zw 1:5, 12.5 mmol of Zw was added to the basic mixture of 50 μL of $HAuCl_4{\cdot}3H_2O$ (50 mM) in 10 mL of deionized water and 10 μL of NaOH (2 M) under stirring for 5 min. Then, 100 μL of freshly prepared $NaBH_4$ (50 mM) was added to the solution and stirred for 15 hours. The solution changed quickly from colorless to brownish indicating the growth of Au NCs. Afterwards, the solution containing AuZw NCs was purified three times using 3 kDa cut-off filters (Amicon ultra, Millipore) to remove the excess of free ligands. The pH was adjusted to 7 and the AuZw NC solution was kept refrigerated until use.

Instrumentation. UV-vis spectra in solution were recorded using an AvaSpec-2048 fiber optic spectrometer and an AvaLight-DH-S deuterium halogen light source. Fluorescence spectra were measured using a Fluoromax-4 Horiba fluorescence spectrophotometer. The light source for the present HRS and TPA experiments was a mode-locked femtosecond Ti:sapphire laser delivering at the fundamental wavelength of 800 nm pulses with a duration of about 140 femtoseconds at a repetition rate of 76 MHz, as described in ref. 43. Two-photon excited fluorescence measurements were performed with a customized confocal microscope (TE2000-U, Nikon Inc.) in which the excitation light entrance has been modified to allow free-space laser beam input, instead of the original optical-fiber light input. The luminescence was excited at 780 nm with a mode-locked frequency-doubled femtosecond Er-doped fiber laser (C-Fiber 780, MenloSystems GmbH), as described in ref. 18 and 44.

Computational details

For the gold atoms the 19-e^- relativistic effective core potential (19-e^- RECP) from the Stuttgart group[45] taking into account scalar relativistic effects has been employed. For all atoms, split valence polarization atomic basis sets (SVP) have been used.[46] Coulomb-attenuated version of Becke's three-parameter non-local exchange functional together with the Lee–Yang–Parr gradient-corrected correlation functional (CAM-B3LYP)[47] have been employed to calculate optical properties. This approach has been used to determine OPA and TPA spectra (DALTON[48,49] program) for optimized structures of $Au_{12}L_4$ (L = S–CH_2–CH_2–CH_2–S or zwitterionic ligand). In order to determine OPA and TPA for both systems with Au:Zw ratio 1:1 and 1:5 the two-layer quantum mechanics/molecular mechanics QM/MM approach[50] has been used. QM part includes $Au_{12}Zw_4$ (Zw = full ligand) and for the MM part the UFF force field[55] has been employed. Polarizable embedding-quantum mechanics (PEQM) method with monopoles taken from UFF force field, implemented in Dalton package programs[48,49] has been used within the QM/MM approach for calculation of linear and nonlinear properties. One- and two-photon absorption spectra were determined employing quadratic response properties within the time-dependent density functional theory (TDDFT).[48,49] For the calculation of TPA cross section (σ),[51] the two-photon absorption probability (δ) is needed which can be obtained from two-photon absorption transition matrices from the ground to the excited state using either single residue or double residue quadratic response procedure[52,53]

In order to simulate penetration of water molecules in both systems with Au:Zw ratios 1:1 and 1:5, 500 neutral water molecules have been included in MM part within QM/MM approach for the optimization of geometries. In addition, we formed the model by taking into account the distances from central Au atom to each water molecule in order to obtain radial distribution of the density of water molecules using R-studio software.[54]

D. Conclusions

To summarize, the introduction of bidentate thiol zwitterionic ligands to cap the metallic kernel is another efficient approach to enhance nonlinear response in particular two-photon excitation fluorescence; The larger the ligand shell the higher the two-photon

excitation fluorescence signal. Our QM/MM approach allowed for adequate description of key optical signatures of zwitterion functionalized gold clusters. These findings open the road for gaining insight into the origin of luminescence enhancement caused by different surface shell protection strategies such as introduction of bulky counter-ions or protein templating AuNCs, for which explicit templates at the molecular level are required.

Conflicts of interest

There are no conflicts to declare.

Acknowledgements

This research was partially supported by the project STIM-REI, Contract Number: KK.01.1.1.01.0003, funded by the European Union through the European Regional Development Fund – the Operational Programme Competitiveness and Cohesion 2014–2020 (KK.01.1.1.01). We would also like to acknowledge the financial support received from the French-Croatian project ''International Laboratory for Nano Clusters and Biological Aging, LIA NCBA''. The authors would like to thank Christophe Moulin for his help with the confocal microscope.

Notes and references

1 R. Jin, *Nanoscale*, 2010, **2**, 343–362.
2 L. Y. Chen, C. W. Wang, Z. Q. Yuan and H. T. Chang, *Anal. Chem.*, 2015, **87**, 216–229.
3 H. Z. Yu, B. Rao, W. Jiang, S. Yang and M. Z. Zhu, *Coord. Chem. Rev.*, 2019, **378**, 595–617.
4 X. Kang and M. Zhu, *Chem. Soc. Rev.*, 2019, **48**, 2422–2457.
5 Z. Wu and R. Jin, *Nano Lett.*, 2010, **10**, 2568–2573.
6 A. Kim, C. Zeng, M. Zhou and R. Jin, *Part. Part. Syst. Charact.*, 2017, **34**, 1600388.
7 Y. Lin, P. Charchar, A. J. Christofferson, M. R. Thomas, N. Todorova, M. M. Mazo, Q. Chen, J. Doutch, R. Richardson, I. Yarovsky and M. M. Stevens, *J. Am. Chem. Soc.*, 2018, **140**, 18217–18226.
8 Z. Luo, X. Yuan, Y. Yu, Q. Zhang, D. T. Leong, J. Y. Lee and J. Xie, *J. Am. Chem. Soc.*, 2012, **134**, 16662–16670.
9 N. Goswami, Q. Yao, Z. Luo, J. Li, T. Chen and J. Xie, *J. Phys. Chem. Lett.*, 2016, **7**, 962–975.
10 B. Musnier, K. D. Wegner, C. Comby-Zerbino, V. Trouillet, M. Jourdan, I. Häusler, R. Antoine, J.-L. Coll, U. Resch-Genger and X. Le Guével, *Nanoscale*, 2019, **11**, 12092–12096.
11 S. Wang, X. Meng, A. Das, T. Li, Y. Song, T. Cao, X. Zhu, M. Zhu and R. Jin, *Angew. Chem., Int. Ed.*, 2014, **53**, 2376–2380.
12 G. Soldan, M. A. Aljuhani, M. S. Bootharaju, L. G. AbdulHalim, M. R. Parida, A.-H. Emwas, O. F. Mohammed and O. M. Bakr, *Angew. Chem., Int. Ed.*, 2016, **55**, 5749–5753.
13 X. Le Guével, V. Trouillet, C. Spies, K. Li, T. Laaksonen, D. Auerbach, G. Jung and M. Schneider, *Nanoscale*, 2012, **4**, 7624–7631.
14 D. Mishra, S. Wang, Z. Jin, Y. Xin, E. Lochner and H. Mattoussi, *Phys. Chem. Chem. Phys.*, 2019, **21**, 21317–21328.
15 D. Mishra, V. Lobodin, C. Zhang, F. Aldeek, E. Lochner and H. Mattoussi, *Phys. Chem. Chem. Phys.*, 2018, **20**, 12992–13007.
16 H. Fakhouri, M. Perić, F. Bertorelle, P. Dugourd, X. Dagany, I. Russier-Antoine, P.-F. Brevet, V. Bonačić-Koutecký and R. Antoine, *Phys. Chem. Chem. Phys.*, 2019, **21**, 12091–12099.
17 K. Pyo, V. D. Thanthirige, K. Kwak, P. Pandurangan, G. Ramakrishna and D. Lee, *J. Am. Chem. Soc.*, 2015, **137**, 8244–8250.
18 F. Bertorelle, C. Moulin, A. Soleilhac, C. Comby-Zerbino, P. Dugourd, I. Russier-Antoine, P.-F. Brevet and R. Antoine, *ChemPhysChem*, 2018, **19**, 165–168.
19 X. L. Guevel, O. Tagit, C. E. Rodríguez, V. Trouillet, M. Pernia Leal and N. Hildebrandt, *Nanoscale*, 2014, **6**, 8091–8099.
20 A. Yahia-Ammar, D. Sierra, F. Mérola, N. Hildebrandt and X. Le Guével, *ACS Nano*, 2016, **10**, 2591–2599.
21 Y. Chen, D. M. Montana, H. Wei, J. M. Cordero, M. Schneider, X. Le Guével, O. Chen, O. T. Bruns and M. G. Bawendi, *Nano Lett.*, 2017, **17**, 6330–6334.
22 D. Shen, M. Henry, V. Trouillet, C. Comby-Zerbino, F. Bertorelle, L. Sancey, R. Antoine, J.-L. Coll, V. Josserand and X. L. Guével, *APL Mater.*, 2017, **5**, 053404.
23 F. Aldeek, M. A. H. Muhammed, G. Palui, N. Zhan and H. Mattoussi, *ACS Nano*, 2013, **7**, 2509–2521.
24 E. Porret, L. Sancey, A. Martín-Serrano, M. I. Montañez, R. Seeman, A. Yahia-Ammar, H. Okuno, F. Gomez, A. Ariza, N. Hildebrandt, J.-B. Fleury, J.-L. Coll and X. Le Guével, *Chem. Mater.*, 2017, **29**, 7497–7506.
25 E. Porret, M. Jourdan, B. Gennaro, C. Comby-Zerbino, F. Bertorelle, V. Trouillet, X. Qiu, C. Zoukimian, D. Boturyn, N. Hildebrandt, R. Antoine, J.-L. Coll and X. Le Guével, *J. Phys. Chem. C*, 2019, DOI: 10.1021/acs.jpcc.9b08492.
26 X.-Y. Xie, P. Xiao, X. Cao, W.-H. Fang, G. Cui and M. Dolg, *Angew. Chem., Int. Ed.*, 2018, **57**, 9965–9969.
27 C. M. Aikens, *Acc. Chem. Res.*, 2018, **51**, 3065–3073.
28 K. L. D. M. Weerawardene and C. M. Aikens, *J. Am. Chem. Soc.*, 2016, **138**, 11202–11210.
29 K. L. D. M. Weerawardene, E. B. Guidez and C. M. Aikens, *J. Phys. Chem. C*, 2017, **121**, 15416–15423.
30 R. D. Senanayake, E. B. Guidez, A. J. Neukirch, O. V. Prezhdo and C. M. Aikens, *J. Phys. Chem. C*, 2018, **122**, 16380–16388.
31 C. Comby-Zerbino, M. Perić, F. Bertorelle, F. Chirot, P. Dugourd, V. Bonačić-Koutecký and R. Antoine, *Nanomaterials*, 2019, **9**, 457.
32 S. Banerjee, J. A. Montgomery and J. A. Gascón, *J. Mater. Sci.*, 2012, **47**, 7686–7692.
33 V. Rojas-Cervellera, L. Raich, J. Akola and C. Rovira, *Nanoscale*, 2017, **9**, 3121–3127.
34 V. Rojas-Cervellera, C. Rovira and J. Akola, *J. Phys. Chem. Lett.*, 2015, **6**, 3859–3865.
35 F. Bertorelle, I. Russier-Antoine, N. Calin, C. Comby-Zerbino, A. Bensalah-Ledoux, S. Guy, P. Dugourd, P.-F. Brevet, Z. Sanader, M. Krstic, V. Bonacic-Koutecky and R. Antoine, *J. Phys. Chem. Lett.*, 2017, **8**, 1979–1985.

36 F. Bertorelle, I. Russier-Antoine, C. Comby-Zerbino, F. Chirot, P. Dugourd, P.-F. Brevet and R. Antoine, *ACS Omega*, 2018, **3**, 15635–15642.
37 I. Russier-Antoine, F. Bertorelle, M. Vojkovic, D. Rayane, E. Salmon, C. Jonin, P. Dugourd, R. Antoine and P.-F. Brevet, *Nanoscale*, 2014, **6**, 13572–13578.
38 V. Bonačić-Koutecký, J. Pittner, M. Boiron and P. Fantucci, *J. Chem. Phys.*, 1999, **110**, 3876–3886.
39 Y. Ato, A. Hayashi, H. Koga, K. Tada, T. Kawakami, S. Yamanaka and M. Okumura, *J. Comput. Chem.*, 2019, **40**, 222–228.
40 M. Okumura, Y. Kitagawa, T. Kawakami and M. Haruta, *Chem. Phys. Lett.*, 2008, **459**, 133–136.
41 K. Sakata, Y. Ato, K. Tada, H. Koga, S. Yamanaka, T. Kawakami, T. Saito and M. Okumura, *Chem. Lett.*, 2016, **45**, 344–346.
42 J. Park, J. Nam, N. Won, H. Jin, S. Jung, S. Jung, S.-H. Cho and S. Kim, *Adv. Funct. Mater.*, 2011, **21**, 1558–1566.
43 I. Russier-Antoine, F. Bertorelle, N. Calin, Z. Sanader, M. Krstic, C. Comby-Zerbino, P. Dugourd, P.-F. Brevet, V. Bonacic-Koutecky and R. Antoine, *Nanoscale*, 2017, **9**, 1221–1228.
44 V. Bonačić-Koutecký and R. Antoine, *Nanoscale*, 2019, **11**, 12436–12448.
45 D. Andrae, U. Häußermann, M. Dolg, H. Stoll and H. Preuß, *Theor. Chim. Acta*, 1990, **77**, 123–141.
46 F. Weigend and R. Ahlrichs, *Phys. Chem. Chem. Phys.*, 2005, **7**, 3297–3305.
47 T. Yanai, D. P. Tew and N. C. Handy, *Chem. Phys. Lett.*, 2004, **393**, 51–57.
48 K. Aidas, C. Angeli, K. L. Bak, V. Bakken, R. Bast, L. Boman, O. Christiansen, R. Cimiraglia, S. Coriani, P. Dahle, E. K. Dalskov, U. Ekström, T. Enevoldsen, J. J. Eriksen, P. Ettenhuber, B. Fernández, L. Ferrighi, H. Fliegl, L. Frediani, K. Hald, A. Halkier, C. Hättig, H. Heiberg, T. Helgaker, A. C. Hennum, H. Hettema, E. Hjertenæs, S. Høst, I.-M. Høyvik, M. F. Iozzi, B. Jansík, H. J. A. Jensen, D. Jonsson, P. Jørgensen, J. Kauczor, S. Kirpekar, T. Kjærgaard, W. Klopper, S. Knecht, R. Kobayashi, H. Koch, J. Kongsted, A. Krapp, K. Kristensen, A. Ligabue, O. B. Lutnæs, J. I. Melo, K. V. Mikkelsen, R. H. Myhre, C. Neiss, C. B. Nielsen, P. Norman, J. Olsen, J. M. H. Olsen, A. Osted, M. J. Packer, F. Pawlowski, T. B. Pedersen, P. F. Provasi, S. Reine, Z. Rinkevicius, T. A. Ruden, K. Ruud, V. V. Rybkin, P. Sałek, C. C. M. Samson, A. S. de Merás, T. Saue, S. P. A. Sauer, B. Schimmelpfennig, K. Sneskov, A. H. Steindal, K. O. Sylvester-Hvid, P. R. Taylor, A. M. Teale, E. I. Tellgren, D. P. Tew, A. J. Thorvaldsen, L. Thøgersen, O. Vahtras, M. A. Watson, D. J. D. Wilson, M. Ziolkowski and H. Ågren, *Wiley Interdiscip. Rev.: Comput. Mol. Sci.*, 2014, **4**, 269–284.
49 Dalton, a molecular electronic structure program, Release v2016.0, 2017, see http://daltonprogram.org.
50 D. Buceta, N. Busto, G. Barone, J. M. Leal, F. Domínguez, L. J. Giovanetti, F. G. Requejo, B. García and M. A. López-Quintela, *Angew. Chem., Int. Ed.*, 2015, **54**, 7612–7616.
51 L. Frediani, Z. Rinkevicius and H. Ågren, *J. Chem. Phys.*, 2005, **122**, 244104.
52 N. H. List, R. Zaleśny, N. A. Murugan, J. Kongsted, W. Bartkowiak and H. Ågren, *J. Chem. Theory Comput.*, 2015, **11**, 4182–4188.
53 P. Norman, *Phys. Chem. Chem. Phys.*, 2011, **13**, 20519–20535.
54 RStudio Team, RStudio: Integrated Development for R. RStudio, Inc., Boston, MA, 2015, http://www.rstudio.com/.
55 A. K. Rappe, C. J. Casewit, K. S. Colwell, W. A. Goddard III and W. M. Skiff, *J. Am. Chem. Soc.*, 1992, **114**, 10024–10035.

JPCCCK

SEPTEMBER 3, 2020
VOLUME 124
NUMBER 35

pubs.acs.org/JPCC

THE JOURNAL OF PHYSICAL CHEMISTRY C

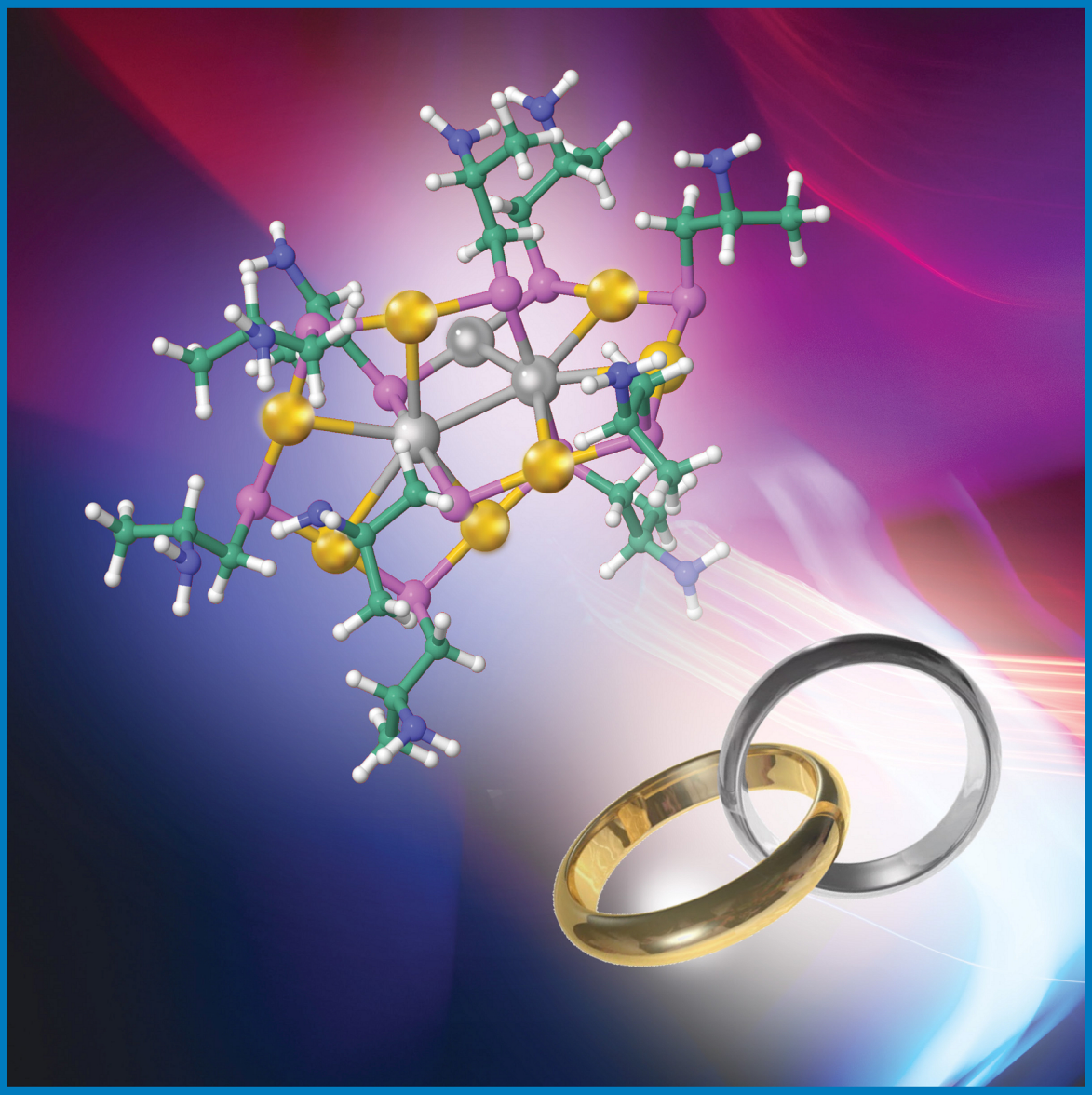

ACS Publications
Most Trusted. Most Cited. Most Read.

www.acs.org

THE JOURNAL OF PHYSICAL CHEMISTRY C

pubs.acs.org/JPCC Article

Rationale Strategy to Tune the Optical Properties of Gold Catenane Nanoclusters by Doping with Silver Atoms

Srestha Basu, Martina Perić Bakulić, Hussein Fakhouri, Isabelle Russier-Antoine, Christophe Moulin, Pierre-François Brevet, Vlasta Bonačić-Koutecký,* and Rodolphe Antoine*

Cite This: J. Phys. Chem. C 2020, 124, 19368−19374 Read Online

ABSTRACT: We report the chemical substitution-mediated doping of silver atoms into $Au_{10}SG_{10}$ (SG: glutathione) catenane nanoclusters (NCs) in a controllable manner. Two levels of doping were conducted leading to two silver-doped $Au_{10-x}Ag_xSG_{10}$ nanoclusters (with x = 0−2 and x = 1−4). Optical studies reveal that nanoclusters with a high level of doping (x = 1−4) show a blue shift in absorption and a significant red shift of ∼50 nm in the two-photon-excited emission spectrum with respect to pristine $Au_{10}SG_{10}$. The preservation of the catenane structure is confirmed by comparing the experimental and computational X-ray diffraction patterns and absorption spectra of $Au_{10}SG_{10}$ and its silver-doped analogs. In order to better address the structure−property relationship in such catenane clusters, further theoretical investigations were performed at the DFT level. A high-energy shift of the S_1 state is evidenced in the calculated one-photon absorption spectra due to a larger s to d gap in silver caused by smaller relativistic effects in comparison to the gold atoms. Furthermore, the red shift in the two-photon excited emission band of the clusters is due to significantly larger calculated relaxation of the first excited state in nanoclusters with a high level of silver doping.

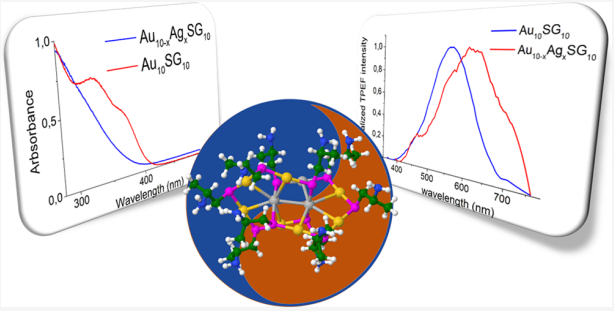

INTRODUCTION

The supramolecular chemistry of gold and, in particular, of gold thiolate leads to fascinating structural motifs with enhanced optical properties.[1] A plethora of synthetic routes have permitted to propose a large number of gold nanohybrid systems ranging from plasmonic gold nanoparticles,[2] atomically precise gold nanoclusters (NCs),[3] and self-assembled Au-containing thiolated coordination polymers.[4,5] Regarding optical properties, it has been well established in the literature that the emission properties of gold nanohybrid systems is strongly dictated by the number and the nature of the metal atoms and the stabilizing ligands.[6,7] Thus, rationale strategies have been proposed to tune the intrinsic emission properties of nanoclusters as a function of their chemical composition. The "doping" strategy stands out as an important one.[8] For instance, doping of gold nanohybrid systems with silver has been demonstrated to lead to enhanced nonlinear optical properties.[9] In context of improving their attractiveness for multiphoton bioimaging applications, multiphoton excited emission should be pushed further toward the near-infrared window.[10,11]

Silver-doped gold nanoclusters[12] display efficient two-photon excited luminescence[13] and second harmonic conversion.[14] However, for a rational design of nanoclusters with enhanced optical properties, elucidation of the structure−property relationship is of pivotal importance. Doping leads either to preservation or transformation of the nanocluster structure.[7] Furthermore, the correspondence between the optical properties and the heteroatom substitution is still scarcely explored.[15] Liu[16] conducted a time-dependent density-functional theory (TDDFT) study on the excited states and charge redistribution in response to light absorption on single-atom-doped Au_{25} nanoclusters, highlighting different absorption features upon Ag, Cu, Pd, and Pt doping. The nature and position of the lowest excited electronic states are also sensitive to silver doping.[17] Other factors like relativistic effects (mainly due to the Au atoms), the exact spatial position of metal dopants, and the heteronuclear Au−Ag bonds have also been reported to affect the fluorescence intensity of gold-doped nanoclusters.[18] From an experimental point of view, developing synthetic routes with atomically precise silver doping of gold nanoclusters with X-ray single-crystal-resolved structures has largely improved our understanding on these structure−optical property relationship.[19,20]

In this regard, a well-defined structural motif for nanoclusters is an essential prerequisite. We have recently reported a facile

Received: June 15, 2020
Revised: July 19, 2020
Published: July 20, 2020

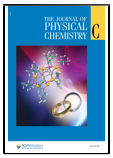

https://dx.doi.org/10.1021/acs.jpcc.0c05402
J. Phys. Chem. C 2020, 124, 19368−19374

"one-pot-one-size" synthesis of $Au_{10}(SR)_{10}$ nanoclusters with SR as glutathione (SG) or thioglycolic acid (TGA).[21−23] The distinct X-ray powder diffraction pattern of $Au_{10}SG_{10}$ was utilized as a signature for homoleptic gold−glutathione catenanes with two Au_5SG_5 interconnected rings ([5,5]).[22] Herein, a rationale strategy for tuning optical properties is reported with chemical substitution by silver atom doping of the $Au_{10}SG_{10}$ catenane system in a controllable manner, leading to silver-doped $Au_{10-x}Ag_xSG_{10}$ nanoclusters with different levels of doping (e.g., x = 0−2 and x = 1−4). The preservation of the catenane structure is confirmed by comparing experimental and computational X-ray diffraction patterns and absorption spectra of $Au_{10}SG_{10}$ and its silver-doped analogs. Density-functional theory (DFT) study evidences that the ground state geometry changes upon Ag doping are not large. Chiroptical and nonlinear optical properties, i.e., two-photon emission spectra and first hyperpolarizabilities of silver-doped Au nanoclusters are also reported. Interestingly, these optical studies reveal that $Au_{10-x}Ag_xSG_{10}$ with x = 1−4 shows a blue shift in absorption and a significant red shift in the two-photon emission spectrum in contrast to $Au_{10}SG_{10}$. A complementary first-principles theoretical analysis has been performed with a focus on the changes of the optical properties of catenane structures upon silver doping.

METHODS

Materials. Tetracholoroauric acid ($HAuCl_4{\cdot}3H_2O$) was purchased from Alfa Aesar. L-Glutathione was procured from Carl Roth. Methanol, diethyl ether, and silver trifluoroacetate acetate were procured from Sigma-Aldrich. All chemicals were used as received without further purification. Ultrapure milli-Q water was used for experimental purpose.

Synthesis of $Au_{10}SG_{10}$. L-Glutathione (~235 mg) was added in a round bottom flask and was dissolved in 35 mL methanol using 2 mL triethylamine. To this methanolic solution of glutathione, ~100 mg of $HAuCl_4.3H_2O$ was added. The solution was stirred for ~24 h. This led to formation of a pale yellow colored solution. To this solution, sodium hydroxide (~2 mL) was added till precipitation. The dispersion was centrifuged at a speed of ~10,000 rpm for ~10 min. The supernatant was discarded and the so-obtained pellet was redispersed in 1 mL of NH_4OH and 2 mL water. This led to complete solubilization of the pellet. The solution was further added with methanol to allow reprecipitation. The dispersion was centrifuged for 10 min at a speed of 10,000 rpm. The pellet was dissolved in 10 mL water and further added with 1 mL acetic acid. The solution was left undisturbed for ~12 h, which led to precipitation of pure $Au_{10}SG_{10}$. The precipitate was collected by centrifugation and was further dissolved in 2 mL water. Reprecipitation with methanol was carried out and the so-obtained pellet was dried under air for further use.

Synthesis of $Au_{10-x}Ag_xSG_{10}$ with x = 0−2. In order to synthesize $Au_{10-x}Ag_xSG_{10}$ with x = 0−2, a protocol similar to that of $Au_{10}SG_{10}$ was followed—the only difference being that in the very first step following addition of $HAuCl_4.3H_2O$ to a methanolic solution of L-glutathione, ~11 mg of silver trifluoroacetate (dissolved in minimum amount of methanol) was added to the same solution. The purification process of the doped clusters remained the same as that of $Au_{10}SG_{10}$.

Synthesis of $Au_{10-x}Ag_xSG_{10}$ with x = 1−4. In order to synthesize $Au_{10-x}Ag_xSG_{10}$ with x = 1−4, a protocol similar to that of $Au_{10}SG_{10}$ was followed—the only difference being that in the very first step following addition of $HAuCl_4.3H_2O$ to a methanolic solution of L-glutathione, ~60 mg of silver trifluoroacetate (dissolved in minimum amount of methanol) was added to the same solution. The purification process of the doped clusters remained the same as that of $Au_{10}SG_{10}$.

Gel Preparation. Bis-acrylamide (~3 g) and ~8.7 g of acrylamide were dissolved in 21 mL of water and was sonicated till complete solubilization. Separately, 49 mg/490 μL of ammonium peroxodisulphate solution was freshly prepared. Furthermore, the required amounts of $Au_{10}SG_{10}$ and $Au_{10-x}Ag_xSG_{10}$ with x = 1−4 were dissolved in formerly prepared solution of acrylamide and bis-acrylamide to achieve a final concentration of 750 μM in. Thereafter, 1 mL of the solutions containing clusters and doped clusters were added in a gel bath. Following this, 10 μL of N,N,N',N'-Tetramethylethylenediamine(TEMED) and 10 μL of ammonium peroxodisulphate were added to the gel bath. The system was left undisturbed till complete gelation.

INSTRUMENTATION

Electrospray Ionization Mass Spectrometry (ESI-MS). ESI-MS was performed on a commercial quadrupole time-of-flight (micro-qTOF, Bruker-Daltonics, Bremen, Germany, mass resolution 10,000). The samples were prepared to a final concentration of approximately 50 μM in methanol. The samples were analyzed in negative ion mode; each data point was the summation of spectra over 5 min.

UV−vis and Circular Dichroism (CD) Spectroscopy. UV−vis and CD spectra were recorded at IBCP Lyon France on a Chirascan spectrometer. CD was carried out on a Chirascan CD (Applied Photophysics). The data were collected at 1 nm intervals in the wavelength range of 200−500 nm at 20 °C, using a temperature-controlled chamber. A 0.01 cm cuvette containing 30 μL of NC sample at 50 μM was used for all the measurements. Each spectrum represents the average of three scans, and sample spectra were corrected for buffer background by subtracting the average spectrum of the buffer alone.

X-ray diffraction (XRD). XRD is carried out on a PANalytical EMPYREAN diffractometer with a PIXcel 3D using Cu Kα radiation and a high-resolution theta−theta goniometer.

NLO Measurements. The setup for hyper-Rayleigh scattering (HRS) and two-photon excited fluorescence (TPEF) has been described in detail in previous works.[24−25] HRS measurements were performed using a modelocked femtosecond Ti:sapphire laser delivering at the fundamental wavelengths between 785 and 810 nm pulses with a duration of about 140 fs at a repetition rate of 80 MHz. A fundamental beam was focused by a low numerical aperture microscope objective into a 0.5 cm spectrophotometric cell containing the aqueous solutions. For the TPEF signal, the wavelength of the spectrometer (Jobin Yvon, iHR320 spectrometer) was scanned between 350 and 750 nm detected with a photomultiplier tube (model H11890−210, Hamamatsu). For reference materials, we have chosen fluorescein dye. From the literature, we assume at an excitation wavelength of 780 nm: σ_2 (fluorescein) = 33.3 GM using a quantum yield of 0.9 and a two-photon absorption cross-section of 37 GM. In addition, TPEF measurements were performed on nanocluster-containing gels with a customized confocal microscope. The luminescence was excited at 780 nm with a modelocked frequency-doubled femtosecond Er-doped fiber laser (C-Fiber 780, MenloSystems GmbH). The laser spectrum was bound by two filters (FELH0750 and FESH0800, Thorlabs Inc.). The output power of the femtosecond laser was

https://dx.doi.org/10.1021/acs.jpcc.0c05402
J. Phys. Chem. C 2020, 124, 19368−19374

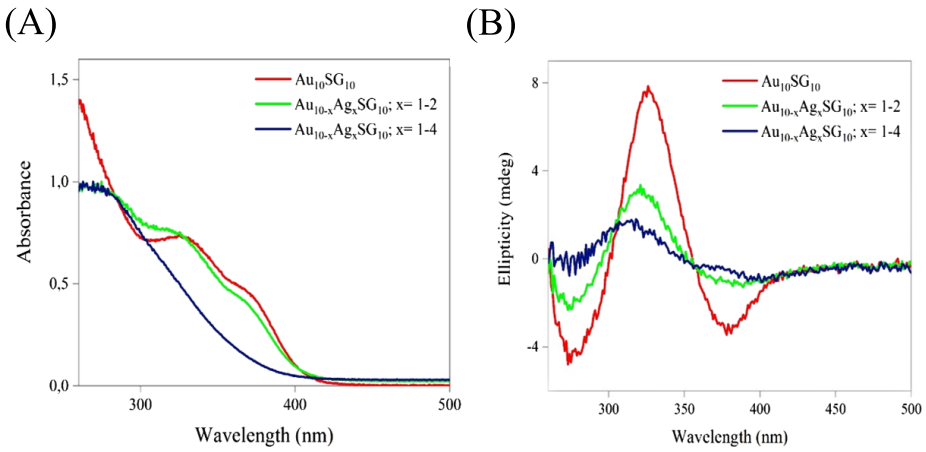

Figure 1. (A) UV−vis absorption and (B) CD spectra of the as-synthesized $Au_{10}SG_{10}$, Au_{10}-xAg_xSG_{10} ($x = 1-2$), and $Au_{10-x}Ag_xSG_{10}$ ($x = 1-4$) NCs in aqueous solution.

62 mW. The laser beam was focused by a Nikon Plan Fluor Ph1 DLL objective (10x/0.30 NA). The emitted signal was collected in epifluorescence illumination mode. The two-photon fluorescence emission was separated from the incident light through a dichroic mirror (NFD01−785, IDEX Health & Science LLC). A FESH0750 filter was used in order to remove the residual photons coming from the excitation laser and collect visible 350−750 nm fluorescence. The two-photon fluorescence emission spectra were recorded using an iHR320 spectrometer equipped with a 53,024 grating from Horiba Jobin Yvon and detected using a −20 °C cooled photomultiplier tube (R943−02, Hamamatsu Photonics).

COMPUTATIONAL DETAILS

The structural properties have been determined employing the DFT method with the B3LYP functional[26−28] and split valence polarization (SVP) atomic basis set[29] as implemented in TURBOMOLE 7.4.[30] Optical properties (one-photon absorption (OPA), two-photon absorption (TPA), CD, and β hyperpolarizabilities) have been determined using TDDFT[31,32] and a quadratic response[33,34] approach as implemented in the DALTON program package.[35,36] The same AO basis set has been used as for structural properties except for the ligands for which 6-31G basis set[37−40] has been employed. In the lowest-energy [5,5] catenane structures, $Au_{10}L_{10}$, Au_9AgL_{10} $Au_7Ag_3L_{10}$, L labels the chiral ligand ($-SCH_2CH(NH_2)CH_3$). For gold and silver atoms 19 e^- relativistic effective core potential (19 e^- RECP) taking into account scalar relativistic effects has been employed.[41] The Debye formula serves to calculate XRD patterns.[42]

RESULTS AND DISCUSSION

Experimentally, Au_{10} clusters stabilized by glutathione, with the molecular formula $Au_{10}SG_{10}$, were synthesized following a method previously reported by our group.[22] Unambiguous assignment of $Au_{10}SG_{10}$ was achieved by high-resolution ESI-MS (see Figure S1 in Supporting Information). In the next step, systematic doping of the as-synthesized $Au_{10}SG_{10}$ with silver atoms was performed by adding optimized amounts of silver trifluoroacetate. Briefly, the strategy of the study is to perform gradual doping of $Au_{10}SG_{10}$ with silver atoms by varying the amount of silver trifluoroacetate reacting with $Au_{10}SG_{10}$. Evidence of doping with silver atoms of the Au_{10} nanoclusters with the appearance of $Au_{10-x}Ag_xSG_{10}$ nanoclusters was obtained from high-resolution ESI-MS (see Figures S2 and S3 in Supporting Information). These syntheses led to a distribution of $Au_{10-x}Ag_xSG_{10}$ systems with x ranging from 0−2 and with x ranging from 1−4 for the two silver-doped gold nanocluster samples, respectively.

Next, we investigated the effect of gradual silver doping on the optical and chiroptical properties of $Au_{10}SG_{10}$. As evident from Figure 1A, the UV−vis absorption spectrum of $Au_{10}SG_{10}$ shows two discernible bands at 331 and 369 nm, respectively. Instead, the UV−vis absorbance spectrum of $Au_{10-x}Ag_xSG_{10}$ with x = 0−2 shows slight blue-shifted bands at 324 and 364 nm, and the UV−vis spectrum of $Au_{10-x}Ag_xSG_{10}$ with x = 1−4 shows a monotonic increase of intensity below 390 nm with no discernable shoulder. Thus, it is observed that systematic doping of $Au_{10}SG_{10}$ with a varying number of silver atoms leads to blue shift of the onset of absorption from 410 to 390 nm. In an allied vein, and in order to verify whether a similar trend of variation is observed in the chiroptical properties of the ligated Au_{10} clusters as well as for further corroboration with the UV−vis absorption results, CD studies were performed. As can be observed from Figure 1B, the CD spectrum of $Au_{10}SG_{10}$ shows a strong peak at 326 nm. However, the peaks in the CD spectrum of $Au_{10-x}Ag_xSG_{10}$ with x = 0−2 and x = 1−4 were observed to occur at 321 and 312 nm, i.e., slightly blue-shifted compared to that of $Au_{10}SG_{10}$ and with decreasing values of ellipticity (see Figure 1B).

Under UV light, aqueous solutions of $Au_{10}SG_{10}$ and silver-doped nanoclusters showed extremely weak fluorescence. However, in our previous study, it was found that $Au_{10}SG_{10}$ presented large first hyperpolarizability and two-photon excitation fluorescence (TPEF).[22] In the current study, the TPEF emission spectrum of $Au_{10-x}Ag_xSG_{10}$ with x = 1−4 was recorded and compared with that of $Au_{10}SG_{10}$. Notably, the normalized TPEF emission spectrum of $Au_{10}SG_{10}$ shows a maximum at 555 nm, while the maximum of the TPEF emission spectrum of $Au_{10-x}Ag_xSG_{10}$ with x = 1−4 is observed to occur at 605 nm (see Figure 2). Thus, doping $Au_{10}SG_{10}$ with silver atoms leads to a significant bathochromic shift of ∼50 nm. The superimposed (non-normalized) emission spectra of $Au_{10}SG_{10}$ and $Au_{10-x}Ag_xSG_{10}$ with x = 1−4 in gels with a cluster concentration of 750 μM are shown in the Supporting Information (see Figure S4). The TPEF spectrum of

https://dx.doi.org/10.1021/acs.jpcc.0c05402
J. Phys. Chem. C 2020, 124, 19368−19374

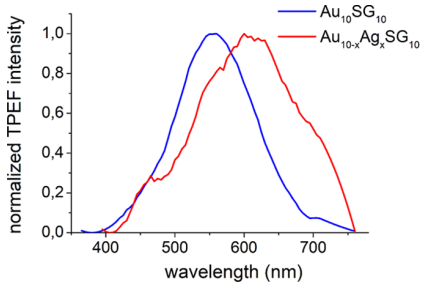

Figure 2. Normalized two-photon excited fluorescence spectra at excitation wavelength 780 nm of $Au_{10}SG_{10}$ compared to that of silver-doped $Au_{10-x}Ag_xSG_{10}$ (x = 1−4) in gels with the same concentration ∼750 μM. TPEF measurements were performed on nanocluster-containing gels with a customized confocal microscope.

$Au_{10-x}Ag_xSG_{10}$; x = 0−2 was also recorded. Interestingly, the TPEF spectrum of the $Au_{10-x}Ag_xSG_{10}$ nanocluster (x = 0−2) showed a less pronounced bathochromic shift in comparison to $Au_{10-x}Ag_xSG_{10}$; x = 1−4 (Figure S5). In addition, the absolute TPEF cross-section of $Au_{10-x}Ag_xSG_{10}$ with x = 1−4 was measured to be 0.0024 ± 0.0016 GM (780 nm laser excitation). Also, the effect of chemical substitution by silver doping on the first hyperpolarizability (β) value of $Au_{10}SG_{10}$ was evaluated. Intriguingly, as opposed to a high β value of $85(9) \times 10^{-30}$ esu for $Au_{10}SG_{10}$, a much reduced hyperpolarizability value of $14(6) \times 10^{-30}$ esu is found for $Au_{10-x}Ag_xSG_{10}$ with x = 1−4 (see Figure S6 in Supporting Information).

An important question concerns the preservation of the catenane structure upon silver doping. In order to gain an insight into the structural property of the as-synthesized $Au_{10}SG_{10}$ and those doped with silver atoms, structural X-ray powder diffraction (XRPD) analysis was conducted (see Figure S7 in Supporting Information). For pure Au_{10} nanoclusters, three possible isomers, namely, [5,5] and [6,4] catenanes and the crownlike structure, have been found as the lowest-energy structures (see Figure S7). Among these isomeric structures, the preserved [5,5] catenane structure has been found to be the lowest-energy one for both Au_9AgSG_{10} and $Au_7Ag_3SG_{10}$. Silver doping was found to have no significant effect on the global structure, bond lengths, and bond angles of the catenane rings. In doped isomers, the silver atoms are located at the center of the catenane structure, as shown in Figure 3. With computation of the XRPD pattern of Au_9AgSG_{10} and $Au_7Ag_3SG_{10}$, the best agreement is obtained for the [5,5] catenane structure preserved upon doping with silver atoms (see Figure S7). The OPA spectra calculated using a TDDFT approach for the lowest-energy [5,5] catenane structures for $Au_{10}SG_{10}$, Au_9AgSG_{10} and $Au_7Ag_3SG_{10}$ is shown in Figure 3A with a chiral $-SCH_2CH(NH_2)CH_3$ ligand as a model for glutathione. The first excited states involved in OPA are located between 360 and 330 nm. The leading excitations responsible for the excitation of the S_1 state are also shown in Figure 3A and involve s to p excitation located on the gold atoms, s to p excitation located on the Ag and Au atoms, and s to s excitation located on the Ag atoms for the pure Au, the Ag-doped, and the Ag_3-doped ligated clusters, respectively. A blue shift of the S_1 state has been observed as a function of the number of silver atoms doped in the catenane structure. This blue shift originates from a larger s to d gap in silver atoms due to smaller relativistic effects with respect to the gold atoms. The comparison with the measured features, and in particular the blue shift in the absorption spectrum, confirms that the catenane structure remains preserved upon silver doping. Similar blue-shifted chiroptical features for the $Au_7Ag_3SG_{10}$ system compared with $Au_{10}SG_{10}$ have been also found for the calculated CD spectra with the chiral ligand $-SCH_2CH(NH_2)CH_3$, as shown in Figure S8 in Supporting Information.

A strong decrease of the first hyperpolarizability β for an excitation wavelength of 800 nm was observed upon silver doping. Two effects might explain this decrease: (i) structural changes of the Ag-doped $Au_{10}SG_{10}$ nanoclusters into more symmetrical structures (since second harmonic generation is only allowed for noncentrosymmetric structures) as compared to undoped nanoclusters and/or (ii) resonance effects between the OPA and TPA states.[11,43] Since we have confirmed previously that catenane structures remain preserved upon silver doping, hypothesis (i) can be excluded, although the exact position of silver atoms in the catenane structure may affect the symmetry of the structure. Furthermore, the calculated first hyperpolarizabilities β for the [5,5] catenane structure (see Table S1 in Supporting Information) for $Au_{10}SG_{10}$, Au_9AgSG_{10} and $Au_7Ag_3SG_{10}$ are in good agreement with the experimental values. Consequently, the decrease in hyperpolarizability of $Au_{10}SG_{10}$ upon silver doping is rather attributed to resonance effects. Due to blue-shifted S_1 states, the resonance with the S_1 state is not more efficient for $Au_7Ag_3SG_{10}$ in contrast to $Au_{10}SG_{10}$, as illustrated for the TPA spectra calculated using a TDDFT approach for the lowest-energy [5,5] catenane structures for $Au_{10}SG_{10}$, Au_9AgSG_{10} and $Au_7Ag_3SG_{10}$ shown in Figure 3B. It is worth mentioning that first hyperpolarizability β for silver-doped Au nanoclusters should increase as illustrated for an excitation wavelength of 700 nm (see Table S1 in Supporting Information).

Finally, one of the most significant effects of silver doping on the nonlinear optical properties of the clusters is the prominent bathochromic shift in the TPEF emission spectra. The red shift of ∼50 nm in the TPEF spectrum of $Au_{10-x}Ag_xSG_{10}$ (x = 1−4) may stem from altered relaxation of the S_1 first excited state of silver-doped gold clusters as opposed to $Au_{10}SG_{10}$. A plausible mechanism interpreting the red shift in the TPEF emission spectrum of $Au_{10-x}Ag_xSG_{10}$ (x = 1−4), in comparison to that of $Au_{10}SG_{10}$, has been proposed based on the significantly different magnitudes in relaxation of the S_1 state upon silver doping (see Figure 4). In summary, doping by silver atoms does not influence OPA spectra whereas the TPA cross-section is slightly increased by three silver atoms doping. In contrast, the minimum of the S_1 state is lowered by approximately 1.5 eV for three silver atoms doping with respect to the pure gold-ligated cluster for which the lowering of the S_1 state is only 0.21 eV. The reason for the different lowering energies is the breaking of the silver−gold bonds in the first excited state of the three silver atom-doped clusters (see Figure 4).

This means that in addition to silver doping, the structural properties play an important role in determining TPEF properties. For large cluster sizes a metallic core is formed in which doping by Ag atoms contributes to delocalization of electrons of the Au core. Therefore, in these cases a smaller bathochromic shift in the TPEF emission spectra can be expected than in the case of the catenane structure containing more directional metallic bonds. In fact, strong influence of Ag doping on nonlinear optical properties has been also shown for silver-doped gold-cysteine supramolecular assemblies, which contain directional metallic bonds.[9]

https://dx.doi.org/10.1021/acs.jpcc.0c05402
J. Phys. Chem. C 2020, 124, 19368−19374

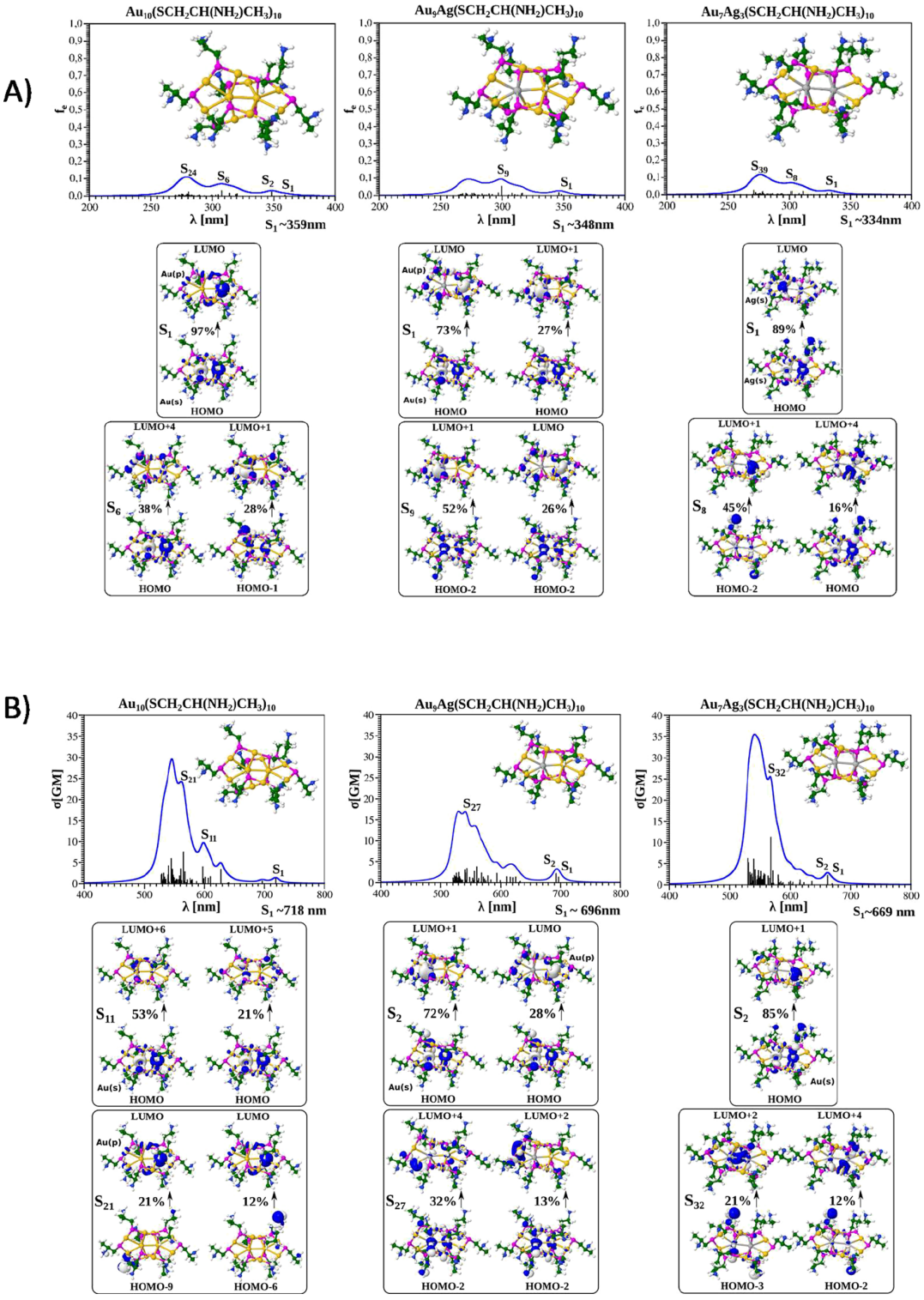

Figure 3. (A) TDDFT OPA spectrum for $Au_{10}L_{10}$, Au_9AgL_{10} $Au_7Ag_3L_{10}$ nanoclusters (with the chiral ligand $-SCH_2CH(NH_2)CH_3$) for the lowest-energy [5,5] catenane. Leading excitations responsible for the characteristic features of OPA are shown in the bottom panels. (B) TDDFT TPA spectrum for $Au_{10}L_{10}$, Au_9AgL_{10} $Au_7Ag_3L_{10}$ nanoclusters (with the chiral ligand $-SCH_2CH(NH_2)CH_3$) for the lowest-energy [5,5] catenane. Leading excitations responsible for the characteristic features of TPA are shown in the bottom panels.

CONCLUSIONS

In summary, we report a rationale chemical strategy for the substitution of heteroatoms to alter the nonlinear optical properties of clusters with catenane structures. Notably, the strategy developed herein allows the fine-tuning of the multiphoton excitation properties, preserving the structure of the nanoclusters. This is important, given the wide utility of

https://dx.doi.org/10.1021/acs.jpcc.0c05402
J. Phys. Chem. C 2020, 124, 19368−19374

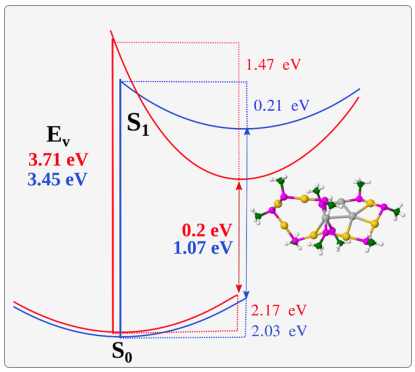

Figure 4. Calculated relaxation of the first excited state S_1 of pure gold-ligated clusters (blue) versus three silver atom-doped-ligated clusters (red) with the corresponding structure.

catenane-like structures in catalysis and in molecular mechanics with molecular rotors. Furthermore, the experimental findings on the variation of the structure-guided optical properties of the clusters, as a function of the number of doped heteroatoms, has been confirmed based on first principle theoretical calculations. In particular, the observed blue shift in the spectra is due to the larger s−d gap of Ag atoms because of smaller relativistic effects as compared to the case of Au atoms. The difference between the TPEF spectra is due to the Ag−Au bond breaking in the S_1 state, absent in the case of the Au−Au bond. A facile and robust chemical strategy allowing alteration of the absorption/emission characteristics of atomic clusters can serve as a future key-point for fine-tuning of nanocluster applications.

■ ASSOCIATED CONTENT

Supporting Information

The Supporting Information is available free of charge at https://pubs.acs.org/doi/10.1021/acs.jpcc.0c05402.

ESI-MS spectra of nanoclusters, two-photon excited fluorescence spectra at excitation wavelength 780 nm of nanoclusters in gels, HRS line intensity of nanoclusters in aqueous solutions, experimental and calculated XRD patterns of nanoclusters, DFT calculated CD spectra of the pure gold-ligated cluster and the silver-doped one, and DFT-calculated first hyperpolarizabilities for pure gold and silver-doped-ligated clusters at different wavelengths. (PDF)

■ AUTHOR INFORMATION

Corresponding Authors

Vlasta Bonačić-Koutecký − *Center of Excellence for Science and Technology-Integration of Mediterranean Region (STIM), Faculty of Science, University of Split, 21000 Split, Croatia; Interdisciplinary Center for Advanced Science and Technology (ICAST) at University of Split, 21000 Split, Croatia; Department of Chemistry, Humboldt Universitat zu Berlin, 12489 Berlin, Germany;* orcid.org/0000-0001-6142-5932; Email: vbk@cms.hu-berlin.de

Rodolphe Antoine − *Univ Lyon, Université Claude Bernard Lyon 1, CNRS, Institut Lumière Matière, F-69622 Lyon, France;* orcid.org/0000-0001-5682-8550; Email: rodolphe.antoine@univ-lyon1.fr

Authors

Srestha Basu − *Univ Lyon, Université Claude Bernard Lyon 1, CNRS, Institut Lumière Matière, F-69622 Lyon, France*

Martina Perić Bakulić − *Center of Excellence for Science and Technology-Integration of Mediterranean Region (STIM), Faculty of Science, University of Split, 21000 Split, Croatia;* orcid.org/0000-0002-9134-5500

Hussein Fakhouri − *Univ Lyon, Université Claude Bernard Lyon 1, CNRS, Institut Lumière Matière, F-69622 Lyon, France; Center of Excellence for Science and Technology-Integration of Mediterranean Region (STIM), Faculty of Science, University of Split, 21000 Split, Croatia*

Isabelle Russier-Antoine − *Univ Lyon, Université Claude Bernard Lyon 1, CNRS, Institut Lumière Matière, F-69622 Lyon, France*

Christophe Moulin − *Univ Lyon, Université Claude Bernard Lyon 1, CNRS, Institut Lumière Matière, F-69622 Lyon, France*

Pierre-François Brevet − *Univ Lyon, Université Claude Bernard Lyon 1, CNRS, Institut Lumière Matière, F-69622 Lyon, France;* orcid.org/0000-0002-9097-0187

Complete contact information is available at: https://pubs.acs.org/10.1021/acs.jpcc.0c05402

Notes

The authors declare no competing financial interest.

■ ACKNOWLEDGMENTS

This research was partially supported by the project STIM-REI, Contract Number: KK.01.1.1.01.0003, funded by the European Union through the European Regional Development Fund − the Operational Programme Competitiveness and Cohesion 2014−2020 (KK.01.1.1.01). V.B.K., M.P.B., and H.F. acknowledge computational facilities of the HPC computer within the STIM-REI project, Doctoral study of Biophysics at the University of Split as well as Prof. Miroslav Radman at MedILS and Split-Dalmatia County for support. We would also like to acknowledge the financial support received from the French-Croatian project "International Laboratory for Nano Clusters and Biological Aging, LIA NCBA".

■ REFERENCES

(1) Antoine, R. Supramolecular Gold Chemistry: From Atomically Precise Thiolate-Protected Gold Nanoclusters to Gold-Thiolate Nanostructures. *Nanomaterials* **2020**, *10*, 377.

(2) Goldmann, C.; Lazzari, R.; Paquez, X.; Boissière, C.; Ribot, F.; Sanchez, C.; Chanéac, C.; Portehault, D. Charge Transfer at Hybrid Interfaces: Plasmonics of Aromatic Thiol-Capped Gold Nanoparticles. *ACS Nano* **2015**, *9*, 7572−7582.

(3) Jin, R.; Zeng, C.; Zhou, M.; Chen, Y. Atomically Precise Colloidal Metal Nanoclusters and Nanoparticles: Fundamentals and Opportunities. *Chem. Rev.* **2016**, *116*, 10346−10413.

(4) Veselska, O.; Demessence, A. D10 Coinage Metal Organic Chalcogenolates: From Oligomers to Coordination Polymers. *Coord. Chem. Rev.* **2018**, *355*, 240−270.

(5) Ungor, D.; Dékány, I.; Csapó, E. Reduction of Tetrachloroaurate-(III) Ions with Bioligands: Role of the Thiol and Amine Functional Groups on the Structure and Optical Features of Gold Nanohybrid Systems. *Nanomaterials* **2019**, *9*, 1229.

(6) Wu, Z.; Jin, R. On the Ligand's Role in the Fluorescence of Gold Nanoclusters. *Nano Lett.* **2010**, *10*, 2568−2573.

(7) Kang, X.; Zhu, M. Tailoring the Photoluminescence of Atomically Precise Nanoclusters. *Chem. Soc. Rev.* **2019**, *48*, 2422−2457.

(8) Jin, R.; Nobusada, K. Doping and Alloying in Atomically Precise Gold Nanoparticles. *Nano Res.* **2014**, *7*, 285−300.

(9) Fakhouri, H.; Perić, M.; Bertorelle, F.; Dugourd, P.; Dagany, X.; Russier-Antoine, I.; Brevet, P.-F.; Bonačić-Koutecký, V.; Antoine, R. Sub-100 Nanometer Silver Doped Gold−Cysteine Supramolecular Assemblies with Enhanced Nonlinear Optical Properties. *Phys. Chem. Chem. Phys.* **2019**, *21*, 12091−12099.
(10) Olesiak-Banska, J.; Waszkielewicz, M.; Obstarczyk, P.; Samoc, M. Two-Photon Absorption and Photoluminescence of Colloidal Gold Nanoparticles and Nanoclusters. *Chem. Soc. Rev.* **2019**, *48*, 4087−4117.
(11) Bonačić-Koutecký, V.; Antoine, R. Enhanced Two-Photon Absorption of Ligated Silver and Gold Nanoclusters: Theoretical and Experimental Assessments. *Nanoscale* **2019**, *11*, 12436−12448.
(12) Brach, K.; Waszkielewicz, M.; Olesiak-Banska, J.; Samoc, M.; Matczyszyn, K. Two-Photon Imaging of 3d Organization of Bimetallic Auag Nanoclusters in DNA Matrix. *Langmuir* **2017**, *33*, 8993−8999.
(13) Brach, K.; Olesiak-Banska, J.; Waszkielewicz, M.; Samoc, M.; Matczyszyn, K. DNA Liquid Crystals Doped with AuAg Nanoclusters: One-Photon and Two-Photon Imaging. *J. Mol. Liq.* **2018**, *259*, 82−87.
(14) Van Steerteghem, N.; Van Cleuvenbergen, S.; Deckers, S.; Kumara, C.; Dass, A.; Häkkinen, H.; Clays, K.; Verbiest, T.; Knoppe, S. Symmetry Breaking in Ligand-Protected Gold Clusters Probed by Nonlinear Optics. *Nanoscale* **2016**, *8*, 12123−12127.
(15) Guidez, E. B.; Mäkinen, V.; Häkkinen, H.; Aikens, C. M. Effects of Silver Doping on the Geometric and Electronic Structure and Optical Absorption Spectra of the Au25−NAgN(Sh)18− (N = 1, 2, 4, 6, 8, 10, 12) Bimetallic Nanoclusters. *J. Phys. Chem. C* **2012**, *116*, 20617−20624.
(16) Liu, S. Single-Atom Doping on Thiolate-Protected Gold Nanoclusters: A Tddft Study on the Excited States. *Mater. Res. Express* **2019**, *6*, No. 1150g3.
(17) Muniz-Miranda, F.; Menziani, M. C.; Pedone, A. Influence of Silver Doping on the Photoluminescence of Protected AgNAu25−N Nanoclusters: A Time-Dependent Density Functional Theory Investigation. *J. Phys. Chem. C* **2015**, *119*, 10766−10775.
(18) Xie, X.-Y.; Xiao, P.; Cao, X.; Fang, W.-H.; Cui, G.; Dolg, M. The Origin of the Photoluminescence Enhancement of Gold-Doped Silver Nanoclusters: The Importance of Relativistic Effects and Heteronuclear Gold−Silver Bonds. *Angew. Chem., Int. Ed.* **2018**, *57*, 9965−9969.
(19) Wang, S.; Meng, X.; Das, A.; Li, T.; Song, Y.; Cao, T.; Zhu, X.; Zhu, M.; Jin, R. A 200-Fold Quantum Yield Boost in the Photoluminescence of Silver-Doped AgXAu25−X Nanoclusters: The 13 Th Silver Atom Matters. *Angew. Chem., Int. Ed.* **2014**, *53*, 2376−2380.
(20) van der Linden, M.; van Bunningen, A. J.; Amidani, L.; Bransen, M.; Elnaggar, H.; Glatzel, P.; Meijerink, A.; de Groot, F. M. F. Single Au Atom Doping of Silver Nanoclusters. *ACS Nano* **2018**, *12*, 12751−12760.
(21) Comby-Zerbino, C.; Perić, M.; Bertorelle, F.; Chirot, F.; Dugourd, P.; Bonačić-Koutecký, V.; Antoine, R. Catenane Structures of Homoleptic Thioglycolic Acid-Protected Gold Nanoclusters Evidenced by Ion Mobility-Mass Spectrometry and Dft Calculations. *Nanomaterials* **2019**, *9*, 457.
(22) Bertorelle, F.; Russier-Antoine, I.; Calin, N.; Comby-Zerbino, C.; Bensalah-Ledoux, A.; Guy, S.; Dugourd, P.; Brevet, P.-F.; Sanader, Ž.; Krstić, M.; et al. Au10(SG)10: A Chiral Gold Catenane Nanocluster with Zero Confined Electrons Optical Properties and First-Principles Theoretical Analysis. *J. Phys. Chem. Lett.* **2017**, *8*, 1979−1985.
(23) Comby-Zerbino, C.; Bertorelle, F.; Chirot, F.; Dugourd, P.; Antoine, R. Structural Insights into Glutathione-Protected Gold Au10−12(SG)10−12 Nanoclusters Revealed by Ion Mobility Mass Spectrometry. *Eur. Phys. J. D* **2018**, *72*, 144.
(24) Russier-Antoine, I.; Bertorelle, F.; Calin, N.; Sanader, Z.; Krstic, M.; Comby-Zerbino, C.; Dugourd, P.; Brevet, P.-F.; Bonacic-Koutecky, V.; Antoine, R. Ligand-Core Nlo-Phores: A Combined Experimental and Theoretical Approach to the Two-Photon Absorption and Two-Photon Excited Emission Properties of Small-Ligated Silver Nanoclusters. *Nanoscale* **2017**, *9*, 1221−1228.
(25) Russier-Antoine, I.; Bertorelle, F.; Vojkovic, M.; Rayane, D.; Salmon, E.; Jonin, C.; Dugourd, P.; Antoine, R.; Brevet, P.-F. Non-Linear Optical Properties of Gold Quantum Clusters: The Smaller the Better. *Nanoscale* **2014**, *6*, 13572−13578.
(26) Becke, A. D. Density-Functional Exchange-Energy Approximation with Correct Asymptotic-Behavior. *Phys. Rev. A* **1988**, *38*, 3098−3100.
(27) Becke, A. D. A New Mixing of Hartree-Fock and Local Density-Functional Theories. *J. Chem. Phys.* **1993**, *98*, 1372−1377.
(28) Lee, C. T.; Yang, W. T.; Parr, R. G. Development of the Colle-Salvetti Correlation-Energy Formula into a Functional of the Electron Density. *Phys. Rev. B* **1988**, *37*, 785−789.
(29) Weigend, F.; Ahlrichs, R. Balanced Basis Sets of Split Valence, Triple Zeta Valence and Quadruple Zeta Valence Quality for H to Rn: Design and Assessment of Accuracy. *Phys. Chem. Chem. Phys.* **2005**, *7*, 3297−3305.
(30) *V7.4, T. A Development of University of Karlsruhe and Forschungszentrum Karlsruhe Gmbh, 1989−2007, Turbomole Gmbh since 2007*. Available from http://www.Turbomole.Com 2019
(31) Bertorelle, F.; Hamouda, R.; Rayane, D.; Broyer, M.; Antoine, R.; Dugourd, P.; Gell, L.; Kulesza, A.; Mitric, R.; Bonacic-Koutecky, V. Synthesis, Characterization and Optical Properties of Low Nuclearity Liganded Silver Clusters: Ag31(SG)19 and Ag15(SG)11. *Nanoscale* **2013**, *5*, 5637−5643.
(32) Bonacic-Koutecky, V.; Kulesza, A.; Gell, L.; Mitric, R.; Antoine, R.; Bertorelle, F.; Hamouda, R.; Rayane, D.; Broyer, M.; Tabarin, T.; et al. Silver cluster-biomolecule hybrids: From basics towards sensors. *Phys. Chem. Chem. Phys.* **2012**, *14*, 9282−9290.
(33) List, N. H.; Zaleśny, R.; Murugan, N. A.; Kongsted, J.; Bartkowiak, W.; Ågren, H. Relation between Nonlinear Optical Properties of Push−Pull Molecules and Metric of Charge Transfer Excitations. *J. Chem. Theory Comput.* **2015**, *11*, 4182−4188.
(34) Norman, P. A Perspective on Nonresonant and Resonant Electronic Response Theory for Time-Dependent Molecular Properties. *Phys. Chem. Chem. Phys.* **2011**, *13*, 20519−20535.
(35) *Dalton, a Molecular Electronic Structure Program*, Release Dalton 2016. See http://daltonprogram.Org.
(36) Aidas, K.; Angeli, C.; Bak, K. L.; Bakken, V.; Bast, R.; Boman, L.; Christiansen, O.; Cimiraglia, R.; Coriani, S.; Dahle, P.; et al. The Dalton quantum chemistry program system. *WIREs Comput. Mol. Sci.* **2014**, *4*, 269−284.
(37) Rassolov, V. A.; Pople, J. A.; Ratner, M. A.; Windus, T. L. 6-31G* Basis Set for Atoms K through Zn. *J. Chem. Phys.* **1998**, *109*, 1223−1229.
(38) Francl, M. M.; Pietro, W. J.; Hehre, W. J.; Binkley, J. S.; Gordon, M. S.; DeFrees, D. J.; Pople, J. A. Self-Consistent Molecular Orbital Methods Xxiii. A Polarization-Type Basis Set for Second-Row Elements. *J. Chem. Phys.* **1982**, *77*, 3654−3665.
(39) Dill, J. D.; Pople, J. A. Self-Consistent Molecular Orbital Methods. Xv. Extended Gaussian-Type Basis Sets for Lithium, Beryllium, and Boron. *J. Chem. Phys.* **1975**, *62*, 2921−2923.
(40) Hehre, W. J.; Ditchfield, R.; Pople, J. A. Self—Consistent Molecular Orbital Methods Xii. Further Extensions of Gaussian—Type Basis Sets for Use in Molecular Orbital Studies of Organic Molecules. *J. Chem. Phys.* **1972**, *56*, 2257−2261.
(41) Andrae, D.; Haeussermann, U.; Dolg, M.; Stoll, H.; Preuss, H. Energy-Adjusted Ab Initio Pseudopotentials for the Second and Third Row Transition Elements. *Theor. Chim. Acta* **1990**, *77*, 123.
(42) Guinier, A. *X-ray Diffraction in Crystals, Imperfect Crystals, and Amorphous Bodies*; W.H. Freeman: San Francisco, 1963.
(43) Hu, Z.; Jensen, L. Importance of Double-Resonance Effects in Two-Photon Absorption Properties of Au25(SR)18−. *Chem. Sci.* **2017**, *8*, 4595−4601.

https://dx.doi.org/10.1021/acs.jpcc.0c05402
J. Phys. Chem. C 2020, 124, 19368−19374

communications chemistry

ARTICLE

https://doi.org/10.1038/s42004-021-00497-z OPEN

Functionalized Au_{15} nanoclusters as luminescent probes for protein carbonylation detection

Guillaume F. Combes[1,2], Hussein Fakhouri[1,3], Christophe Moulin[3], Marion Girod[4], Franck Bertorelle[3], Srestha Basu[3], Romain Ladouce[2], Martina Perić Bakulić[1], Željka Sanader Maršić[5], Isabelle Russier-Antoine[3], Pierre-François Brevet[3], Philippe Dugourd[3], Anita Krisko[6], Katarina Trajković[1,2], Miroslav Radman[1,2,7], Vlasta Bonačić-Koutecký[1,8,9]✉ & Rodolphe Antoine[3]✉

Atomically precise, ligand-protected gold nanoclusters (AuNCs) attract considerable attention as contrast agents in the biosensing field. However, the control of their optical properties and functionalization of surface ligands remain challenging. Here we report a strategy to tailor AuNCs for the precise detection of protein carbonylation—a causal biomarker of ageing. We produce $Au_{15}SG_{13}$ (SG for glutathione) with atomic precision and functionalize it with a thiolated aminooxy moiety to impart protein carbonyl-binding properties. Mass spectrometry and molecular modelling reveal the key structural features of $Au_{15}SG_{12}$-Aminooxy and its reactivity towards carbonyls. Finally, we demonstrate that $Au_{15}SG_{12}$-Aminooxy detects protein carbonylation in gel-based 1D electrophoresis by one- and two-photon excited fluorescence. Importantly, to our knowledge, this is the first application of an AuNC that detects a post-translational modification as a nonlinear optical probe. The significance of post-translational modifications in life sciences may open avenues for the use of $Au_{15}SG_{13}$ and other nanoclusters as contrast agents with tailored surface functionalization and optical properties.

[1] Center of Excellence for Science and Technology-Integration of Mediterranean Region (STIM), Faculty of Science, University of Split, Split, Croatia. [2] Mediterranean Institute for Life Sciences (MedILS), Split, Croatia. [3] Univ Lyon, Univ Claude Bernard Lyon 1, CNRS, Institut Lumière Matière, Villeurbanne F-69622, France. [4] Univ Lyon, CNRS, Université Claude Bernard Lyon 1, Institut des Sciences Analytiques, UMR 5280, 5 rue de la Doua, Villeurbanne F-69100, France. [5] Faculty of Science, University of Split, Split, Republic of Croatia. [6] Department of Experimental Neurodegeneration, University Medical Center Goettingen, Göttingen, Germany. [7] Université R. Descartes-Paris 5, Faculté de Médecine, site Cochin, Paris, France. [8] Interdisciplinary Center for Advanced Science and Technology (ICAST) at University of Split, Split, Croatia. [9] Chemistry Department, Humboldt University of Berlin, Berlin, Germany. ✉email: vbk@cms.hu-berlin.de; rodolphe.antoine@univ-lyon1.fr

Proteins carry out and assure the maintenance of almost all cellular functions, lending support to a paradigm arguing that aging and age-related diseases (ARDs) are complex consequences of the cumulative oxidative damage to proteins[1,2]. Previous research has gathered evidence supporting the hypotheses that healthy aging is an increasing biological noise, a consequence of diffuse proteome oxidation, whereas ARDs appear associated with excessive oxidation of particular susceptible proteins sensitized by mutations predisposing to disease[2]. Protein carbonylation, an irreversible oxidative damage to proteins can affect most amino acids[3]. Indeed, an increase in protein carbonyls appears as a biomarker of cellular and organismal aging[4].

Different methods have been developed for the detection and quantification of carbonylated proteins as commonly used markers of protein oxidation[4–7]. Since protein carbonyls have no distinguished UV or visible optical properties, specific chemical probes are required for their visualization[6,7]. The use of fluorophores with carbonyl-reactive groups enables direct detection and quantitation of carbonyls on the proteins subjected to one- and two-dimensional electrophoresis (1DE and 2DE, respectively) using fluorescence imaging scanner[4]. For instance, cyanine hydrazide is currently used in the two-dimensional gel electrophoresis methodology. For accurate detection, this complex analysis requires special equipment and reagents[8–10]. Moreover, the hydrazone bond formed between the cyanine hydrazide and protein carbonyls is usually sensitive to acidic environment and narrow pH range conditions are required to optimize the efficient binding of cyanine-hydrazide fluorescent dye to its carbonyl targets. Recently, it has been reported that near-infrared (NIR) fluorescence using NIR dyes offers certain advantages over visible-range fluorescence, particularly the lack of autofluorescence of biological molecules in the NIR[11]. To improve the specificity and sensitivity of carbonyl detection necessary for diagnostics and prognostic purposes, there is room for advanced strategies.

One promising strategy for the detection of biomolecules consists of using nonlinear optical processes (NLO) involving multiple IR photon excitations (in the NIR-IR window, i.e. 700–800 nm)[12,13]. Also, the high spatial resolution of two-photon absorption (2PA or TPA) is a strong added value for bioimaging applications[14]. Ligand-protected gold nanoclusters (AuNCs) with gold kernel composed of few dozen of atoms possess molecule-like properties[15] such as luminescence[16,17]. Such AuNCs can exhibit strong photoluminescence from ultraviolet to the NIR region[18,19]. Also, their bleaching rate is very slow, demonstrating their superior photostability[20,21]. In addition, ligand-protected AuNCs exhibit outstanding biocompatibility, which makes their in vitro and in vivo bio-applications a rich research area[22–27]. As compared to dyes, ligand-protected AuNCs present much greater two-photon absorption cross sections[13,28,29], making them promising candidates for multiphoton excited fluorescence microscopy[30–32]. As pioneered by Murray and co-workers[33], surface functionalization of AuNCs, in particular their functionalization through ligand-exchange strategy[34], grants them high versatility, while selective functionality is incorporated onto the ligand-protected NCs by exchanging the surface protecting ligand with desired molecules containing appropriate functional groups.

In this work, we conducted the proof-of-concept study for developing the first NC-based imaging system for protein carbonylation detection. The NCs were liganded with glutathione (SG) and produced at the atomic precision with the exact formula $Au_{15}SG_{13}$. Such NCs were then functionalized with a thiolated aminooxy probe to gain protein carbonyl-binding properties. Using mass spectrometry (MS) approach, we then showed that the resulting NCs bind carbonylated proteins through the formation of an oxime bond between the aminooxy-containing thiolated ligand on the NC and the carbonylated amino acid on the protein. Molecular modeling was performed to reveal the key features of functionalized NCs and to evaluate the robustness of the oxime bond upon exposure to the solvent. Finally, we demonstrate that such functionalized AuNCs can detect protein carbonyls in gel-based 1DE analysis by one-photon fluorescence and two-photon excited fluorescence imaging.

Results

Synthesis and characterization of $Au_{15}SG_{13}$ and $Au_{15}SG_{12}$-Ao NCs. Here, we have developed a synthetic protocol to produce atomically precise thiolated aminooxy-functionalized gold NCs with protein carbonyl-binding properties. Initially, non-functionalized, glutathione-protected gold NCs ($Au_{15}SG_{13}$) were synthesized (Fig. 1a). We have chosen $Au_{15}SG_{13}$ as a basis for further modifications due to its small size, simplicity of its synthesis, good stability in water, and excellent optical properties in dried polyacrylamide matrix. FT-IR spectra of $Au_{15}SG_{13}$ NCs and pure glutathione GSH are given in Supplementary Fig. S1a, b. The ligation of glutathione in the form of the thiolate (SG) to the Au core was confirmed by the absence of the absorption band at ν(S-H) = 2523 cm^{-1} in the FTIR spectrum of the as-prepared NCs sample, as already found in the seminal work published by Negishi and Tsukuda[35]. Supplementary Fig. S1c shows the TEM image of the as-prepared $Au_{15}SG_{13}$ NCs. The particles with sizes of 1–2 nm are barely discernible in the image. From the XPS data (Supplementary Table S1), we find the Au/S atomic ratio to be 1.26 ± 0.13, which is compatible with the composition of $Au_{15}SG_{13}$ (the expected value is 1.15). Upon synthesis, the quality of $Au_{15}SG_{13}$ was assessed using negative-mode ESI-MS. This analysis confirmed monodispersity of the synthesized NCs. A charge state distribution was observed from $[M-4H]^{4-}$ through $[M-6H]^{6-}$. Deconvolution of charge states from 4- through 6- revealed a mass of 6928 Da for the $Au_{15}SG_{13}$, consistent with its calculated mass (Supplementary Fig. S2a).

To develop NCs with carbonyl-binding properties, $Au_{15}SG_{13}$ had to be functionalized by the replacement of one glutathione with a carbonyl-reactive agent. Hydrazides (Hz) and aminooxy (Ao) are commonly used carbonyl-reactive chemical groups and they form different kinds of bonds with protein carbonyls–hydrazone (Hz) and oxime (Ao) bonds. Since oxime bonds appear to be more stable than hydrazone bonds[36,37], we opted for the Ao to functionalize $Au_{15}SG_{13}$. Functionalized NCs $Au_{15}SG_{12}$(3-Aminooxy)-1-propanethiol (termed as $Au_{15}SG_{12}$-Ao) was generated by the replacement of one glutathione on $Au_{15}SG_{13}$ with the Ao through a ligand-exchange procedure (Fig. 1b).

To characterize the synthesized $Au_{15}SG_{12}$-Ao, the reaction mix was analyzed using negative-mode ESI-MS and a new peak corresponding to $Au_{15}SG_{12}$-Ao for the charge state 4- was observed, as expected (Fig. 1c). Experimentally determined isotopic patterns of the different NCs were in perfect agreement with their simulated ESI-MS patterns (Supplementary Fig. S2b, c) and confirmed the stoichiometry of $Au_{15}SG_{13}$ (Supplementary Fig. S2b) and $Au_{15}SG_{12}$-Ao (Supplementary Fig. S2c). Of note, increasing the concentration of the Ao led to the exchange of more than one SG ligand (Fig. 1d and Supplementary Fig. S2d, e). ESI-MS was also applied to monitor the number of Ao ligand exchanged in $Au_{15}SG_{13}$ species following the addition of Ao in solution at different concentrations. Supplementary Fig. S2d, e shows the evolution in ligand exchange as a function of the concentration of Ao ligand. Clearly, adding 0.1–0.3 equivalent of Ao allows for controlling of ligand exchange to just one.

We next compared UV-vis absorption and emission spectra of $Au_{15}SG_{13}$ and $Au_{15}SG_{12}$-Ao (Supplementary Fig. S2f). The two NCs displayed similar main features of the spectra. The linear optical absorption spectra were composed of a monotonous

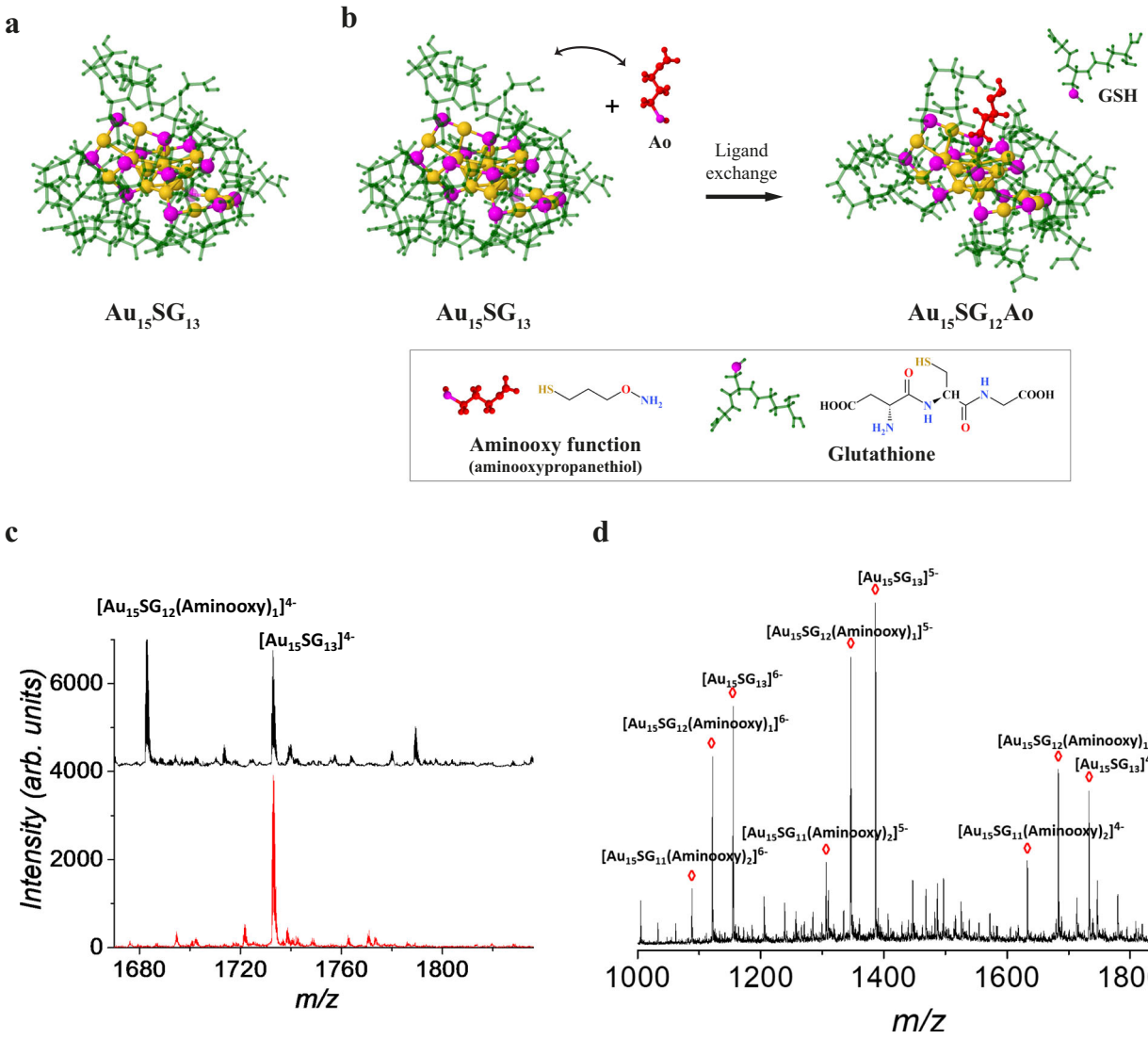

Fig. 1 Synthesis and characterization of $Au_{15}SG_{13}$ and $Au_{15}SG_{12}$-Ao. a Density functional theory (DFT) structure of the gold NCs ($Au_{15}SG_{13}$). **b** DFT structures illustrate the ligand-exchange strategy to functionalize the NCs with an aminooxy (Ao) function ($Au_{15}SG_{12}$-Ao). Atoms and molecules are labeled as following: S-magenta, Au-gold, glutathione-green, and aminooxypropanethiol-red **c** Zoom of the ESI mass spectrum of $Au_{15}SG_{13}$ and $Au_{15}SG_{12}$Ao NCs corresponding to the *m/z* region labeled by a blue rectangle in supplementary Fig. S2a. A new peak corresponding to $Au_{15}SG_{12}$-Ao is observed following the ligand-exchange reaction. **d** Mass spectra showing exchange of more than one SG ligand.

increase of absorption below 500–550 nm. Photoluminescence spectra displayed a broad band extending in the NIR region and centered around 650−700 nm.

To determine the structure of NC after the ligand exchange, we performed molecular modeling based on the combination of density functional theory (DFT) and semi-empirical quantum method PM7 approach (see Computational details). The structure of $Au_{15}SG_{13}$ was proposed by De-en Jiang[38] using the density functional theory (DFT). According to this model, $Au_{15}SG_{13}$ contains a cyclic [Au(I)-SG] pentamer interlocked with two trimer motifs protecting the tetrahedral Au_4 core. Such structural assignment was supported by comparison to the powder X-ray diffraction pattern and, via time-dependent DFT calculations, to the optical and chiroptical (CD) absorption spectra[39]. We evaluated the influence of the Ao position on the overall structure of the liganded $Au_{15}SG_{13}$ NC. Two possible exchanges out of thirteen are presented in structures I and II (Supplementary Fig. S2g). In both structures, H-bond networks between neighboring SG ligands and the Ao ligand are present. Interestingly, the Ao in structure I is more buried in the SG ligand environment than the Ao in structure II. Such differences in Ao accessibility may influence their reactivity with carbonyls.

Interaction of $Au_{15}SG_{12}$-Ao with protein carbonyls. Since protein carbonylation occurs on solvent-exposed amino acids, we predicted that $Au_{15}SG_{12}$-Ao would react with carbonylated proteins through the formation of an extremely stable oxime bond between the amino group of the Ao attached to the NC and carbonyl groups on the amino acids (Fig. 2a). To test this prediction empirically, we used two model substrates: leupeptin (N-acetyl-L-leucyl-L-leucyl-L-argininal), a natural tripeptide inhibitor of serine proteases containing a carbonyl group, and oxidized lysozyme as a model protein.

Interaction of $Au_{15}SG_{12}$-Ao with leupeptin. If $Au_{15}SG_{12}$-Ao can bind protein carbonyls, we would expect the formation of a stable [$Au_{15}SG_{12}$-Ao–leupeptin] complex upon mixing of the $Au_{15}SG_{12}$-Ao with leupeptin (Fig. 2b). To get insight into the formation of such complex and test specificity of $Au_{15}SG_{12}$-Ao for a carbonyl on

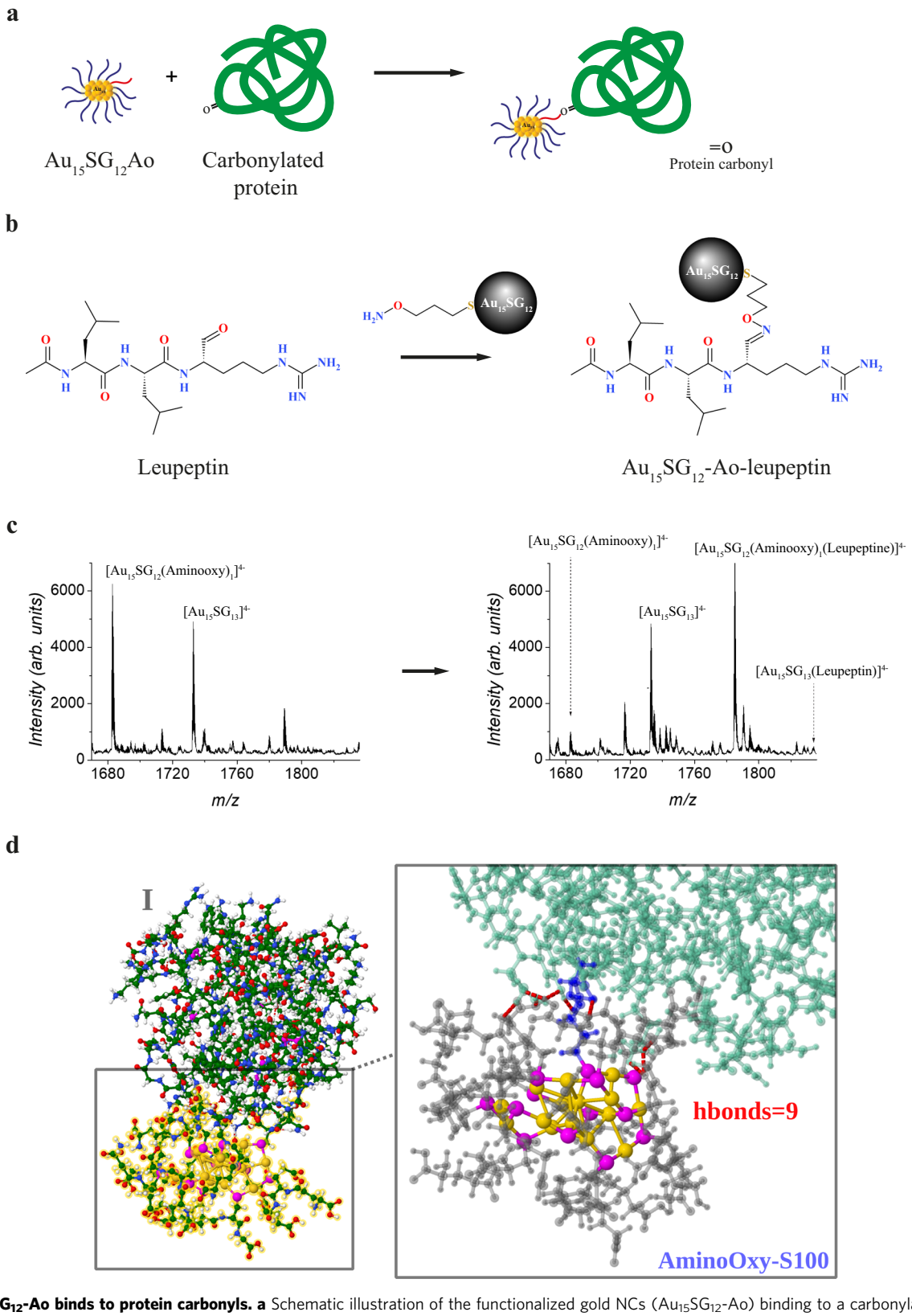

Fig. 2 $Au_{15}SG_{12}$-Ao binds to protein carbonyls. a Schematic illustration of the functionalized gold NCs ($Au_{15}SG_{12}$-Ao) binding to a carbonylated protein. **b** Illustration of the reaction of the Ao group of 3-(Aminooxy)-1-propanethiol forming an oxime linkage with the aldehyde of leupeptin. **c** ESI-MS spectrum following the formation of the stable oxime linkages: a new peak corresponding to $Au_{15}SG_{12}$-Ao-leupeptin is observed. **d** The QM/MM structures obtained by using two-layer ONIOM illustrating the interaction of liganded AuNC with lysozyme. Interface between liganded NCs $Au_{15}SG_{12}$-Ao and the protein is enlarged (**right**) illustrating Ao-serine oxime bond and hydrogen bonding network. (SG-gray, Au-gold, S-magenta, lysozyme-green, Ao-Serine oxime bond-blue, H-bonds-dotted in red).

leupeptin, a mixture of $Au_{15}SG_{13}$ and $Au_{15}SG_{12}$-Ao was analyzed by negative-mode ESI-MS before and after addition of leupeptin (Fig. 2c). As predicted, after the addition of leupeptin a new peak was detected under the charge state 4-, which corresponded to the newly formed [$Au_{15}SG_{12}$-Ao-leupeptin] complex. Note that the precursor $Au_{15}SG_{12}$-Ao has almost disappeared demonstrating its high reaction rate with leupeptin. Importantly, the $Au_{15}SG_{13}$ peak was unchanged, indicating that the non-functionalized NC does not react unspecifically with leupeptin under indicated conditions.

Characterization of oxidized lysozyme. We next aimed to test whether $Au_{15}SG_{12}$-Ao reacts specifically with amino acids carbonylated upon oxidation of a protein. To that end, we performed a multifaceted analysis of the NC-protein complex using oxidized lysozyme as a model protein. Lysozyme is a single chain polypeptide of 129 amino acids that we used previously in systematic protein carbonylation studies[40]. To induce carbonylation of the lysozyme we chose the metal-catalyzed oxidation (MCO). The MCO occurs in vitro by Fenton reaction whereby ascorbic acid and iron-chloride generate highly reactive oxygen species (ROS such as hydroxyls) that react with proteins and generate carbonyl groups on susceptible amino acids[5]. To confirm the efficiency of the MCO, we measured carbonylation of the lysozyme by a Western Blot-based method (Supplementary Fig. S3a, Supplementary Data 1 and 2 Figs. S8, S14) and by a quantitative 2,4-Dinitrophenylhydrazine (DNPH) colorimetric assay (Supplementary Fig. S3b and Supplementary Data 2 Fig. S15)[41]. Both approaches revealed a significant increase in carbonylation in oxidized lysozyme as compared to non-oxidized control under indicated conditions.

To identify and quantify carbonylated amino acids on the oxidized lysozyme, sequence database search and tandem mass spectrometry MS/MS analysis were performed (Supplementary Fig. S3c). To search for oxidized peptides, we implemented user-defined variable modifications corresponding to a list of known carbonyl modifications from the literature[42], which were derivatized with DNPH (Oxi-DNP method). For the MS/MS analysis, we labeled carbonylated amino acids with DNPH since DNPH-tagged-carbonylated peptides display the best results with this method. Namely, DNPH tag has better ionization efficiencies and additionally stabilizes labile modifications such as Michael adducts as compared to alternative aminooxy probes[43]. The combined digest data provided 61.2% sequence coverage for the lysozyme subjected to MCO. Nineteen Oxi-DNP modified peptides were identified with confidence in the derivatized MCO-lysozyme (Supplementary Fig. S3c). Among the identified carbonylation sites, tryptophans (W) appeared as the most frequently oxidized amino acids. As a control, same analysis was performed on a non-oxidized lysozyme treated with DNPH and no modified peptides were detected.

Quantification of detected oxidized peptides has been done at the MS^1 level (Supplementary Fig. S3c). To estimate the amount of oxidized versus the non-oxidized protein peak areas for each oxidized peptide were normalized to the areas of the corresponding non-oxidized peptides in the control samples (Supplementary Fig. S3d). Approximately 1.3 % of the total protein amount has been oxidized, with W^{108}, K^{13}, and W^{62} as the most intense carbonylated sites.

Molecular modeling of lysozyme–$Au_{15}SG_{12}$-Ao complex revealing the key role of liganded AuNC. To visualize the positions on the protein of the empirically determined carbonylated sites (Supplementary Fig. S3c), those sites (K^{13}, S^{24}, W^{28}, T^{43}, W^{62}, P^{79}, S^{81}, L^{83}, S^{85}, I^{98}, S^{100}, W^{108}, Q^{121}, W^{123}, and I^{124}) were mapped on the 3D structure of lysozyme obtained by X-ray analysis (Supplementary Fig. S3e)[44]. While most of these residues were found on the protein surface and are thus easily accessible to ROS, the carbonylated tryptophan residues W^{28} and W^{123} were buried inside the protein skeleton. This is likely due to protein misfolding caused by the initial carbonylation of the surface residues and subsequent exposure to ROS of the previously hidden parts of the polypeptide.

To characterize the linkage between $Au_{15}SG_{12}$-Ao and carbonylated amino acid, we next conducted molecular modeling on an example of S^{100} on the surface of the lysozyme (Fig. 2d). Of note, the modeling has been performed on non-oxidized protein because the structure of carbonylated lysozyme is not available. In order to include the natural environment of the $Au_{15}SG_{12}$-Ao–oxidized lysozyme complex, we also evaluated the robustness of the oxime bond towards solvent accessibility. This analysis revealed that glutathione ligands play the protective role with respect to the thiolated aminooxy ligand while allowing it to form the interface with carbonylated lysozyme. Penetration of water was significantly low suggesting that the Ao linkage is protected from the external environment by the glutathione surrounding (Supplementary Fig. S3f). The key result is the H-bond network formed by glutathione ligands that protect the oxime bond between the Ao and a carbonylated residue on the protein. Together, these data justify the use of liganded AuNCs for the detection of protein carbonylation.

MS-based detection of $Au_{15}SG_{12}$-Ao grafted on carbonylated amino acids within the oxidized lysozyme. To obtain evidence that $Au_{15}SG_{12}$-Ao is specific for carbonylated amino acids, i.e. that it is grafted directly on the carbonylated amino acid residue on the oxidized lysozyme, we next made attempts to measure directly the mass of $Au_{15}SG_{12}$-Ao bound to oxidized lysozyme. However, due to low levels of carbonylation (<1%) no NC attached to the oxidized lysozyme was detected by mass spectrometry (MALDI-MS technique), as evidenced by lack of any mass peak larger than that of the parent oxidized lysozyme. Hence we used an alternative approach where we analyzed the oxidized protein derivatized with $Au_{15}SG_{12}$-Ao after subsequent degradation of the grafted NC and trypsin digestion, whereby the putative oxime bond between the aminooxy on the NC and carbonylated amino acids on the protein remained intact. Degradation of the NC was necessary since NC-grafted peptides are too large to be analyzed directly by LC-MS/MS and it was achieved by cysteine treatment which destabilizes bonds between the glutathiones and the gold core of the NC. The modified peptides were obtained after neutralization of ungrafted Ao groups and precipitation of the degraded gold-cysteine polymers. After this treatment, the residual modification on the grafted carbonylated sites should be an Ao-C3-thiol group. The sample was then reduced by dithiothreitol and alkylated with iodoacetamide (IAM) before digestion with trypsin. As the IAM can react with the free thiols remaining on the carbonylated sites, the carbonyl modifications[5] derivatized with Ao-C3-thiol-IAM were implemented for the database search. Seven peptides with these modifications were identified using Protein prospector (Table 1). We found modifications corresponding to the direct binding of $Au_{15}SG_{12}$-Ao to carbonylated amino acids on W^{28}, W^{123} and I^{98}—the same residues that we had identified as carbonylated in the previous analysis (Supplementary Fig. S3d). These results indicate that the $Au_{15}SG_{12}$-Ao is grafted directly on the carbonylated sites of the lysozyme. Of note, S^{100}, the carbonylated residue analyzed by molecular modeling (Fig. 2d) was not found among Ao-binding sites, likely due to degradation of the respective peptides.

Application of $Au_{15}SG_{12}$-Ao for detection of carbonylated proteins in polyacrylamide gels. We next tested whether labeling of carbonylated proteins with $Au_{15}SG_{12}$-Ao is applicable for the

Table 1 List of oxidized peptides identified in MCO-lysozyme sample labeled with Ao-C3-Thiol-IAM after degradation of the $Au_{15}SG_{12}$-Ao NCs, using Protein Prospector.

m/z	z	Peptide + Ao-C3-Thiol-IAM modification	Error ppm	Score	Expect	Area in FMS
399.8528	3	CELAAAMKR^{14}[+148.0307]	−8.2	30.2	7.50E−04	4.15E+05
961.7669	3	GYSLGNW^{28}[+148.0307]VCAAKFESNFNTQATNR	−2.6	41.2	7.50E−10	5.96E+05
961.7669	3	GYSLGNWVCA^{31}[+148.0307]AKFESNFNTQATNR	−2.6	40.9	1.70E−09	5.44E+06
952.7581	3	GYSLGNW^{28}[+121.0098]VCAAKFESNFNTQATNR	−8.1	46.2	2.50E−08	4.23E+05
952.0914	3	GYSLGNW^{28}[+119.0041]VCAAKFESNFNTQATNR	−8.6	45	1.20E−07	2.21E+05
651.3103	3	KI^{98}[+148.0307]VSDGNGMNAWVAWR	−8	25.9	1.30E−04	9.10E+05
388.1763	3	GTDVQAW^{123}[+119.0041]IR	−14	30.2	7.50E−04	1.37E+04

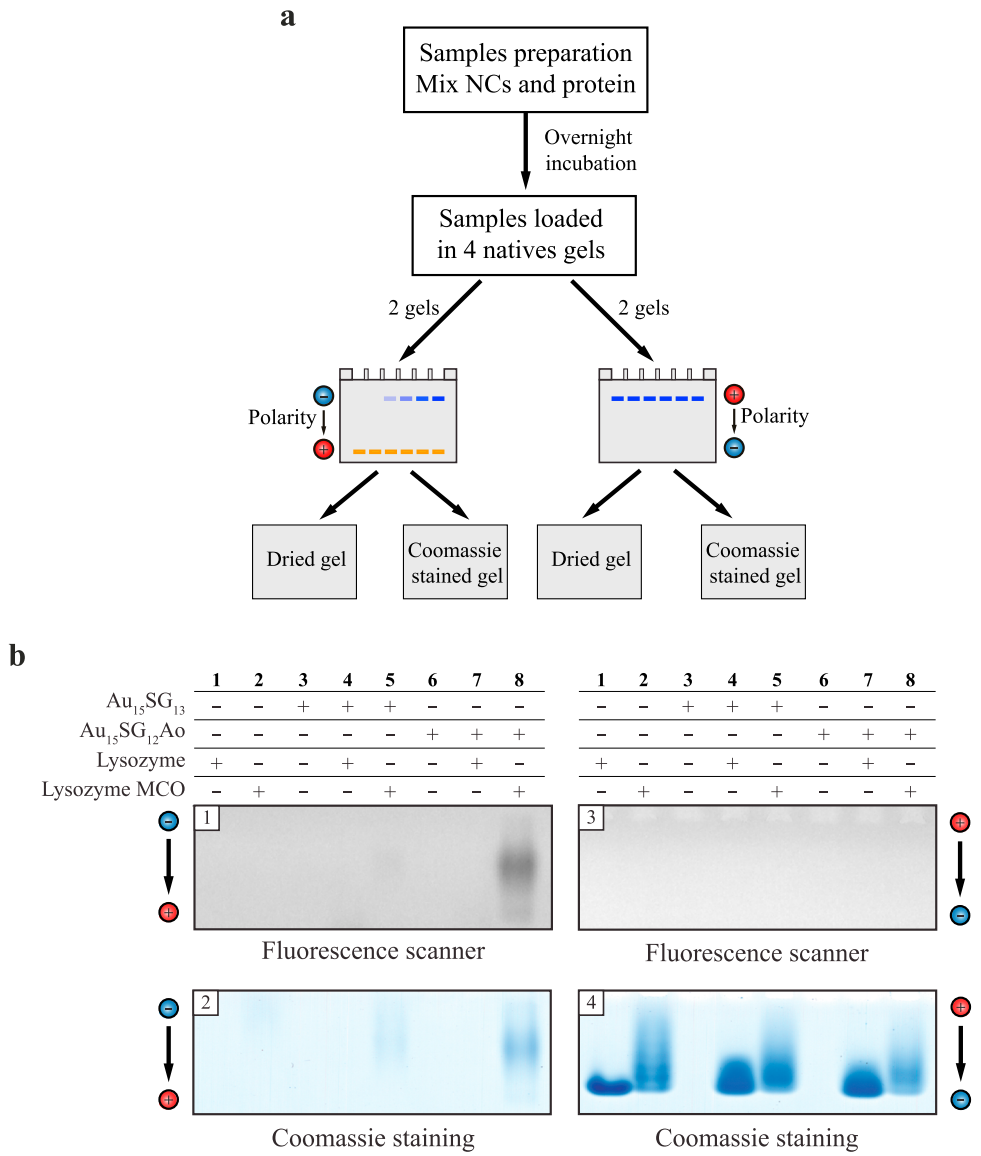

Fig. 3 $Au_{15}SG_{12}$-Ao can detect carbonylated proteins in polyacrylamide gels. a Schematic representation of the experimental setup for NCs migration in gels. **b** Four identical sets of samples were simultaneously migrated on native polyacrylamide gels with electricity direction from anode to cathode (gels 1 and 2) or from cathode to anode (gels 3 and 4). Gels 1 and 3 were dried and imaged by a fluorescence imaging scanner. Gels 2 and 4 were stained using Coomassie staining and images were obtained using a gel scanner. The displayed images are representative of three replicates. Source data and replicates for (**b**) are provided in Supplementary Data 1 Figs. S5-7.

detection of the protein–NC complexes in polyacrylamide gels. As the NCs are sensitive to detergents and can react with free thiols commonly present in the buffers used in sodium-dodecyl sulfate polyacrylamide gel electrophoresis (SDS-PAGE), native PAGE was applied in these experiments. As the first step, individual migration properties were determined for the NC and for the oxidized lysozyme during native PAGE. To that end, we applied PAGE both with the conventional (migration direction from anode to cathode) and with the inverted polarity (migration direction from cathode to anode) (Fig. 3a, Supplementary Fig. S4 and Supplementary Data 1 Fig. S13). Visualization of the NC in the gels was achieved using fluorescence imaging, whereas the

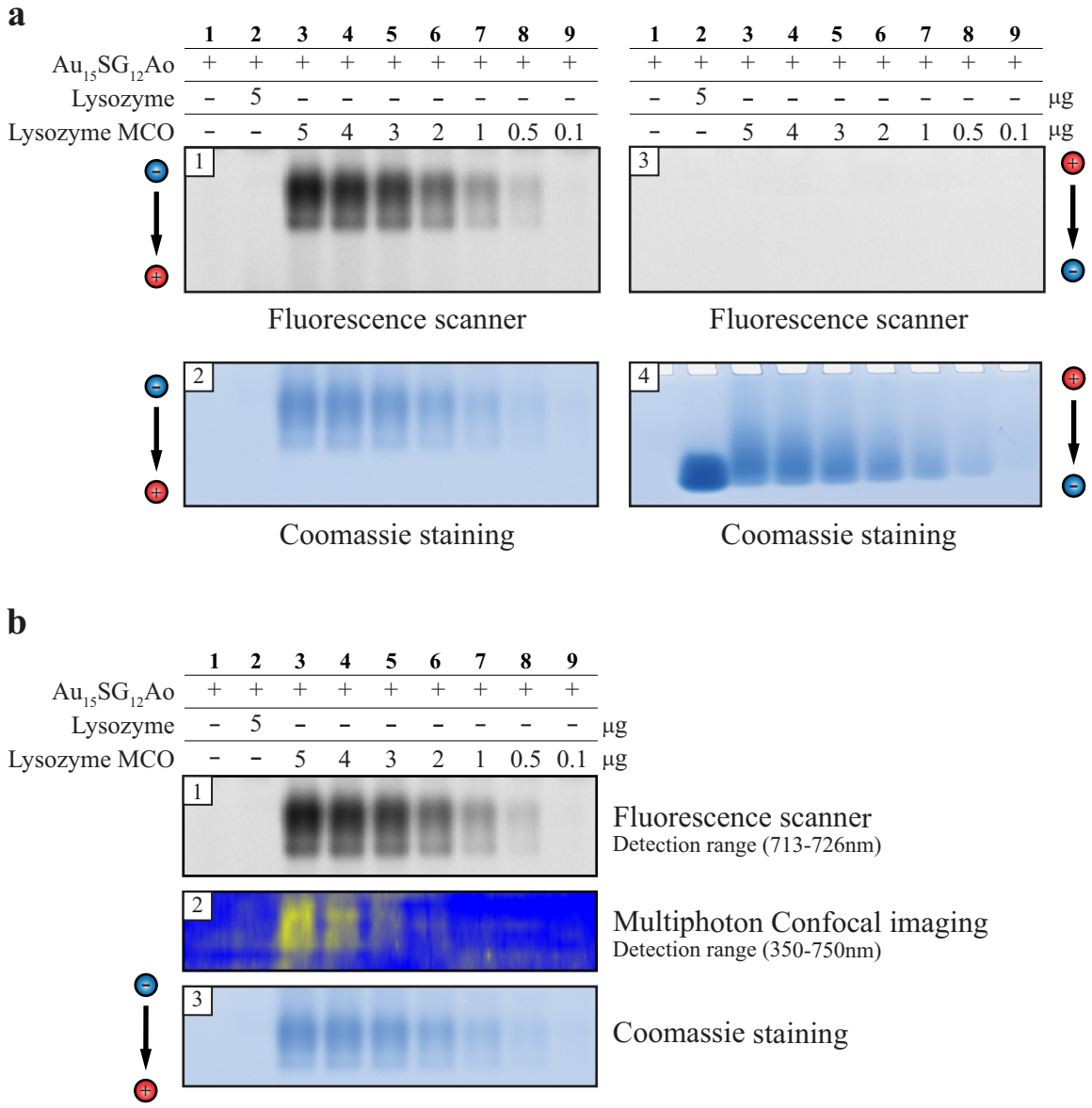

Fig. 4 $Au_{15}SG_{12}$-Ao in-gel signal responds to the lysozyme quantity. a The in-gel signal of $Au_{15}SG_{12}$-Ao decreases with the lowering of the oxidized lysozyme amounts. Gels 1 and 3 were dried and imaged using a fluorescence scanner. Gels 2 and 4 were stained using Coomassie staining and images were obtained using a gel scanner. The displayed images are representative of three replicates. **b** Comparison of $Au_{15}SG_{12}$-Ao for detection of carbonylated proteins in gels by one-photon excited fluorescence scanner and multiphotonic (two-photon excited fluorescence) confocal imaging. The displayed images are representative of three replicates. Source data and replicates for (**a**) are provided in Supplementary Data 1 Figs. S9–11 and source data for (**b**) is provided in Supplementary Data 1 Fig. S12.

proteins were visualized using Coomassie staining. Interestingly, NC and the lysozyme displayed opposing migration properties: while NC was detectable in the gel exposed to the conventional polarity, the lysozyme (both oxidized and non-oxidized) that has isoelectric point of 11.35 under given conditions migrated into the gel only upon inversion of the polarity (Supplementary Fig. S4). Hence, we subjected a mixture of $Au_{15}SG_{12}$-Ao with the oxidized lysozyme along with corresponding controls to native PAGE (Fig. 3b and Supplementary Data 1 Figs. S5-7), expecting to detect the stable complex formed between the protein and the NC in one of the two gels. Indeed, we observed co-migration of the $Au_{15}SG_{12}$-Ao and the oxidized protein, which was consistent with our result that NCs are grafted on the carbonylated sites of the protein (Fig. 3b, gels 1 and 2, lane 8). The complex was globally negatively charged since it migrated from anode to cathode (Fig. 3b, gels 1 and 2) and no fluorescence was observed in the gel upon migration from cathode to anode (Fig. 3b, gels 3 and 4). Furthermore, there was no detectable complex of $Au_{15}SG_{12}$-Ao with the non-oxidized protein (Fig. 3b, gels 1 and 2, lane 7), indicating that there were no unspecific, carbonyl-unrelated interactions between the protein and the NC. Importantly, little to no fluorescence was observed upon native PAGE of the $Au_{15}SG_{13}$ - oxidized lysozyme mixture (Fig. 3b, lane 5), further supporting the absence of unspecific interactions between the NC and the protein (Table 1).

We next evaluated the potential of the NC for quantitative analysis of protein carbonyls. Fixed concentration of 500 µM $Au_{15}SG_{12}$-Ao was incubated with a decreasing range of concentrations of the lysozyme (50–1 µM corresponding to 5–0.1 µg protein loaded in the gel) and the reaction products were migrated on native PAGE (Fig. 4a and Supplementary Data 1 Figs. S9–11). An obvious decrease in the fluorescent signal

corresponding to NC correlated with decreasing amounts of oxidized lysozyme, indicating that NC-based assays can be developed for quantifying the amount of carbonyls on a protein. Finally, we tested the applicability of NCs in protein carbonylation detection in polyacrylamide gels using biphotonic confocal microscopy and observed an intense two-photon excited fluorescent signal for higher protein quantities (Fig. 4b and Supplementary Data 1 Fig. S12).

Together, these data establish a novel NC, $Au_{15}SG_{12}$-Ao, as suitable for specific detection of protein carbonyls by PAGE while offering photostability and biocompatible optical properties.

Discussion

Herein, we conducted a proof of concept study for developing the first NC-based imaging system for protein carbonylation detection. To that end, we synthesized an NC with protein carbonyl-binding properties and demonstrated the ability of such NC to detect carbonylation of an oxidized model protein in gel-based analyses by one-photon fluorescence imaging and by two-photon excited fluorescence confocal imaging.

Furthermore, we have developed a protocol for an easy synthesis of atomically precise Au_{15} NCs and for their functionalization with a thiolated Ao probe via simple ligand exchange. These NCs were highly reactive towards protein carbonyls and they formed a stable oxime bond between the aminooxy on the NC and the natural or oxidation-induced carbonyls on leupeptin and on lysozyme, respectively. Molecular modeling was conducted to evaluate the exposure of such oxime bond to solvents. This approach evidenced the protective effect on the oxime bond of glutathione ligands surrounding the thiolated Ao thus demonstrating the robustness of the linkage between the NC and carbonylated proteins. This protective effect of glutathione clearly adds value to the NC-based as compared to dye-based approaches for labeling carbonyls.

We also demonstrated that the functionalized NCs can act as one- and two-photon excitation fluorescence contrast agents for the detection of protein carbonyls in polyacrylamide gels. Importantly, we were able to detect NC-oxidized protein complexes by multiphoton microscopy, where both the excitation wavelength (~800 nm) and the detection of TPEF photons (up to 750 nm) can be in the NIR range. If applied in vivo, this strategy could offer definitive advantages over visible-range fluorescence, particularly the lack of interfering autofluorescence typical for biological molecules. Another advantage of using metal NCs as opposed to commonly used dyes is that they are biocompatible, soluble, photostable and likely to pass through the cellular membranes due to their small size. The noble AuNCs composed of a small number of atoms stabilized by a peptide ligand might thus be further developed as agents for the detection of carbonyls within cells and tissues.

Features of the NCs that give them tremendous potential for exploitation are their modular nature and versatility. These features provide room for improvement and opportunities for adaptation of the NCs for various purposes by optimization of their size and by the choice of ligands. In this proof-of-concept study, we have observed a correlation between the NC fluorescence and the amount of protein carbonyls, uncovering the potential of the NC for quantitative analyses. This NC could thus be further refined to gain higher sensitivity and to provide highly quantitative data. Moreover, to the best of our knowledge, this is the first study where the nonlinear optical properties of NC have been used to detect a post-translational modification on a protein. Given the extreme importance of post-translational modifications in life sciences, this pioneering study could lead to many alternative applications of the NCs.

In addition to the presented results, significant future applications of AuNCs may be in imaging of carbonylated proteins in fixed or live cells, allowing for quantification, as well as localization and transport studies of carbonylated proteins. Such studies advance understanding of the role of protein carbonylation in aging and ARDs.

Methods

$Au_{15}SG_{13}$ NCs synthesis. Approximately, 235 mg of L-Glutathione (GSH) was dissolved under stirring conditions (at 45 °C) in 35 mL of methanol. 4 mL tributylamine was added to this mixture, which led to solubilization of GSH in methanol. This clear solution was further supplied with ~100 mg of $HAuCl_4.3H_2O$ previously dissolved in 4 mL water. The resulting solution was stirred for 5 min and further supplied with ~50 mg of trimethylamine borane ($TMA\text{-}BH_3$) after 2 h of stirring under 45–50 °C. The resulting solution was then stirred overnight at room temperature. After 24 h of stirring, the solution acquired a yellow color, and 1 mL NH_4OH was added to induce precipitation. The resulting dispersion was centrifuged at 6000 rpm for 3–4 min. The supernatant was discarded and the pellet was redispersed in minimum water. The solution was supplied with methanol to induced further precipitation. The dispersion was centrifuged again at 6000 rpm for 3-4 min and the so obtained pellet was dissolved in 10 mL water and 2 mL of glacial acetic acid. The solution was left unperturbed for 4 h (minimum). This led to the precipitation of Au_{10} NCs. The pellet was discarded and the supernatant was re-supplied with methanol to induce further precipitation. Following another cycle of precipitation, the pellet was dispersed in methanol and diethyl ether and dried overnight under vacuum.

$Au_{15}SG_{12}$-Ao preparation. $Au_{15}SG_{13}$ NCs were post functionalized via ligand-exchange reaction with aminooxypropanethiol as functional ligand using two methods. $Au_{15}SG_{13}$ was used as mother solution for both methods. In the method 1, a solution of Aminooxy corresponding to the desired quantities (0.1 to 1 equivalent relative to $Au_{15}SG_{13}$) was added to a water solution of $Au_{15}SG_{13}$ (1 mg/ml, pH ~ 8.5). The obtained solution was stirried at room temperature for 3 h (method 1). For method 2, the same protocol is used, except that aminooxy is added fractionally (0.1 equivalent of Aminooxy every 30 min) at ambient temperature or at 45 °C. It is worth mentioning that the products with varying numbers of aminooxypropanethiol could not be separated further. Instead, to purify the mixture of products from other NCs comprising of varying numbers of gold atoms, the product was precipitated with methanol/acetic acid solution.

Oxidation protocols. For metal-catalyzed oxidation (MCO), the protocol was based on Maisonneuve et al.[45]. Lysozyme from chicken egg white (Sigma) was dissolved in phosphate-buffered saline 1×, pH 7.4 (PBS–Roth) at 5 mg/ml. Oxidation was performed by supplementing 300 µL of protein solution (1.5 mg) with a freshly prepared mixture of ascorbic acid/$FeCl_3$ (Sigma/Kemika) with final concentrations of 25 mM/100 µM. 3 h incubation at RT was performed in a thermomixer at 500 rpm. Oxidation was stopped by the addition of 1 mM EDTA (Fluka) and cooling in ice.

Carbonyl detection by Western Blotting. For the Western Blot, carbonyls were derivatized with 10 mM EZ-Link™ Alkoxyamine-PEG4-Biotin (Thermofisher) for 3H at RT. Samples were subjected to gel electrophoresis using the Mini-Protean® Tetra Cell system (Bio-Rad). Gels were cast homemade using Acrylamide/bisacrylamide (Fisher Bioreagent), APS (Biosolve), TEMED (Sigma) and Tris-glycine buffer. Linear gels (20%) were cast and used for sample migration. Proteins were then transferred to a PVDF membrane the Trans-Blot Turbo Transfer System (BioRad) with 25 V constant (up to 1.0 A) for 30 min. Membranes were stained with Red Ponceau dye (Sigma) to assess transfer efficiency and total protein loading. Membranes were then blocked with TBS-Tween 0.05%–Milk 5% buffer for 30 min at room temperature with shaking. Next, membranes were incubated for 1h at RT with Streptavidin-Alexa Fluor 700 (Invitrogen) probes resuspended. At every step after blocking, membranes were washed 4 times 5 min with TBS-Tween 0.05%. Finally, Typhoon™ FLA 9500 biomolecular imager (GE Healthcare) was used to measure fluorescence. Experiments were performed in triplicates. All quantifications were performed using ImageLab software (Bio-rad) and the statistical analysis was performed in GraphPad Software.

MS proteomics. Sample preparation. Prior to LC-MS/MS analysis, the MCO protein was grafted with DNPH. Proteins samples were derivatized with 10 mM of DNPH (final concentration) at RT for 30 min with shaking (500 rpm). Neutralization of the reaction was done using 1 M Ammonium bicarbonate solution to reach pH 8.

Also, MCO protein grafted with the aminooxy NC was degraded with cysteine. 300 µL of 500 µg of MCO lysozyme labeled with an excess of $Au_{15}SG_{12}$-Ao were diluted in 700 µL of a 10 mM NaCl aqueous solution. Then, 200 µL of acetone was added to neutralize ungrafted aminooxy groups. Solution was left overnight before starting the NC degradation. For this, we used a large excess of cysteine by adding

100 µL of cysteine (10 mM). The solution was sonicated 45 min and 1 mL of methanol was added before another 45 min of sonication. Then, 50 µL of glacial acetic acid was added to complete precipitation of gold-cysteine polymer. The precipitate was removed by centrifugation (11000 rpm/10 min) and the supernatant was evaporated under vacuum. The lysozyme was redispersed in 0.5 mL of water before sample preparation for MS analysis (i.e. reduction, alkylation, and digestion).

Derivatized protein samples were then reduced in 8 M urea, 15 mM dithiothreitol (DTT) at 60 °C for 40 min, and then alkylated with 35 mM iodoacetamide (IAM) at room temperature in the dark for 40 min. To reduce the urea concentration, the samples were diluted 5-fold with ammonium bicarbonate (AMBIC) before overnight digestion at 37 °C with trypsin (type IX-S from Porcine Pancreas) using a 1:30 (w/w) enzyme to substrate ratio. Digestion was stopped by the addition of formic acid (FA) to a final concentration of 0.5%.

All samples were desalted and concentrated using Oasis HLB 3cc (60 mg) reversed-phase cartridges (Waters, Milford, MA, USA) (elution with 1.5 mL of methanol containing 0.5% FA). All samples were evaporated to dryness and resuspended in 150 µL of water/acetonitrile (ACN) (90:10, v/v) containing 0.5% FA. All solutions were stored at −18 °C before use.

MS Proteomics. Instrumentation and Operating Conditions. Mass spectrometry analyses were performed on a hybrid quadrupole-orbitrap Q-Exactive® mass spectrometer (Thermo Fisher Scientific, San Jose, CA, USA) equipped with a HESI ion source coupled to a Surveyor HPLC-MS pump (Thermo Fisher Scientific, San Jose, CA, USA) and a PAL Auto-sampler (CTC Analytics, Switzerland).

The HPLC separation was carried out on an XBridge C18 column (100 × 2.1 mm, 3.5 µm) from Waters. The HPLC mobile phase consisted of water containing formic acid 0.1% (v/v) as eluent A, and ACN containing formic acid 0.1% (v/v) as eluent B. Elution was performed at a flow rate of 300 µL/min. The elution sequence, for the digested protein samples, included a linear gradient from 10% to 60% of eluent B for 52 min, then a plateau at 95 % of eluent B for 4 min. The gradient was returned to the initial conditions and held there for 4 min. The injection volume was 10 µL.

Ionization was achieved using electrospray in the positive ionization mode with an ion spray voltage of 4 kV. The sheath gas and the auxiliary gas (nitrogen) flow rates were respectively set at 35 and 10 (arbitrary unit) with a HESI vaporizer temperature of 400 °C. The ion transfer capillary temperature was 300 °C with a sweep gas (nitrogen) flow rate at 5 (arbitrary unit). The S-lens RF was set at 90 (arbitrary unit). The Automatic Gain Control (AGC) target was 3×10^6 and the maximum injection time was set at 250 ms. Experiments were done in data-dependent top 10 modes. The full MS scans were done over an *m/z* 300-1500 range with a resolution of 35000. For the data-dependent MS/MS scans, the resolution was set at 17500, isolation 2 *m/z*, with a normalized collision energy of 28 (arbitrary unit). To exclude the redundant processing of dominant ions and allow selection of low abundant oxidized peptides, a dynamic exclusion time of 20 s was set.

MS proteomics. Peptide and protein identification and quantification. Fragmentation data were converted to peak lists using PAVA RawRead and searched against sequences of Gallus Gallus (Chicken) proteins contained in the Swissprot human database (downloaded 2017.11.01, 556006 entries) using Protein Prospector[46]. All searches used the following parameters: mass tolerances in MS and MS/MS modes were 20 ppm and 0.2 Daltons, respectively. Trypsin was designated as the enzyme and up to two missed cleavages were allowed. Carbamidomethylation of cysteine residues was designated as a fixed modification. The considered standard variable modifications were N-terminal acetylation, N-terminal glutamine conversion to pyroglutamate and methionine oxidation. The maximum allowed expected value was set at up to 0.01 (protein) and 0.05 (peptide). To search for oxidized peptides, user-defined variable modifications, corresponding to a list of 43 known carbonyl modifications from the literature[9,42] derivatized with DNP (Oxi-DNP) or after degradation of the $Au_{15}SG_{12}$-Ao NC (Ao-C3-thiol-IAM), were implemented. All peptides identified in a top10 analysis have been quantified by using the MS1 filtering tool in Skyline. The peptides have been integrated allowing a match tolerance of 0.055 *m/z* and a minimum isotope dot product of 0.9. All integrations have been verified manually and the total area of each peptide has been reported for the most intense charge states.

Experimental setup for protein carbonyls detection with NCs in 1D gel electrophoresis. After oxidation of the recombinant protein with MCO protocol as described previously, recombinant protein and NCs were resuspended in PBS 1X and were incubated at a final concentration of 50 µM (Fig. 3 and Fig. 4) and 500 µM, respectively, at 10°C overnight in a rotating shaker. The concentration of protein and NCs were modified to 137 µM and 50 µM respectively for multiphoton confocal imaging. Samples were then supplemented with 10% glycerol, loaded in 15% or 20% homemade Tris-Glycine gels, and migrated with Tris-glycine buffer 1× (25–192 mM). Migration polarity was done as indicated in the figures. Before drying, gels were equilibrated in a 20% ethanol/5% glycerol solution for 20 min and then placed in a drying frame (Serva) for a minimum of 48 h. Typhoon™ FLA 9500 biomolecular imager (GE Healthcare) was used to detect fluorescence of these gels as described below. Protein staining in the gel was performed using a Coomassie staining solution (Ammonium sulfate 10%–phosphoric acid 10%–Coomassie G250 0.12% and ethanol 20%) overnight with shaking at room temperature followed by destaining with distilled H_2O. Gels were scanned with the BIO-5000 Plus VIS Gel Scanner from Serva. All experiments were performed in triplicate.

One-photon fluorescence setup. One-photon fluorescence measurements were performed with Typhoon™ FLA 9500 biomolecular imager using a 473 nm (blue LD laser—for NCs detection) or a 685 nm laser (Red LD laser—for AlexaFluor700 detection) for excitation and a BPFR700 (R715) filter to collect the emitted fluorescence in the wavelength range from 713 nm to 726 nm.

Two-photon fluorescence setup. Two-photon fluorescence measurements were performed with a customized confocal microscope (TE2000-U, Nikon Inc.) in which the excitation light entrance has been modified to allow free-space laser beam input, instead of the original optical-fiber light input. The luminescence was excited at 780 nm with a mode-locked frequency-doubled femtosecond Er-doped fiber laser (C-Fiber 780, MenloSystems GmbH). The laser spectrum was bounded by two filters (FELH0750 and FESH0800, Thorlabs Inc.). The output power of the femtosecond laser was 62 mW. The laser beam was focused by a Nikon Plan Fluor Ph1 DLL objective (10×/0.30 NA). The sample was XY scanned by the inner microscope motorized stage and galvanoscanner (confocal C1 head, Nikon Inc.), and the Z scan was performed by the inner microscope motorized focus. The emitted signal was collected in epifluorescence illumination mode. The two-photon fluorescence emission was separated from the incident light through a dichroic mirror (NFD01-785, IDEX Health & Science LLC). A FESH0750 filter was used in order to remove the photons coming from the excitation laser and collect visible 350-750 nm fluorescence on the inner microscope photomultiplier tube. TPEF intensity raster scans performed at several Z positions of the gel (size of the gel image: 60 × 48 mm). Time per each point (0.25 mm×1 mm): (61 µs × 2 × 128 × 128 for averaging).

Computational. In order to determine the structural properties of $Au_{15}SG_{12}$-Ao liganded cluster and protein-liganded cluster the following procedures have been used. First, QM/MM method within ONIOM two layer[47–49] approach implemented in Gaussian[50] has been employed for $Au_{15}SG_{12}$-Ao liganded cluster. Au_{15}, sulfur atoms and 3-(Aminooxy)-1-propanethiol have been included in QM. For the gold atoms the 19-e^- relativistic effective core potential (19-e^- RECP) from the Stuttgart group[51] taking into account scalar relativistic effects has been used. For atoms within QM, split valence polarization atomic basis sets (SVP)[52] and the hybrid B3LYP functional[53–56] have been employed. In MM part UFF force field[57] has been employed for all ligands, with exception of 3-(Aminooxy)-1-propanethiol. In order to analyze the hydrogen bonding network the obtained ONIOM two layer B3LYP/UFF structures have been reoptimized using SEQM PM7[58] where gold and sulfur atoms have been frozen. Notice that Au-Au distances are overestimated within PM7 approach[59]. Two isomers of $Au_{15}SG_{12}$-Ao have been obtained using PM7 and single point DFT (B3LYP) calculations as shown in Supplementary Fig S2g. The structure in Fig. 2d including Lysozyme has been obtained by QM/MM approach. QM part is treated by PM7 and describes interface between liganded cluster and protein. It contains Au_{15}, sulfur atoms from glutathiones and Ao-Serine bond. The other ligands and the rest of the protein have been included in MM where UFF force field was employed. In order to simulate penetration of water molecules into $Au_{15}SG_{12}$-Ao-Lysozyme 800 neutral H_2O molecules have been added to MM part within QM/MM approach for the optimization of geometry. In addition, distances from Ao-Serine100 bond to each water molecule were taken into account in order to obtain the radial distribution of the density of water molecules using R-studio software[60] (cf Supplementary Fig. S3f).

Data availability

Data available on request from the authors.

Received: 27 November 2020; Accepted: 2 March 2021;
Published online: 14 May 2021

References

1. Krisko, A. & Radman, M. Protein damage, ageing and age-related diseases. *Open Biol.* **9**, 12 (2019).
2. Reeg, S. & Grune, T. Protein oxidation in aging: does it play a role in aging progression? *Antioxid. Redox Signal.* **23**, 239–255 (2015).
3. Havelund, J. F. et al. A biotin enrichment strategy identifies novel carbonylated amino acids in proteins from human plasma. *J. Proteom.* **156**, 40–51 (2017).
4. Baraibar, M. A., Ladouce, R. & Friguet, B. Proteomic quantification and identification of carbonylated proteins upon oxidative stress and during cellular aging. *J. Proteom.* **92**, 63–70 (2013).

5. Hawkins, C. L. & Davies, M. J. Detection, identification, and quantification of oxidative protein modifications. *J. Biol. Chem.* **294**, 19683–19708 (2019).
6. Yan, L.-J. & Forster, M. J. Chemical probes for analysis of carbonylated proteins: a review. *J. Chromatogr. B* **879**, 1308–1315 (2011).
7. Levine, R. L., Williams, J. A., Stadtman, E. P. & Shacter, E. in *Methods in Enzymology* (ed. Packer, L.) Vol. 233, Ch 37, 346–357 (Academic Press, 1994).
8. Rogowska-Wrzesinska, A., Wojdyla, K., Nedić, O., Baron, C. P. & Griffiths, H. R. Analysis of protein carbonylation — pitfalls and promise in commonly used methods. *Free Radic. Res.* **48**, 1145–1162 (2014).
9. Bachi, A., Dalle-Donne, I. & Scaloni, A. Redox proteomics: chemical principles, methodological approaches and biological/biomedical promises. *Chem. Rev.* **113**, 596–698 (2013).
10. Tamarit, J. et al. Analysis of oxidative stress-induced protein carbonylation using fluorescent hydrazides. *J. Proteom.* **75**, 3778–3788 (2012).
11. Escobedo, J. O., Rusin, O., Lim, S. & Strongin, R. M. NIR dyes for bioimaging applications. *Curr. Opin. Chem. Biol.* **14**, 64–70 (2010).
12. Terenziani, F., Katan, C., Badaeva, E., Tretiak, S. & Blanchard-Desce, M. Enhanced two-photon absorption of organic chromophores: theoretical and experimental assessments. *Adv. Mater.* **20**, 4641–4678 (2008).
13. Bonačić-Koutecký, V. & Antoine, R. Enhanced two-photon absorption of ligated silver and gold nanoclusters: theoretical and experimental assessments. *Nanoscale* **11**, 12436–12448 (2019).
14. Pawlicki, M., Collins, H. A., Denning, R. G. & Anderson, H. L. Two-photon absorption and the design of two-photon dyes. *Angew. Chem. Int. Ed.* **48**, 3244–3266 (2009).
15. Chakraborty, I. & Pradeep, T. Atomically precise clusters of noble metals: emerging link between atoms and nanoparticles. *Chem. Rev.* **117**, 8208–8271 (2017).
16. Jin, R. Quantum sized, thiolate-protected gold nanoclusters. *Nanoscale* **2**, 343–362 (2010).
17. Jin, R., Zeng, C., Zhou, M. & Chen, Y. Atomically precise colloidal metal nanoclusters and nanoparticles: fundamentals and opportunities. *Chem. Rev.* **116**, 10346–10413 (2016).
18. Kang, X. & Zhu, M. Tailoring the photoluminescence of atomically precise nanoclusters. *Chem. Soc. Rev.* **48**, 2422–2457 (2019).
19. Li, Q. et al. Structural distortion and electron redistribution in dual-emitting gold nanoclusters. *Nat. Commun.* **11**, 2897 (2020).
20. Chen, P.-F. et al. Fluorescence depletion properties of insulin–gold nanoclusters. *Biomed. Opt. Express* **6**, 3066–3073 (2015).
21. Weng, B., Lu, K.-Q., Tang, Z., Chen, H. M. & Xu, Y.-J. Stabilizing ultrasmall Au clusters for enhanced photoredox catalysis. *Nat. Commun.* **9**, 1543 (2018).
22. Kaur, N., Aditya, R. N., Singh, A. & Kuo, T.-R. Biomedical applications for gold nanoclusters: recent developments and future perspectives. *Nanoscale Res. Lett.* **13**, 302 (2018).
23. Luo, Z., Zheng, K. & Xie, J. Engineering ultrasmall water-soluble gold and silver nanoclusters for biomedical applications. *Chem. Commun.* **50**, 5143–5155 (2014).
24. Porret, E., Le Guevel, X. & Coll, J. L. Gold nanoclusters for biomedical applications: toward in vivo studies. *J. Mat. Chem. B* **8**, 2216–2232 (2020).
25. Bai, Y. L., Shu, T., Su, L. & Zhang, X. J. Fluorescent gold nanoclusters for biosensor and bioimaging application. *Crystals* **10**, 12 (2020).
26. Chang, T.-K. et al. Metabolic mechanism investigation of antibacterial active cysteine-conjugated gold nanoclusters in Escherichia coli. *ACS Sustain. Chem. Eng.* **7**, 15479–15486 (2019).
27. Cheng, T.-M. et al. Quantitative Analysis of glucose metabolic cleavage in glucose transporters overexpressed cancer cells by target-specific fluorescent gold nanoclusters. *Anal. Chem.* **90**, 3974–3980 (2018).
28. Olesiak-Banska, J., Waszkielewicz, M., Obstarczyk, P. & Samoc, M. Two-photon absorption and photoluminescence of colloidal gold nanoparticles and nanoclusters. *Chem. Soc. Rev.* **48**, 4087–4117 (2019).
29. Antoine, R. & Bonačić-Koutecký, V. *Liganded Silver and gold Quantum Clusters. Towards a New Class of Nonlinear Optical Nanomaterials* (Springer, 2018).
30. Polavarapu, L., Manna, M. & Xu, Q.-H. Biocompatible glutathione capped gold clusters as one- and two-photon excitation fluorescence contrast agents for live cells imaging. *Nanoscale* **3**, 429–434 (2011).
31. Brach, K., Waszkielewicz, M., Olesiak-Banska, J., Samoc, M. & Matczyszyn, K. Two-photon imaging of 3D organization of bimetallic AuAg nanoclusters in DNA matrix. *Langmuir* **33**, 8993–8999 (2017).
32. Bertorelle, F. et al. Bulky counterions: enhancing the two-photon excited fluorescence of gold nanoclusters. *ChemPhysChem* **19**, 165–168 (2018).
33. Templeton, A. C., Wuelfing, W. P. & Murray, R. W. Monolayer-protected cluster molecules. *Acc. Chem. Res.* **33**, 27–36 (2000).
34. Cao, Y. et al. Control of single-ligand chemistry on thiolated Au25 nanoclusters. *Nat. Commun.* **11**, 5498 (2020).
35. Negishi, Y., Nobusada, K. & Tsukuda, T. Glutathione-protected gold clusters revisited: bridging the gap between gold(I)–thiolate complexes and thiolate-protected gold nanocrystals. *J. Am. Chem. Soc.* **127**, 5261–5270 (2005).
36. Kalia, J. & Raines, R. T. Hydrolytic stability of hydrazones and oximes. *Angew. Chem. Int. Ed.* **47**, 7523–7526 (2008).
37. Kölmel, D. K. & Kool, E. T. Oximes and hydrazones in bioconjugation: mechanism and catalysis. *Chem. Rev.* **117**, 10358–10376 (2017).
38. Jiang, D.-e, Overbury, S. H. & Dai, S. Structure of Au15(SR)13 and Its Implication for the origin of the nucleus in thiolated gold nanoclusters. *J. Am. Chem. Soc.* **135**, 8786–8789 (2013).
39. Tlahuice-Flores, A., Jose-Yacamán, M. & Whetten, R. L. On the structure of the thiolated Au15 cluster. *Phys. Chem. Chem. Phys.* **15**, 19557–19560 (2013).
40. Girod, M. et al. Structural basis of protein oxidation resistance: a lysozyme study. *PLoS ONE* **9**, 12 (2014).
41. Augustyniak, E. et al. Validation of protein carbonyl measurement: a multi-centre study. *Redox Biol.* **4**, 149–157 (2015).
42. Rykær, M., Svensson, B., Davies, M. J. & Hägglund, P. Unrestricted mass spectrometric data analysis for identification, localization, and quantification of oxidative protein modifications. *J. Proteome Res.* **16**, 3978–3988 (2017).
43. Chand Bollineni, R., Fedorova, M. & Hoffmann, R. Qualitative and quantitative evaluation of derivatization reagents for different types of protein-bound carbonyl groups. *Analyst* **138**, 5081–5088 (2013).
44. Weiss, M. S., Palm, G. J. & Hilgenfeld, R. Crystallization, structure solution and refinement of hen egg-white lysozyme at pH 8.0 in the presence of MPD. *Acta Crystallogr. D* **56**, 952–958 (2000).
45. Maisonneuve, E. et al. Rules governing selective protein carbonylation. *PLoS ONE* **4**, e7269 (2009).
46. Chalkley, R. J., Baker, P. R., Medzihradszky, K. F., Lynn, A. J. & Burlingame, A. L. In-depth analysis of tandem mass spectrometry data from disparate instrument types. *Mol. Cell Proteom.* **7**, 2386–2398 (2008).
47. Svensson, M. et al. ONIOM: a multilayered integrated MO + MM method for geometry optimizations and single point energy predictions. A test for diels −alder reactions and Pt(P(t-Bu)3)2 + H2 oxidative addition. *J. Phys. Chem.* **100**, 19357–19363 (1996).
48. Lundberg, M., Kawatsu, T., Vreven, T., Frisch, M. J. & Morokuma, K. Transition states in a protein environment—ONIOM QM:MM modeling of isopenicillin N synthesis. *J. Chem. Theory Comput.* **5**, 222–234 (2009).
49. Dapprich, S., Komáromi, I., Byun, K. S., Morokuma, K. & Frisch, M. J. A new ONIOM implementation in Gaussian98. Part I. The calculation of energies, gradients, vibrational frequencies and electric field derivatives1Dedicated to Professor Keiji Morokuma in celebration of his 65th birthday.1. *J. Mol. Structure: THEOCHEM* **461-462**, 1–21 (1999).
50. Frisch, G. *Gaussian 16 Rev. C.01* (Gaussian Inc., 2016).
51. Andrae, D., Haeussermann, U., Dolg, M., Stoll, H. & Preuss, H. Energy-adjusted ab initio pseudopotentials for the second and third row transition elements. *Theor. Chim. Acta* **77**, 123 (1990).
52. Weigend, F. & Ahlrichs, R. Balanced basis sets of split valence, triple zeta valence and quadruple zeta valence quality for H to Rn: design and assessment of accuracy. *Phys. Chem. Chem. Phys.* **7**, 3297–3305 (2005).
53. Becke, A. D. A new mixing of Hartree-Fock and local density-functional theories. *J. Chem. Phys.* **98**, 1372–1377 (1993).
54. Lee, C. T., Yang, W. T. & Parr, R. G. Development of the Colle-Salvetti correlation-energy formula into a functional of the electron density. *Phys. Rev. B* **37**, 789 (1988).
55. Vosko, S. H., Wilk, L. & Nusair, M. Accurate spin-dependent electron liquid correlation energies for local spin density calculations: a critical analysis. *Can. J. Phys.* **58**, 1200–1211 (1980).
56. Stephens, P. J., Devlin, F. J., Chabalowski, C. F. & Frisch, M. J. Ab initio calculation of vibrational absorption and circular dichroism spectra using density functional force fields. *J. Phys. Chem.* **98**, 11623–11627 (1994).
57. Rappe, A. K., Casewit, C. J., Colwell, K. S., Goddard, W. A. & Skiff, W. M. UFF, a full periodic table force field for molecular mechanics and molecular dynamics simulations. *J. Am. Chem. Soc.* **114**, 10024–10035 (1992).
58. Stewart, J. J. P. Optimization of parameters for semiempirical methods VI: more modifications to the NDDO approximations and re-optimization of parameters. *J. Mol. Modeling* **19**, 1–32 (2013).
59. Mato, J. & Guidez, E. B. Accuracy of the PM6 and PM7 methods on bare and thiolate-protected gold nanoclusters. *J. Phys. Chem. A* **124**, 2601–2615 (2020).
60. RStudio Team. *RStudio: Integrated Development for R. RStudio* (PBC, 2020). http://www.rstudio.com/.

Acknowledgements

This research was supported by the project STIM-REI, Contract Number: KK.01.1.1.01.0003, funded by the European Union through the European Regional Development Fund—the Operational Programme Competitiveness and Cohesion 2014–2020 (KK.01.1.1.01). V.B.K., M.P.B., and H.F. acknowledge computational facilities of the HPC computer within the STIM-REI project, Doctoral study of Biophysics at University of Split as well as Prof. Miroslav Radman at MedILS and Split-Dalmatia County for support. M.G. acknowledge the French National Research Agency for the financial support (Grant Agreement ANR-18-CE29-0002-01 HyLOxi). We would also

like to acknowledge the financial support received from the French-Croatian project "International Laboratory for Nano Clusters and Biological Aging, LIA NCBA". The authors would like to thank Céline Brunon and Esther Jarrossay from Science et Surface (www.science-et-surface.fr) for XPS and FTIR spectra.

Author contributions

R.A., V.B.-K., M.R., and A.K. conceived the initial idea and coordinated the work. F.B. synthesized and prepared the NCs, assisted with S.B. H.F. recorded and analyzed mass spectra. C.M. conducted nonlinear optics imaging, supervised by P.-F.B. and I.R.-A. M.P.B., Z.S.M., and V.B.-K. performed and analyzed the theoretical results. M.G. conducted proteomics-based MS protocols, measurements and analysis. G.F.C. developed gel strategies, assisted with R.L. and performed fluorescence measurements supervised by K.T. R.A., P.D., M.R., and V.B.-K. supervised and financed the project. R.A., G.F.C., K.T., and V.B.-K. wrote the paper. All authors provided critical feedback and helped to shape the final manuscript.

Competing interests

The authors declare no competing interests

Additional information

Supplementary information The online version contains supplementary material available at https://doi.org/10.1038/s42004-021-00497-z.

Correspondence and requests for materials should be addressed to V.B.-K. or R.A.

Chapter 4

Conclusions and Future Aspects: Towards Unique Applications of Noble Metal Nanoclusters in Biosensorics

Theoretical study of optical properties of thiolated noble metal clusters and bio-nano hybrids conducted in this doctoral thesis provided insight into the origin of optical properties of various systems explored. New theoretical-experimental strategies were introduced for improving the structural and optical properties of bio-nano hybrid systems for the application in medical diagnostics and biosensorics.

In summary, exploration of two research paths; i) noble metal bio-nano hybrids and ii) thiolated noble metal nanoclusters, resulted in an overview of optical properties of the various systems: from silver trimer intercalated in DNA through powerful Wan der Waals noncovalent bonding and silver doped gold-cysteine supramolecular assemblies to remarkable noble metal thiolated gold nanoclusters and their ability to be functionalized for specific detection.

DNA molecule was presented as a unique example of silver trimer protection "shell" with a wide range of application possibilities. Depending on the nucleotide bases surrounding the nanocluster, large transition-dipole moments are induced, necessary for the enhancement of TPA cross-sections. Large TPA cross-sections occurred around 530 nm for the Ag_3^+ and (GCGC) nucleotide bases interaction. Since the infrared regime is important for deep tissue penetration, TPA cross-sections of modest 10 GM are obtained which can also benefit to deep tissue penetration.

The doping strategy was incorporated both for bio-nano hybrids of supramolecular gold-

cysteine assemblies and thiolated gold catenane nanoclusters resulting in altering the optical properties, particularly nonlinear TPA spectra. Changing the ligand shell content towards a ratio with more zwitterionic ligands for $Au_{12}Zw_4$ nanocluster resulted in large transition-dipole moments as well as large TPA cross-sections owning to rigidification effect.

The important research contribution of this thesis is to further stimulate theoretical and experimental research towards developing tools for early cancer diagnostics, as well as towards medical diagnostics in general applications. Atomically precise thiolated noble metal nanoclusters and bio-nano hybrids are an interesting class of nanomaterials with remarkable features such as low toxicity, good biocompatibility, and suitable for specific functionalization aiming toward tumor biomarker recognition. Their optical properties, particularly nonlinear, enabled the first time labeling and visualizing nanocluster-tumor biomarkers. Additionally, recent advances in the molecular diagnostics of cancer with focus on liganded noble metal nanoclusters are presented in Appendix B [73].

This doctoral thesis illuminated the enormous potential of noble metal liganded nanoclusters and bio-nano hybrids in medical diagnostics and sparked new experimental and theoretical research ahead. With this being stated, it is safe to stay that there is indeed plenty of room at the bottom. In closing, further exploration of the design of new nanostructured materials will expand more due to the properties of these systems that take their roles in numerous applications such as catalysis, biosensing, bioimaging, and materials science in general. New and improved characterization tools will be required as well as an improved theoretical approach that already needs adjustment and improvement for the exploration of large systems measured experimentally. A bright future looms on the horizon of technology at the nanoscale; a regime where each atom counts.

Appendices

Appendix A

Catenane Structures of Homoleptic Thioglycolic Acid-Protected Gold Nanoclusters

Reproduced from:

Clothilde Comby-Zerbino, Martina Perić, Franck Bertorelle, Fabien Chirot, Philippe Dugourd, Vlasta Bonačić-Koutecký and Rodolphe Antoine, "Catenane Structures of Homoleptic Thioglycolic Acid-Protected Gold Nanoclusters Evidenced by Ion Mobility-Mass Spectrometry and DFT Calculations", *Nanomaterials*, **2019**, 9, 3, 457

nanomaterials

MDPI

Article

Catenane Structures of Homoleptic Thioglycolic Acid-Protected Gold Nanoclusters Evidenced by Ion Mobility-Mass Spectrometry and DFT Calculations

Clothilde Comby-Zerbino [1], Martina Perić [2], Franck Bertorelle [1], Fabien Chirot [3], Philippe Dugourd [1], Vlasta Bonačić-Koutecký [2,4] and Rodolphe Antoine [1,*]

1 Institut Lumière Matière UMR 5306, Université Claude Bernard Lyon 1, CNRS, Univ Lyon, F-69100 Villeurbanne, France; clothilde.zerbino@univ-lyon1.fr (C.C.-Z.); franck.bertorelle@univ-lyon1.fr (F.B.); philippe.dugourd@univ-lyon1.fr (P.D.)
2 Center of Excellence for Science and Technology-Integration of Mediterranean region (STIM) at Interdisciplinary Center for Advanced Sciences and Technology (ICAST), University of Split, Poljička cesta 35, HR-21000 Split, Croatia; martina@stim.unist.hr (M.P.); vbk@stim.unist.hr (V.B.-K.)
3 Institut des Sciences Analytiques UMR 5280, Université Claude Bernard Lyon 1, ENS de Lyon, CNRS, Univ Lyon, 5 rue de la Doua, F-69100 Villeurbanne, France; fabien.chirot@univ-lyon1.fr
4 Department of Chemistry, Humboldt Universitat zu Berlin, Brook-Taylor-Strasse 2, 12489 Berlin, Germany
* Correspondence: rodolphe.antoine@univ-lyon1.fr; Tel.: +33-472-43-1085

Received: 21 February 2019; Accepted: 16 March 2019; Published: 19 March 2019

Abstract: Thiolate-protected metal nanoclusters have highly size- and structure-dependent physicochemical properties and are a promising class of nanomaterials. As a consequence, for the rationalization of their synthesis and for the design of new clusters with tailored properties, a precise characterization of their composition and structure at the atomic level is required. We report a combined ion mobility-mass spectrometry approach with density functional theory (DFT) calculations for determination of the structural and optical properties of ultra-small gold nanoclusters protected by thioglycolic acid (TGA) as ligand molecules, $Au_{10}(TGA)_{10}$. Collision cross-section (CCS) measurements are reported for two charge states. DFT optimized geometrical structures are used to compute CCSs. The comparison of the experimentally- and theoretically-determined CCSs allows concluding that such nanoclusters have catenane structures.

Keywords: gold nanoclusters; thiolate; catenane; ion mobility; DFT calculations

1. Introduction

Thiolate-protected metal nanoclusters (NCs) are a promising class of nanomaterials due to fascinating molecular-like properties along with well-defined molecular structures [1–3]. However, their physicochemical properties are highly size- and structure-dependent. As a consequence, for the rationalization of their synthesis and for the design of new clusters with tailored properties, a precise characterization of their composition and structure at the atomic level is required.

The structural features of stoichiometric $Au_n(SR)_n$ gold nanoclusters (SR:thiolate ligand) was predicted to change from single rings to interlocked ring motifs (i.e., catenane structures) when $n \geq 10$ [4]. The interlocked ring motif is a unique feature of homoleptic $[Au(I)\text{-}SR]_x$ complexes found in $Au_{10}(SR)_{10}$, $Au_{11}(SR)_{11}$, and $Au_{12}(SR)_{12}$ [5–7]. More importantly, the catenane-like staple motifs predicted for $Au_{15}(SR)_{13}$ and $Au_{24}(SR)_{20}$ suggest that, at a Au/SR ratio approaching 1/1, the interlocked staple motifs may become a widespread conformation in thiolate-protected metal nanoclusters [8–10]. Moreover, the $Au_{10}(SR)_{10}$ catenane structure was recently identified as the best structural candidate for the Au local structure in bovine serum albumin protein-stabilized

gold nanoclusters [11]. We reported in a recent work, a "one-pot–one-size" synthesis of $Au_{10}(SG)_{10}$ NCs (SG:glutathione:γ-L-glutamyl-L-cysteinylglycine) characterized by electrospray MS. The X-ray diffraction pattern of $Au_{10}(SG)_{10}$ was utilized as fingerprints for homoleptic gold–glutathione catenanes [7]. Regarding optical properties, enhanced second harmonic response and circular dichroism signals in the spectral region of 250–400 nm were observed due to this catenane structure exhibiting a centrosymmetry-broken structure [7]. Recently, Chevrier et al. confirmed the catenane structure by using synchrotron-based X-ray absorption fine structure (XAFS) spectroscopy [11]. As a complement to these powder-based structural characterization techniques requiring X-ray beams or synchrotron facilities, mass spectrometry-based techniques performed on gas phase nanoclusters ions may provide information on 3D molecular structures. In particular, ion mobility spectrometry (IMS) has been used for the characterization of gas-phase ligand-protected metal nanoclusters [12–19]. IMS separation is based on the different velocities adopted by ions travelling in an inert gas under a low electric field. The drift time of the ions through the IMS tube depends on the ratio between their collision cross-section (CCS) with the gas and their charge, thus allowing isomer discrimination. Our groups showed how IMS studies can provide insight into the size of glutathione-protected gold nanoclusters, as well as in the structural determination of inorganic nanoclusters [16,18,19].

In a previous recent work, we reported an ion mobility-mass spectrometry (IM-MS) approach for the analysis of homoleptic $Au_{10\text{-}12}(SG)_{10\text{-}12}$ nanoclusters. CCS measurements were reported for different charge states for $Au_{10}(SG)_{10}$, $Au_{11}(SG)_{11}$, and $Au_{12}(SG)_{12}$ nanoclusters [18]. Strong charge-state effects on experimental CCS values were observed and attributed to charge-induced glutathione unfolding. However, the importance of core structure and the ligand conformations on the total CCS was difficult to disentangle due to conformational effects of such a flexible peptide ligand. The IMS technique was not sufficient to discriminate between different possible structures (in particular catenane structures) for the core.

This discrimination could be easier if smaller and more rigid ligands are used for protection, where charge-induced ligand unfolding effects will be minimized. In this case, the structural characterization of clusters may thus be possible by comparing the arrival time distribution profiles recorded by ion mobility mass spectrometry with theoretical calculations using molecular modelling (density functional theory, DFT) and subsequent collision cross-section calculations using projection approximation. Here, we report a combined ion mobility and spectrometry approach with DFT calculations for the analysis of a stoichiometric gold nanocluster ligated by thioglycolic acid $Au_{10}(TGA)_{10}$ (TGA; see Figure S1 in the Supplementary Materials) as ligand molecules. Collision cross-section (CCS) measurements are reported for two charge states. DFT calculations have been performed to optimize different candidate structures for which CCSs were computed. The comparison of the experimentally- and theoretically-determined CCSs allows concluding about the catenane structures of such nanoclusters.

2. Materials and Methods

Materials and synthesis protocol: All the chemicals were commercially available and were used without purification. $HAuCl_4 \cdot 3H_2O$, trifluoroacetic acid (TFA), and methanol (HPLC grade) were purchased from Carl Roth (Lauterbourg, France). Thioglycolic acid (TGA), NaOH, and NH_4OH were purchased from Sigma-Aldrich (Saint-Quentin Fallavier, France). Milli-Q water with a resistivity of 18.2 MΩ cm^{-1} was used for all experiments. $Au_{10}(TGA)_{10}$ NC was prepared as described in [7] with TGA as the ligand instead of glutathione. Briefly, 70 mg of TGA (≈53 µL) were diluted in 35 mL of methanol and 2 mL of triethylamine. Then, 100 mg of $HAuCl_4 \cdot 3H_2O$ in 15 mL of water were added, and the solution was stirred overnight at ambient temperature. To induce precipitation, 2 mL of 1 M NaOH solution were added, and the solution was centrifuged (10 min at 11,000 rpm).

Ion mobility-mass spectrometry: Ion mobility measurements were performed using an ion mobility spectrometer as described in [20]. Measurements were done using a fresh mixture of $Au_{10}(TGA)_{10}$, prepared in an aqueous solution to a concentration of about 50 µM and directly

electrosprayed using a syringe pump. Mobility measurements were done by injecting ion bunches in the drift tube filled with 4.0 Torr helium, in which a constant drift field was maintained through the controlled voltage drop across the tube. The temperature of the whole instrument was kept at 296 K. After their drift, ions were transferred to a reflector time-of-flight mass spectrometer. Mass spectra were finally recorded as a function of the IMS drift time, allowing for extraction of arrival time distributions (ATDs) for ions with any desired mass-to-charge ratio. Collision cross-sections (CCS) were extracted from ATDs as described in [21]. Using this method, the error of the experimental CCS was estimated to be 2%.

Computational: The structural and absorption properties of $Au_{10}(TGA)_{10}$ were determined using the DFT and its time-dependent version TD-DFT approach [22,23]. For gold atoms, a 19-electron relativistic effective core potential (19e-RECP) was employed [24]. The structural and spectroscopic properties of $Au_{10}(TGA)_{10}$ were obtained at the PBE0/Def2-SVP level of theory [25,26].

3. Results and Discussion

3.1. Characterization of $Au_{10}(TGA)_{10}$

The formation of $Au_{10}(TGA)_{10}$ NCs as the product was confirmed by electrospray ionization-mass spectrometry (ESI-MS) in negative mode (see the inset in Figure 1). A charge state distribution of the general formula $[M-nH^+]^{n-}$ ($2 \leq n \leq 4$) was observed for the $Au_{10}(TGA)_{10}$. The additional peaks observed in MS spectra were due to smaller stoichiometric $(AuTGA)_n$ complexes ($n \leq 6$) originating from the "in-source" fragmentation of the $Au_{10}(TGA)_{10}$ clusters (as evidenced by collision-induced dissociation experiments; see Figure S2 in the Supplementary Materials).

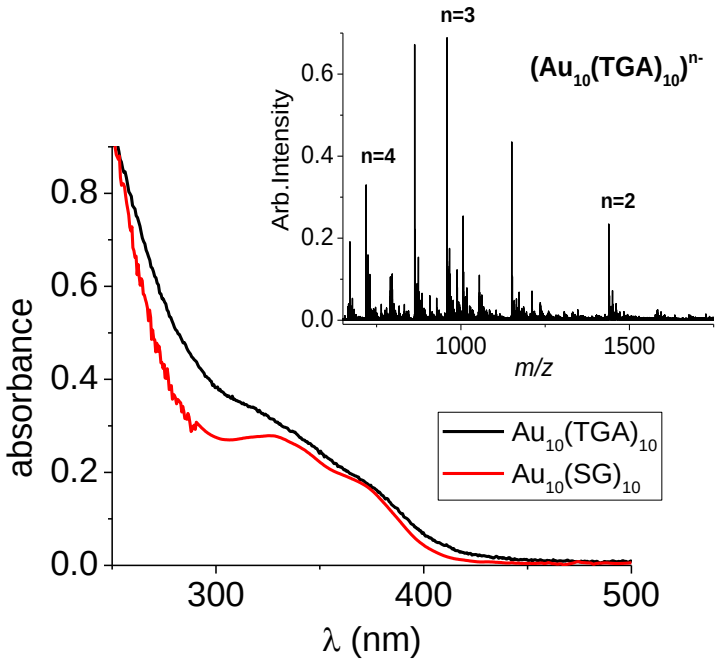

Figure 1. Experimental absorption spectra of $Au_{10}(SR)_{10}$ nanoclusters (NCs) (with SR = thioglycolic acid (TGA)and SG (see [7]). (Inset) Electrospray ionization ESI mass spectrum of the as-synthesized $Au_{10}(TGA)_{10}$ NCs.

Concerning the optical properties, the one-photon absorption spectrum of the as-synthesized $Au_{10}(TGA)_{10}$ NCs showed a monotonic increase of intensity below 390 nm and a shoulder at ~310 nm. There was similarity with the absorption spectrum of the previously-reported $Au_{10}(SG)_{10}$ NCs (see Figure 1) [7].

3.2. Theoretical Investigation of the Structural and Optical Properties of $Au_{10}(TGA)_{10}$

The DFT method has been used to determine the structures of the $Au_{10}(SR)_{10}$ NCs based on the results obtained by a genetic algorithm search method [4]. The [5,5] catenane structure containing two interpenetrating −AuSR− pentagons was found to be the most stable structure (Figure 2a). The [6,4] structure containing four- and six-membered Au rings interpenetrating each other (Figure 2b) and the crown-like structure (Figure 2c) was higher in energy. The structure of these three isomers is shown in Figure 2. Interestingly, the size of TGA ligand along with the size of the crown and the Au-S bond length allowed for a rich hydrogen-bonding network within the TGA ligands, leading to a "ball-like" shape for the crown-like structure.

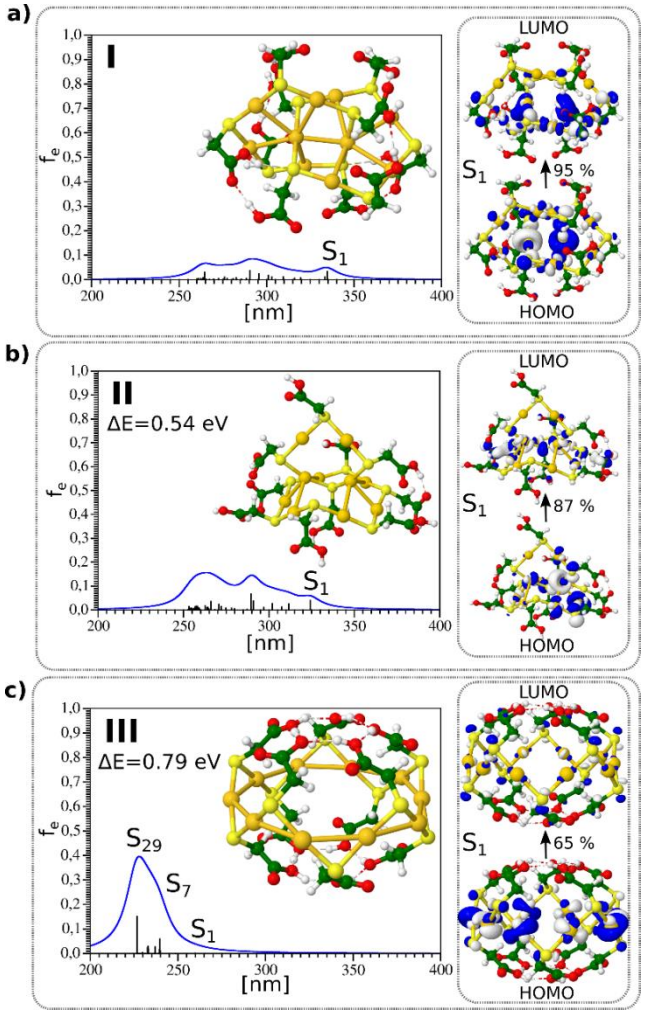

Figure 2. TD-DFT absorption spectrum and structure for three lowest energy isomers of $Au_{10}(TGA)_{10}$ shown in (**a**–**c**) respectively. Leading excitations responsible for the characteristic features of absorption are illustrated on the right side. HOMO-LUMO for isomers I, II, and III are 4.54, 4.62, and 5.55 eV, respectively.

The absorption spectra calculated using a TD-DFT approach for the three isomers with catenane structures are also shown in Figure 2. For the [5,5] and [6,4] catenane structures, the first excited states were located between 320 and 350 nm. The leading excitations responsible for S_1 and S_2 excited states shown also in Figure 2 involved Au–Au aurophilic subunits bound to neighboring sulfur atoms and arose from the penetration of the two rings into each other. The absorption spectrum for the crown-like structure obtained from the TD-DFT approach differed considerably from those of other two isomers.

3.3. Catenane Structures of Homoleptic $Au_{10}(TGA)_{10}$ Evidenced by Ion Mobility-Mass Spectrometry and DFT Calculations

In order to characterize the structural properties of $Au_{10}(TGA)_{10}$ NCs, we conducted ion mobility-mass spectrometry (IM–MS) measurements. The extracted arrival time distributions (ATDs) were mainly monomodal for the two- and three-charge states of $Au_{10}(TGA)_{10}$, indicating that the corresponding clusters presented essentially a single structural type, and the width of the peaks was compatible with a single structural type being present (see Figures S3 and S4 in the Supplementary Materials). In addition, Figure S4 in the Supplementary Materials shows that the arrival time distributions (ATDs) for $[Au_{10}(TGA)_{10}-2H]^{2-}$ and $[Au_{10}(TGA)_{10}-3H]^{3-}$ were very close to the predicted ATDs by the Fick law. The observed ATDs peaks were thus limited by the experimental instrumental resolution. This means that the observed single peaks in ATDs corresponded to single structures, and other possible effects (conformational freedom and especially motion around the Au–S bond in the TGA ligand and possible interconversions between ligand conformations) cannot be resolved.

The experimental CCSs determined for different charge states for $Au_{10}(TGA)_{10}$ nanoclusters are given in Table 1. The collision cross-section for the three-charge state was only slightly higher by ~4% than that for the two-charge state. This finding is in contrast with $Au_{10}(SG)_{10}$, where a charge-induced unfolding due to Coulomb repulsion between charged moieties was observed, producing more dramatic effects on the CCS [18]. Indeed, for $Au_{10}(SG)_{10}$, the increase in the collision cross-section as a function of charge was more important (by ~6.5%). Furthermore, the size of the glutathione ligand was in the same order as the size of the metallic core. This indicates that the charging of the TGA ligand molecule played a minor role in the total collision cross-section of $Au_{10}(TGA)_{10}$. This means that the overall structure of the NCs was not significantly modified by the charge, as confirmed by DFT structures obtained for neutral $Au_{10}(TGA)_{10}$ and $[Au_{10}(TGA)_{10}-2H]^{2-}$ (see Figure S5 in the Supplementary Materials). For the two charge state, the CCS value calculated from the [5,5] and [6,4] catenane structures matched the experimental CCS value, confirming that core geometry was consistent with a catenane-like form for $Au_{10}(TGA)_{10}$ nanoclusters.

Table 1. Experimental and calculated collision cross-section (CCS) values for three isomers of $Au_{10}(TGA)_{10}$ NCs are given. The influence of charge has been experimentally determined (error bars are in brackets). For this purpose, the trajectory method has been used [27]. The DFT structures obtained for $[Au_{10}(TGA)_{10}-2H]^{2-}$ are given in Figure S5 in the Supplementary Materials.

CCS of $Au_{10}(TGA)_{10}$ (Å^2)	$Au_{10}(TGA)_{10}$ neutral	$[Au_{10}(TGA)_{10}-2H]^{2-}$	$[Au_{10}(TGA)_{10}-3H]^{3-}$
Exp.		225 (5)	235 (5)
[5,5] catenane	212	220	
[6,4] catenane	228	230	
Crown-like	196	196	

4. Conclusions

The chemistry of the sulfur–gold bond is extremely rich and leads to hybrid materials. Such materials encompass gold thiolate coordination oligomers, for instance $Au_n(SR)_n$ and atomically well-defined clusters $Au_n(SR)_m$, or supramolecular assemblies like $-(AuSR)_\infty-$. The catenane-like structure is a unique feature of $Au_n(SR)_n$ complexes, but certainly also in thiolate-protected metal nanoclusters at a low Au/SR ratio limit (i.e., approaching 1:1). Unraveling the total structure of gold nanoclusters is of paramount importance for their characterization. Unfortunately, the use of X-ray crystallography is problematic for homoleptic thiolate-protected metal nanoclusters, because sample crystallization requires extremely high purity and stability. Additional characterization tools able to distinguish structural isomers are thus highly desirable. The DFT approach provides information about catenane-like structures for the two lowest energy isomers. The TDDFT absorption features allows for the structural assignment to experimental data, as well. Ion mobility-mass spectrometry

(IM-MS) has proven to be a useful complement to MS due to its ability to separate ions based on their "shape". In this work, we used this coupling and additionally reported collision cross-sections (CCS) for selected gas phase charge states of $Au_{10}(TGA)_{10}$ cluster ions. Charge effects on the CCS were found negligible for a simple and small thiolated ligand (thioglycolic acid (TGA)). Furthermore, the comparison of CCS values from different structural isomers of $Au_{10}(TGA)_{10}$ obtained at the DFT level of theory has permitted confirming the catenane structure for such nanoclusters.

Supplementary Materials: The following are available online at http://www.mdpi.com/2079-4991/9/3/457/s1: Figure S1: Chemical structure of thioglycolic acid (TGA). Figure S2: Collision-induced dissociation spectra of $(Au_{10}(TGA)_{10})^{3-}$. Figure S3: ATDs recorded for two charge states of $Au_{10}(TGA)_{10}$ in negative mode. Figure S4: ATDs recorded for two charge states of $Au_{10}(TGA)_{10}$ compared to the fick law. Figure S5: DFT structures obtained for $[Au_{10}(TGA)_{10}-2H]^{2-}$.

Author Contributions: R.A. conceived of the initial idea and coordinated the work. F.B. synthesized and prepared the nanoclusters. C.C.-Z. measured CCS and recorded mass spectra. M.P. and V.B.-K. performed and analyzed the theoretical results. C.C.-Z. and F.C. analyzed the results. R.A., P.D. and V.B.-K. supervised and financed the project. R.A. and V.B.-K. wrote the paper. All the authors provided critical feedback and helped to shape the final manuscript.

Funding: This research was partially supported by the project STIM – REI, Contract Number KK.01.1.1.01.0003, funded by the European Union through the European Regional Development Fund—the Operational Programme Competitiveness, and Cohesion 2014–2020 (KK.01.1.1.01). (V.B.-K and M.P.) We would like to acknowledge the financial support from the French-Croatian project "International Laboratory for Nano Clusters and Biological Aging, LIA NCBA".

Acknowledgments: V.B.-K. and M.P acknowledge the Center for Advanced Computing and Modelling (CNRM) for providing computing resources of the supercomputer Bura at the University of Rijeka and SRCE at University of Zagreb, Croatia.

Conflicts of Interest: The authors declare no conflict of interest.

References

1. Jin, R.; Zeng, C.; Zhou, M.; Chen, Y. Atomically Precise Colloidal Metal Nanoclusters and Nanoparticles: Fundamentals and Opportunities. *Chem. Rev.* **2016**, *116*, 10346–10413. [CrossRef] [PubMed]
2. Chakraborty, I.; Pradeep, T. Atomically Precise Clusters of Noble Metals: Emerging Link between Atoms and Nanoparticles. *Chem. Rev.* **2017**, *117*, 8208–8271. [CrossRef] [PubMed]
3. Antoine, R. Atomically precise clusters of gold and silver: A new class of nonlinear optical nanomaterials. *Front. Res. Today* **2018**, *1*, 01001. [CrossRef]
4. Liu, Y.; Tian, Z.; Cheng, L. Size evolution and ligand effects on the structures and stability of (AuL)n (L = Cl, SH, SCH3, PH2, P(CH3)2, n = 1-13) clusters. *RSC Adv.* **2016**, *6*, 4705–4712. [CrossRef]
5. Wiseman, M.R.; Marsh, P.A.; Bishop, P.T.; Brisdon, B.J.; Mahon, M.F. Homoleptic Gold Thiolate Catenanes. *J. Am. Chem. Soc.* **2000**, *122*, 12598–12599. [CrossRef]
6. Chui, S.S.-Y.; Chen, R.; Che, C.-M. A Chiral [2]Catenane Precursor of the Antiarthritic Gold(I) Drug Auranofin. *Angew. Chem. Int. Ed.* **2006**, *45*, 1621–1624. [CrossRef] [PubMed]
7. Bertorelle, F.; Russier-Antoine, I.; Calin, N.; Comby-Zerbino, C.; Bensalah-Ledoux, A.; Guy, S.; Dugourd, P.; Brevet, P.-F.; Sanader, Ž.; Krstić, M.; et al. Au10(SG)10: A Chiral Gold Catenane Nanocluster with Zero Confined Electrons. Optical Properties and First-Principles Theoretical Analysis. *J. Phys. Chem. Lett.* **2017**, *8*, 1979–1985. [CrossRef] [PubMed]
8. Jiang, D.-E.; Overbury, S.H.; Dai, S. Structure of Au15(SR)13 and Its Implication for the Origin of the Nucleus in Thiolated Gold Nanoclusters. *J. Am. Chem. Soc.* **2013**, *135*, 8786–8789. [CrossRef]
9. Pei, Y.; Pal, R.; Liu, C.; Gao, Y.; Zhang, Z.; Zeng, X.C. Interlocked Catenane-Like Structure Predicted in Au24(SR)20: Implication to Structural Evolution of Thiolated Gold Clusters from Homoleptic Gold(I) Thiolates to Core-Stacked Nanoparticles. *J. Am. Chem. Soc.* **2012**, *134*, 3015–3024. [CrossRef] [PubMed]
10. Pei, Y.; Wang, P.; Ma, Z.; Xiong, L. Growth-Rule-Guided Structural Exploration of Thiolate-Protected Gold Nanoclusters. *Accounts Chem. Res.* **2019**, *52*, 23–33. [CrossRef]
11. Chevrier, D.M.; Thanthirige, V.D.; Luo, Z.; Driscoll, S.; Cho, P.; MacDonald, M.A.; Yao, Q.; Guda, R.; Xie, J.; Johnson, E.R.; et al. Structure and formation of highly luminescent protein-stabilized gold clusters. *Chem. Sci.* **2018**, *9*, 2782–2790. [CrossRef]

12. Angel, L.A.; Majors, L.T.; Dharmaratne, A.C.; Dass, A. Ion Mobility Mass Spectrometry of Au25(SCH2CH2Ph)18 Nanoclusters. *ACS Nano* **2010**, *4*, 4691–4700. [CrossRef] [PubMed]
13. Harkness, K.M.; Fenn, L.S.; Cliffel, D.E.; McLean, J.A. Surface Fragmentation of Complexes from Thiolate Protected Gold Nanoparticles by Ion Mobility-Mass Spectrometry. *Anal. Chem.* **2010**, *82*, 3061–3066. [CrossRef] [PubMed]
14. Baksi, A.; Harvey, S.R.; Natarajan, G.; Wysocki, V.H.; Pradeep, T. Possible isomers in ligand protected Ag11 cluster ions identified by ion mobility mass spectrometry and fragmented by surface induced dissociation. *Chem. Commun.* **2016**, *52*, 3805–3808. [CrossRef] [PubMed]
15. Baksi, A.; Ghosh, A.; Mudedla, S.K.; Chakraborty, P.; Bhat, S.; Mondal, B.; Krishnadas, K.R.; Subramanian, V.; Pradeep, T. Isomerism in Monolayer Protected Silver Cluster Ions: An Ion Mobility-Mass Spectrometry Approach. *J. Phys. Chem. C* **2017**, *121*, 13421–13427. [CrossRef]
16. Daly, S.; Choi, C.M.; Zavras, A.; Krstić, M.; Chirot, F.; Connell, T.U.; Williams, S.J.; Donnelly, P.S.; Antoine, R.; Giuliani, A.; et al. Gas-Phase Structural and Optical Properties of Homo- and Heterobimetallic Rhombic Dodecahedral Nanoclusters [Ag14–nCun(C≡CtBu)12X]+ (X = Cl and Br): Ion Mobility, VUV and UV Spectroscopy, and DFT Calculations. *J. Phys. Chem. C* **2017**, *121*, 10719–10727. [CrossRef]
17. Ligare, M.R.; Baker, E.S.; Laskin, J.; Johnson, G.E. Ligand induced structural isomerism in phosphine coordinated gold clusters revealed by ion mobility mass spectrometry. *Chem. Commun.* **2017**, *53*, 7389–7392. [CrossRef] [PubMed]
18. Comby-Zerbino, C.; Bertorelle, F.; Chirot, F.; Dugourd, P.; Antoine, R. Structural insights into glutathione-protected gold Au10−12(SG)10−12 nanoclusters revealed by ion mobility mass spectrometry. *Eur. Phys. J. D* **2018**, *72*, 144. [CrossRef]
19. Soleilhac, A.; Bertorelle, F.; Comby-Zerbino, C.; Chirot, F.; Calin, N.; Dugourd, P.; Antoine, R. Size Characterization of Glutathione-Protected Gold Nanoclusters in the Solid, Liquid and Gas Phases. *J. Phys. Chem. C* **2017**, *121*, 27733–27740. [CrossRef]
20. Simon, A.-L.; Chirot, F.; Choi, C.M.; Clavier, C.; Barbaire, M.; Maurelli, J.; Dagany, X.; MacAleese, L.; Dugourd, P. Tandem ion mobility spectrometry coupled to laser excitation. *Rev. Sci. Instrum.* **2015**, *86*, 094101. [CrossRef]
21. Revercomb, H.E.; Mason, E.A. Theory of plasma chromatography/gaseous electrophoresis. *Anal. Chem.* **1975**, *47*, 970–983. [CrossRef]
22. Bonačić-Koutecký, V.; Kulesza, A.; Gell, L.; Mitrić, R.; Antoine, R.; Bertorelle, F.; Hamouda, R.; Rayane, D.; Broyer, M.; Tabarin, T.; et al. Silver cluster–biomolecule hybrids: From basics towards sensors. *Phys. Chem. Chem. Phys.* **2012**, *14*, 9282–9290. [CrossRef] [PubMed]
23. Bertorelle, F.; Hamouda, R.; Rayane, D.; Broyer, M.; Antoine, R.; Dugourd, P.; Gell, L.; Kulesza, A.; Mitric, R.; Bonacic-Koutecky, V. Synthesis, characterization and optical properties of low nuclearity liganded silver clusters: Ag31(SG)19 and Ag15(SG)11. *Nanoscale* **2013**, *5*, 5637–5643. [CrossRef] [PubMed]
24. Andrae, D.; Häußermann, U.; Dolg, M.; Stoll, H.; Preuß, H. Energy-adjustedab initio pseudopotentials for the second and third row transition elements. *Theor. Chi. Acta* **1990**, *77*, 123–141. [CrossRef]
25. Adamo, C.; Barone, V. Toward reliable density functional methods without adjustable parameters: The PBE0 model. *J. Chem. Phys.* **1999**, *110*, 6158–6170. [CrossRef]
26. Weigend, F.; Ahlrichs, R. Balanced basis sets of split valence, triple zeta valence and quadruple zeta valence quality for H to Rn: Design and assessment of accuracy. *Phys. Chem. Chem. Phys.* **2005**, *7*, 3297–3305. [CrossRef] [PubMed]
27. Larriba-Andaluz, C.; Hogan, C.J., Jr. Collision cross section calculations for polyatomic ions considering rotating diatomic/linear gas molecules. *J. Chem. Phys.* **2014**, *141*, 194107. [CrossRef] [PubMed]

Appendix B

Nanotechnology in Tumor Biomarker Detection

Guillaume F. Combes, Ana-Marija Vučković, Martina Perić Bakulić, Rodolphe Antoine, Vlasta Bonačić-Koutecky and Katarina Trajković, "Nanotechnology in Tumor Biomarker Detection: The Potential of Liganded Nanoclusters as Nonlinear Optical Contrast Agents for Molecular Diagnostics of Cancer", *Cancers*, **2021**, 13, 16, 4206

cancers

MDPI

Review

Nanotechnology in Tumor Biomarker Detection: The Potential of Liganded Nanoclusters as Nonlinear Optical Contrast Agents for Molecular Diagnostics of Cancer

Guillaume F. Combes [1,2,†], Ana-Marija Vučković [1,2,†], Martina Perić Bakulić [1], Rodolphe Antoine [3], Vlasta Bonačić-Koutecky [1,4,5] and Katarina Trajković [1,2,*]

1 Center of Excellence for Science and Technology-Integration of Mediterranean Region (STIM), Faculty of Science, University of Split, 21000 Split, Croatia; guillaume.combes@medils.hr (G.F.C.); anamarija.vuckovic@medils.hr (A.-M.V.); martina@stim.unist.hr (M.P.B.); vbk@cms.hu-berlin.de (V.B.-K.)
2 Mediterranean Institute for Life Sciences (MedILS), 21000 Split, Croatia
3 UMR 5306, Centre National de la Recherche Scientifique (CNRS), Institute Lumière Matière, Claude Bernard University Lyon 1, F-69622 Villeurbanne, France; rodolphe.antoine@univ-lyon1.fr
4 Interdisciplinary Center for Advanced Science and Technology (ICAST), University of Split, 21000 Split, Croatia
5 Chemistry Department, Humboldt University of Berlin, 12489 Berlin, Germany
* Correspondence: katarina.trajkovic@medils.hr
† These authors contributed equally to this work.

Simple Summary: The key factor in preventing premature death from cancer is an early and accurate diagnosis. While common diagnostic procedures are successful in the detection and rough description of a tumor mass, a deeper insight into cancer's molecular features is needed to optimize the treatment and increase the chances of survival. Nanotechnology can aid the molecular diagnostics of cancers through a design of nanomaterials that can simultaneously recognize specific cancer-associated molecules, so-called tumor biomarkers, and allow for their visualization by different imaging techniques. With a recent explosion in the production of various nanomaterials, the selection of the most suitable nanomaterial for tumor biomarker detection becomes a challenge. In this article, we review recent advances in the molecular diagnostics of cancer using nanotechnology and focus on liganded noble metal quantum nanoclusters, a class of ultrasmall nanomaterials with distinctive structural and optical properties, as tools in tumor biomarker detection.

Abstract: Cancer is one of the leading causes of premature death, and, as such, it can be prevented by developing strategies for early and accurate diagnosis. Cancer diagnostics has evolved from the macroscopic detection of malignant tissues to the fine analysis of tumor biomarkers using personalized medicine approaches. Recently, various nanomaterials have been introduced into the molecular diagnostics of cancer. This has resulted in a number of tumor biomarkers that have been detected in vitro and in vivo using nanodevices and corresponding imaging techniques. Atomically precise ligand-protected noble metal quantum nanoclusters represent an interesting class of nanomaterials with a great potential for the detection of tumor biomarkers. They are characterized by high biocompatibility, low toxicity, and suitability for controlled functionalization with moieties specifically recognizing tumor biomarkers. Their non-linear optical properties are of particular importance as they enable the visualization of nanocluster-labeled tumor biomarkers using non-linear optical techniques such as two-photon-excited fluorescence and second harmonic generation. This article reviews liganded nanoclusters among the different nanomaterials used for molecular cancer diagnosis and the relevance of this new class of nanomaterials as non-linear optical probe and contrast agents.

Keywords: tumor biomarker; cancer diagnostics; molecular diagnostics of cancer; liganded noble metal quantum nanocluster; precision medicine; bioimaging; contrast agents; nonlinear optics; two-photon-excited fluorescence

check for updates

Citation: Combes, G.F.; Vučković, A.-M.; Perić Bakulić, M.; Antoine, R.; Bonačić-Koutecky, V.; Trajković, K. Nanotechnology in Tumor Biomarker Detection: The Potential of Liganded Nanoclusters as Nonlinear Optical Contrast Agents for Molecular Diagnostics of Cancer. *Cancers* **2021**, *13*, 4206. https://doi.org/10.3390/cancers13164206

Academic Editor: Tatjana Paunesku

Received: 7 July 2021
Accepted: 19 August 2021
Published: 21 August 2021

1. Cancer Diagnostics and Nanotechnology

1.1. Cancer Diagnostics: From Macroscopic Description to Molecular Diagnostics and Precision Medicine

Cancer is one of the leading causes of premature death globally [1]. In 2020, the GLOBOCAN online database estimated almost 10 million cancer deaths in 185 countries for 36 types of cancer [2]. Furthermore, cancer patients with comorbidities have higher chances of dying from non-cancer-related causes [3], which further increases the overall health and economic impact of cancer. So far, the most efficient strategy to reduce cancer mortality and comorbidity rates and, consequently, the associated burden on the health care system has been the early detection and diagnosis of cancer. However, despite tremendous efforts, the early detection of cancer remains challenging, mainly due to the complex nature of cancer. Moreover, fine features of specific tumors, which can be instructional in designing and customizing therapeutic approaches, often escape standard diagnostic procedures.

Traditionally, clinicians have been able to reveal the presence of cancer only upon the development of the first symptoms, which usually happens after a tumor mass has reached a substantial size or even after the spreading of metastases. Samples of such tumors can be extracted by tissue biopsies and characterized using standardized histopathological techniques that enable the rough description and categorization of cancer cells. Nevertheless, as biopsies are limited to small amounts of cancer tissue, this procedure provides little information about the overall heterogeneity of cancers. Moreover, such invasive tissue sampling cannot be performed repeatedly as it may inflict complications [4].

Some limitations of tissue biopsies have been overcome by the development of imaging approaches, whereby entire tumors are visualized in situ. The foundations laid more than a century ago by the discovery of X-rays [5] have allowed for the development of techniques such as X-ray computed tomography (CT), positron emission tomography (PET), single-photon emission computed tomography (SPECT), and magnetic resonance imaging (MRI) (Table 1). These methods have an improved diagnostic capacity relative to tissue biopsy as they can provide information about cancer processes, location, and stage [6]. In particular, anatomy-based imaging (CT and MRI) provides information about the location, size, and morphology of the cancer, and function-based imaging (PET and SPECT) map physiological and biological processes within the cancer. Combining anatomy-based imaging with function-based imaging further increases diagnostic power. The introduction of hybrid imaging such as SPECT/CT, PET/CT, optical/CT, and PET/MRI has improved diagnostic accuracy in oncology, but equipment and operational costs account for their slow implementation [7]. Another imaging approach, optical molecular imaging, is holding great promise for cancer diagnosis. Optical imaging (OI) can currently reach wide spatial imaging scales, ranging from cells to organ systems, which renders this technology extremely appealing for medical imaging. Moreover, OI has at its disposal diverse contrast mechanisms (using light absorption and emission methods as well as hybrid OI approaches) for distinguishing normal from pathologic processes and tissues in both small animal and human studies. Typically, complex methods are needed to extract quantitative data from deep tissues.

In the 1970s, with the development of nuclear medicine and the application of radioisotope tracers that are internalized by cancer cells [8], the focus shifted to the molecular events associated with cancer. An example of such an approach is the application of 2-^{18}F-fluorodeoxyglucose (FDG), a glucose analog whose accumulation increases in cancer cells relying on glucose metabolism [9,10]. FDG is still extensively used for detection by PET imaging of various cancers, including breast and colorectal cancers, melanomas, and lymphomas. However, FDG labeling has limited specificity since non-cancer cells can also metabolize glucose. The need for increased specificity has prompted a search for new tumor-specific entities, with the goal to develop reliable detection strategies that will aid the early detection of cancer.

The shift towards the molecular profiling of cancer in the late 20th century has paved a road to a precision medicine approach where molecular profiling is combined with

large biomedical data sets and used for precision diagnostics, prognostics, and therapeutic strategies in the cancer field [11]. A fundamental goal of precision medicine is to provide effective therapeutic strategies for patients based on their individual cellular, molecular, and biomarker characteristics, along with their unique genetic and environmental factors [12]. Hence, the terms "precision medicine" and "personalized medicine" are often used interchangeably. This approach is driven by technological advances, the interpretation of -omics data, and the development of targeted therapies based on the identification of tumor biomarkers [13,14].

Table 1. Techniques used for cancer diagnosis.

Diagnostic Method	Principle	Technique	Detection Agent/Visualization
Imaging	Function-based	PET	Radioactive tracers that produce positrons/Scanner
	Function-based	SPECT	Radioactive tracers that emit gamma rays/Scanner
	Anatomy-based	MRI	Magnet, radiofrequency/Scanner
	Anatomy-based	CT	X-ray/Scanner
	Hybrid (anatomy- and function-based)	PET/CT, PET/MRI, SPECT/CT	Combination of radioactive tracer and imaging modality
	Optical	PA, SERS	Luminescent probe/Scanner
Molecular diagnostics	Gene amplification	PCR	DNA sequencing
	Cytogenetic analysis—hybridization of nucleic acids in cells/tissues	FISH	Fluorescent labels/Fluorescent microscopy
	Hybridization of nucleic acids in microplates	DNA microarrays	Labels/Microscopy
	Immunoassay for protein detection	ELISA	Luminescent probe/Plate reader

Tumor biomarkers are specific entities produced by cancer cells that can be found in the tumor itself or in the tissues and body fluids of patients. Altered levels of a wide range of entities, such as cells, proteins, peptides, post-translational modifications, metabolites, nucleic acids, and genetic variations, can reveal the presence of cancer in the body as well as help in individualized risk factor assessments, prognostics, and therapy response prediction [15]. Additionally, monitoring patients' response to treatment can identify molecular alterations occurring during treatment and help navigate the course of the therapy. For instance, genomic alternations such as specific mutations in breast cancer 1 (*BRCA1*) and breast cancer 2 (*BRCA2*) genes are well-established tumor biomarkers used for breast cancer risk assessment, meaning that women bearing these mutations are predisposed to develop breast cancer [16,17]. Moreover, it has been shown that the BRCA status predicts the responsiveness to therapies that interfere with DNA repair machinery, such as cisplatin or olaparib [18,19]; in particular, patients that do not bear these specific mutations are unlikely to respond to such treatments. Hence, unnecessary exposure to toxic therapies can be avoided by genotyping patients. This example highlights the complexity of cancer and the need for the discovery of effective tumor biomarkers that will help in achieving the goals of precision medicine and allow the stratification of patients.

1.2. Methods in Molecular Diagnostics of Cancer

The development of methods for analysis and the monitoring of the tumor biomarker landscape during tumorigenesis is of great importance for accurate cancer diagnostics and the design of personalized therapeutic options. Indeed, the introduction of genomics, epigenetics, proteomics, metabolomics, informatics, and imaging techniques has greatly improved our understanding of cancer's molecular features and allowed for improved survival prospects for patients by matching tumor characteristics with complementary therapy [20]. These methods are applicable to the analyses of tumor tissue biopsies as well as liquid biopsies, which contain biomarkers released by the tumor into bodily fluids, such as circulating tumor nucleic acids and circulating tumor cells (CTC) [21,22].

At present, the characterization of the cancer genome is performed by polymerase chain reaction (PCR) assays, high-throughput DNA microarrays, or fluorescence in situ hybridization (FISH) [23,24]. These techniques enabled the detection of short tandem repeats [25], loss of heterozygosity [26], alterations in DNA methylation status, and various

mutations. For instance, sequencing for genetic alterations in human epidermal growth factor receptor (*EGFR*), human epidermal growth factor receptor 2 (*HER2*), vascular endothelial growth factor (*VEGFR*), rearranged during transfection (*RET*) tyrosine kinase, mesenchymal–epithelial transition factor (*MET*), mitogen-activated protein kinase (*MEK*), anaplastic lymphocyte kinase (*ALK*), and ROS proto-oncogene 1 (*ROS1*) has allowed for precision therapy of non-small cell lung cancer, liver cancer, breast cancer, and renal cell carcinoma based on matching the individual's cancer mutations with a specific tyrosine kinase inhibitor as a treatment of choice [27,28].

Specific detection and identification of protein biomarkers in clinics have been mainly accomplished by various immunological techniques based on labeling sensors, where the final result is proportional to the amount of label bound to the targeted molecule [29,30]. The enzyme-linked immunosorbent assay (ELISA) is widely used for protein detection and quantification and is based on the use of specific binding surfaces decorated with antibodies that capture protein biomarkers from various body fluids. Protein biomarkers are then revealed by enzyme-labeled antibodies [31] that produce a fluorescent signal/color that corresponds to the amount of biomarker immobilized by the capturing antibody. ELISA displays high sensitivity–for instance, it can already detect the prostate-specific antigen (PSA), which is used for prostate cancer screening, at a concentration of 100 pg/mL [32]. However, the use of a single cancer protein biomarker is not sufficient for accurate cancer detection, as PSA can also be detected in patients with benign prostatic hyperplasia [33]. Therefore, to improve diagnostic accuracy, various multiplex immunoassays that combine the antibody-labeled detection of different protein biomarkers are needed. An example of a multiplex immunoassay is the FDA-approved OVA1® test that combines the detection of multiple serum-derived protein cancer antigen 125 (CA 125), transferrin, apolipoprotein A-I (APOA1), β2-microglobulin, and transthyretin with software calculations to predict ovarian malignancy [34]. In the second generation OVA2® (Overa) test, the latter two-protein biomarkers are replaced with human epididymis protein 4 (HE4) and follicle-stimulating hormone (FSH), having improved accuracy and reduced false results [35,36]. Due to their high sensitivity, immunological techniques are also used for the detection of CTC. For example, the CellSearch® system uses nanoparticles labeled with antibodies that target the epithelial cell adhesion molecule (EpCAM) to separate CTC from other cells present in the blood of patients with metastatic colorectal, breast, or prostate cancer. Immunomagnetic separation is followed by the immunocytological detection of various cytokeratins and leukocyte common antigen CD45 as well as the analysis of the cellular nuclei using a fluorescence microscope.

The recently developed CancerSEEK test [37] combines the multiplex measurement of genetic alterations in ctDNA with the measurement of protein levels of CA 125, cancer antigen 19-9 (CA 19-9), carcinoembryonic antigen (CEA), osteopontin (OPN), prolactin (PRL), myeloperoxidase (MPO), tissue inhibitor of metalloproteinases 1 (TIMP1), and hepatocyte growth factor (HGF) in blood samples. Through the measurement of ctDNA and protein biomarkers, the CancerSEEK tumor biomarker detection test displays 69–98% sensitivity in detecting liver, ovarian, stomach, esophageal, and pancreatic cancer.

1.3. Metallic Nanomaterials in Detection of Tumor Biomarkers

1.3.1. Nanotechnology in Cancer Diagnostics: From Large Nanoparticles (NPs) to Nanoclusters (NCs)

Despite the progress in understanding cancer biology, the diagnostics of cancer still faces many challenges [38]. Currently used clinical procedures are often invasive and unpleasant and have limited potential to detect specific molecular events [39]. Hence, there is a great need to improve cancer diagnostics by developing tools that might complement the existing clinical approaches or novel, non-invasive alternatives with enhanced specificity and sensitivity.

In the past few decades, nano-sized devices have undergone rapid development due to their immense potential in biomedical applications [40]. Their ability to act on a cellular or subcellular level has prompted an enormous number of studies exploring a large panel

of organic (liposomes, micelles, biopolymeric NPs, dendrimers) and inorganic (metal NPs, quantum dots, carbon nanotubes, nanoshells, nanocrystals) nanomaterials. The versatility of nanomaterials offers room for the optimization of their stability, selectivity, biological targeting properties, and detection. Some nanomaterials have already been introduced to (pre-)clinical cancer diagnostics, as is the case with iron oxide nanoparticles, which are used as a contrast agent for MRI imaging [41,42]. Importantly, suitable surface modification of nanomaterials enables their selective binding to a specific biological target, thus opening opportunities for the expansion of use of metal-based nanomaterials in various therapeutic and targeting systems [43].

Over the past few decades, various metal-based nanomaterials, composed of gold, silver, or copper, have been synthesized for molecular imaging and drug delivery purposes. Among all metallic nanomaterials, gold nanomaterials exhibit superior stability and optical properties and generally have lower toxicity, which makes them good candidates for potential clinical applications in diagnostics and therapy [44] and, in particular, in personalized medicine approaches.

Generally, metallic nanomaterials can be classified into three size groups: large NPs, small NPs, and quantum nanoclusters (NCs) [45]. Large NPs are larger than 50 nm and can be seen as small metal spheres [46], the optical properties of which depend on their volume and dielectric constant. For the second group of small NPs, with the size of 2–50 nm, the dielectric function becomes size-dependent, and the optical response is of a plasmonic nature. Finally, NCs are drastically different due to their ultrasmall size (<2 nm) and molecule-like properties, characterized by quantum discrete states. Of note, nanomaterial solutions are often heterogeneous in terms of individual particle sizes as it is difficult to achieve uniformity during synthesis, and, moreover, the agglomeration of individual particles can occur [47]. Average uniformity is expressed as a polydispersity index (PDI)—the square of the standard deviation of the particle diameter distribution divided by the mean particle diameter. PDI reflects the quality of the nanomaterial solution, and it is relevant to their clinical application.

1.3.2. Functionalization of Nanomaterials

The use of nanomaterials for cancer diagnostics is based on the functionalization of their surface by various ligands that serve to (1) maintain their physicochemical properties in vitro and in the biological environment (structural functionalization) and (2) provide them with specific target-recognition properties (specializing functionalization) [48,49]. Structural functionalization is used to protect the metallic nanomaterial from harsh conditions (such as suboptimal pH) as well as to reduce its toxicity and improve bioavailability. Compounds containing sulfur, such as cysteine (Cys), glutathione (GSH), mercaptopropionic acid (MPA), bidentate dihydrolipoic acid (DHLA), and thiolated polyethylene glycol (PEG), are the most common ligands used for structural functionalization.

Specializing functionalization adds various recognition moieties to metallic nanomaterials, which makes them competent to efficiently detect specific molecular targets and deliver drugs to desired destinations within the biological systems [50]. Those recognition moieties include peptides, antibodies, proteins, aptamers, small molecules, or polymers, and they enable the binding of functionalized nanomaterials to a specific tumor entity. The resulting complex between a tumor entity and nanomaterial can then be detected by suitable imaging techniques.

The addition of a recognition moiety can be achieved by a ligand exchange strategy based on the replacement of a structural ligand with a specific biomolecule or by a conjugation strategy that allows the binding of the molecule of interest to the structural ligands on the metallic nanomaterial. The ligand substitution induces size and structure transformation, and, generally, this approach is more difficult to apply on small NPs than on NCs [51].

Conjugation is usually based on the activation of the carboxylic acid of the protective ligand with N-(3-dimethylaminopropyl)-N*-ethylcarbodiimide hydrochloride (EDC),

which allows the formation of amide bonds between carboxyl groups of the ligand with amine residues on the protein surface. One such example is the work of Jazayeri et al., where a PEGylated gold nanoparticle was conjugated with an anti-PSA antibody using an EDC/N-hydroxylsuccinimide (NHS) linker [52]. The conjugation of antibodies such as anti-EGFR [53] and anti-Her2 [54–56] is of particular interest as they are already in clinical use for cancer detection and effective tumor targeting [57]. Over the recent years, the addition of a variety of ligands by conjugation [58–62] has become the method of choice as it offers tremendous opportunities in molecular recognition and targeting.

1.3.3. Tumor Biomarker Detection by Metallic Nanomaterials

In the past couple of decades, a number of metallic nanomaterials targeting various tumor biomarkers have been developed (reviewed in [63–65]). Here, we summarize recent examples of such nanomaterials, mostly metal NPs and NCs (Table 2). Many of them recognize receptors overexpressed on the surface of malignant cells, including the folate receptor, EGFR, HER2, GLUT, GRPR, and CCR5. Selection of the plasma-membrane-located receptors as targets is a reasonable strategy in the design of nanomaterials as it increases the probability that the nanomaterial will encounter the target and get internalized into the cells. In such instances, specializing ligands are either the natural ligands (e.g., folic acid for the folate receptor or glucose for GLUT) or peptides, aptamers, and antibodies designed to specifically target the receptors.

Metallic nanomaterials bound to their molecular targets can be detected using multiple techniques, the choice of which depends on the properties of the nanomaterial and the compatibility of these techniques with the type of nanomaterial-labeled biosample—cell line, tissue, liquid biopsy, or the entire organism. While some nanomaterials, such as AuNCs, are intrinsically luminescent in the range from visible to near-infrared (NIR) light [66,67], others require adaptation to the desired detection method by functionalization. In cell culture samples, such nanomaterials can be detected using fluorescence microscopy or less common methods, such as inductively coupled plasma mass spectrometry (ICP-MS), inductively coupled plasma atomic emission spectroscopy (ICP-AES), auto-metallography, and surface-enhanced Raman spectroscopy (SERS) [56,68,69]. Nanomaterial-labeled liquid biopsies (human serum and urine) allow the application of other methods such as fluorescence spectroscopy, colorimetric detection, and surface plasmon resonance (SPR) biosensors [70,71]. Finally, nanomaterials can be detected in vivo, e.g., in xenografted mice using MRI, nuclear imaging methods (SPECT, PET/CT, autoradiography), NIR fluorescence imaging systems, or photoacoustic imaging. For MRI, it is required for the nanomaterials to include or to be coated with a heavy metal such as iron oxide or gadolinium [72,73]. On the other hand, nuclear imaging methods require the labeling of the nanomaterials with radioisotopes [74]. Among these techniques, relatively novel photoacoustic imaging has been viewed as one of the most promising imaging techniques due to a relatively large imaging depth (up to 1 cm) [75]. This non-invasive imaging modality uses the optical properties of the nanomaterial and is compatible with both AuNPs and AuNCs [76–78].

Despite the huge variety of different nanomaterials developed for cancer diagnostics, only a small number have progressed to clinical trials [64]. Currently, there are 27 nanoparticles under clinical investigation for cancer diagnostics registered in clinicaltrials.gov. Despite their potential for biomedical applications, there are still biological (e.g., biodistribution, metabolism, pharmacokinetics), technological, safety, and regulatory challenges that need to be thoroughly investigated [65].

Table 2. Examples of cancer biomarker detection by different types of metallic nanomaterials.

Biomarker Detection			Functionalization		Nanoparticle/Nanocluster			
Method	**Biomarker**	**Model**	**Type of Ligand**	**Ligand**	**Composition**	**Dimension (nm)**	**PDI**	**Ref.**
Fluorescence microscopy	Folate receptor	Lung, breast cancer cell lines	Small molecule	Folic Acid	Au_{25}-BSA	~1/~8 (aggregates)	-	[58]
	PrP^c	Colorectal cancer cell line	Oligonucleotide	PrPC aptamer	AuNPs	13/20 (NPs/NPs + PrPc)	-	[79]
	EGFR	Lung cancer cell lines	Protein	EGFR-specific scFv	Fe_3O_4/AuNPs	30/76.3 (NPs/NPs + scFv)	-	[80]
	HER2	Breast cancer cell lines	Peptide	Anti-HER2 peptide	Fe_3O_4/AuNPs-Cy5.5	~12	0.08	[81]
	-	In vitro blood–brain barrier model	Amino acid	L-Dopa	AuNCs-SG	1.4	-	[82]
	CD44 receptor	Lung, breast cancer cell lines	Glycosaminoglycans	Hyaluronic acid	Au-SG-Graphene oxide	2	-	[83]
	Glutathione	Cervical, liver, colon cancer cell lines	Protein	Transferrin	AuNCs	4.72 ± 0.5	-	[84]
	Methionine level	Lung, liver, breast cancer cell lines	Amino acid	Methionine	Au-MET-MPA	5.6	0.118	[85]
	PD-L1	Colon cancer cell line	Antibody	anti-PD-L1 Ab	AuNPs-PEG	40.0 ± 3.1	-	[86]
	GLUT1	Breast cancer cell line	Small molecule	Glucose	AuNPs	47 (DLS)	0.15	[87]
	Neuron	In vitro blood–brain barrier model Mouse	Extracellular vesicle	Exosome	AuNPs	105 ± 10.1 (DLS)	0.430 ± 0.06	[88]
	Neuron	Rat	Protein	WGA-HRP	AuNPs-MSA	5.2 ± 1.3	-	[89]
	Folate receptor	Ovarian cancer cell line	Small molecule	Folic acid	AuNCs-BSA	25 ± 12 (DLS)	-	[90]
	Thyroid	Thyroid carcinoma cancer cell line	Chemical element	^{127}Iodine	AuNCs-BSA-I^{127}	6.4 (DLS)	-	[68]
	Calreticulin	Colon, breast cancer cell lines	Antibody	Anti-calreticulin Ab	AuNCs-MSA	2	-	[91]
	HER2	Breast cancer cell lines	Oligonucleotide	Affibody-DNA	AuNPs	18.5 ± 1.1/31.7 ± 1.3 (NPs/NPs + affibody) (DLS)	-	[92]
	HER2	Stomach cancer cell lines	Antibody	Tmab	AuNPs	85.39 ± 0.68 (DLS)	-	[93]
	PSMA	Prostate cancer cell lines	Peptide	PSMA-1	AuNPs-PEG-Pc4	5.5 ± 0.4 (AuNPs-PEG)	-	[94]
	Folate receptor	Bone, cervical, lung cancer cell lines	Small molecule	Folic acid	$Au_{22}SG_{18}$	1.4	-	[95]
	Leukemia cells	Leukemia cancer cell line	Oligonucleotide	KH1C12 aptamer	Fe_3O_4/AuNPs	26	-	[72]

Table 2. *Cont.*

Biomarker Detection			Functionalization		Nanoparticle/Nanocluster			
Method	**Biomarker**	**Model**	**Type of Ligand**	**Ligand**	**Composition**	**Dimension (nm)**	**PDI**	**Ref.**
Colorimetric	MMP9	Colon cancer mice urine	Peptide	Protease-cleavable peptide	AuNCs-SG	~1.5	-	[96]
	Citrate	Prostate cancer—Human urine			AuNCs-Cys	4–6	-	[97]
	hCG	Testicular cancer—Human urine Serum	Peptide	hCG-specific peptide aptamer	AuNPs	13	-	[98]
Fluorescence spectroscopy	Alkaline phosphatase	Human serum	Small molecule	Pyridoxal phosphate	AuNCs-BSA	1.95	-	[99]
	Glutathione	Glutathione	Small molecule	Folic acid	AuNCs-BSA-rGO	<2	-	[100]
ICP-MS	MMP9	Colon cancer—Human urine	Peptide	Protease-cleavable peptide	AuNCs-SG	~1.5	-	[96]
	HER2	Breast cancer cell lines	Antibody Peptide	Trastuzumab HIV-TAT cell-penetrating peptide	AuNPs-PEG	87.35 ± 0.41 (DLS)	0.17	[56]
	GLUT	Xenografted breast cancer mice	Small molecule	Glucose	AuNPs	47 (DLS)	-	[87]
ICP-AES	EGFR	Epidermoid carcinoma cancer cell line	Antibodies	VHH 122 Ab Cetuximab	AuNPs-PEG	28/42/45/63 (DLS) (NPs/+PEG/+VHH/+cet)	0.22/0.30/0.31/0.24	[101]
	Folate receptor HER2	Breast cancer cell line	Small molecule Antibody	Folic Acid Herceptin	AuNCs-BSA	4.2/9.8 (NCs/NCs + FA + HER)	-	[102]
	-	In vitro blood–brain barrier model	Amino acid	L-Dopa	AuNCs-SG	1.4	-	[82]
	Thyroid	Patient-derived xenografted thyroid cancer mice	Chemical element	^{127}Iodine	AuNCs-BSA-I^{127}	6.4 (DLS)	-	[68]
	EGFR	Lung and colorectal cancer cell line Xenografted colorectal cancer mice	Antibody	Cetuximab	AuNPs-PEG	78.3 ± 0.7 (DLS)	-	[103]

Table 2. *Cont.*

Biomarker Detection			Functionalization		Nanoparticle/Nanocluster			
Method	**Biomarker**	**Model**	**Type of Ligand**	**Ligand**	**Composition**	**Dimension (nm)**	**PDI**	**Ref.**
	CA 19.9 antigen	Pancreatic cancer cell lines Xenografted pancreatic cancer mice	Antibody	5B1 antibody	AuNPs-Zr^{89}	34.86 (DLS)	0.27	[104]
SPR biosensor	CEA	Colon cancer—Human plasma	Antibody	Anti-CEA Ab	AuNPs	30 ± 6 (NPs)	-	[70,71]
LSPR biosensor	PSA	Prostate cancer—Protein (PSA)	Antibody	Anti-PSA Ab	AuNPs-PEG	25	-	[52]
SERS	CD19	Leukemia cancer cell line	Antibody	Anti-CD19 Ab	AuNPs-PEG-MGITC	60 (DLS)	-	[105]
	CEA	Breast and lung cancer cell lines	Antibody	Anti-CEA Ab	AuNPs-Fe_3O_4-ATP-4	~20 (DLS)	-	[106]
	MCSP, MCAM, ErbB3, LNGFR	Melanoma, breast cancer cell lines Human plasma	Antibodies	Anti-MCSP, anti-MCAM, anti-ErbB3, anti-LNGFR, Abs	AuNPs-MBA, AuNPs-BA-TFM, AuNPs-DNTB, AuNPs-MPY.	60 (NPs alone)	-	[69]
MRI	EGFR	Xenografted lung cancer mice	Protein	EGFR-specific scFv	Fe_3O_4/AuNPs	30 (NPs alone) 76.3 (NPs + scFv)	-	[80]
	Leukemia cells	Leukemia cancer cell line	Oligonucleotide	KH1C12 aptamer	Fe_3O_4/AuNPs	26	-	[72]
	Nucleolin	Breast cancer cell line	Oligonucleotide	AS1411 aptamer	AuNPs-DO3A-Gd(III)	3.4 ± 0.6	-	[73]
NIR fluorescence imaging system	HER2	Xenografted breast cancer mice	Peptide	Anti-HER2 peptide	Fe_3O_4/AuNPs-Cy5.5	~12	0.08	[81]
	EGFR	Xenografted lung cancer mice	Protein	EGFR-specific scFv	Fe3O4/AuNPs	30 (NPs alone) 76.3 (NPs + scFv)	-	[80]
	-	Mouse	Amino acid	L-Dopa	AuNCs-SG	1.4	-	[82]
	Methionine level	Xenografted breast and lung cancer mice	Amino acid	Methionine	AuNCs-MET-MPA	5.6	0.118	[85]
	-	Mouse	-	-	AuNPs-SG-Au^{198}	2.6 ± 0.3	-	[107]

Table 2. *Cont.*

Biomarker Detection			Functionalization		Nanoparticle/Nanocluster			
Method	**Biomarker**	**Model**	**Type of Ligand**	**Ligand**	**Composition**	**Dimension (nm)**	**PDI**	**Ref.**
SPECT	PSMA	Xenografted prostate cancer mice	Peptide	PSMA-1	AuNPs-PEG-Pc4	5.5 ± 0.4 (AuNPs-PEG)	-	[94]
	Thyroid	Patient-derived xenografted thyroid cancer mice	Chemical element	^{127}Iodine	AuNCs-BSA-I^{127}	6.4 (DLS)	-	[68]
	Folate receptor	Mouse	Small molecule	Folic acid	$Au_{22}SG_{18}$	1.4	-	[95]
	-	Mouse	-	-	AuNPs-SG-Au^{198}	2.6 ± 0.3	-	[107]
	CCR5	Xenografted breast cancer mice	Peptide	D-Ala1-peptide T-amide	^{199}AuNPs-PEG	5	-	[108]
PET/CT	LHRH receptor	Xenografted lung cancer mice	Peptide	LHRH peptide	AuNCs-HSA-I^{124}	2	-	[74]
	Thyroid	Patient-derived xenografted thyroid cancer mice	Chemical element	^{127}Iodine	AuNCs-BSA-I^{127}	6.4 (DLS)		[68]
	EGFR	Xenografted epidermoid carcinoma cancer mice	Antibodies	VHH 122 Ab Cetuximab	AuNPs-PEG	28/42/45/63(DLS) (NPs/+PEG/+VHH/+cet)	0.22/0.30/ 0.31/0.24	[101]
	CA 19.9 antigen	Pancreatic cancer cell lines Xenografted pancreatic cancer mice	Antibody	5B1 antibody	AuNPs-Zr^{89}	34.86 (DLS)	0.27	[104]
-	EGFR	Colon cancer cell lines	Antibody	Anti-EGFR Ab	AuNPs	14.9 ± 1.23	-	[109]
Auto-radiography	CCR5	Xenografted breast cancer mice	Peptide	D-Ala1-peptide T-amide	^{199}AuNPs-PEG	5	-	[108]
Auto-metallography	EGFR	Glioblastoma, fibrosarcoma cancer cell lines	Antibody	Cetuximab	AuNPs	2.4 ± 0.28	-	[110]
Photoacoustic imaging	EGFR	Epidermoid carcinoma cancer cell line	Antibody	Anti-EGFR Ab	AuNPs	5	-	[76]
	GRPR	Prostate cancer cell lines Xenografted prostate cancer mice	Peptides	GRPR-targeting peptides	Au nanorod	8 ± 2 nm (W)/49 ± 8 nm (L)	-	[77]

2. Potential of Quantum Nanoclusters as Non-Linear Optical Probes in Molecular Diagnostics of Cancer

Given the variety of options for nanomaterials as well as for the specializing and structural ligands, the choice of an optimal nanodevice in designing strategies for tumor biomarker detection presents a challenge. In this section, we elaborate on opportunities provided by optical molecular imaging as a technique for biomarker detection and gold NCs as non-linear optical (NLO) probes. NCs are particularly interesting due to their distinctive physicochemical properties. However, these unique properties of the NCs are often poorly recognized in the literature, promoting the perception of the NCs as merely a smaller version of NPs. Here, we emphasize the key physicochemical features of the NCs, in particular those features responsible for their biocompatible optical properties that might be relevant for their application in cancer diagnostics.

2.1. Non-Linear Optical Techniques and Nanomaterials

Optical molecular imaging is holding great promise in cancer diagnosis. However, a critical issue for photo-induced imaging is the capability of light to penetrate tissues. Since tissues such as blood, fat, and skin inherently interact with any incident light, leading to light absorption and/or scattering, it is essential for OI to operate at wavelengths where light attenuation is minimal. The first NIR (NIR-I) window, between 700 and 900 nm, and, more interestingly, the second (NIR-II) window fulfill this requirement for biological imaging (Figure 1a) [111]. Thus, any contrast agents with small optical gaps and, hence, with absorption (and possibly emission) in the NIR-II (1000–1400 nm) are highly desired (Figure 1b). For this purpose, a plethora of exogenous contrast agents has been developed, including inorganic imaging contrast agents and organic probes [111]. However, a major challenge concerns the elucidation of the biocompatibility, pharmacokinetics, and long-term toxicological profiles of such NIR-II contrast agents.

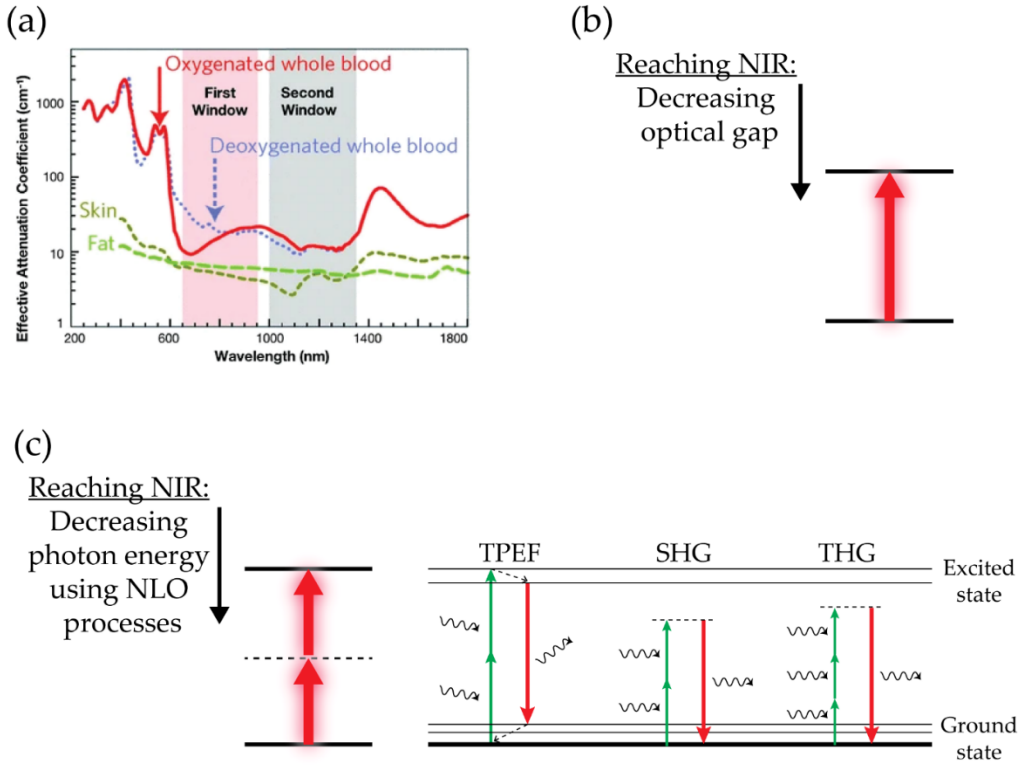

Figure 1. Optical imaging in biological samples. (**a**) Tissues such as skin, fat, and blood (oxygenated and deoxygenated) attenuate light in a wavelength-dependent manner due to absorption and scattering. Attenuation is the lowest in the first (NIR-I, 700–900 nm, shaded in pink) or second near-infrared window (NIR-II, 1000–1700 nm, shaded in grey). Image adapted from [112] with permission from Springer Nature. (**b**,**c**) Strategies for reaching the NIR-I and NIR-II windows: using chromophores with small optical gaps (**b**) or applying NLO techniques (SHG, THG, and TPEF) (**c**). Images adapted from [113].

As an alternative to using chromophores with small optical gaps, NLO techniques such as second harmonic generation (SHG) and two-photon-excited fluorescence (TPEF) can be exploited (Figure 1c) [114]. SHG is a phenomenon whereby two photons with the same frequency get combined during interaction with a non-linear material, generating a new photon with twice the energy of the initial photons while conserving the coherence of interaction. TPEF is based on simultaneous excitation with two photons, followed by the emission of light with shorter wavelengths, and it is an incoherent phenomenon involving radiative absorption and re-emission. In both cases, the photon energy can match the second (NIR-II) window for biological imaging due to the inherent multi-photon process. Thanks to the complementary information that they can provide, as well as the enhanced contrasts and improved resolution, SHG and TPEF have gained overwhelming popularity among biologists and have emerged as promising tools in the field of pre-clinical and clinical cancer research.

In particular, TPEF imaging has become popular in tissue imaging due to its advantages of longer wavelength excitation (>1000 nm), which minimizes auto-fluorescence and bleaching and allows for a higher 3D resolution and deep tissue imaging in comparison to one-photon fluorescent microscopy [115]. Moreover, a study performed by Lianhuang Li et al. showed that TPEF combined with SHG helped in identifying early gastric cancer by assessing cell size and collagen alternations without using exogenous contrast agents [116]. Interestingly, the sensitivity of such NLO techniques can be dramatically enhanced using exogenous contrast agents with NLO properties. Some organic dyes have already been applied in multi-photon imaging, but their performance has been hampered due to their rapid photo-bleaching and limited two-photon absorption (TPA) cross-sections [117]. Quantum dots might be a superior option for multi-photon imaging as they display large two-photon absorption cross-sections [118], but their strong cytotoxicity and photon-blinking behavior [119] limit their applicability. Designing highly efficient second-order NLO-phores is largely a matter of the fine combination of a high density of delocalized electrons in a symmetrical or unsymmetrical environment. Recent advances in the field of nanotechnology have allowed for the development of nanostructures that display higher diffusion through tissues along with high TPA cross-sections [113,120]. In particular, as discussed below, NLO characteristics of liganded noble metal NCs and the possibility of their functionalization with specific recognition moieties hold promise for the integration of such NCs with tools of precision medicine that might help in early cancer detection as well as the stratification of patients and the development of treatment options.

2.2. Quantum Nanoclusters—General Features

NCs are an extremely appealing family of nanomaterials, in particular for bio-imaging applications. NCs are characterized by a small number of metal atoms (between a few and hundreds of atoms) and by molecular-like discrete states for which strong fluorescence might occur. The connection between their structural and optical properties arises in the size regime, in which "each atom counts", meaning that the removal or addition of a single metal atom can substantially change structural and optical properties. However, NCs have to be stabilized and protected from the environment in order to prevent their degradation or aggregation. The protection of noble metal NCs from photo-dissociation by inorganic matrices or solid gas has been used since 1987 [121]. Dickson et al. first reported in 2002 [122] the role of organic scaffolds, e.g., DNA oligomers, in the synthesis of silver NCs as both metal cluster protection and the key ingredient for enhancing NC emission in the visible to NIR regime. This dual role of ligands is quite general and has found an application in boosting the NLO properties of liganded gold and silver NCs.

A large variety of ligands, including amino acids, peptides, proteins, small organic molecules, polymers, DNA, and dendrimers, can be used for the protection of NCs. Figure 2 illustrates different ways to form and stabilize NCs in solution [123,124]. Various ligand-engineering strategies have been developed to enhance the emissive properties of NCs [67]. Among the large variety of ligand families, thiolated molecules are particularly suitable

due to strong Au-S binding. Additionally, thiols can be found in organic ligands but also in natural biomolecules such as peptides and proteins. AuNCs with an appropriate choice of thiol-containing ligands present with extremely good stability and biocompatibility and attractive emissive properties, i.e., strong emitted fluorescence. These properties authorize in vitro and in vivo detection of thiolated NCs by multimodal imaging techniques. The wavelength of NC luminescence can be tuned from near-ultraviolet (UV) to the IR region, allowing their detection by X-ray CT, OI, MRI, or photoacoustic imaging. Importantly, NCs demonstrate higher brightness and photo-stability in comparison to organics dyes, which are prone to photobleaching [125].

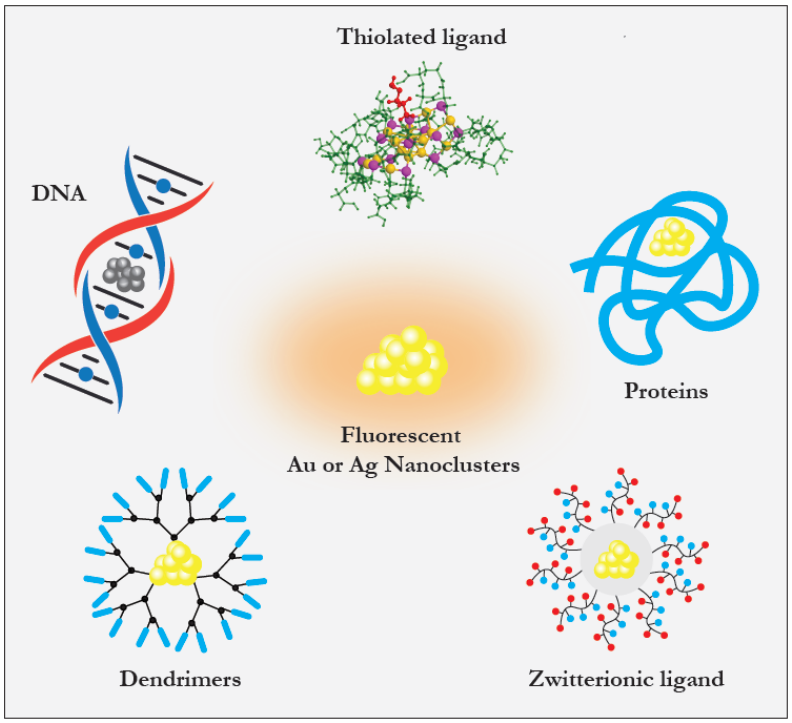

Figure 2. Metal nanoclusters protected with different scaffolds.

The ligand selection is of key importance not only for optimizing the optical properties of the NCs but also for developing their targeting competency. NCs can be functionalized during the initial synthesis by the addition of selected target-binding molecules directly on the surface of NCs, e.g., via covalent attachment (post-functionalization) or by ligand exchange after liganded NC synthesis if the target molecule of interest has a thiol group (see Section 2.4.3). Finally, sufficient biocompatibility with minimal toxicity is required to qualify any liganded NC as a good candidate for biomedical imaging.

2.3. Biological Properties of AuNCs

2.3.1. Cellular Uptake—Internalization Mechanisms and Cytotoxicity

The cellular uptake of AuNCs has been studied in multiple cellular systems [126]. It has been shown that the internalization of NCs is energy-dependent [127,128] and relies on multiple endocytic mechanisms such as clathrin-mediated endocytosis and micropinocytosis. The caveolin-mediated pathway is also involved, albeit to a lesser extent. Following their uptake, AuNCs were ultimately transferred to the lysosomes and were not able to reach the nucleus even after 24 h of incubation with the cells [127]. The time dimension of AuNC uptake was studied in BaF3 cells using an AuNC biofunctionalized with an aptamer to target the IL6 receptor [129]. This study has shown that the NCs were bound to the cellular membrane after 10 min of incubation with the cells and were internalized into the cells after an additional 10 min. The cellular uptake of AuNCs has also been demonstrated

in an in vitro model of the blood–brain barrier (BBB) using an AuNC functionalized with l-3,4-dihydroxyphenylalanine (L-Dopa) to target the brain and cross BBB [82].

The nature of the ligands may affect the cellular uptake of AuNCs. For instance, zwitterionic ligands seem to be more supportive of AuNC internalization than the PEGylated ones in human-derived monocyte dendritic cells [130]. Similarly, MPA-liganded AuNCs were taken up more efficiently than GSH-AuNCs in the normal human colon mucosal epithelial cell line NCM460 [131].

Generally, the cellular uptake of nanomaterials depends on their size and cell type. Controversial results exist about the efficiency of AuNC uptake relative to other nanomaterials. For instance, the internalization of NCs is relatively low compared to larger particles such as quantum dots [132] in the reticuloendothelial system (RES)—phagocytic cells that clear the circulation and tissues from particles and soluble substances. However, in human dendritic cells, AuNCs are internalized via the endocytic pathway more efficiently than the larger AuNPs.

Importantly, when internalized, AuNCs might cause perturbations in the cellular environment. Recently, a study on human primary astrocytes demonstrated that AuNCs were not inert within the cells. Even though no significant cell loss has been observed for AuNC concentrations below 10 μM, alterations were detected in the organellar and redox-responsive transcription factor homeostasis [133]. These effects may also depend on the nature of the ligands. For instance, the type of ligand may determine the type of immune response in dendritic cells [130] as well as the state of intracellular redox signaling [131].

2.3.2. Biodistribution

Nanomaterials can reach and accumulate in tumors via passive and active targeting. While active targeting depends on specific interactions between nanomaterials and tumors (see Section 1.3.3), passive tumor targeting by nanomaterials precedes the active targeting and is essential to create an opportunity for the occurrence of specific interactions. Indeed, passive and preferential targeting of the tumors by both NPs and NCs have been observed, and this phenomenon has been named the enhanced permeability and retention effect (EPR) [132,134]. EPR can be explained by the presence of pores with sizes of up to 2000 nm within tumors [135]. These pores represent inter-endothelial gaps formed during angiogenesis in the tumors, and they allow NPs to accumulate in cancer tissues at higher concentrations than in normal tissues. Thus, this passive accumulation of NPs in tumors takes advantage of the pathophysiological properties of the tumor tissue. Despite being the foundation of tumor-targeted drug delivery and the NP accumulation principle, the EPR effect in patients has been recently questioned [136,137]; the mechanism of entry of NPs into solid tumors appears to be more intricate than considered earlier [138]. Either way, passive tumor targeting by nanomaterials has certain disadvantages, such as arbitrary targeting, inefficient dispersion of the NPs, and variability among different tumor types and different patients [137]. Interestingly, the EPR effect is generally more pronounced in animal models than in cancer patients, which hampers understanding of the NC biodistribution and translation to clinic of the results obtained in animal studies.

The biodistribution of NPs and NCs is affected by their interaction with the environment, and this interaction differs for NPs and NCs. Upon administration, NPs are rapidly exposed to protein-rich biological fluids. These proteins interact with the NPs and form a protein corona on their surface [139]. Such protein coronas affect the size and charge of the NPs [140] as well as their stability, dispersibility, pharmacokinetics, and toxicity profiles [141]. Ultimately, the biodistribution of decorated NPs is altered, and they may even get recognized by the immune system (RES). It has been demonstrated that the protein corona promotes the cellular uptake of the NPs by the immune cells of the RES. To avoid recognition by the immune system, PEGylation of the NPs was introduced, which resulted in an increase in the blood circulation of the NPs as a side effect [142].

Currently, little is known about the nano–bio interactions of NCs, and it is still unclear how they interact with proteins from the biological environment. Interestingly, Yin et al.

showed that the conventional protein corona model in DHLA-liganded AuNCs does not apply, and they coined the term "protein complex" for proteins bound to NCs [143]. More studies are required to characterize the NC–protein interaction and its impact on the biodistribution, cellular uptake, and cytotoxicity of the NCs.

The fine-tuning of nanomaterial biodistribution within tissues and cells can be achieved by active targeting, as described in Section 1.3.3. A variety of ligands can be used for this purpose, and they are usually small molecules that specifically interact with receptors overexpressed at the surface of the tumor cells. Antibodies, aptamers, or peptides are often used since they target proteins on the cell surface [74] and increase the probability of endocytosis of the nanomaterials by tumor cells.

2.3.3. Toxicity and Clearance

Clinical application of the nanomaterials depends on their toxicity and clearance from the body. Regarding the overall toxicity of nanomaterials, it is important to consider their toxic effects both in vitro and in vivo. High toxicity in vitro (in the cell culture models) can be counteracted in vivo by efficient clearance and vice versa.

The size, shape, surface properties, and chemical composition of the nanomaterials are critical determinants of their toxicity and clearance [144]. However, the results of various toxicological studies are controversial, making it difficult to derive straightforward conclusions. While some researchers have shown that nanomaterials smaller than 5 nm (which include the NCs) are more toxic than the larger ones, both in vitro [145–147] and in vivo, in the zebrafish model [148], others have reported the opposite results in vivo [149–151].

Clearance mechanisms have been well described for NPs [152]. Three systems are involved in the clearance of NPs. The first one is the RES, where macrophages phagocytose large NPs (>6 nm), leading to extended retention (up to 6 months) of the partially digested NPs in the body. The second clearance pathway is hepatobiliary excretion [153]. This pathway is also utilized by NPs larger than 6 nm, and their retention, in this case, lasts for up to a couple of weeks. The third elimination route is renal excretion, where the glomerular capillary walls act as a filter for NPs smaller than 6 nm [154]. Renal clearance is often preferred because of the fast and efficient removal of NPs (hours to days), especially non-degradable noble metal NPs [152]. With their small size (<2nm), Au liganded NCs are cleared in vivo through the renal system, which makes them excellent candidates for clinical applications.

Given that the biological safety of nanomaterials depends on many intrinsic and extrinsic factors, including their biological environment, toxicity must be evaluated for each specific NC.

2.4. Structure, Optical Properties, and Functionalization of Quantum Nanoclusters

2.4.1. Structure of Quantum Nanoclusters

To synthesize AuNCs containing only several atoms, an appropriate combination of parameters such as temperature, stabilizers, reduction method, and the initial ratio of metal salt to stabilizer is needed. The atomic precision and molecular purity of AuNC can be reached using size-focused methodology [155–157]. In addition, the use of ligands is crucial not only for the stabilization of AuNCs but also for tailoring their fluorescent properties. Suitable ligands with electron-rich atomic groups can enhance the fluorescence of AuNCs due to the charge transfer between the ligands and the metal core [158]. Thiols are commonly employed as ligands for noble metal NCs because of the strong affinity of sulfur to noble metals, especially to gold. Moreover, thiol-containing molecules are good stabilizers for AuNCs. Among thiols, GSH has played a key role in the production of AuNCs [159–161].

A distinctive feature of atomically precise ligand-protected noble metal NCs is the connection between their structure and their spectroscopic properties. The properties of such NCs can be determined using experimental and theoretical approaches, which provide complementary information. Different techniques, such as X-ray crystallography,

mass spectrometry, X-ray powder diffraction (XRPD), and nuclear magnetic resonance (NMR) spectroscopy, have been used for the characterization of AuNCs [45,123,162,163]. The structure of some NCs has been resolved experimentally by means of a single crystal X-ray diffraction [123].

Theoretical approaches include density functional theory (DFT) and time-dependent density functional theory (TDDFT), where a basic variable, the many-body wavefunction, is replaced by a density function. The TDDFT approach allows the calculation of the photoabsorption spectra for relatively large systems after the structural properties have been determined by DFT. Despite significant approximations, these theoretical approaches are useful for predictions of structural and optical properties of both protected and unprotected NCs [164].

The combined experimental and theoretical findings resulted in a scheme depicting the link between the structure and optical properties of the liganded AuNCs (Figure 3). In that scheme (upper panel), the AuNC is presented as a multi-shell system that consists of three components: a metal core, the metal–ligand interface with staple motifs, and surface ligands. Surface thiolate ligands (SRs) do not just passivate the gold core but build staples or semi-rings, $Au(SR)_2$ (-RS-Au-RS) or $Au_2(SR)_3$ (-RS-Au-S(R)-Au-SR-), that bind to the core surface and serve as its protection. The existence of three shells enables a ligand-to-metal core charge transfer (LMCT) or ligand-to-metal metal charge transfer (LMMCT). In both cases, communication can occur either through direct bonding or through the donation of electron-rich ligand groups. NIR and visible absorption of AuNCs is always a consequence of charge transfer, which occurs either due to metal–metal electron transitions or via LMCT and LMMCT (Figure 3, bottom panel). For instance, Zhou and coworkers revealed that the visible and NIR emissions of Au_{25} NCs originate from the surface state and Au_{13} core state, respectively [165].

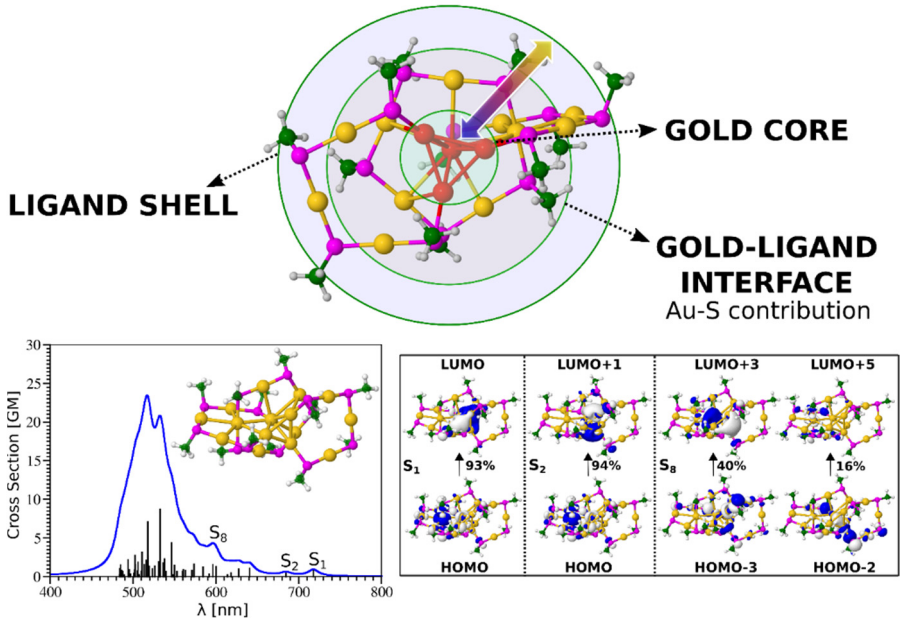

Figure 3. Diagram showing the view of liganded gold nanoclusters as multi-shell system on an example of $Au_{15}(SCH_3)_{13}$ (**upper panel**). TDDFT two-photon absorption spectrum (**bottom left**) and molecular orbitals (**bottom right**) involved in transitions for an $Au_{15}(SCH_3)_{13}$ nanocluster. The upper scheme was adapted from [45] (p. 18). For theoretical methods used for the **bottom panel**, see [113].

2.4.2. Quantum Nanoclusters as Non-Linear Optical Probes

Liganded silver and gold NCs represent an emerging class of extremely interesting optical materials due to their remarkable NLO characteristics. SHG and/or TPA/TPEF processes can reach the highest corresponding cross-sections by a rational design of "ligand–

core" templates and by controlling the NC size and/or asymmetry (Figure 4). A direct correlation between the structure and (multi)photonic properties of these nano-objects has been determined via experimental and theoretical investigations of the structure–property relationship (Figure 5). The TPA cross-section of liganded noble metal NCs is several orders of magnitude larger than that of commercially available dyes. These enhanced NLO properties are due to a subtle balance between resonance effects (position of transitions vs. laser excitation) and large transition dipole moments (due to ligand-to-core charge transfer character of excitations). On the other hand, the structure asymmetry (inherent to the metal core and/or brought by the asymmetric arrangement of surface ligands) in NCs can boost the SHG process (sensitive to non-centrosymmetric systems) [166], as evidenced by the enhanced NLO properties of $Au_{15}SG_{13}$ [167].

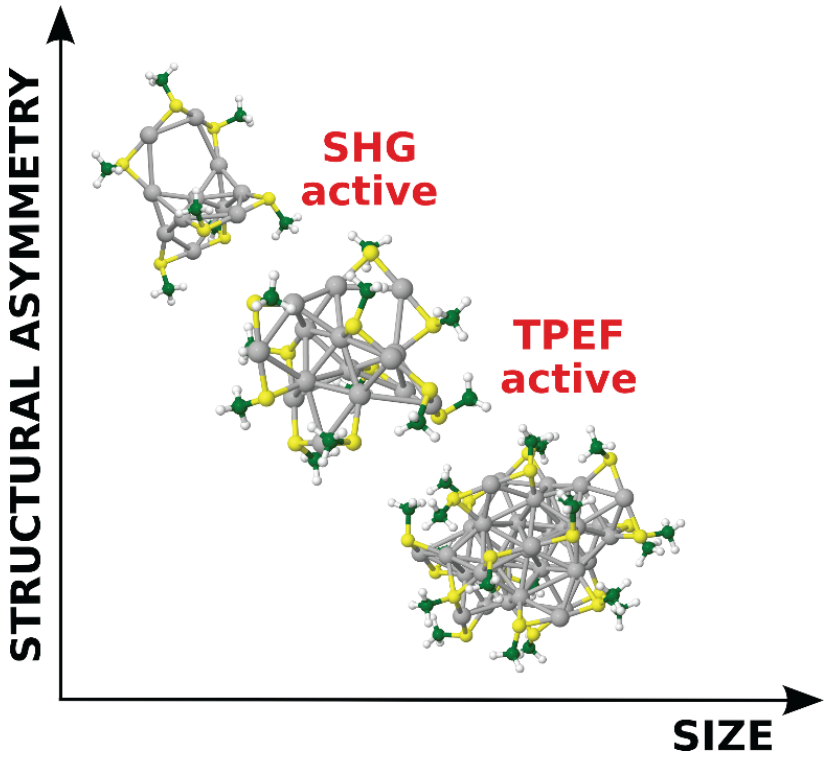

Figure 4. NLO properties of liganded metal nanoclusters as a function of size and asymmetry (Ag_{11}, Ag_{15}, and Ag_{32} are shown as examples).

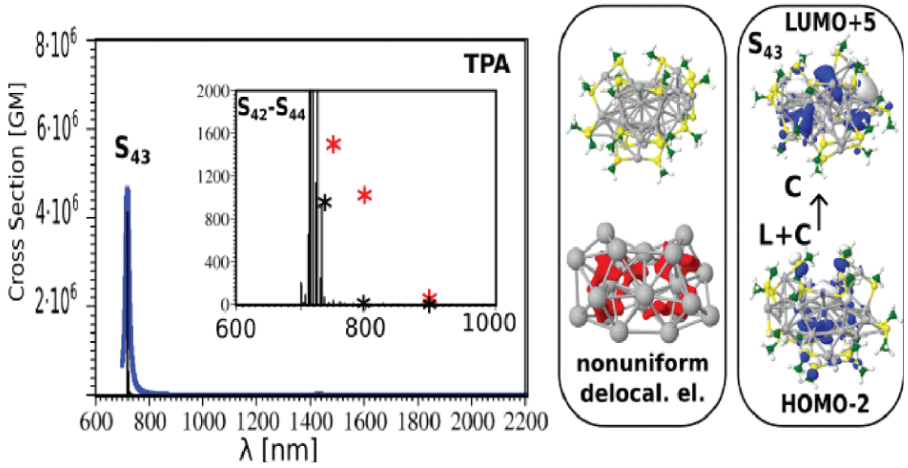

Figure 5. TDDFT TPA absorption spectrum (and experimental values in insets, red crosses) and molecular orbitals involved in transitions for $Ag_{31}(SCH3)_{19}$ nanoclusters (right side). Giant TPA cross-sections have been reported.

2.4.3. Functionalization of Quantum Nanoclusters

Functionalization is of crucial importance for creating tumor-biomarker-specific NCs with optimal bio-compatible optical properties. One of the great advantages of NCs is their suitability for efficient and controlled functionalization. Small organic molecules and biomolecules are commonly added to the NC surface as fluorophores to shift the optical properties of NCs towards the NIR region. Drugs, photosensitizers, or radiosensitizers can be used for functionalization for cancer therapy or as targeting molecules that interact specifically with receptors overexpressed at the surface of tumor cells. Such interfacial engineering of AuNCs for biomedical applications has been recently reviewed by Xie's group [168]. One efficient approach to functionalization is a direct synthesis of AuNCs, with the molecule of interest containing a terminal thiol group that can bind to the metal surface. For instance, Le Guevel et al. [169] started with zwitterionic sulfobetaine-stabilized AuNCs that have the capacity to accumulate in brain tumors. To further improve the tumor uptake of these AuNCs, they functionalized them with arginine, and the resulting AuSG-2Arg exhibited rapid accumulation in cancer cells, thus being potentially interesting for radiotherapy enhancement [170]. A second approach is based on the post-functionalization of NCs, whereby click chemistry and succinimidyl ester reactions were used to covalently bind molecules of interest to the protective ligand [125].

A third approach, the ligand exchange strategy, is based on the replacement of the preexisting structural ligand with a specializing ligand containing a thiol group. The ligand exchange strategy is possible due to the unique structural features of the NCs, which can be prepared with atomic precision. This is in stark contrast to larger NPs, for which the control of surface functionalization is not possible. In addition to adding specific recognition properties to the NC, introducing a controlled number of functional ligand molecules by a ligand exchange strategy can also boost NCs' NLO properties. Indeed, this ligand exchange will induce symmetry breaking in NCs, leading to efficient second-order nonlinear scattering, in particular for SHG signals, as demonstrated by Verbiest and colleagues [171]. Ligand shell engineering through ligand exchange can also increase the stability of metal NCs' surface and lead to rigidification effects, enhancing their fluorescence properties [172,173]. The introduction of functional ligands through a ligand exchange strategy may also enhance their non-linear photoluminescence through a subtle interplay of metal–ligand interaction.

An example of a successfully applied ligand exchange strategy to introduce a specific recognition moiety into NCs is a recent generation of thiolated aminooxy-functionalized AuNCs, which can interact with protein carbonyls and be detected using optical methods (Figure 6) [167]. $Au_{15}SG_{13}$ NCs were readily functionalized by one or several thiolated

aminooxy molecules (3-(aminooxy)-1-propanethiol) via a ligand exchange procedure. The as-prepared functionalized aminooxy-Au15 NCs were reacted with carbonylated proteins. The targeted carbonylated proteins were then detected either by one-photon fluorescence (with a fluorescence scanner) or by TPEF (with a multi-photon confocal microscope). Protein carbonylation at the molecular level on model lysozyme was validated by computation chemistry to better evaluate the nature of binding between the NCs and the protein carbonyls (see Figure 4). Altogether, this is proof of principle that functionalized liganded AuNCs can serve for the detection of carbonylation sites and might be more efficient than organic dyes. Such rational design of novel functional bi-thiolate-protected metal NCs with controllable surface chemistry could pave the way towards many similar practical applications, particularly in the molecular diagnostics of cancer.

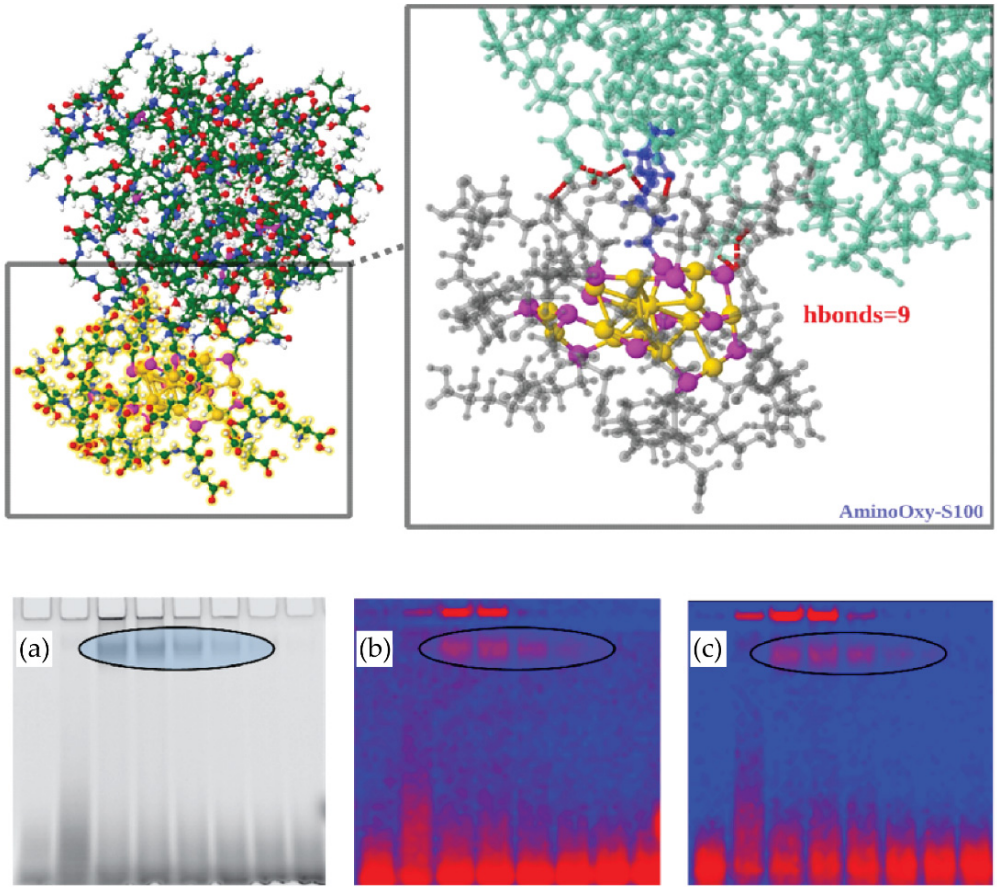

Figure 6. Detection of protein carbonyls using aminooxy-liganded AuNCs (top panel). Quantum mechanics/molecular mechanics (QM/MM) (two-layer ONIOM [174]) interacting with lysozyme. The interface between liganded cluster $Au_{15}(SG)_{12}$(3-(aminooxy)-1-propanethiol)1 and protein is enlarged (right side), illustrating the aminooxy-serine oxyme bond and the hydrogen-bonding network (SG—grey; Au—gold; S—magenta; lysozyme—green; oxyme bond—blue; h-bonds—dotted in red). Figure adapted from [167] (bottom panel). Au15-targeted carbonylated proteins detected on gels by fluorescence scanner (**a**) and multiphoton confocal imaging (**b**,**c**). Laser excitation was at 780 nm, and emitted photons were detected with (**b**) visible range (350–700 nm) and (**c**) IR range (>850 nm). Ellipses: Fixed concentration of 500 μM $Au_{15}(SG)_{12}$(3-(aminooxy)-1-propanethiol)1 was incubated with a decreasing range of concentrations of the lysozyme (50–1 μM, corresponding to 5–0.1 μg protein loaded in the gel).

2.4.4. Application of the AuNCs in Cancer Diagnostics

To date, numerous AuNCs have been developed for the detection of tumor biomarkers such as the folate receptor, calreticulin, citrate, or the LHRH receptor (see Table 2). While

many of them have been studied in cell lines, there are examples where they have been tested in liquid biopsies such as human urine and even in vivo in mouse models of cancer. For instance, Cys-AuNCs have been used to indirectly quantify the amount of citrate—a biomarker of early stages of prostate cancer—in a colorimetric assay applied in human urine [97]. This assay is based on a citrate-mediated inhibition of the intrinsic peroxidase-mimetic activity of Cys-AuNCs. Another example is an AuNC liganded with a tumor-targeting LHRH peptide and labeled with iodine-124, which has been used as a PET tracer for lung cancer in xenografted mice [74]. Even though AuNCs are still insufficiently explored, these and other similar studies pave the way for their future application in the clinical setting.

3. Conclusions—Perspectives

Various nanomaterials have been developed as tools of precision medicine for the detection of tumor biomarkers. Liganded metal nanomaterials such as NPs and NCs are structurally highly versatile, thus providing numerous opportunities for specific applications. They can be adapted to detect different biomarkers and for visualization by different imaging techniques through the selection of suitable specializing (biomarker recognition moieties) and structural ligands, respectively. Given the increasing number of newly developed nanomaterials and options for their detection, the choice of a specific nanomaterial in a desired application becomes a challenge. In this review, we have discussed atomically precise ligand-protected noble metal NCs and their properties relevant for tumor biomarker detection (summarized in Figure 7). They are characterized by non-linear optical properties that are compatible with biological samples and allow for deep-tissue imaging. Moreover, their functionalization can be precisely controlled. Finally, they can be rapidly eliminated from the body via the renal clearance system. Together, these considerations emphasize the value of NCs as tools in the molecular diagnostics of cancer.

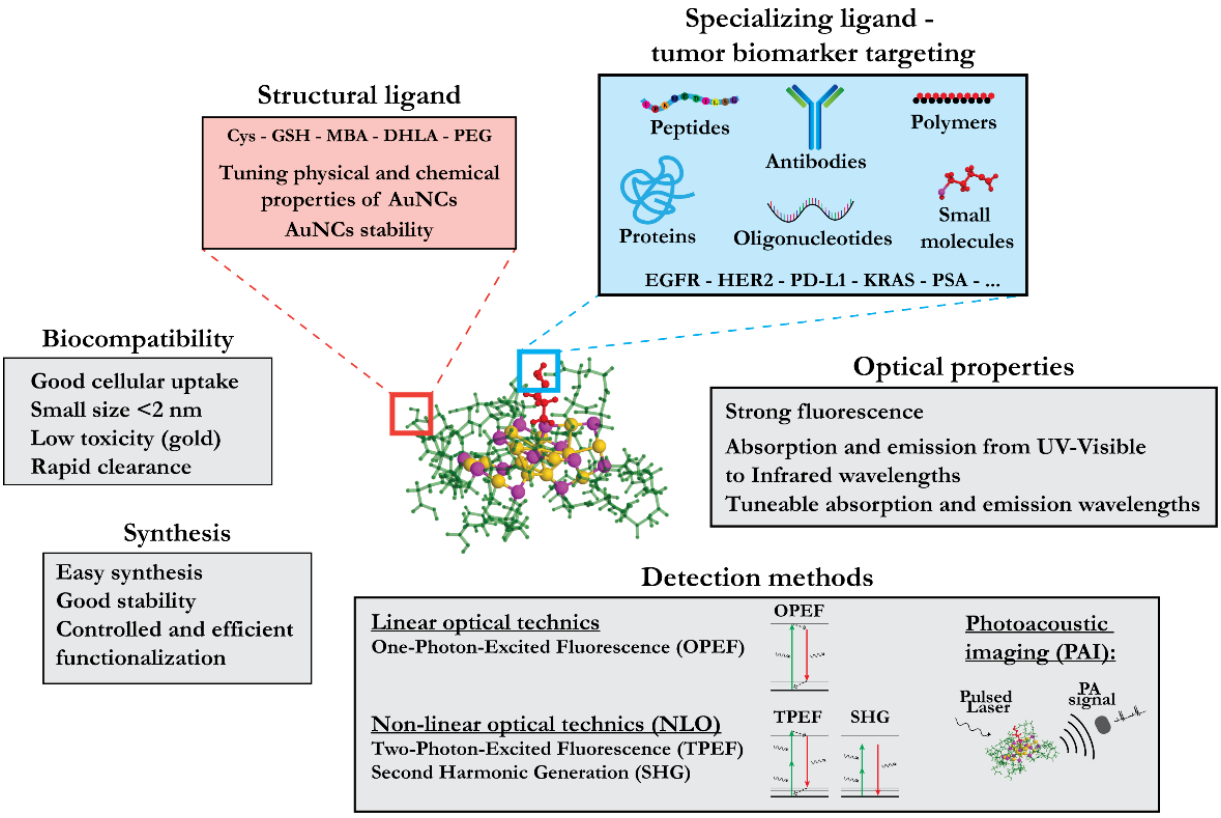

Figure 7. Summarized properties of liganded AuNCs as cancer diagnostics agents.

Author Contributions: All authors participated in the writing and editing of the manuscript as well as in the preparation of the figures. All authors have read and agreed to the published version of the manuscript.

Funding: This research was supported by the project STIM-REI (Contract Number: KK.01.1.1.01.0003), funded by the European Union through the European Regional Development Fund—the Operational Programme "Competitiveness and Cohesion" 2014–2020 (KK.01.1.1.01).

Acknowledgments: V.B.-K. and M.P.B. acknowledge the computational facilities of the HPC computer within the STIM-REI project, the doctoral study of biophysics at the University of Split as well as Miroslav Radman at MedILS and Split-Dalmatia County for their support.

Conflicts of Interest: The authors declare no conflict of interest.

Abbreviations

AuNC	Gold nanocluster
AuNP	Gold nanoparticle
BBB	Blood–brain barrier
BRCA	Breast cancer gene
CA 125	Cancer antigen 125
CA 19-9	Cancer antigen 19-9
CCR5	C-C chemokine receptor type 5
CEA	Carcinoembryonic antigen
CT	Computed tomography
CTC	Circulating tumor cell
DFT	Density functional theory
DHLA	Bidentate dihydrolipoic acid
DLS	Dynamic light scattering
EGFR	Epidermal growth factor receptor
ELISA	Enzyme-linked immunosorbent assay
EPR	Enhanced permeability and retention effect
erbB3	Erb-B2 Receptor Tyrosine Kinase 3
FDG	2-^{18}F-fluorodeoxyglucose
GLUT1	Glucose transporter 1
GRPR	Gastrin-releasing peptide receptor
GSH	Glutathione
hCG	Human chorionic gonadotropin
HER2	Human epidermal growth factor receptor 2
ICP-AES	Inductively coupled plasma atomic emission spectroscopy
ICP-MS	Inductively coupled plasma mass spectrometry
IR	Infrared
L-DOPA	l-3,4-dihydroxyphenylalanine
LMCT	Ligand-to-metal core charge transfer
LMMCT	Ligand to metal-metal charge transfer
LNGFR	Low-affinity nerve growth factor receptor
MCAM	Melanoma cell adhesion molecule
MCSP	Melanoma-associated chondroitin sulfate proteoglycan
MMP9	Matrix metallopeptidase 9
MPA	Mercaptopropionic acid
MRI	Magnetic resonance imaging
NC	Nanocluster
NIR	Near infrared
NLO	Nonlinear optics
NP	Nanoparticle
OI	Optical imaging
PDI	Polydispersity index
PD-L1	Programmed death-ligand 1
PEG	Polyethylene glycol
PET	Positron emission tomography

PrPC	Cellular prion protein
PSA	Prostate-specific antigen
PSMA	Prostate-specific membrane antigen
QM/MM	Quantum mechanics/molecular mechanics
RES	Reticulo-endothelial system
SERS	Surface-enhanced Raman spectroscopy
SHG	Second harmonic generation
SPECT	Single-photon emission computed tomography
SPR	Surface plasmon resonance
SR	Surface thiolate ligands
TDDFT	Time-dependent density functional theory
THG	Third harmonic generation
TPA	Two-photon absorption
TPEF	Two-photon-excited fluorescence
UV	Ultraviolet

References

1. Bray, F.; Laversanne, M.; Weiderpass, E.; Soerjomataram, I. The Ever-Increasing Importance of Cancer as a Leading Cause of Premature Death Worldwide. *Cancer* **2021**, *127*, 3029–3030. [CrossRef]
2. Sung, H.; Ferlay, J.; Siegel, R.L.; Laversanne, M.; Soerjomataram, I.; Jemal, A.; Bray, F. Global Cancer Statistics 2020: GLOBOCAN Estimates of Incidence and Mortality Worldwide for 36 Cancers in 185 Countries. *CA Cancer J. Clin.* **2021**, *71*, 209–249. [CrossRef] [PubMed]
3. Edwards, B.K.; Noone, A.M.; Mariotto, A.B.; Simard, E.P.; Boscoe, F.P.; Henley, S.J.; Jemal, A.; Cho, H.; Anderson, R.N.; Kohler, B.A.; et al. Annual Report to the Nation on the Status of Cancer, 1975–2010, Featuring Prevalence of Comorbidity and Impact on Survival among Persons with Lung, Colorectal, Breast, or Prostate Cancer. *Cancer* **2014**, *120*, 1290–1314. [CrossRef]
4. Overman, M.J.; Modak, J.; Kopetz, S.; Murthy, R.; Yao, J.C.; Hicks, M.E.; Abbruzzese, J.L.; Tam, A.L. Use of Research Biopsies in Clinical Trials: Are Risks and Benefits Adequately Discussed? *J. Clin. Oncol.* **2013**, *31*, 17–22. [CrossRef]
5. Kułakowski, A. The Contribution of Marie Skłodowska-Curie to the Development of Modern Oncology. *Anal. Bioanal. Chem.* **2011**, *400*, 1583–1586. [CrossRef]
6. García-Figueiras, R.; Baleato-González, S.; Padhani, A.R.; Luna-Alcalá, A.; Vallejo-Casas, J.A.; Sala, E.; Vilanova, J.C.; Koh, D.M.; Herranz-Carnero, M.; Vargas, H.A. How Clinical Imaging Can Assess Cancer Biology. *Insights Imaging* **2019**, *10*, 1–35. [CrossRef] [PubMed]
7. Cal-Gonzalez, J.; Rausch, I.; Sundar, L.K.S.; Lassen, M.L.; Muzik, O.; Moser, E.; Papp, L.; Beyer, T. Hybrid Imaging: Instrumentation and Data Processing. *Front. Phys.* **2018**, *6*, 47. [CrossRef]
8. Phelps, M.E.; Hoffman, E.J.; Mullani, N.A.; Ter-Pogossian, M.M. Application of Annihilation Coincidence Detection to Transaxial Reconstruction Tomography. *J. Nucl. Med.* **1975**, *16*, 210–224.
9. Di Chiro, G.; DeLaPaz, R.L.; Brooks, R.A.; Sokoloff, L.; Kornblith, P.L.; Smith, B.H.; Patronas, N.J.; Kufta, C.V.; Kessler, R.M.; Johnston, G.S.; et al. Glucose Utilization of Cerebral Gliomas Measured by [18F] Fluorodeoxyglucose and Positron Emission Tomography. *Neurology* **1982**, *32*, 1323. [CrossRef] [PubMed]
10. Gambhir, S.S. Molecular Imaging of Cancer with Positron Emission Tomography. *Nat. Rev. Cancer* **2002**, *2*, 683–693. [CrossRef] [PubMed]
11. McGrath, S.; Ghersi, D. Building towards Precision Medicine: Empowering Medical Professionals for the next Revolution. *BMC Med. Genom.* **2016**, *9*, 23. [CrossRef]
12. National Research Council. *Toward Precision Medicine: Building a Knowledge Network for Biomedical Research and a New Taxonomy of Disease*; National Academies Press: Washington, DC, USA, 2012; ISBN 0309222222. [CrossRef]
13. Jameson, J.L.; Longo, D.L. Precision Medicine—Personalized, Problematic, and Promising. *N. Engl. J. Med.* **2015**, *372*, 2229–2234. [CrossRef]
14. Ashley, E.A. Towards Precision Medicine. *Nat. Rev. Genet.* **2016**, *17*, 507–522. [CrossRef]
15. Kumar, S.; Mohan, A.; Guleria, R. Biomarkers in Cancer Screening, Research and Detection: Present and Future: A Review. *Biomarkers* **2006**, *11*, 385–405. [CrossRef] [PubMed]
16. Tung, N.M.; Garber, J.E. BRCA1/2 Testing: Therapeutic Implications for Breast Cancer Management. *Br. J. Cancer* **2018**, *119*, 141–152. [CrossRef] [PubMed]
17. Owens, D.K.; Davidson, K.W.; Krist, A.H.; Barry, M.J.; Cabana, M.; Caughey, A.B.; Doubeni, C.A.; Epling, J.W.; Kubik, M.; Landefeld, C.S.; et al. Risk Assessment, Genetic Counseling, and Genetic Testing for BRCA-Related Cancer: US Preventive Services Task Force Recommendation Statement. *JAMA* **2019**, *322*, 652–665. [CrossRef]
18. Tutt, A.; Robson, M.; Garber, J.E.; Domchek, S.M.; Audeh, M.W.; Weitzel, J.N.; Friedlander, M.; Arun, B.; Loman, N.; Schmutzler, R.K.; et al. Oral Poly(ADP-Ribose) Polymerase Inhibitor Olaparib in Patients with BRCA1 or BRCA2 Mutations and Advanced Breast Cancer: A Proof-of-Concept Trial. *Lancet* **2010**, *376*, 235–244. [CrossRef]

19. Farmer, H.; McCabe, H.; Lord, C.J.; Tutt, A.H.J.; Johnson, D.A.; Richardson, T.B.; Santarosa, M.; Dillon, K.J.; Hickson, I.; Knights, C.; et al. Targeting the DNA Repair Defect in BRCA Mutant Cells as a Therapeutic Strategy. *Nature* **2005**, *434*, 917–921. [CrossRef]
20. Morash, M.; Mitchell, H.; Beltran, H.; Elemento, O.; Pathak, J. The Role of Next-Generation Sequencing in Precision Medicine: A Review of Outcomes in Oncology. *J. Pers. Med.* **2018**, *8*, 30. [CrossRef]
21. De Rubis, G.; Rajeev Krishnan, S.; Bebawy, M. Liquid Biopsies in Cancer Diagnosis, Monitoring, and Prognosis. *Trends Pharmacol. Sci.* **2019**, *40*, 172–186. [CrossRef] [PubMed]
22. Mattox, A.K.; Bettegowda, C.; Zhou, S.; Papadopoulos, N.; Kinzler, K.W.; Vogelstein, B. Applications of Liquid Biopsies for Cancer. *Sci. Transl. Med.* **2019**, *11*, 1–4. [CrossRef]
23. Stratton, M.R.; Campbell, P.J.; Futreal, P.A. The Cancer Genome. *Nature* **2009**, *458*, 719–724. [CrossRef]
24. Vogelstein, B.; Papadopoulos, N.; Velculescu, V.E.; Zhou, S.; Diaz, L.A.; Kinzler, K.W. Cancer Genome Landscapes. *Science* **2013**, *340*, 1546–1558. [CrossRef]
25. Li, K.; Luo, H.; Huang, L.; Luo, H.; Zhu, X. Microsatellite Instability: A Review of What the Oncologist Should Know. *Cancer Cell Int.* **2020**, *20*, 16. [CrossRef] [PubMed]
26. Moynahan, M.E.; Jasin, M. Loss of Heterozygosity Induced by a Chromosomal Double-Strand Break. *Proc. Natl. Acad. Sci. USA* **1997**, *94*, 8988–8993. [CrossRef] [PubMed]
27. Liu, D. Cancer Biomarkers for Targeted Therapy. *Biomark. Res.* **2019**, *7*, 1–7. [CrossRef] [PubMed]
28. Thomson, R.J.; Moshirfar, M.; Ronquillo, Y. *Tyrosine Kinase Inhibitors*; StatPearls Publishing: Treasure Island, FL, USA, 2021.
29. Füzéry, A.K.; Levin, J.; Chan, M.M.; Chan, D.W. Translation of Proteomic Biomarkers into FDA Approved Cancer Diagnostics: Issues and Challenges. *Clin. Proteom.* **2013**, *10*, 13. [CrossRef]
30. Liu, R.; Ye, X.; Cui, T. Recent Progress of Biomarker Detection Sensors. *Yosetsu Gakkai Ronbunshu/Q. J. Japan Weld. Soc.* **2020**, *38*, 193–198. [CrossRef]
31. Tighe, P.J.; Ryder, R.R.; Todd, I.; Fairclough, L.C. ELISA in the Multiplex Era: Potentials and Pitfalls. *Proteom. Clin. Appl.* **2015**, *9*, 406–422. [CrossRef]
32. Acevedo, B.; Perera, Y.; Ruiz, M.; Rojas, G.; Benítez, J.; Ayala, M.; Gavilondo, J. Development and Validation of a Quantitative ELISA for the Measurement of PSA Concentration. *Clin. Chim. Acta* **2002**, *317*, 55–63. [CrossRef]
33. Pinsky, P.F.; Prorok, P.C.; Kramer, B.S. Prostate Cancer Screening—A Perspective on the Current State of the Evidence. *N. Engl. J. Med.* **2017**, *376*, 1285–1289. [CrossRef]
34. Muinao, T.; Deka Boruah, H.P.; Pal, M. Multi-Biomarker Panel Signature as the Key to Diagnosis of Ovarian Cancer. *Heliyon* **2019**, *5*, e02826. [CrossRef]
35. Coleman, R.L.; Herzog, T.J.; Chan, D.W.; Munroe, D.G.; Pappas, T.C.; Smith, A.; Zhang, Z.; Wolf, J. Validation of a Second-Generation Multivariate Index Assay for Malignancy Risk of Adnexal Masses. *Am. J. Obstet. Gynecol.* **2016**, *215*, 82.e1–82.e11. [CrossRef] [PubMed]
36. Ueland, F.R.; Desimone, C.P.; Seamon, L.G.; Miller, R.A.; Goodrich, S.; Podzielinski, I.; Sokoll, L.; Smith, A.; Van Nagell, J.R.; Zhang, Z. Effectiveness of a Multivariate Index Assay in the Preoperative Assessment of Ovarian Tumors. *Obstet. Gynecol.* **2011**, *117*, 1289–1297. [CrossRef]
37. Cohen, J.D.; Li, L.; Wang, Y.; Thoburn, C.; Afsari, B.; Danilova, L.; Douville, C.; Javed, A.A.; Wong, F.; Mattox, A.; et al. Detection and Localization of Surgically Resectable Cancers with a Multi-Analyte Blood Test. *Science* **2018**, *359*, 926–930. [CrossRef]
38. Pashayan, N.; Pharoah, P.D.P. The Challenge of Early Detection in Cancer. *Science* **2020**, *368*, 589–590. [CrossRef] [PubMed]
39. Choi, Y.E.; Kwak, J.W.; Park, J.W. Nanotechnology for Early Cancer Detection. *Sensors* **2010**, *10*, 428–455. [CrossRef]
40. Srinivas, P.R.; Barker, P.; Srivastava, S. Nanotechnology in Early Detection of Cancer. *Lab. Investig.* **2002**, *82*, 657–662. [CrossRef]
41. Harisinghani, M.G.; Barentsz, J.; Hahn, P.F.; Deserno, W.M.; Tabatabaei, S.; van de Kaa, C.H.; de la Rosette, J.; Weissleder, R. Noninvasive Detection of Clinically Occult Lymph-Node Metastases in Prostate Cancer. *N. Engl. J. Med.* **2003**, *348*, 2491–2499. [CrossRef]
42. Wang, Y.X.J.; Hussain, S.M.; Krestin, G.P. Superparamagnetic Iron Oxide Contrast Agents: Physicochemical Characteristics and Applications in MR Imaging. *Eur. Radiol.* **2001**, *11*, 2319–2331. [CrossRef] [PubMed]
43. Dadfar, S.M.; Roemhild, K.; Drude, N.I.; von Stillfried, S.; Knüchel, R.; Kiessling, F.; Lammers, T. Iron Oxide Nanoparticles: Diagnostic, Therapeutic and Theranostic Applications. *Adv. Drug Deliv. Rev.* **2019**, *138*, 302–325. [CrossRef] [PubMed]
44. Alkilany, A.M.; Murphy, C.J. Toxicity and Cellular Uptake of Gold Nanoparticles: What We Have Learned so Far? *J. Nanopart. Res.* **2010**, *12*, 2313–2333. [CrossRef] [PubMed]
45. Antoine, R.; Bonačić-Koutecký, V. *Liganded Silver and Gold Quantum Clusters. Towards a New Class of Nonlinear Optical Nanomaterials*; Springer: Cham, Switzerland, 2018; ISBN 9783319647425. [CrossRef]
46. Kreibig, U.; Vollmer, M. *Optical Properties of Metal Clusters*; Springer: Berlin/Heidelberg, Germany, 1995; Volume 25, ISBN 978-3-642-08191-0. [CrossRef]
47. Raval, N.; Maheshwari, R.; Kalyane, D.; Youngren-Ortiz, S.R.; Chougule, M.B.; Tekade, R.K. Importance of Physicochemical Characterization of Nanoparticles in Pharmaceutical Product Development. In *Basic Fundamentals of Drug Delivery*; Academic Press: Cambridge, MA, USA, 2019; pp. 369–400. [CrossRef]
48. Song, X.-R.; Goswami, N.; Yang, H.-H.; Xie, J. Functionalization of Metal Nanoclusters for Biomedical Applications. *Analyst* **2016**, *141*, 3126. [CrossRef]

49. Sanità, G.; Carrese, B.; Lamberti, A. Nanoparticle Surface Functionalization: How to Improve Biocompatibility and Cellular Internalization. *Front. Mol. Biosci.* **2020**, *7*, 381. [CrossRef]
50. Yoo, J.; Park, C.; Yi, G.; Lee, D.; Koo, H. Active Targeting Strategies Using Biological Ligands for Nanoparticle Drug Delivery Systems. *Cancers* **2019**, *11*, 640. [CrossRef]
51. Yan, N.; Xia, N.; Wu, Z. Metal Nanoparticles Confronted with Foreign Ligands: Mere Ligand Exchange or Further Structural Transformation? *Small* **2020**, *17*, 2000609. [CrossRef]
52. Jazayeri, M.H.; Amani, H.; Pourfatollah, A.A.; Avan, A.; Ferns, G.A.; Pazoki-Toroudi, H. Enhanced Detection Sensitivity of Prostate-Specific Antigen via PSA-Conjugated Gold Nanoparticles Based on Localized Surface Plasmon Resonance: GNP-Coated Anti-PSA/LSPR as a Novel Approach for the Identification of Prostate Anomalies. *Cancer Gene Ther.* **2016**, *23*, 365–369. [CrossRef] [PubMed]
53. Roncato, F.; Rruga, F.; Porcù, E.; Casarin, E.; Ronca, R.; Maccarinelli, F.; Realdon, N.; Basso, G.; Alon, R.; Viola, G.; et al. Improvement and Extension of Anti-EGFR Targeting in Breast Cancer Therapy by Integration with the Avidin-Nucleic-Acid-Nano-Assemblies. *Nat. Commun.* **2018**, *9*, 1–11. [CrossRef]
54. Hainfeld, J.F.; O'Connor, M.J.; Dilmanian, F.A.; Slatkin, D.N.; Adams, D.J.; Smilowitz, H.M. Micro-CT Enables Microlocalisation and Quantification of Her2-Targeted Gold Nanoparticles within Tumour Regions. *Br. J. Radiol.* **2011**, *84*, 526–533. [CrossRef]
55. Chattopadhyay, N.; Cai, Z.; Kwon, Y.L.; Lechtman, E.; Pignol, J.P.; Reilly, R.M. Molecularly Targeted Gold Nanoparticles Enhance the Radiation Response of Breast Cancer Cells and Tumor Xenografts to X-Radiation. *Breast Cancer Res. Treat.* **2013**, *137*, 81–91. [CrossRef]
56. Cruz, E.; Kayser, V. Synthesis and Enhanced Cellular Uptake In Vitro of Anti-HER2 Multifunctional Gold Nanoparticles. *Cancers* **2019**, *11*, 870. [CrossRef]
57. Goddard, Z.R.; Marín, M.J.; Russell, D.A.; Searcey, M. Active Targeting of Gold Nanoparticles as Cancer Therapeutics. *Chem. Soc. Rev.* **2020**, *49*, 8774–8789. [CrossRef] [PubMed]
58. Retnakumari, A.; Setua, S.; Menon, D.; Ravindran, P.; Muhammed, H.; Pradeep, T.; Nair, S.; Koyakutty, M. Molecular-Receptor-Specific, Non-Toxic, near-Infrared-Emitting Au Cluster-Protein Nanoconjugates for Targeted Cancer Imaging. *Nanotechnology* **2010**, *21*, 055103. [CrossRef] [PubMed]
59. Stella, B.; Arpicco, S.; Peracchia, M.T.; Desmaële, D.; Hoebeke, J.; Renoir, M.; D'Angelo, J.; Cattel, L.; Couvreur, P. Design of Folic Acid-Conjugated Nanoparticles for Drug Targeting. *J. Pharm. Sci.* **2000**, *89*, 1452–1464. [CrossRef]
60. Song, L.; Falzone, N.; Vallis, K.A. EGF-Coated Gold Nanoparticles Provide an Efficient Nano-Scale Delivery System for the Molecular Radiotherapy of EGFR-Positive Cancer. *Int. J. Radiat. Biol.* **2016**, *92*, 716–723. [CrossRef]
61. Meyers, J.D.; Cheng, Y.; Broome, A.M.; Agnes, R.S.; Schluchter, M.D.; Margevicius, S.; Wang, X.; Kenney, M.E.; Burda, C.; Basilion, J.P. Peptide-Targeted Gold Nanoparticles for Photodynamic Therapy of Brain Cancer. *Part. Part. Syst. Charact.* **2015**, *32*, 448–457. [CrossRef] [PubMed]
62. Cheng, Y.; Meyers, J.D.; Agnes, R.S.; Doane, T.L.; Kenney, M.E.; Broome, A.-M.; Burda, C.; Basilion, J.P. Addressing Brain Tumors with Targeted Gold Nanoparticles: A New Gold Standard for Hydrophobic Drug Delivery? *Small* **2011**, *7*, 2301–2306. [CrossRef]
63. Ye, F.; Zhao, Y.; El-Sayed, R.; Muhammed, M.; Hassan, M. Advances in Nanotechnology for Cancer Biomarkers. *Nano Today* **2018**, *18*, 103–123. [CrossRef]
64. Zhang, Y.; Li, M.; Gao, X.; Chen, Y.; Liu, T. Nanotechnology in Cancer Diagnosis: Progress, Challenges and Opportunities. *J. Hematol. Oncol.* **2019**, *12*, 137. [CrossRef] [PubMed]
65. Huang, H.; Feng, W.; Chen, Y.; Shi, J. Inorganic Nanoparticles in Clinical Trials and Translations. *Nano Today* **2020**, *35*, 100972. [CrossRef]
66. Li, Q.; Zhou, D.; Chai, J.; So, W.Y.; Cai, T.; Li, M.; Peteanu, L.A.; Chen, O.; Cotlet, M.; Wendy Gu, X.; et al. Structural Distortion and Electron Redistribution in Dual-Emitting Gold Nanoclusters. *Nat. Commun.* **2020**, *11*, 1–9. [CrossRef] [PubMed]
67. Kang, X.; Zhu, M. Tailoring the Photoluminescence of Atomically Precise Nanoclusters. *Chem. Soc. Rev.* **2019**, *48*, 2422–2457. [CrossRef]
68. Chen, X.; Zhu, H.; Huang, X.; Wang, P.; Zhang, F.; Li, W.; Chen, G.; Chen, B. Novel Iodinated Gold Nanoclusters for Precise Diagnosis of Thyroid Cancer. *Nanoscale* **2017**, *9*, 2219–2231. [CrossRef]
69. Wang, J.; Wuethrich, A.; Sina, A.A.I.; Lane, R.E.; Lin, L.L.; Wang, Y.; Cebon, J.; Behren, A.; Trau, M. Tracking Extracellular Vesicle Phenotypic Changes Enables Treatment Monitoring in Melanoma. *Sci. Adv.* **2020**, *6*, eaax3223. [CrossRef]
70. Špringer, T.; Chadtová Song, X.; Ermini, M.L.; Lamačová, J.; Homola, J. Functional Gold Nanoparticles for Optical Affinity Biosensing. *Anal. Bioanal. Chem.* **2017**, *409*, 4087–4097. [CrossRef]
71. Ermini, M.L.; Chadtová Song, X.; Špringer, T.; Homola, J. Peptide Functionalization of Gold Nanoparticles for the Detection of Carcinoembryonic Antigen in Blood Plasma via SPR-Based Biosensor. *Front. Chem.* **2019**, *7*, 40. [CrossRef]
72. Haghighi, F.H.; Binaymotlagh, R.; Mirahmadi-Zare, S.Z.; Hadadzadeh, H. Aptamer/Magnetic Nanoparticles Decorated with Fluorescent Gold Nanoclusters for Selective Detection and Collection of Human Promyelocytic Leukemia (HL-60) Cells from a Mixture. *Nanotechnology* **2020**, *31*, 025605. [CrossRef] [PubMed]
73. Elbaz, N.; Chauhan, R.; James, K.T.; Malik, D.A.; Zhu, M.; Elbaz, A.; Keynton, R.S.; Ng, C.K.; Bates, P.J.; Malik, T.; et al. Gold Nanoparticles Conjugate Cancer-Targeting Aptamer and Gadolinium Chelate for MR Cancer Imaging. In Proceedings of the 2018 IEEE International Symposium on Signal Processing and Information Technology, ISSPIT 2018, Louisville, KY, USA, 6–8 December 2018; IEEE: Piscataway, NJ, USA, 2019; pp. 520–525. [CrossRef]

74. Han, W.; Yang, W.; Gao, F.; Cai, P.; Wang, J.; Wang, S.; Xue, J.; Gao, X.; Liu, Y. Iodine-124 Labeled Gold Nanoclusters for Positron Emission Tomography Imaging in Lung Cancer Model. *J. Nanosci. Nanotechnol.* **2019**, *20*, 1375–1382. [CrossRef]
75. Yao, J.; Wang, L.V. Photoacoustic Tomography: Fundamentals, Advances and Prospects. *Contrast Media Mol. Imaging* **2011**, *6*, 332–345. [CrossRef]
76. Han, S.; Bouchard, R.; Sokolov, K.V. Molecular Photoacoustic Imaging with Ultra-Small Gold Nanoparticles. *Biomed. Opt. Express* **2019**, *10*, 3472. [CrossRef] [PubMed]
77. Chen, Y.S.; Zhao, Y.; Yoon, S.J.; Gambhir, S.S.; Emelianov, S. Miniature Gold Nanorods for Photoacoustic Molecular Imaging in the Second Near-Infrared Optical Window. *Nat. Nanotechnol.* **2019**, *14*, 465–472. [CrossRef]
78. Shen, D.; Henry, M.; Trouillet, V.; Comby-Zerbino, C.; Bertorelle, F.; Sancey, L.; Antoine, R.; Coll, J.L.; Josserand, V.; Le Guével, X. Zwitterion Functionalized Gold Nanoclusters for Multimodal near Infrared Fluorescence and Photoacoustic Imaging. *APL Mater.* **2017**, *5*, 053404. [CrossRef]
79. Go, G.; Lee, C.S.; Yoon, Y.M.; Lim, J.H.; Kim, T.H.; Lee, S.H. Prpc Aptamer Conjugated–Gold Nanoparticles for Targeted Delivery of Doxorubicin to Colorectal Cancer Cells. *Int. J. Mol. Sci.* **2021**, *22*, 1976. [CrossRef] [PubMed]
80. Lu, Y.; Huang, J.; Li, F.; Wang, Y.; Ding, M.; Zhang, J.; Yin, H.; Zhang, R.; Ren, X. EGFR-Specific Single-Chain Variable Fragment Antibody-Conjugated Fe_3O_4/Au Nanoparticles as an Active MRI Contrast Agent for NSCLC. *Magn. Reson. Mater. Phys. Biol. Med.* **2021**, *34*, 581–591. [CrossRef]
81. Mu, Q.; Kievit, F.M.; Kant, R.J.; Lin, G.; Jeon, M.; Zhang, M. Anti-HER2/Neu Peptide-Conjugated Iron Oxide Nanoparticles for Targeted Delivery of Paclitaxel to Breast Cancer Cells. *Nanoscale* **2015**, *7*, 18010–18014. [CrossRef]
82. Nair, L.V.; Nair, R.V.; Shenoy, S.J.; Thekkuveettil, A.; Jayasree, R.S. Blood Brain Barrier Permeable Gold Nanocluster for Targeted Brain Imaging and Therapy: An: In Vitro and in Vivo Study. *J. Mater. Chem. B* **2017**, *5*, 8314–8321. [CrossRef] [PubMed]
83. Yang, Y.; Wang, S.; Wang, C.; Tian, C.; Shen, Y.; Zhu, M. Engineered Targeted Hyaluronic Acid–Glutathione-Stabilized Gold Nanoclusters/Graphene Oxide–5-Fluorouracil as a Smart Theranostic Platform for Stimulus-Controlled Fluorescence Imaging-Assisted Synergetic Chemo/Phototherapy. *Chem. Asian J.* **2019**, *14*, 1418–1423. [CrossRef] [PubMed]
84. Zhao, H.; Wen, X.; Li, W.; Li, Y.; Yin, C. A Copper-Mediated on-off-on Gold Nanocluster for Endogenous GSH Sensing to Drive Cancer Cell Recognition. *J. Mater. Chem. B* **2019**, *7*, 2169–2176. [CrossRef] [PubMed]
85. Chen, H.; Li, B.; Ren, X.; Li, S.; Ma, Y.; Cui, S.; Gu, Y. Multifunctional Near-Infrared-Emitting Nano-Conjugates Based on Gold Clusters for Tumor Imaging and Therapy. *Biomaterials* **2012**, *33*, 8461–8476. [CrossRef] [PubMed]
86. Emami, F.; Banstola, A.; Vatanara, A.; Lee, S.; Kim, J.O.; Jeong, J.-H.; Yook, S. Doxorubicin and Anti-PD-L1 Antibody Conjugated Gold Nanoparticles for Colorectal Cancer Photochemotherapy. *Mol. Pharm.* **2019**, *16*, 1184–1199. [CrossRef] [PubMed]
87. Yi, Y.; Kim, H.J.; Zheng, M.; Mi, P.; Naito, M.; Kim, B.S.; Min, H.S.; Hayashi, K.; Perche, F.; Toh, K.; et al. Glucose-Linked Sub-50-Nm Unimer Polyion Complex-Assembled Gold Nanoparticles for Targeted SiRNA Delivery to Glucose Transporter 1-Overexpressing Breast Cancer Stem-like Cells. *J. Control. Release* **2019**, *295*, 268–277. [CrossRef]
88. Khongkow, M.; Yata, T.; Boonrungsiman, S.; Ruktanonchai, U.R.; Graham, D.; Namdee, K. Surface Modification of Gold Nanoparticles with Neuron-Targeted Exosome for Enhanced Blood–Brain Barrier Penetration. *Sci. Rep.* **2019**, *9*, 8278. [CrossRef]
89. Zhang, Y.; Buttry Walker, J.; Minic, Z.; Liu, F.; Goshgarian, H.; Mao, G. Transporter Protein and Drug-Conjugated Gold Nanoparticles Capable of Bypassing the Blood-Brain Barrier. *Sci. Rep.* **2016**, *6*, 25794. [CrossRef] [PubMed]
90. Hada, A.M.; Craciun, A.M.; Focsan, M.; Borlan, R.; Soritau, O.; Todea, M.; Astilean, S. Folic Acid Functionalized Gold Nanoclusters for Enabling Targeted Fluorescence Imaging of Human Ovarian Cancer Cells. *Talanta* **2021**, *225*, 121960. [CrossRef] [PubMed]
91. Ramesh, B.S.; Giorgakis, E.; Lopez-Davila, V.; Dashtarzheneha, A.K.; Loizidou, M. Detection of Cell Surface Calreticulin as a Potential Cancer Biomarker Using Near-Infrared Emitting Gold Nanoclusters. *Nanotechnology* **2016**, *27*, 285101. [CrossRef] [PubMed]
92. Zhang, C.; Zhang, F.; Han, M.; Wang, X.; Du, J.; Zhang, H.; Li, W. Co-Delivery of 5-Fluorodeoxyuridine and Doxorubicin via Gold Nanoparticle Equipped with Affibody-DNA Hybrid Strands for Targeted Synergistic Chemotherapy of HER2 Overexpressing Breast Cancer. *Sci. Rep.* **2020**, *10*, 1–14. [CrossRef] [PubMed]
93. Kubota, T.; Kuroda, S.; Kanaya, N.; Morihiro, T.; Aoyama, K.; Kakiuchi, Y.; Kikuchi, S.; Nishizaki, M.; Kagawa, S.; Tazawa, H.; et al. HER2-Targeted Gold Nanoparticles Potentially Overcome Resistance to Trastuzumab in Gastric Cancer. *Nanomed. Nanotechnol. Biol. Med.* **2018**, *14*, 1919–1929. [CrossRef]
94. Mangadlao, J.D.; Wang, X.; McCleese, C.; Escamilla, M.; Ramamurthy, G.; Wang, Z.; Govande, M.; Basilion, J.P.; Burda, C. Prostate-Specific Membrane Antigen Targeted Gold Nanoparticles for Theranostics of Prostate Cancer. *ACS Nano* **2018**, *12*, 3714–3725. [CrossRef]
95. Pyo, K.; Ly, N.H.; Yoon, S.Y.; Shen, Y.; Choi, S.Y.; Lee, S.Y.; Joo, S.W.; Lee, D. Highly Luminescent Folate-Functionalized Au_{22} Nanoclusters for Bioimaging. *Adv. Healthc. Mater.* **2017**, *6*, 1700203. [CrossRef]
96. Loynachan, C.N.; Soleimany, A.P.; Dudani, J.S.; Lin, Y.; Najer, A.; Bekdemir, A.; Chen, Q.; Bhatia, S.N.; Stevens, M.M. Renal Clearable Catalytic Gold Nanoclusters for in Vivo Disease Monitoring. *Nat. Nanotechnol.* **2019**, *14*, 883–890. [CrossRef]
97. Abarghoei, S.; Fakhri, N.; Borghei, Y.S.; Hosseini, M.; Ganjali, M.R. A Colorimetric Paper Sensor for Citrate as Biomarker for Early Stage Detection of Prostate Cancer Based on Peroxidase-like Activity of Cysteine-Capped Gold Nanoclusters. *Spectrochim. Acta Part A Mol. Biomol. Spectrosc.* **2019**, *210*, 251–259. [CrossRef]
98. Chang, C.C.; Chen, C.P.; Lee, C.H.; Chen, C.Y.; Lin, C.W. Colorimetric Detection of Human Chorionic Gonadotropin Using Catalytic Gold Nanoparticles and a Peptide Aptamer. *Chem. Commun.* **2014**, *50*, 14443–14446. [CrossRef]

99. Halawa, M.I.; Gao, W.; Saqib, M.; Kitte, S.A.; Wu, F.; Xu, G. Sensitive Detection of Alkaline Phosphatase by Switching on Gold Nanoclusters Fluorescence Quenched by Pyridoxal Phosphate. *Biosens. Bioelectron.* **2017**, *95*, 8–14. [CrossRef] [PubMed]
100. Wong, X.Y.; Quesada-González, D.; Manickam, S.; New, S.Y.; Muthoosamy, K.; Merkoçi, A. Integrating Gold Nanoclusters, Folic Acid and Reduced Graphene Oxide for Nanosensing of Glutathione Based on "Turn-off" Fluorescence. *Sci. Rep.* **2021**, *11*, 2375. [CrossRef] [PubMed]
101. Ashton, J.R.; Gottlin, E.B.; Patz, E.F.; West, J.L.; Badea, C.T. A Comparative Analysis of EGFR-Targeting Antibodies for Gold Nanoparticle CT Imaging of Lung Cancer. *PLoS ONE* **2018**, *13*, e0206950. [CrossRef] [PubMed]
102. Samani, R.K.; Tavakoli, M.B.; Maghsoudinia, F.; Motaghi, H.; Hejazi, S.H.; Mehrgardi, M.A. Trastuzumab and Folic Acid Functionalized Gold Nanoclusters as a Dual-Targeted Radiosensitizer for Megavoltage Radiation Therapy of Human Breast Cancer. *Eur. J. Pharm. Sci.* **2020**, *153*, 105487. [CrossRef] [PubMed]
103. Pedrosa, P.; Corvo, M.L.; Ferreira-Silva, M.; Martins, P.; Carvalheiro, M.C.; Costa, P.M.; Martins, C.; Martins, L.M.D.R.S.; Baptista, P.V.; Fernandes, A.R. Targeting Cancer Resistance via Multifunctional Gold Nanoparticles. *Int. J. Mol. Sci.* **2019**, *20*, 5510. [CrossRef] [PubMed]
104. Sobol, N.B.; Korsen, J.A.; Younes, A.; Edwards, K.J.; Lewis, J.S. ImmunoPET Imaging of Pancreatic Tumors with 89Zr-Labeled Gold Nanoparticle–Antibody Conjugates. *Mol. Imaging Biol.* **2021**, *23*, 84–94. [CrossRef] [PubMed]
105. Nguyen, C.T.; Nguyen, J.T.; Rutledge, S.; Zhang, J.; Wang, C.; Walker, G.C. Detection of Chronic Lymphocytic Leukemia Cell Surface Markers Using Surface Enhanced Raman Scattering Gold Nanoparticles. *Cancer Lett.* **2010**, *292*, 91–97. [CrossRef]
106. Qiu, Y.; Deng, D.; Deng, Q.; Wu, P.; Zhang, H.; Cai, C. Synthesis of Magnetic Fe_3O_4-Au Hybrids for Sensitive SERS Detection of Cancer Cells at Low Abundance. *J. Mater. Chem. B* **2015**, *3*, 4487–4495. [CrossRef]
107. Zhou, C.; Hao, G.; Thomas, P.; Liu, J.; Yu, M.; Sun, S.; Öz, O.K.; Sun, X.; Zheng, J. Near-Infrared Emitting Radioactive Gold Nanoparticles with Molecular Pharmacokinetics. *Angew. Chem. Int. Ed.* **2012**, *51*, 10118–10122. [CrossRef]
108. Zhao, Y.; Pang, B.; Luehmann, H.; Detering, L.; Yang, X.; Sultan, D.; Harpstrite, S.; Sharma, V.; Cutler, C.S.; Xia, Y.; et al. Gold Nanoparticles Doped with ^{199}Au Atoms and Their Use for Targeted Cancer Imaging by SPECT. *Adv. Healthc. Mater.* **2016**, *5*, 928–935. [CrossRef] [PubMed]
109. Liszbinski, R.B.; Romagnoli, G.G.; Gorgulho, C.M.; Basso, C.R.; Pedrosa, V.A.; Kaneno, R. Anti-EGFR-Coated Gold Nanoparticles in Vitro Carry 5-Fluorouracil to Colorectal Cancer Cells. *Materials* **2020**, *13*, 375. [CrossRef]
110. Groysbeck, N.; Stoessel, A.; Donzeau, M.; Da Silva, E.C.; Lehmann, M.; Strub, J.M.; Cianferani, S.; Dembélé, K.; Zuber, G. Synthesis and Biological Evaluation of 2.4 Nm Thiolate-Protected Gold Nanoparticles Conjugated to Cetuximab for Targeting Glioblastoma Cancer Cells via the EGFR. *Nanotechnology* **2019**, *30*, 184005. [CrossRef]
111. Duan, Y.; Liu, B. Recent Advances of Optical Imaging in the Second Near-Infrared Window. *Adv. Mater.* **2018**, *30*, 1802394. [CrossRef]
112. Smith, A.M.; Mancini, M.C.; Nie, S. Second Window for in Vivo Imaging Andrew. *Nat. Nanotechnol.* **2009**, *4*, 710–711. [CrossRef]
113. Bonacic-Koutecky, V.; Antoine, R. Enhanced Two-Photon Absorption of Ligated Silver and Gold Nanoclusters: Theoretical and Experimental Assessments. *Nanoscale* **2019**, *11*, 12436–12448. [CrossRef]
114. Thomas, G.; Van Voskuilen, J.; Gerritsen, H.C.; Sterenborg, H.J.C.M. Advances and Challenges in Label-Free Nonlinear Optical Imaging Using Two-Photon Excitation Fluorescence and Second Harmonic Generation for Cancer Research. *J. Photochem. Photobiol. B Biol.* **2014**, *141*, 128–138. [CrossRef]
115. Vogler, N.; Heuke, S.; Bocklitz, T.W.; Schmitt, M.; Popp, J. Multimodal Imaging Spectroscopy of Tissue. *Annu. Rev. Anal. Chem.* **2015**, *8*, 359–387. [CrossRef]
116. Li, L.; Kang, D.; Huang, Z.; Zhan, Z.; Feng, C.; Zhou, Y.; Tu, H.; Zhuo, S.; Chen, J. Multimodal Multiphoton Imaging for Label-Free Monitoring of Early Gastric Cancer. *BMC Cancer* **2019**, *19*, 295. [CrossRef]
117. Terenziani, F.; Katan, C.; Badaeva, E.; Tretiak, S.; Blanchara-Desce, M. Enhanced Two-Photon Absorption of Organic Chromophores: Theoretical and Experimental Assessments. *Adv. Mater.* **2008**, *20*, 4641–4678. [CrossRef]
118. Zhou, J.; Yang, Y.; Zhang, C.Y. Toward Biocompatible Semiconductor Quantum Dots: From Biosynthesis and Bioconjugation to Biomedical Application. *Chem. Rev.* **2015**, *115*, 11669–11717. [CrossRef]
119. Hu, R.; Yong, K.T.; Roy, I.; Ding, H.; Law, W.C.; Cai, H.; Zhang, X.; Vathy, L.A.; Bergey, E.J.; Prasad, P.N. Functionalized Near-Infrared Quantum Dots for In vivo Tumor Vasculature Imaging. *Nanotechnology* **2010**, *21*, 145105. [CrossRef]
120. Olesiak-Banska, J.; Waszkielewicz, M.; Obstarczyk, P.; Samoc, M. Two-Photon Absorption and Photoluminescence of Colloidal Gold Nanoparticles and Nanoclusters. *Chem. Soc. Rev.* **2019**, *48*, 4087–4117. [CrossRef]
121. Markus, R.; Schwentner, N. *Physics and Chemistry of Small Clusters*; Springer: Boston, MA, USA, 1987. [CrossRef]
122. Zheng, J.; Dickson, R.M. Individual Water-Soluble Dendrimer-Encapsulated Silver Nanodot Fluorescence. *J. Am. Chem. Soc.* **2002**, *124*, 13982–13983. [CrossRef]
123. Jin, R.; Zeng, C.; Zhou, M.; Chen, Y. Atomically Precise Colloidal Metal Nanoclusters and Nanoparticles: Fundamentals and Opportunities. *Chem. Rev.* **2016**, *116*, 10346–10413. [CrossRef]
124. Chakraborty, I.; Pradeep, T. Atomically Precise Clusters of Noble Metals: Emerging Link between Atoms and Nanoparticles. *Chem. Rev.* **2017**, *117*, 8208–8271. [CrossRef] [PubMed]
125. Porret, E.; Le Guével, X.; Coll, J.L. Gold Nanoclusters for Biomedical Applications: Toward: In Vivo Studies. *J. Mater. Chem. B* **2020**, *8*, 2216–2232. [CrossRef]

126. Polavarapu, L.; Manna, M.; Xu, Q.H. Biocompatible Glutathione Capped Gold Clusters as One- and Two-Photon Excitation Fluorescence Contrast Agents for Live Cells Imaging. *Nanoscale* **2011**, *3*, 429–434. [CrossRef]
127. Yang, L.; Shang, L.; Nienhaus, G.U. Mechanistic Aspects of Fluorescent Gold Nanocluster Internalization by Live HeLa Cells. *Nanoscale* **2013**, *5*, 1537–1543. [CrossRef]
128. Muraca, F.; Boselli, L.; Castagnola, V.; Dawson, K.A. Ultrasmall Gold Nanoparticle Cellular Uptake: Influence of Transient Bionano Interactions. *ACS Appl. Bio Mater.* **2020**, *3*, 3800–3808. [CrossRef]
129. Mutas, M.; Strelow, C.; Kipp, T.; Mews, A. Specific Binding and Internalization: An Investigation of Fluorescent Aptamer-Gold Nanoclusters and Cells with Fluorescence Lifetime Imaging Microscopy. *Nanoscale* **2018**, *10*, 20453–20461. [CrossRef] [PubMed]
130. Fernández, T.D.; Pearson, J.R.; Leal, M.P.; Torres, M.J.; Blanca, M.; Mayorga, C.; Le Guével, X. Intracellular Accumulation and Immunological Properties of Fluorescent Gold Nanoclusters in Human Dendritic Cells. *Biomaterials* **2015**, *43*, 1–12. [CrossRef]
131. Tay, C.Y.; Yu, Y.; Setyawati, M.I.; Xie, J.; Leong, D.T. Presentation Matters: Identity of Gold Nanocluster Capping Agent Governs Intracellular Uptake and Cell Metabolism. *Nano Res.* **2014**, *7*, 805–815. [CrossRef]
132. Wu, X.; He, X.; Wang, K.; Xie, C.; Zhou, B.; Qing, Z. Ultrasmall Near-Infrared Gold Nanoclusters for Tumor Fluorescence Imaging in Vivo. *Nanoscale* **2010**, *2*, 2244–2249. [CrossRef]
133. Gran, E.R.; Bertorelle, F.; Fakhouri, H.; Antoine, R.; Perić Bakulić, M.; Sanader Maršić, Ž.; Bonačić-Koutecký, V.; Blain, M.; Antel, J.; Maysinger, D. Size and Ligand Effects of Gold Nanoclusters in Alteration of Organellar State and Translocation of Transcription Factors in Human Primary Astrocytes. *Nanoscale* **2021**, *13*, 3173–3183. [CrossRef]
134. Fang, J.; Nakamura, H.; Maeda, H. The EPR Effect: Unique Features of Tumor Blood Vessels for Drug Delivery, Factors Involved, and Limitations and Augmentation of the Effect. *Adv. Drug Deliv. Rev.* **2011**, *63*, 136–151. [CrossRef] [PubMed]
135. Hashizume, H.; Baluk, P.; Morikawa, S.; McLean, J.W.; Thurston, G.; Roberge, S.; Jain, R.K.; McDonald, D.M. Openings between Defective Endothelial Cells Explain Tumor Vessel Leakiness. *Am. J. Pathol.* **2000**, *156*, 1363–1380. [CrossRef]
136. Wilhelm, S.; Tavares, A.J.; Dai, Q.; Ohta, S.; Audet, J.; Dvorak, H.F.; Chan, W.C.W. Analysis of Nanoparticle Delivery to Tumours. *Nat. Rev. Mater.* **2016**, *1*, 1–12. [CrossRef]
137. Lammers, T. Macro-Nanomedicine: Targeting the Big Picture. *J. Control. Release* **2019**, *294*, 372–375. [CrossRef]
138. Sindhwani, S.; Syed, A.M.; Ngai, J.; Kingston, B.R.; Maiorino, L.; Rothschild, J.; MacMillan, P.; Zhang, Y.; Rajesh, N.U.; Hoang, T.; et al. The Entry of Nanoparticles into Solid Tumours. *Nat. Mater.* **2020**, *19*, 566–575. [CrossRef]
139. Aggarwal, P.; Hall, J.B.; McLeland, C.B.; Dobrovolskaia, M.A.; McNeil, S.E. Nanoparticle Interaction with Plasma Proteins as It Relates to Particle Biodistribution, Biocompatibility and Therapeutic Efficacy. *Adv. Drug Deliv. Rev.* **2009**, *61*, 428–437. [CrossRef]
140. Dobrovolskaia, M.A.; Patri, A.K.; Zheng, J.; Clogston, J.D.; Ayub, N.; Aggarwal, P.; Neun, B.W.; Hall, J.B.; McNeil, S.E. Interaction of Colloidal Gold Nanoparticles with Human Blood: Effects on Particle Size and Analysis of Plasma Protein Binding Profiles. *Nanomed. Nanotechnol. Biol. Med.* **2009**, *5*, 106–117. [CrossRef]
141. Shi, J.; Kantoff, P.W.; Wooster, R.; Farokhzad, O.C. Cancer Nanomedicine: Progress, Challenges and Opportunities. *Nat. Rev. Cancer* **2017**, *17*, 20–37. [CrossRef]
142. Arturson, P.; Laakso, T.; Edman, P. Acrylic Microspheres in Vivo IX: Blood Elimination Kinetics and Organ Distribution of Microparticles with Different Surface Characteristics. *J. Pharm. Sci.* **1983**, *72*, 1415–1420. [CrossRef] [PubMed]
143. Yin, M.M.; Chen, W.Q.; Lu, Y.Q.; Han, J.Y.; Liu, Y.; Jiang, F.L. A Model beyond Protein Corona: Thermodynamics and Binding Stoichiometries of the Interactions between Ultrasmall Gold Nanoclusters and Proteins. *Nanoscale* **2020**, *12*, 4573–4585. [CrossRef] [PubMed]
144. Adewale, O.B.; Davids, H.; Cairncross, L.; Roux, S. Toxicological Behavior of Gold Nanoparticles on Various Models: Influence of Physicochemical Properties and Other Factors. *Int. J. Toxicol.* **2019**, *38*, 357–384. [CrossRef] [PubMed]
145. Pan, Y.; Leifert, A.; Ruau, D.; Neuss, S.; Bornemann, J.; Schmid, G.; Brandau, W.; Simon, U.; Jahnen-Dechent, W. Gold Nanoparticles of Diameter 1.4 Nm Trigger Necrosis by Oxidative Stress and Mitochondrial Damage. *Small* **2009**, *5*, 2067–2076. [CrossRef] [PubMed]
146. Coradeghini, R.; Gioria, S.; García, C.P.; Nativo, P.; Franchini, F.; Gilliland, D.; Ponti, J.; Rossi, F. Size-Dependent Toxicity and Cell Interaction Mechanisms of Gold Nanoparticles on Mouse Fibroblasts. *Toxicol. Lett.* **2013**, *217*, 205–216. [CrossRef]
147. Boyoglu, C.; He, Q.; Willing, G.; Boyoglu-Barnum, S.; Dennis, V.A.; Pillai, S.; Singh, S.R. Microscopic Studies of Various Sizes of Gold Nanoparticles and Their Cellular Localizations. *ISRN Nanotechnol.* **2013**, *2013*, 123838. [CrossRef]
148. Truong, L.; Tilton, S.C.; Zaikova, T.; Richman, E.; Waters, K.M.; Hutchison, J.E.; Tanguay, R.L. Surface Functionalities of Gold Nanoparticles Impact Embryonic Gene Expression Responses. *Nanotoxicology* **2013**, *7*, 192–201. [CrossRef] [PubMed]
149. Chen, Y.-S.; Hung, Y.-C.; Liau, I.; Huang, G.S. Assessment of the In Vivo Toxicity of Gold Nanoparticles. *Nanoscale Res. Lett.* **2009**, *4*, 858–864. [CrossRef] [PubMed]
150. Cho, W.-S.; Kim, S.; Han, B.S.; Son, W.C.; Jeong, J. Comparison of Gene Expression Profiles in Mice Liver Following Intravenous Injection of 4 and 100 Nm-Sized PEG-Coated Gold Nanoparticles. *Toxicol. Lett.* **2009**, *191*, 96–102. [CrossRef] [PubMed]
151. Glazer, E.S.; Zhu, C.; Hamir, A.N.; Borne, A.; Thompson, C.S.; Curley, S.A. Biodistribution and Acute Toxicity of Naked Gold Nanoparticles in a Rabbit Hepatic Tumor Model. *Nanotoxicology* **2011**, *5*, 459–468. [CrossRef] [PubMed]
152. Yu, M.; Zheng, J. Clearance Pathways and Tumor Targeting of Imaging Nanoparticles. *ACS Nano* **2015**, *9*, 6655–6674. [CrossRef] [PubMed]
153. Zhang, Y.N.; Poon, W.; Tavares, A.J.; McGilvray, I.D.; Chan, W.C.W. Nanoparticle–Liver Interactions: Cellular Uptake and Hepatobiliary Elimination. *J. Control. Release* **2016**, *240*, 332–348. [CrossRef]

154. Du, B.; Yu, M.; Zheng, J. Transport and Interactions of Nanoparticles in the Kidneys. *Nat. Rev. Mater.* **2018**, *3*, 358–374. [CrossRef]
155. Zeng, C.; Chen, Y.; Das, A.; Jin, R. Transformation Chemistry of Gold Nanoclusters: From One Stable Size to Another. *J. Phys. Chem. Lett.* **2015**, *6*, 2976–2986. [CrossRef]
156. Jin, R.; Qian, H.; Wu, Z.; Zhu, Y.; Zhu, M.; Mohanty, A.; Garg, N. Size Focusing: A Methodology for Synthesizing Atomically Precise Gold Nanoclusters. *J. Phys. Chem. Lett.* **2010**, *1*, 2903–2910. [CrossRef]
157. Wang, Y.; Bürgi, T. Ligand Exchange Reactions on Thiolate-Protected Gold Nanoclusters. *Nanoscale Adv.* **2021**, *3*, 2710–2727. [CrossRef]
158. Wu, Z.; Jin, R. On the Ligand's Role in the Fluorescence of Gold Nanoclusters. *Nano Lett.* **2010**, *10*, 2568–2573. [CrossRef]
159. Gregory Schaaff, T.; Knight, G.; Shafigullin, M.N.; Borkman, R.F.; Whetten, R.L. Isolation and Selected Properties of a 10.4 Kda Gold:Glutathione Cluster Compound. *J. Phys. Chem. B* **1998**, *102*, 10645–10646. [CrossRef]
160. Negishi, Y.; Nobusada, K.; Tsukuda, T. Glutathione-Protected Gold Clusters Revisited: Bridging the Gap between Gold(I)-Thiolate Complexes and Thiolate-Protected Gold Nanocrystals. *J. Am. Chem. Soc.* **2005**, *127*, 5261–5270. [CrossRef]
161. Negishi, Y.; Takasugi, Y.; Sato, S.; Yao, H.; Kimura, K.; Tsukuda, T. Magic-Numbered Aun Clusters Protected by Glutathione Monolayers (n = 18, 21, 25, 28, 32, 39): Isolation and Spectroscopic Characterization. *J. Am. Chem. Soc.* **2004**, *126*, 6518–6519. [CrossRef] [PubMed]
162. Wu, Z.; Gayathri, C.; Gil, R.R.; Jin, R. Probing the Structure and Charge State of Glutathione-Capped $Au_{25}(SG)_{18}$ Clusters by NMR and Mass Spectrometry. *J. Am. Chem. Soc.* **2009**, *131*, 6535–6542. [CrossRef] [PubMed]
163. Comby-Zerbino, C.; Dagany, X.; Chirot, F.; Dugourd, P.; Antoine, R. The Emergence of Mass Spectrometry for Characterizing Nanomaterials. Atomically Precise Nanoclusters and Beyond. *Mater. Adv.* **2021**, *2*, 4896–4913. [CrossRef]
164. Bellina, B.; Compagnon, I.; Bertorelle, F.; Broyer, M.; Antoine, R.; Dugourd, P.; Gell, L.; Kulesza, A.; Mitrić, R.; Bonačić-Koutecký, V. Structural and Optical Properties of Isolated Noble Metal-Glutathione Complexes: Insight into the Chemistry of Liganded Nanoclusters. *J. Phys. Chem. C* **2011**, *115*, 24549–24554. [CrossRef]
165. Zhou, M.; Song, Y. Origins of Visible and Near-Infrared Emissions in $[Au_{25}(SR)_{18}]^{-}$ Nanoclusters. *J. Phys. Chem. Lett.* **2021**, *12*, 1514–1519. [CrossRef]
166. Russier-Antoine, I.; Bertorelle, F.; Vojkovic, M.; Rayane, D.; Salmon, E.; Jonin, C.; Dugourd, P.; Antoine, R.; Brevet, P.F. Non-Linear Optical Properties of Gold Quantum Clusters. The Smaller the Better. *Nanoscale* **2014**, *6*, 13572–13578. [CrossRef]
167. Combes, G.F.; Fakhouri, H.; Moulin, C.; Girod, M.; Bertorelle, F.; Basu, S.; Ladouce, R.; Bakulić, M.P.; Maršić, Ž.S.; Russier-Antoine, I.; et al. Functionalized Au_{15} Nanoclusters as Luminescent Probes for Protein Carbonylation Detection. *Commun. Chem.* **2021**, *4*, 1–11. [CrossRef]
168. Genji Srinivasulu, Y.; Yao, Q.; Goswami, N.; Xie, J. Interfacial Engineering of Gold Nanoclusters for Biomedical Applications. *Mater. Horiz.* **2020**, *7*, 2596–2618. [CrossRef]
169. Le Guével, X.; Henry, M.; Motto-Ros, V.; Longo, E.; Montañez, M.I.; Pelascini, F.; De La Rochefoucauld, O.; Zeitoun, P.; Coll, J.L.; Josserand, V.; et al. Elemental and Optical Imaging Evaluation of Zwitterionic Gold Nanoclusters in Glioblastoma Mouse Models. *Nanoscale* **2018**, *10*, 18657–18664. [CrossRef]
170. Porret, E.; Jourdan, M.; Gennaro, B.; Comby-Zerbino, C.; Bertorelle, F.; Trouillet, V.; Qiu, X.; Zoukimian, C.; Boturyn, D.; Hildebrandt, N.; et al. Influence of the Spatial Conformation of Charged Ligands on the Optical Properties of Gold Nanoclusters. *J. Phys. Chem. C* **2019**, *123*, 26705–26717. [CrossRef]
171. Van Steerteghem, N.; Van Cleuvenbergen, S.; Deckers, S.; Kumara, C.; Dass, A.; Häkkinen, H.; Clays, K.; Verbiest, T.; Knoppe, S. Symmetry Breaking in Ligand-Protected Gold Clusters Probed by Nonlinear Optics. *Nanoscale* **2016**, *8*, 12123–12127. [CrossRef] [PubMed]
172. Yuan, X.; Goswami, N.; Mathews, I.; Yu, Y.; Xie, J. Enhancing Stability through Ligand-Shell Engineering: A Case Study with $Au_{25}(SR)_{18}$ Nanoclusters. *Nano Res.* **2015**, *8*, 3488–3495. [CrossRef]
173. Shibu, E.S.; Muhammed, M.A.H.; Tsukuda, T.; Pradeep, T. Ligand Exchange of $Au_{25}SG_{18}$ Leading to Functionalized Gold Clusters: Spectroscopy, Kinetics, and Luminescence. *J. Phys. Chem. C* **2008**, *112*, 12168–12176. [CrossRef]
174. Chung, L.W.; Sameera, W.M.C.; Ramozzi, R.; Page, A.J.; Hatanaka, M.; Petrova, G.P.; Harris, T.V.; Li, X.; Ke, Z.; Liu, F.; et al. The ONIOM Method and Its Applications. *Chem. Rev.* **2015**, *115*, 5678–5796. [CrossRef]

CURRICULUM VITAE

MARTINA PERIĆ BAKULIĆ

Date of birth:	05.04.1990.
Place of birth:	Imotski, Croatia
Nationality:	Croatian
e-mail:	martina@stim.unist

EMPLOYMENT

- **2018- present** Research Asistent/PhD at Center of Excellence for Science and Technology-Integration of Mediterranean region (STIM), University of Split, Croatia
- **2016- present** Teaching assistant (external associate) at University of Split (Faculty of Science, Department of Physics), Croatia
- **2016-2017.** Professional training (Internship) at University of Split, Croatia
- **2016-2018.** Volunteering at Interdisciplinary Center for Advanced Science and Technology (ICAST) University of Split, Croatia (Computational design of nano-bio hybrid systems, Density Functional Theory)

EDUCATION

- **2017-2022.** Postgraduate university study in Biophysics, Faculty of Science, University of Split
- **2014-2016.** Magister of physics, Faculty of Science, University of Split
- **2009-2014.** Bachelor of physics, Faculty of Science, University of Split

AWARDS AND SCHOLARSHIPS

- Dean's award at the Faculty of Natural Sciences and Mathematics, University of Split / 24.03. 2017.
- Scholarship of the Government of the French Republic for Professional Development / 2019. (Institut Lumière Matière, SpectroBio laboratory (Dr. Rodolphe Antoine), Lyon, France, 2019)

CONFERENCES AND WORKSHOPS

- Advances in Biomedical Research 2017., MedILS, Split, Croatia Nanoclusters for Better Life 2016. French-Croatian Workshop, Split, Croatia
- Annual International associated laboratory NCBA workshop 2018., Lyon, France
  LECTURE: Optical Properties of Zwitterion Liganded Gold Cluster versus Silver Doped Gold-Cystein Nanowires: Towards New Class of Nonlinear Optical Nanomaterials
- 4th Grandmaster Early-Career Workshop in Physics, 2019, University of Split, Croatia
  POSTER: Tuning nonlinear optical properties of functionalized nanoclusters
- Interdisciplinary Endeavour in Technology at Nanoscale, Water and Environment Research Workshop, 2019, University of Split, Croatia
  POSTER: Design of novel nanostructured biosensing materials and their application in medical diagnostics)
- Annual International associated laboratory NCBA workshop 2019., Lyon, France
  LECTURE: Anchoring of functionalized gold nanoclusters to carbonalyted peptides - A preliminary theoretical investigation
  LECTURE: $Au_{15}SG_{13}$ covalently bound to graphene oxide sheets. Challenging issues.

Publications

MARTINA PERIĆ BAKULIĆ

1. Anna Pniakowska, Krishnadas Kumaranchira Ramankutty, Patryk Obstarczyk, Martina Perić Bakulić, Željka Sanader Maršić, Vlasta Bonačić-Koutecký, Thomas Bürgi, Joanna Olesiak-Bańska, "Gold-doping effect on two-photon absorption and luminescence of atomically precise silver ligated nanoclusters", submitted in *Angew. Chem.*, **2022**

2. Franck Bertorelle, K. David Wegner, Martina Perić Bakulić, Hussein Fakhouri, Clothilde Comby-Zerbino, Amin Sagar, Pau Bernadó, Ute Resch-Genger, Vlasta Bonačić-Koutecký, Xavier Le Guével, and Rodolphe Antoine, "Tailoring NIR-II photoluminescence of single thiolated Au25 nanoclusters by selective binding to proteins", *Chem. Eur. J*, **2022**, **Cover page**, e202200570.

3. Dusica Maysinger, Željka Sanader Maršić, Evan Rizzel Gran, Adeola Shobo, Jun-Ray Macairan, Issan Zhang, Martina Perić Bakulić, Rodolphe Antoine, Gerhard Multhaup, and Vlasta Bonačić-Kouteck*, "Insights into the Impact of Gold Nanoclusters $Au_{10}SG_{10}$ on Human Microglia", *ACS Chem. Neurosci.*, **2022**, 13, 4, 464–476

4. Guillaume F. Combes, Ana-Marija Vučković, Martina Perić Bakulić, Rodolphe Antoine, Vlasta Bonačić-Koutecky and Katarina Trajković, "Nanotechnology in Tumor Biomarker Detection: The Potential of Liganded Nanoclusters as Nonlinear Optical Contrast Agents for Molecular Diagnostics of Cancer", *Cancers*, **2021**, 13, 16, 4206

5. Guillaume F. Combes, Hussein Fakhouri, Christophe Moulin, Marion Girod, Franck Bertorelle, Srestha Basu, Romain Ladouce, Martina Perić Bakulić, Željka Sanader

Maršić, Isabelle Russier-Antoine, Pierre-François Brevet, Philippe Dugourd, Anita Krisko, Katarina Trajković, Miroslav Radman, Vlasta Bonačić-Koutecký and Rodolphe Antoine, "Functionalized Au_{15} nanoclusters as luminescent probes for protein carbonylation detection", *Commun Chem*, **2021**, 4, 69, 2021 Editors' Highlights and Celebrating Women in Chemistry Articles collection

6. Evan Rizzel Gran, Franck Bertorelle, Hussein Fakhouri, Rodolphe Antoine, Martina Perić Bakulić, Željka Sanader Maršić, Vlasta Bonačić-Koutecký, Manon Blain, Jack Antel and Dusica Maysinger, "Size and ligand effects of gold nanoclusters in alteration of organellar state and translocation of transcription factors in human primary astrocytes", *Nanoscale*, **2021**, 13, 432, 3173-3183

7. Franck Bertorelle, Srestha Basu, Hussein Fakhouri, Martina Perić Bakulić, Pierre Mignon, Isabelle Russier-Antoine, Pierre-François Brevet, Sabu Thomas, Nandakumar Kalarikka, and Rodolphe Antoine, "Covalent anchoring of atomically precise glutathione-protected gold nanoclusters on graphene oxide nanosheets", *Nano Ex.*, **2020**, 1, 3

8. Srestha Basu, Martina Perić Bakulić, Hussein Fakhouri, Isabelle Russier-Antoine, Christophe Moulin, Pierre-François Brevet, Vlasta Bonačić-Koutecký*, and Rodolphe Antoine, "Rationale Strategy to Tune the Optical Properties of Gold Catenane Nanoclusters by Doping with Silver Atoms", *J. Phys. Chem. C*, **2020**, 124, 35, 19368–19374, **Cover page**, 10.1021/acs.jpcc.0c05402

9. Martina Perić, Željka Sanader Maršić, Isabelle Russier-Antoine, Hussein Fakhouri, Franck Bertorelle, Pierre-François Brevet, Xavier le Guével, Rodolphe Antoine and Vlasta Bonačić-Koutecký, "Ligand shell size effects on one- and two-photon excitation fluorescence of zwitterion functionalized gold nanoclusters", *Phys. Chem. Chem. Phys.*, **2019**, 21, 23916-23921, HOT PCCP Articles collection

10. Fakhouri, Hussein, Perić, Martina, Bertorelle, Franck, Dugourd, Philippe, Dagany, Xavier, Russier-Antoine, Isabelle, Brevet, Pierre-François, Bonačić-Koutecký, Vlasta, Antoine, Rodolphe, "Sub-100 nanometer silver doped gold–cysteine supramolecular

assemblies with enhanced nonlinear optical properties", *Phys. Chem. Chem. Phys.*, **2019**, 21, 23, 1463-9076, **Cover page**, HOT PCCP Articles collection

11. Clothilde Comby-Zerbino, Martina Perić, Franck Bertorelle, Fabien Chirot, Philippe Dugourd, Vlasta Bonačić-Koutecký and Rodolphe Antoine, "Catenane Structures of Homoleptic Thioglycolic Acid-Protected Gold Nanoclusters Evidenced by Ion Mobility-Mass Spectrometry and DFT Calculations", *Nanomaterials*, **2019**, 9, 3, 457

12. Vlasta Bonačić-Koutecký, Martina Perić, Željka Sanader, "Why Do Silver Trimers Intercalated in DNA Exhibit Unique Nonlinear Properties That Are Promising for Applications?", *J. Phys. Chem. Lett.*, **2018**, 9, 10, 2584–2589

Bibliography

[1] Britain), R. S. G., of Engineering (Great Britain), R. A., Nanoscience and Nanotechnologies: Opportunities and Uncertainties, ser. RS policy document. Royal Society, 2004, https://books.google.hr/books?id=D-m_SgAACAAJ

[2] Vestergaard, M., Kerman, K., Hsing, I., Tamiya, E., Nanobiosensors and Nanobioanalyses. Springer Japan, 2015, https://books.google.hr/books?id=mi2CBwAAQBAJ

[3] Feynman, R. P., "There's plenty of room at the bottom", Resonance, Vol. 16, 1959.

[4] Alvarez, M. M., Khoury, J. T., Schaaff, T. G., Shafigullin, M. N., Vezmar, I., Whetten, R. L., "Optical absorption spectra of nanocrystal gold molecules", The Journal of Physical Chemistry B, Vol. 101, No. 19, 1997, str. 3706-3712, https://doi.org/10.1021/jp962922n

[5] Bonačić-Koutecký, V., Pittner, J., Boiron, M., Fantucci, P., "An accurate relativistic effective core potential for excited states of ag atom: An application for studying the absorption spectra of agn and agn+ clusters", The Journal of Chemical Physics, Vol. 110, No. 8, 1999, str. 3876-3886, https://doi.org/10.1063/1.478242

[6] Bonačić-Koutecky, V., Veyret, V., Mitrić, R., "Ab initio study of the absorption spectra of agn (n=5–8) clusters", The Journal of Chemical Physics, Vol. 115, No. 22, 2001, str. 10 450-10 460, https://aip.scitation.org/doi/abs/10.1063/1.1415077

[7] Song, X.-R., Goswami, N., Yang, H.-H., Xie, J., "Functionalization of metal nanoclusters for biomedical applications", Analyst, Vol. 141, 2016, str. 3126-3140, http://dx.doi.org/10.1039/C6AN00773B

[8] Bonačić-Koutecký, V., Kulesza, A., Gell, L., Mitrić, R., Antoine, R., Bertorelle, F., Hamouda, R., Rayane, D., Broyer, M., Tabarin, T., Dugourd, P., "Silver

cluster–biomolecule hybrids: from basics towards sensors", Phys. Chem. Chem. Phys., Vol. 14, 2012, str. 9282-9290, http://dx.doi.org/10.1039/C2CP00050D

[9] Kulesza, A., Mitrić, R., Bonačić-Koutecký, V., "Theoretical study of structural and optical properties of noble metal cluster–dipeptide hybrids at defect centers of mgo", Phys. Chem. Chem. Phys., Vol. 14, 2012, str. 9330-9335, http://dx.doi.org/10.1039/C2CP23500E

[10] Polavarapu, L., Manna, M., Xu, Q.-H., "Biocompatible glutathione capped gold clusters as one- and two-photon excitation fluorescence contrast agents for live cells imaging", Nanoscale, Vol. 3, 2011, str. 429-434, http://dx.doi.org/10.1039/C0NR00458H

[11] Jin, R., Zeng, C., Zhou, M., Chen, Y., "Atomically precise colloidal metal nanoclusters and nanoparticles: Fundamentals and opportunities", Chemical Reviews, Vol. 116, No. 18, 2016, str. 10 346-10 413, pMID: 27585252, https://doi.org/10.1021/acs.chemrev.5b00703

[12] Qian, H., Zhu, M., Wu, Z., Jin, R., "Quantum sized gold nanoclusters with atomic precision", Accounts of Chemical Research, Vol. 45, No. 9, 2012, str. 1470-1479, pMID: 22720781, https://doi.org/10.1021/ar200331z

[13] Weerawardene, K. D. M., Häkkinen, H., Aikens, C. M., "Connections between theory and experiment for gold and silver nanoclusters", Annual Review of Physical Chemistry, Vol. 69, No. 1, 2018, str. 205-229, pMID: 29490202, https://doi.org/10.1146/annurev-physchem-052516-050932

[14] Jadzinsky, P. D., Calero, G., Ackerson, C. J., Bushnell, D. A., Kornberg, R. D., "Structure of a thiol monolayer-protected gold nanoparticle at 1.1 Å resolution", Science, Vol. 318, No. 5849, 2007, str. 430-433, https://www.science.org/doi/abs/10.1126/science.1148624

[15] Häkkinen, H., Walter, M., Grönbeck, H., "Divide and protect: capping gold nanoclusters with molecular goldthiolate rings", The Journal of Physical Chemistry B, Vol. 110, No. 20, 2006, str. 9927-9931, pMID: 16706449, https://doi.org/10.1021/jp0619787

[16] Chakraborty, I., Pradeep, T., "Atomically precise clusters of noble metals: Emerging link between atoms and nanoparticles", Chemical Reviews, Vol. 117, No. 12, 2017, str. 8208-8271, pMID: 28586213, https://doi.org/10.1021/acs.chemrev.6b00769

[17] Fang, J., Zhang, B., Yao, Q., Yang, Y., Xie, J., Yan, N., "Recent advances in the synthesis and catalytic applications of ligand-protected, atomically precise metal nanoclusters", Coordination Chemistry Reviews, Vol. 322, 2016, str. 1-29, https://www.sciencedirect.com/science/article/pii/S0010854516300066

[18] Yang, X., Wang, E. K., "Chapter 5 synthesis and applications of silver nanoclusters protected by polymers, protein, peptide and short molecules", in Functional Nanometer-Sized Clusters of Transition Metals: Synthesis, Properties and Applications. The Royal Society of Chemistry, 2014, str. 100-130, http://dx.doi.org/10.1039/9781782628514-00100

[19] Mathew, A., Pradeep, T., "Noble metal clusters: Applications in energy, environment, and biology", Particle & Particle Systems Characterization, Vol. 31, No. 10, 2014, str. 1017-1053, https://onlinelibrary.wiley.com/doi/abs/10.1002/ppsc.201400033

[20] Goswami, N., Zheng, K., Xie, J., "Bio-ncs – the marriage of ultrasmall metal nanoclusters with biomolecules", Nanoscale, Vol. 6, 2014, str. 13 328-13 347, http://dx.doi.org/10.1039/C4NR04561K

[21] Liganded silver and gold quantum clusters. Towards a new class of nonlinear optical nanomaterials. Springer, Cham, 2018, https://doi.org/10.1007/978-3-319-64743-2

[22] Göppert-Mayer, M., "Über elementarakte mit zwei quantensprüngen", Annalen der Physik, Vol. 401, No. 3, 1931, str. 273-294, https://onlinelibrary.wiley.com/doi/abs/10.1002/andp.19314010303

[23] Kaiser, W., Garrett, C. G. B., "Two-photon excitation in caf_2: eu^{2+}", Phys. Rev. Lett., Vol. 7, Sep 1961, str. 229–231, https://link.aps.org/doi/10.1103/PhysRevLett.7.229

[24] König, K., "Multiphoton microscopy in life sciences", Journal of Microscopy, Vol. 200, No. 2, str. 83-104, https://onlinelibrary.wiley.com/doi/abs/10.1046/j.1365-2818.2000.00738.x

[25] Terenziani, F., Katan, C., Badaeva, E., Tretiak, S., Blanchard-Desce, M., "Enhanced two-photon absorption of organic chromophores: Theoretical and experimental assessments", Advanced Materials, Vol. 20, No. 24, 2008, str. 4641-4678, https://onlinelibrary.wiley.com/doi/abs/10.1002/adma.200800402

[26] Takamatsu, T., Kitagawa, Y., Akimoto, K., Iwanami, R., Endo, Y., Takashima, K., Okubo, K., Umezawa, M., Kuwata, T., Sato, D., Kadota, T., Mitsui, T., Ikematsu, H., Yokota, H., Soga, K., Takemura, H., "Over 1000 nm near-infrared multispectral imaging system for laparoscopic in vivo imaging", Sensors, Vol. 21, No. 8, 2021, https://www.mdpi.com/1424-8220/21/8/2649

[27] Muhammed, M. A. H., Pradeep, T., Luminescent Quantum Clusters of Gold as Bio-Labels, Demchenko, A. P., (ur.). Berlin, Heidelberg: Springer Berlin Heidelberg, 2010, https://doi.org/10.1007/978-3-642-04701-5_11

[28] Díez, I., Ras, R. H. A., Few-Atom Silver Clusters as Fluorescent Reporters. Berlin, Heidelberg: Springer Berlin Heidelberg, 2010, str. 307–332, https://doi.org/10.1007/978-3-642-04701-5_10

[29] Yau, S. H., Varnavski, O., Goodson, T., "An ultrafast look at au nanoclusters", Accounts of Chemical Research, Vol. 46, No. 7, 2013, str. 1506-1516, pMID: 23651457, https://doi.org/10.1021/ar300280w

[30] Wu, Z., Jin, R., "On the ligand's role in the fluorescence of gold nanoclusters", Nano Letters, Vol. 10, No. 7, 2010, str. 2568-2573, pMID: 20550101, https://doi.org/10.1021/nl101225f

[31] Russier-Antoine, I., Bertorelle, F., Calin, N., Sanader, , Krstić, M., Comby-Zerbino, C., Dugourd, P., Brevet, P.-F., Bonačić-Koutecký, V., Antoine, R., "Ligand-core nlo-phores: a combined experimental and theoretical approach to the two-photon absorption and two-photon excited emission properties of small-ligated silver nanoclusters", Nanoscale, Vol. 9, 2017, str. 1221-1228, http://dx.doi.org/10.1039/C6NR07989J

[32] Bellina, B., Antoine, R., Broyer, M., Gell, L., Sanader, , Mitrić, R., Bonačić-Koutecký, V., Dugourd, P., "Formation and characterization of thioglycolic

acid–silver cluster complexes", Dalton Trans., Vol. 42, 2013, str. 8328-8333, http://dx.doi.org/10.1039/C3DT50485A

[33] Sanader, , Mitrić, R., Bonačić-Koutecký, V., Bellina, B., Antoine, R., Dugourd, P., "The nature of electronic excitations at the metal–bioorganic interface illustrated on histidine–silver hybrids", Phys. Chem. Chem. Phys., Vol. 16, 2014, str. 1257-1261, http://dx.doi.org/10.1039/C3CP52712C

[34] Russier-Antoine, I., Bertorelle, F., Hamouda, R., Rayane, D., Dugourd, P., Sanader, , Bonačić-Koutecký, V., Brevet, P.-F., Antoine, R., "Tuning ag29 nanocluster light emission from red to blue with one and two-photon excitation", Nanoscale, Vol. 8, 2016, str. 2892-2898, http://dx.doi.org/10.1039/C5NR08122J

[35] Sanader, , Krstić, M., Russier-Antoine, I., Bertorelle, F., Dugourd, P., Brevet, P.-F., Antoine, R., Bonačić-Koutecký, V., "Two-photon absorption of ligand-protected ag15 nanoclusters. towards a new class of nonlinear optics nanomaterials", Phys. Chem. Chem. Phys., Vol. 18, 2016, str. 12 404-12 408, http://dx.doi.org/10.1039/C6CP00207B

[36] Bertorelle, F., Russier-Antoine, I., Calin, N., Comby-Zerbino, C., Bensalah-Ledoux, A., Guy, S., Dugourd, P., Brevet, P.-F., Sanader, , Krstić, M., Bonačić-Koutecký, V., Antoine, R., "Au10(sg)10: A chiral gold catenane nanocluster with zero confined electrons. optical properties and first-principles theoretical analysis", The Journal of Physical Chemistry Letters, Vol. 8, No. 9, 2017, str. 1979-1985, pMID: 28398738, https://doi.org/10.1021/acs.jpclett.7b00611

[37] Bonačić-Koutecký, V., Antoine, R., "Enhanced two-photon absorption of ligated silver and gold nanoclusters: theoretical and experimental assessments", Nanoscale, Vol. 11, 2019, str. 12 436-12 448, http://dx.doi.org/10.1039/C9NR01826C

[38] Sokołowska, K., Malola, S., Lahtinen, M., Saarnio, V., Permi, P., Koskinen, K., Jalasvuori, M., Häkkinen, H., Lehtovaara, L., Lahtinen, T., "Towards controlled synthesis of water-soluble gold nanoclusters: Synthesis and analysis", The Journal of Physical Chemistry C, Vol. 123, No. 4, 2019, str. 2602-2612, https://doi.org/10.1021/acs.jpcc.8b11056

[39] Weerawardene, K. D. M., Häkkinen, H., Aikens, C. M., "Connections between theory and experiment for gold and silver nanoclusters", Annual Review of Physical Chemistry, Vol. 69, No. 1, 2018, str. 205-229, pMID: 29490202, https://doi.org/10.1146/annurev-physchem-052516-050932

[40] Knoppe, S., Häkkinen, H., Verbiest, T., Clays, K., "Role of donor and acceptor substituents on the nonlinear optical properties of gold nanoclusters", The Journal of Physical Chemistry C, Vol. 122, No. 7, 2018, str. 4019-4028, https://doi.org/10.1021/acs.jpcc.7b12356

[41] Matus, M. F., Malola, S., Kinder Bonilla, E., Barngrover, B. M., Aikens, C. M., Häkkinen, H., "A topological isomer of the au25(sr)18 nanocluster", Chem. Commun., Vol. 56, 2020, str. 8087-8090, http://dx.doi.org/10.1039/D0CC03334K

[42] Lewars, E. G., "Computational chemistry: Introduction to the theory and applications of molecular and quantum mechanics", Springer, Second Edition.

[43] Atkins, P., Friedman, R., "Molecular quantum mechanics", Oxford University Press, Fourth Edition.

[44] Jensen, F., "Introduction to computational chemistry", Wiley, Second Edition.

[45] Olsen, J., Jo/rgensen, P., "Linear and nonlinear response functions for an exact state and for an mcscf state", The Journal of Chemical Physics, Vol. 82, No. 7, 1985, str. 3235-3264, https://doi.org/10.1063/1.448223

[46] Yarkony, D. R., Modern Electronic Structure Theory. World Scientific Publishing Company, 1995, https://www.worldscientific.com/doi/abs/10.1142/1957-part2

[47] Norman, P., Bishop, D. M., Jensen, H. J. A., Oddershede, J., "Nonlinear response theory with relaxation: The first-order hyperpolarizability", The Journal of Chemical Physics, Vol. 123, No. 19, 2005, str. 194103, https://doi.org/10.1063/1.2107627

[48] Norman, P., Bishop, D. M., Jo/rgen Aa. Jensen, H., Oddershede, J., "Near-resonant absorption in the time-dependent self-consistent field and multiconfigurational self-

consistent field approximations", The Journal of Chemical Physics, Vol. 115, No. 22, 2001, str. 10 323-10 334, https://aip.scitation.org/doi/abs/10.1063/1.1415081

[49] Kristensen, J. K. T. J. P., Kasper; Kauczor, "Quasienergy formulation of damped response theory", The Journal of Chemical Physics, Vol. 131, No. 4, 2009, https://aip.scitation.org/doi/10.1063/1.3173828

[50] Sabin, S. C. E. B. J. R., "Advances in quantum chemistry, combining quantum mechanics and molecular mechanics (some recent progresses in qm/mm methods)", Volume 59, Elsevier, 2010.

[51] Ding,, L. W. C. W. M. C. S. R. R. A. J. P. M. H. G. P. P. T. V. H. X. L. Z. K. F. L. H.-B. L. L., Morokuma, K., "The oniom method and its applications", Chem. Rev., 2015, 115, 5678-5796.

[52] Bonačić-Koutecký, V., Perić, M., Sanader, , "Why do silver trimers intercalated in dna exhibit unique nonlinear properties that are promising for applications?", The Journal of Physical Chemistry Letters, Vol. 9, No. 10, 2018, str. 2584-2589, pMID: 29714485, https://doi.org/10.1021/acs.jpclett.8b00819

[53] Perić, M., Sanader Maršić, , Russier-Antoine, I., Fakhouri, H., Bertorelle, F., Brevet, P.-F., le Guével, X., Antoine, R., Bonačić-Koutecký, V., "Ligand shell size effects on one- and two-photon excitation fluorescence of zwitterion functionalized gold nanoclusters", Phys. Chem. Chem. Phys., Vol. 21, 2019, str. 23 916-23 921, http://dx.doi.org/10.1039/C9CP05262C

[54] Frisch, M. J., Trucks, G. W., Schlegel, H. B., Scuseria, G. E., Robb, M. A., Cheeseman, J. R., Scalmani, G., Barone, V., Petersson, G. A., Nakatsuji, H., Li, X., Caricato, M., Marenich, A. V., Bloino, J., Janesko, B. G., Gomperts, R., Mennucci, B., Hratchian, H. P., Ortiz, J. V., Izmaylov, A. F., Sonnenberg, J. L., Williams-Young, D., Ding, F., Lipparini, F., Egidi, F., Goings, J., Peng, B., Petrone, A., Henderson, T., Ranasinghe, D., Zakrzewski, V. G., Gao, J., Rega, N., Zheng, G., Liang, W., Hada, M., Ehara, M., Toyota, K., Fukuda, R., Hasegawa, J., Ishida, M., Nakajima, T., Honda, Y., Kitao, O., Nakai, H., Vreven, T., Throssell, K., Montgomery, J. A., Jr., Peralta, J. E., Ogliaro, F.,

Bearpark, M. J., Heyd, J. J., Brothers, E. N., Kudin, K. N., Staroverov, V. N., Keith, T. A., Kobayashi, R., Normand, J., Raghavachari, K., Rendell, A. P., Burant, J. C., Iyengar, S. S., Tomasi, J., Cossi, M., Millam, J. M., Klene, M., Adamo, C., Cammi, R., Ochterski, J. W., Martin, R. L., Morokuma, K., Farkas, O., Foresman, J. B., Fox, D. J., "Gaussian~16 Revision C.01", gaussian Inc. Wallingford CT. 2016.

[55] Katz, E., Willner, I., "Integrated nanoparticle–biomolecule hybrid systems: Synthesis, properties, and applications", Angewandte Chemie International Edition, Vol. 43, No. 45, 2004, str. 6042-6108, https://onlinelibrary.wiley.com/doi/abs/10.1002/anie.200400651

[56] Roco, M. C., "Nanotechnology: convergence with modern biology and medicine", Current Opinion in Biotechnology, Vol. 14, No. 3, 2003, str. 337-346, https://www.sciencedirect.com/science/article/pii/S0958166903000685

[57] Ruiz-Hitzky, E., Darder, M., Aranda, P., An Introduction to Bio-nanohybrid Materials. John Wiley Sons, Ltd, 2007, ch. 1, str. 1-40, https://onlinelibrary.wiley.com/doi/abs/10.1002/9783527621446.ch1

[58] Guo, Z., Richardson, J. J., Kong, B., Liang, K., "Nanobiohybrids: Materials approaches for bioaugmentation", Science Advances, Vol. 6, No. 12, 2020, str. eaaz0330, https://www.science.org/doi/abs/10.1126/sciadv.aaz0330

[59] Peyser-Capadona, L., Zheng, J., González, J. I., Lee, T.-H., Patel, S. A., Dickson, R. M., "Nanoparticle-free single molecule anti-stokes raman spectroscopy", Phys. Rev. Lett., Vol. 94, Feb 2005, str. 058301, https://link.aps.org/doi/10.1103/PhysRevLett.94.058301

[60] Petty, J. T., Zheng, J., Hud, N. V., Dickson, R. M., "Dna-templated ag nanocluster formation", Journal of the American Chemical Society, Vol. 126, No. 16, 2004, str. 5207-5212, pMID: 15099104, https://doi.org/10.1021/ja031931o

[61] Petty, J. T., Zheng, J., Hud, N. V., Dickson, R. M., "Dna-templated ag nanocluster formation", Journal of the American Chemical Society, Vol. 126, No. 16, 2004, str. 5207-5212, pMID: 15099104, https://doi.org/10.1021/ja031931o

[62] Vosch, T., Antoku, Y., Hsiang, J.-C., Richards, C. I., Gonzalez, J. I., Dickson, R. M., "Strongly emissive individual dna-encapsulated ag nanoclusters as single-molecule fluorophores", Proceedings of the National Academy of Sciences, Vol. 104, No. 31, 2007, str. 12 616-12 621, https://www.pnas.org/doi/abs/10.1073/pnas.0610677104

[63] Yau, S. H., Abeyasinghe, N., Orr, M., Upton, L., Varnavski, O., Werner, J. H., Yeh, H.-C., Sharma, J., Shreve, A. P., Martinez, J. S., Goodson III, T., "Bright two-photon emission and ultra-fast relaxation dynamics in a dna-templated nanocluster investigated by ultra-fast spectroscopy", Nanoscale, Vol. 4, 2012, str. 4247-4254, http://dx.doi.org/10.1039/C2NR30628J

[64] Petty, J. T., Story, S. P., Hsiang, J.-C., Dickson, R. M., "Dna-templated molecular silver fluorophores", The Journal of Physical Chemistry Letters, Vol. 4, No. 7, 2013, str. 1148-1155, pMID: 23745165, https://doi.org/10.1021/jz4000142

[65] Maksimov, D., Pomogaev, V., Kononov, A., "Excitation spectra of ag3–dna bases complexes: A benchmark study", Chemical Physics Letters, Vol. 673, 2017, str. 11-18, https://www.sciencedirect.com/science/article/pii/S0009261417301069

[66] Buceta, D., Busto, N., Barone, G., Leal, J. M., Domínguez, F., Giovanetti, L. J., Requejo, F. G., García, B., López-Quintela, M. A., "Ag2 and ag3 clusters: Synthesis, characterization, and interaction with dna", Angewandte Chemie International Edition, Vol. 54, No. 26, 2015, str. 7612-7616, https://onlinelibrary.wiley.com/doi/abs/10.1002/anie.201502917

[67] Puddephatt, R. J., "Macrocycles, catenanes, oligomers and polymers in gold chemistry", Chem. Soc. Rev., Vol. 37, 2008, str. 2012-2027, http://dx.doi.org/10.1039/B708622A

[68] Nie, H., Li, M., Hao, Y., Wang, X., Zhang, S. X.-A., "Time-resolved monitoring of dynamic self-assembly of au(i)-thiolate coordination polymers", Chem. Sci., Vol. 4, 2013, str. 1852-1857, http://dx.doi.org/10.1039/C3SC22215B

[69] Nie, H., Li, M., Hao, Y., Wang, X., Gao, S., Wang, P., Ju, B., Zhang, S. X.-A., "Morphology modulation and application of au(i)–thiolate nanostructures", RSC Adv., Vol. 4, 2014, str. 50 521-50 528, http://dx.doi.org/10.1039/C4RA06500J

[70] Zeng, C., Liu, C., Chen, Y., Rosi, N. L., Jin, R., "Atomic structure of self-assembled monolayer of thiolates on a tetragonal au92 nanocrystal", Journal of the American Chemical Society, Vol. 138, No. 28, 2016, str. 8710-8713, pMID: 27355843, https://doi.org/10.1021/jacs.6b04835

[71] "Front cover", Phys. Chem. Chem. Phys., Vol. 21, 2019, str. 12 047-12 047, http://dx.doi.org/10.1039/C9CP90159K

[72] König, J., Jung, T., Grune, T., Protein Carbonylation in Aging and Senescence. John Wiley Sons, Ltd, 2017, ch. 11, str. 272-290, https://onlinelibrary.wiley.com/doi/abs/10.1002/9781119374947.ch11

[73] Combes, G. F., Vučković, A.-M., Perić Bakulić, M., Antoine, R., Bonačić-Koutecky, V., Trajković, K., "Nanotechnology in tumor biomarker detection: The potential of liganded nanoclusters as nonlinear optical contrast agents for molecular diagnostics of cancer", Cancers, Vol. 13, No. 16, 2021, https://www.mdpi.com/2072-6694/13/16/4206


UNIVERSITY OF SPLIT
STIM